Optical Modelling and Instrument Calibration for QUBIC, the Q & U Bolometric Interferometer for Cosmology

by

James Murphy, BSc (Hons)

A thesis submitted for the degree of
Doctor of Philosophy

National University of Ireland, Maynooth
Faculty of Science and Engineering
Experimental Physics Department

August 2022

Head of Department:

Dr. Créidhe O'Sullivan

Supervisor:

Dr. Créidhe O'Sullivan

Contents

NATIONAL UNIVERSITY OF IRELAND, MAYNOOTH

Abstract

Faculty of Science and Engineering
Experimental Physics Department

Doctor of Philosophy

by James Murphy, BSc (Hons)

The current generation of cosmology experiments aims to detect the B-mode polarisation of the cosmic microwave background. The B-modes are experimental proof for the Inflation theory of the early Universe. This thesis contributes to the development, integration, and deployment of one of those experiments, QUBIC. A detailed Physical Optics model of a technical demonstrator optical combiner was developed using the software package GRASP. This model included measured mirror surfaces and rims as well as the internal sources used for the inter-calibration of the detectors. The data produced by these models were used for validation and calibration of the instrument in the laboratory in Astroparticule et Cosmologie in Paris. The models were then expanded to encompass the full QUBIC instrument that will later be deployed in Argentina. A contribution was made to the bespoke QUBIC data analysis software and a project milestone was reached when the first multi-frequency synthesised beam maps were produced in July 2020, thereby demonstrating QUBIC's spectro-imaging capability. Zemax ray-tracing was used to investigate possible optical causes for artefacts that were found in early beam maps. A study of the likely characteristics of the artefacts generated by optical reflections and electronic cross-talk was produced for future reference. Lastly, the application to QUBIC of redundant baseline self-calibration was investigated. Originally developed for radio astronomy, aberrations due to the instrument's off-axis optics have implications for QUBIC's implementation of this calibration technique. At the time of writing, QUBIC has been tested and is being assembled and commissioned in Salta, Argentina, ready to begin observing in the coming months.

Acknowledgements

I never could have imagined that I would be part of an international team building a telescope in Paris and sending it to a high mountain in Argentina to learn about the origins of the Universe. But here we are. There is a long list of friends, family, and colleagues who have supported me throughout my PhD research and are deserving of recognition. The list is impossible to complete here so to those unspecified, you know who you are, thank you.

First and foremost is my supervisor, Dr. Créidhe O'Sullivan. Her guidance was invaluable and taught me more about being a researcher and physicist than I knew there was to learn. It has been an honour to be her student.

Working with the QUBIC collaboration has given me the opportunity to work with and learn from enumerable academic leaders and colleagues from a range of fields in physics and engineering. Thank you to the entire QUBIC team, who have always been supportive and enthusiastic of my research and always ready to collaborate. Dr Jean-Christophe Hamilton, thank you for all your support and inputs on my QUBIC research and your steady hand steering QUBIC to success. Dr Steve Torchinsky's technical wizardry has facilitated the instrument data-analysis throughout this thesis. I am also grateful to have worked with Dr Louise Mousset and Martín Gamboa Lerena who shared extremely useful QUBIC code. Dr Marco De Petris, Dr Michele De Leo, and Dr Antonio Zullo shared useful data that were used in this thesis, thank you.

The staff of the Experimental Physics Department in Maynooth have welcomed and supported me like family. Thank you. I am hugely grateful to Donnacha Gayer and Dr David Burke for working closely with me on optical problems with QUBIC and have provided me with data and models from their own research that saved me countless hours. To my colleagues from the department who I now call my friends, thank you for all of the fruitful and unproductive distractions.

I could not have done this thesis without the support of my close family. My mother, Bríd, has supported me without falter through all of my academic study and goals in life. Her bravery in the face of adversity inspired me throughout my thesis to keep going. The reliable steadfastness of my sister, Aisling, has been integral to the completion of this thesis, thank you. My grandparents, Bríd and Seán, made it possible for me to switch from arts to physics during my undergraduate

study and never even questioned the insanity of it at the time. Without them I would not have had these wonderful years as part of the QUBIC collaboration. My father, Joe, always encouraged the insanity. To my loving girlfriend Laura, who has become a proficient and vocal critic of experimental cosmology research, thank you.

I would also like to acknowledge and express my utmost gratitude to the Irish Research Council. Without the scholarship, none of this would have been possible to begin with.

Go raibh míle maith agaibh.

"We are like dwarfs on the shoulders of giants, so that we can see more than they, and things at a greater distance, not by virtue of any sharpness of sight on our part, or any physical distinction, but because we are carried high and raised up by their giant size."

Attributed to Bernard De Chartres c. 1130

Dedicated to my mother, whose strength and resilience was an ever present inspiration throughout.

List of Figures

List of Tables

Abbreviations

APC	**A**stro**P**article et **C**osmologie
AIG	**A**stronomy **I**nstrumentation **G**roup (Cardiff)
AGN	**A**ctive **G**alactic **N**ucleus
APC	**A**stro **P**article et **C**osmologie
ASIC	**A**pplication **S**pecific **In**ntegrated **C**ircuit
BI	**B**olometric **I**nterferometry
BICEP	**B**ackground **I**maging of **C**osmic **E**xtragalatic **P**olarisation
BRAIN	**B**ackground **RA**diation **IN**terferometer
CDM	**C**old **D**ark **M**atter
CAD	**C**omputer **A**ided **D**esign
CF	**C**arbon **F**ibre
CMB	**C**osmic **M**icrowave **B**ackground
CPU	**C**central **P**rocessing **U**nit
CS	**C**old **S**top
COBE	**C**osmic **B**ackground **Ex**plorer
DMR	**D**ifferential **M**icrowave **R**adiometers
CS	**C**old-**S**top
EM	**E**electro**M**agnetic
FB	**F**ore**b**affle
FFT	**F**ast **F**ourier **T**ransform
FI	**F**ull **I**nstrument
FIRAS	**F**ar **I**nfrared **A**bsolute **S**pectrophotometer
FPGA	**F**ield **P**rogrammable **G**ate **A**rray
FWHM	**F**ull **W**idth **H**alf **M**ax

GBM	**G**aussian **B**eam **M**ode
GRF	**G**lobal **R**eference **F**rame
GS	**G**round **S**hield
GO	**G**eometric **O**ptics
GUI	**G**graphical **U**ser **I**nterface
HFI	**H**igh **F**requency **I**nstrument
HWP	**H**alf **W**ave **P**late
ICFCS	**I**nternal **C**arbon **F**ibre **C**alibration **S**ource
IR	**I**nfra**r**ed
LPE	**L**ow **P**ass **E**dge
LPF	**L**ow **P**ass **F**ilter
MBI	**M**illimeter-wave **B**olometric **I**nterferometer
MU	**M**aynooth **U**niversity
NDF	**N**eutral **D**ensity **F**ilter
PO	**P**hysical **O**ptics
PSF	**P**oint **S**pread **F**unction
PTC	**P**ulse **T**ube **C**ryocooler
PTD	**P**hysical **T**heory of **D**iffraction
QUAD	**Q**UEST **a**t **D**ASI
QUBIC	**Q** & **U** **B**olometric **I**nterferometer for **C**osmology
RGB	**R**ed **G**reen **B**lue
RF	**R**adio **F**requency
RFI	**R**adio **F**requency **I**nterference
RMSE	**R**oot **M**ean **S**quared **E**rror
SNR	**S**ignal-to-**N**oise **R**atio
SQUID	**S**uperconducting **QU**antum **I**nterface **D**evice
TD	**T**echnical **D**emonstrator
TES	**T**ransition **E**dge **S**ensor
TOD	**T**ime **O**rdered **D**ata
UHMW-PE	**U**ltra **H**igh **M**olecular **W**eight **P**olyethylen**e**
WMAP	**W**ilkinson **M**icrowave **A**nisotropy **P**robe

Chapter 1

Introduction

1.1 Introduction

This thesis contributes optical modelling and calibration data analysis for a cosmology telescope called QUBIC. It is planned to use this instrument to study the early Universe. In particular, QUBIC aims to detect B-mode Cosmic Microwave Background (CMB) polarisation anisotropies and thereby find evidence for Inflation, the theory that the Universe expanded exponentially at early times. This thesis began at an exciting time in QUBIC's lifecycle. All components had been designed, manufactured, and sent to a laboratory in Paris for integration and calibration. Four years later, the thesis ends at another exciting stage in QUBIC's lifecycle; QUBIC has just been shipped to Argentina for a final integration before being deployed on-site in Alto Chorrillo for sky observations. Each chapter of this thesis has the overall goal of aiding the calibration and validation of the instrument in preparation for scientific observations of the CMB.

The QUBIC telescope is unique in the fact that it is a bolometric interferometer. This design choice was made so the instrument would have the sensitivity of an imager and the control of systematic effects provided by an interferometer. Systematic effects due to the instrument are a critical issue, making detection of the faint B-mode CMB polarisation anisotropy extremely difficult. The B-mode signal is so weak that the inherent instrument noise and uncertainty in modern cosmology experiments far exceeds the level of the B-mode. There are also Galactic and extra-galactic foregrounds that add strong contamination to a CMB polarisation observations. QUBIC will use a novel technique called spectro-imaging to separate

the foreground contamination and redundant baseline self-calibration to constrain the systematic effects. It is QUBIC's interferometer design that enables QUBIC to characterise and subtract its own systematics, via self-calibration, so that the faint B-mode can be detected[1].

The Experimental Physics Department in the National University of Ireland, Maynooth, also known as Maynooth University (MU), specialises in quasi-optical physics and has contributed to many ground-breaking cosmology and astrophysical telescope experiments in the past such as QUAD (Hinderks et al., (2009) [1]), Planck (Murphy et al., (2010) [2]), and the Herschel Space Observatory (Trappe et al., (2003) [3]). The Experimental Physics Department of MU has provided the QUBIC collaboration with specialised optical modelling expertise in the quasi-optical millimetre-wave region of the electromagnetic (EM) spectrum. This effort has been led by the supervisor of this thesis, Dr. Créidhe O'Sullivan. The QUBIC project originates from the merger of two earlier instruments: the Millimeter-wave Bolometric Interferometer (MBI) (Tucker et al., (2003) [4]) and the Background RAdiation INterferometer (BRAIN) (Polenta et al., (2007) [5]).

This thesis leverages MU's optical expertise to provide model predictions and to analyse calibration measurement data in order to test, validate, and optimise the instrument. This thesis, therefore, contains chapters with typical optical modelling outputs, instrument calibration via data analysis, and chapters that combine both of these aspects. The thesis will first describe the background theory motivating the QUBIC experiment.

1.2 The Cosmic Microwave Background Radiation

1.2.1 The Discovery of the CMB

In 1929, Hubble discovered the velocity-redshift relation for distant galaxies, thereby providing the first observational evidence for the expansion of the Universe (Hubble (1929) [6]). These observations agreed with the theoretical predictions of Lemaître that the Universe was expanding and cooling (Lemaître (1924) [7]). Lemaître

[1]This aspect is explained and developed in Chapter 8.

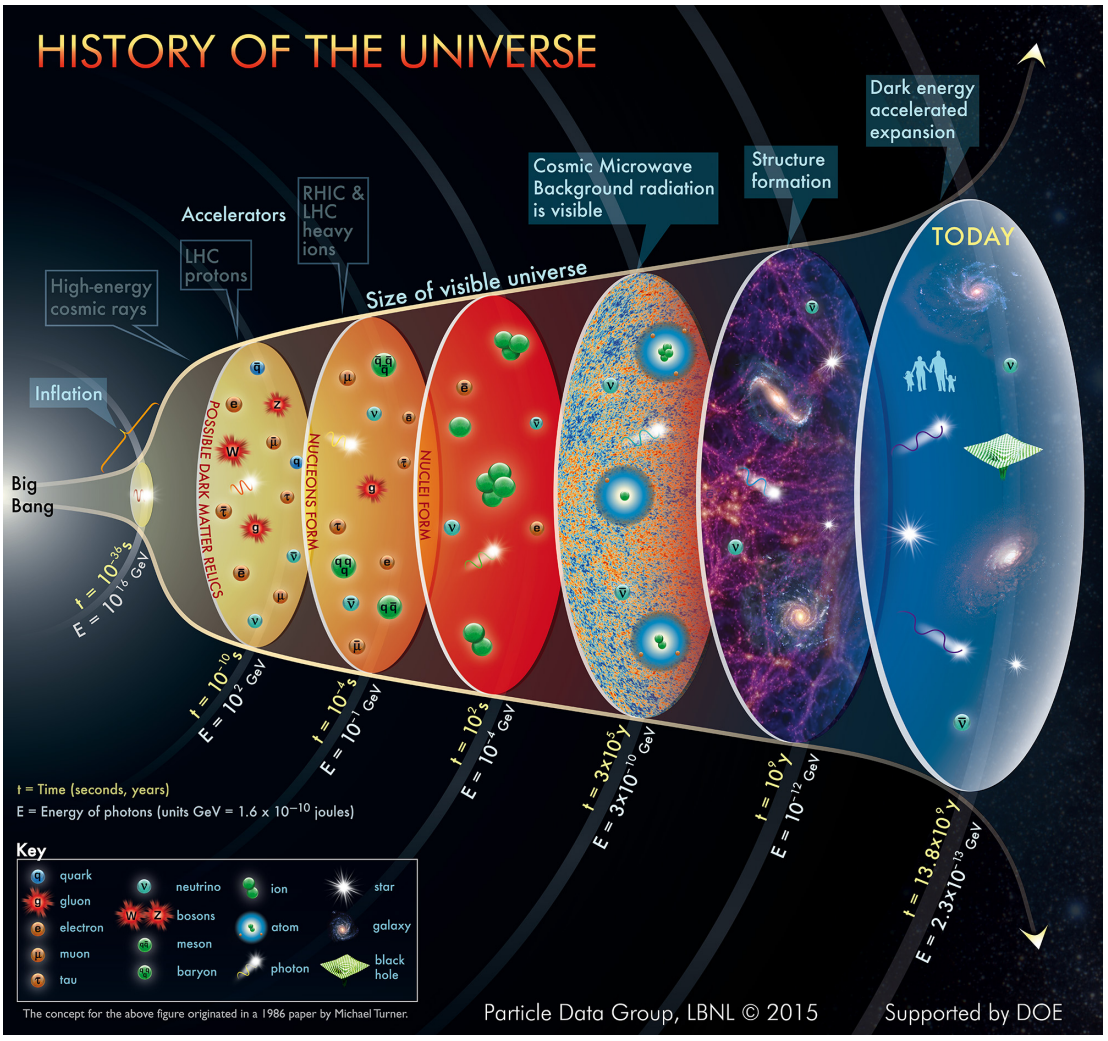

Figure 1.1: An illustration of the evolution of the Universe from the Big Bang until present time. It serves also as a description of the Λ CDM standard model of cosmology. In the first moments after the Big Bang, the universe was a hot and dense primordial plasma which eventually cooled and allowed photons to free-stream and form the CMB. Density perturbations at photon decoupling seeds the large scale structure of the Universe today. *Image credit: Particle Data Group at Lawrence Berkeley National Lab.*

based his work on the Friedman equations (Friedmann (1922) [8]), which are in turn based on developments in General Relativity by Einstein (1917) [9] and de Sitter (1917) [10]. These core theoretical predictions in the 1920s set the stage for the rapid development of a new and distinct field of scientific study.

In 1948, Gamow described a Universe based on Lemaître's expanding and cooling universe which predicted a background of cosmic radiation from the early hot and dense period (Alpher, Bethe, and Gamow (1984) [11]). This is illustrated in Fig. 1.1 and is the modern view of the evolution of the Universe as proposed by Gamow and subsequently developed by modern precision cosmology. Gamow's

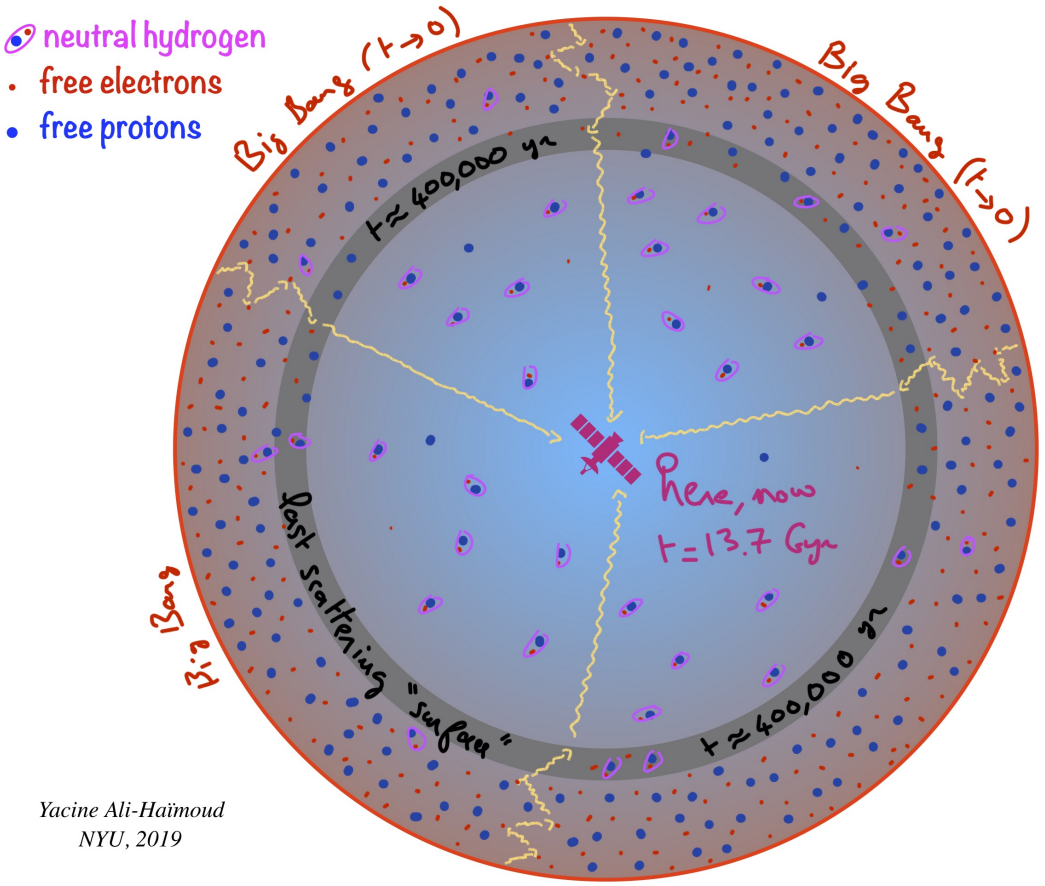

Figure 1.2: This image illustrates the surface of last scattering and how photons travel freely from this time. Before this, Thompson scattering of photons from free electrons kept the mean free path of photons short.

key prediction was that a remnant uniform microwave background would exist and be isotropic over the entire sky.

The microwave background was detected accidentally in 1965 by Penzias and Wilson with a newly built satellite communication antenna when background radiation was observed in all directions. Simultaneously, another research group (with Dicke, Peebles, Roll, and Wilkenson) were planning to build a telescope to make the observation as predicted by Gamow (and Alpher and Hermann). This led to the two groups publishing papers detailing the detection of the CMB at 3 K (Penzias and Wilson (1965) [12] and Dicke, Peebles, Roll, and Wilkenson (1965) [13]). Penzias and Wilson were awarded the Nobel Prize for this landmark achievement.

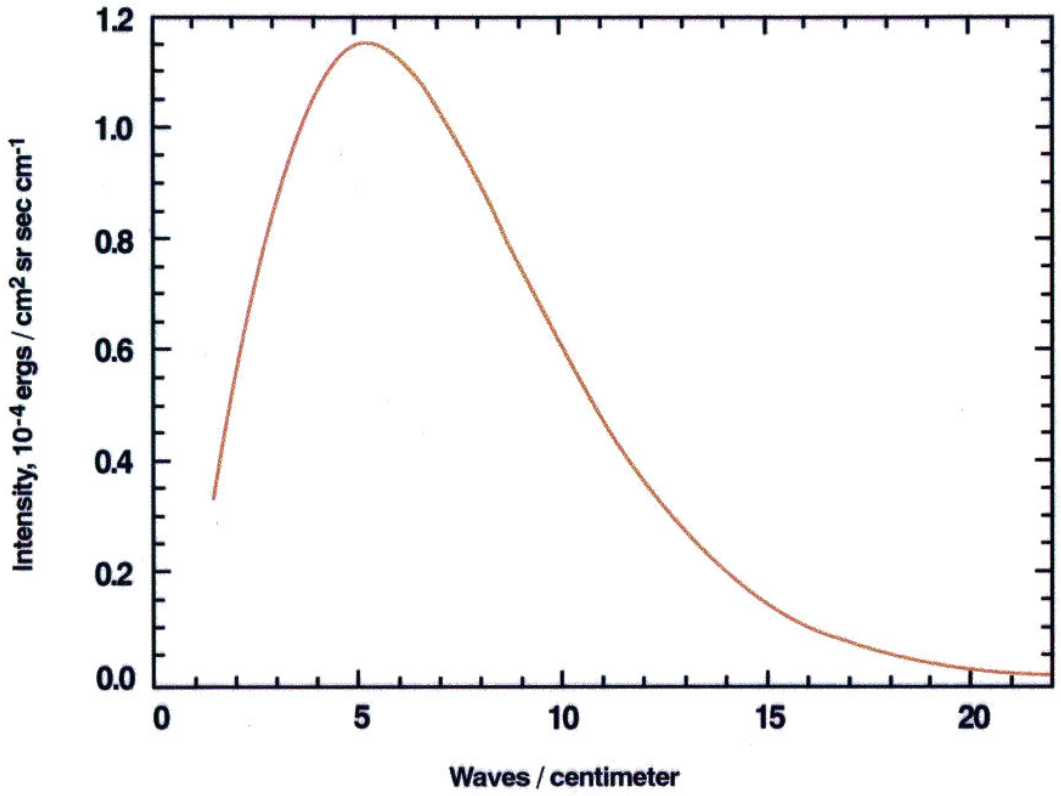

Figure 1.3: Blackbody spectrum measured by the FIRAS instrument on COBE. It measured the CMB temperature as 2.763 K. The error bars are smaller than the linewidth.

1.2.2 The Origin of the CMB

In the initial phases, the Universe was a hot and dense primordial particle soup. Photons ionized atoms as they formed and Thomson scattering from the free electrons kept the mean-free-path of photons short. After 380,000 years the density and temperature of the plasma decreased so that neutral atoms could form (recombination). The Thomson scattering cross section for photons reduced significantly allowing them to travel freely. Where they were last scattered is called the surface of last scattering. Fig. 1.2 shows how photons travelling freely from this time make up the CMB. These photons were the ones observed by Penzias and Wilson. The CMB is the earliest possible observable feature of the Universe and is therefore the prime target of cosmological observation efforts.

The cosmological redshift that occurs as the Universe expands has reduced the temperature of the photons since recombination but they retain their blackbody spectral profile from the hot dense phase. The FIRAS instrument onboard NASA's COBE satellite telescope was able to measure the CMB spectrum with precision

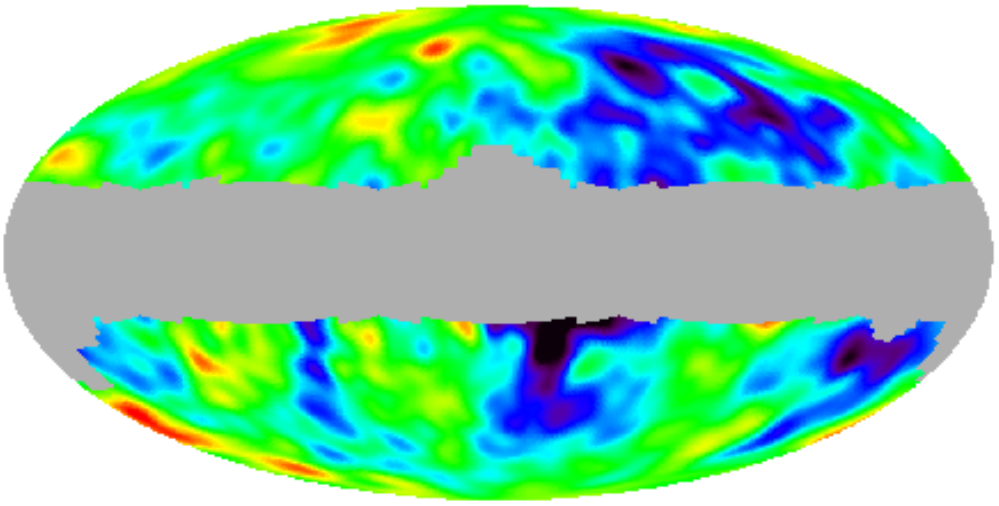

Figure 1.4: COBE DMR 4 year dataset measuring the CMB temperature anisotropy. The Doppler dipole and galactic plane are removed (grey).

and found a fit of the data to a blackbody spectrum at $2.726 \pm 0.010\,\mathrm{K}$. This measurement was described by Mather et al., (1994) [14] and is shown in Fig. 1.3, where the error bars are smaller than the linewidth and the profile is that of a perfect blackbody. This was excellent observational evidence in favour of the Big Bang theory.

1.3 Anisotropies of the CMB

1.3.1 Temperature Anisotropies

Although COBE measured a near-perfectly uniform blackbody spectrum for the CMB, there are reasons to expect to see features in the temperature maps of the surface of last scattering (known as temperature anisotropies). The Doppler effect, due to the Earth's motion through the Universe, results in a dipole anisotropy and this was detected by the DMR instrument on COBE (Smoot et al., (1992) [15]). Due to its non-primordial origin, the dipole is normally subtracted from CMB maps (as in Fig. 1.4) and this anisotropy will not be discussed further.

The perturbations in the primordial plasma that would later go on to form the structure (of galactic groups, superclusters, etc.) seen today also leaves imprints in the form temperature anisotropies. At the time of last scattering, photons coming from over-dense regions are more energetic than those from rarefied regions

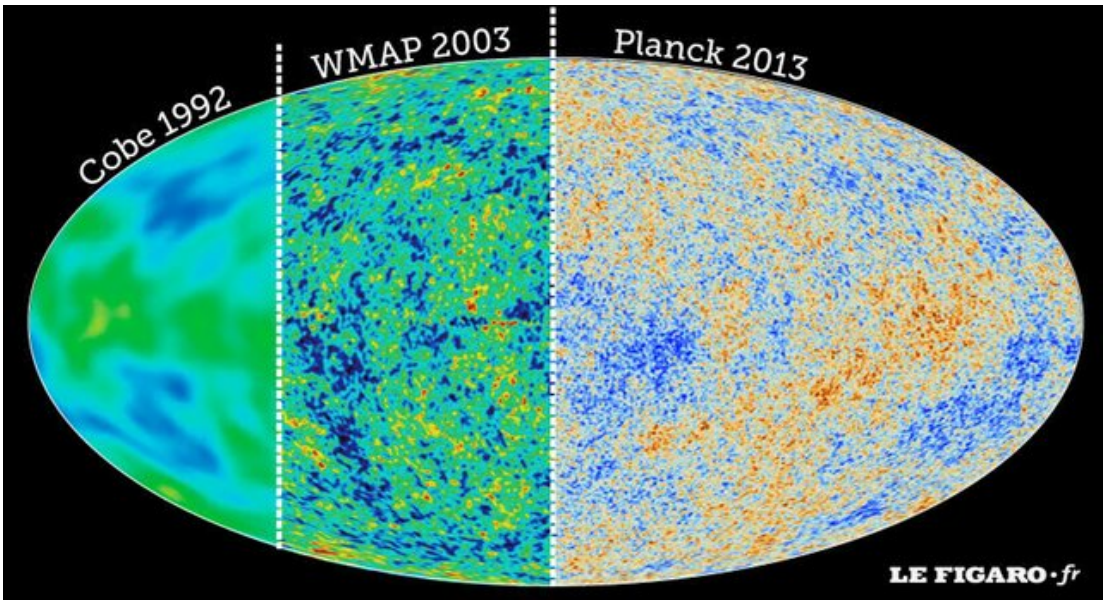

Figure 1.5: Examples of sky maps produced by the landmark CMB satellites COBE, WMAP, and Planck. Each one provided higher precision measurements of the CMB anisotropies. *Image credit: Vazquez, Padilla, and Matos (2020) [16].*

resulting in faint temperature anisotropies (see Sachs and Wolfe (1967) [17] and Hu and Dodelson (2002) [18] for a detailed discussion). These primordial anisotropies were first imaged by the COBE satellite with ever improving measurements (Fig. 1.5) coming from the subsequent missions of WMAP (Bennett et al., (2013) [19]) and Planck (Aghanim et al., (2020) [20]).

1.3.2 The Angular Power Spectrum

Temperature anisotropies are most practically analysed using an angular power spectrum such as that in Fig. 1.6. In a power spectrum, the temperature anisotropy (ΔT) distribution from a map, such as those in Fig. 1.5, is expanded in terms of spherical harmonics, $Y_{\ell m}(\theta, \phi)$:

$$\frac{\Delta T(\theta, \phi)}{T_o} = \sum_{\ell m} a_{\ell m} Y_{\ell m}(\theta, \phi) \tag{1.1}$$

where $a_{\ell m}$ are the expansion coefficients (multipole moments ℓ).

The ℓ multipole gives the angular scale on the sky ($\theta \approx \frac{180^\circ}{\ell}$). $\ell = 0$ is the sky multipole ($T_{CMB} = 2.725$ K) and $\ell = 1$ is the dipole, usually excluded as mentioned

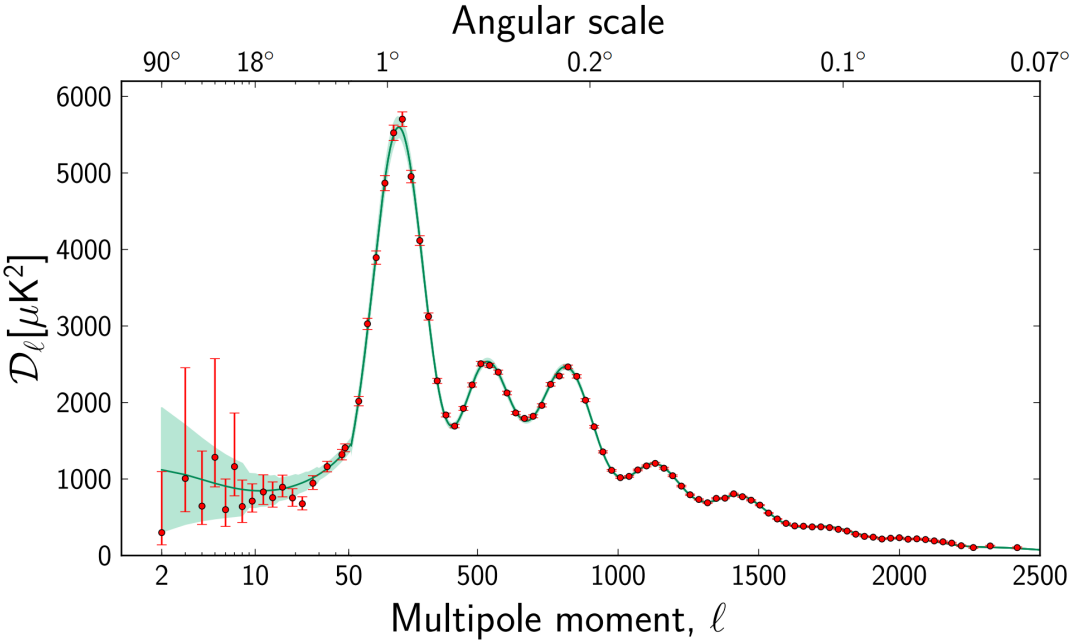

Figure 1.6: The CMB temperature anisotropy measured by the Planck Collaboration (2014) [21]. The lower horizontal axis shows the multipole moments and are related to angular scale in the sky as shown on the upper horizontal axis. The highest temperature anisotropy power occurs at $\approx 1^\circ$ on the sky. The fitted line is that from a six-parameter cosmological model as described in Section 1.5 and the shaded region is the cosmic and sample variance of the fit.

before. The QUBIC instrument is particularly interested in multipoles between $30 < \ell < 200$ (O'Sullivan et al., (2018) [22]). The power in the anisotropies for a given ℓ is given by $D_\ell = \frac{\ell(\ell+1)}{2\pi} C_\ell$ where C_ℓ is calculated by summing over the $2\ell + 1$ independent m harmonics for each multipole, $C_\ell = \langle \sum_m a_{\ell m}^2 \rangle$.

1.3.3 Polarisation Anisotropies

The primordial density perturbations which generate the temperature anisotropies also lead to a polarisation anisotropy in the CMB. Thomson scattering of photons with a quadrupole temperature anisotropy gives rise to a linear polarisation (Fig. 1.7) as described by, for example, Hu and Dodelson (2002) [18]. Quadrupole temperature anisotropies can be described as scalar ($m = 0$), vector ($m = 1$), or tensor ($m = 2$) (Hu and White (1997) [23]). Scalar perturbations arise from the density perturbations while tensor perturbations arise from gravitational waves. Vector perturbations are not expected since there is no physical mechanism for them given by the theory. The total polarisation anisotropy is at the level of about 10% of the temperature anisotropy.

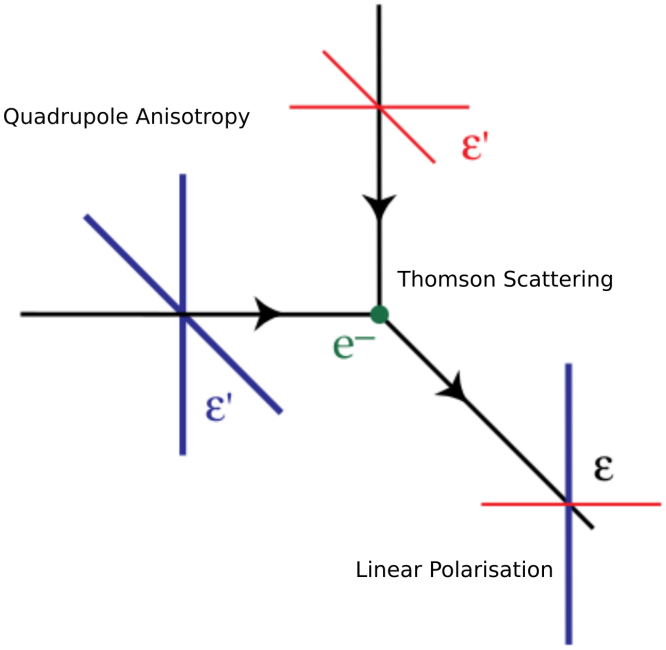

Figure 1.7: Thomson scattering occurs as a quadrupole is formed between over-dense and under-dense regions. Photons from over-dense regions (blue) are higher intensity when compared to photons from the under-dense region (red). Linearly polarised photons are emitted. Reproduced from Hu and White (1997) [23].

While, in practice, polarisation measurements are often made and described in terms of the Stokes parameters I, Q, and U (leading to the adoption of the Q and U in QUBIC), the Stokes Q and U parameters are not invariant under rotation, and it is useful instead to discuss polarisation in terms of the coordinate independent parameters E (curl-free) and B (divergence-free). These are the so called E and B-modes of the CMB polarisation anisotropy. Power spectra for these modes can be constructed in the same way as for the temperature anisotropies. This decomposition is also particularly useful because the scalar density perturbations result in only E-mode polarisation anisotropies, whereas B-modes, a much weaker signal, are produced by gravitational waves. An example of temperature and polarisation spectra are shown in Fig. 1.8. The tensor-to-scalar ratio, r, is a measure of the power in the B-modes relative to that in the E-modes.

The cosmic angular power spectrum, as shown by Fig. 1.8, is commonly used to show and compare the relative contributions of the different anisotropies of the CMB as a function of angular scale (l-multipole). This type of plot demonstrates the faintness of the B-mode polarisation anisotropy in comparison to the E-mode

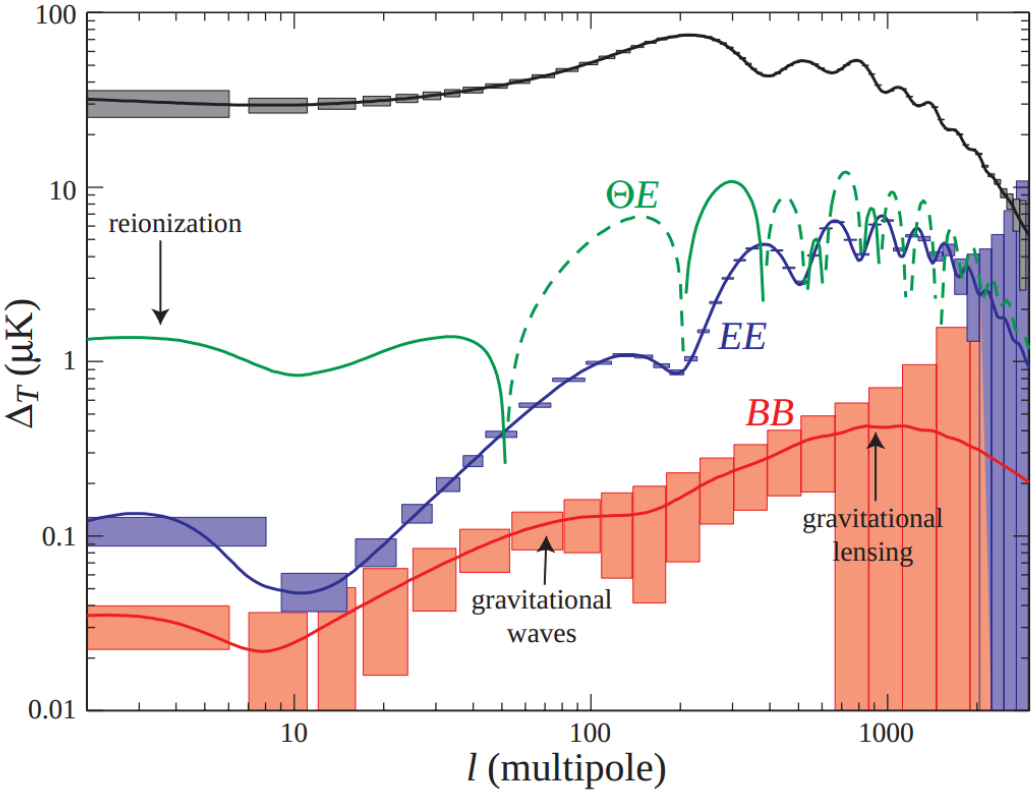

Figure 1.8: Angular power spectra for the CMB anisotropies are shown here. The grey/black line is the temperature anisotropy. EE is the E-mode polarisation anisotropy and BB is the B-mode polarisation anisotropy. ΘE is the temperature-E-mode correlation. The figure illustrates how B-modes from gravitational waves and from lensing occur at different multipoles (Section 1.6). Reproduced from Hu and Dodelson (2002) [18].

polarisation anisotropy and temperature anisotropy.

1.4 Inflation

While the Big Bang theory successfully predicts many of the observed features of the Universe, including the CMB, there are several important observations that cannot be explained.

- Regions of the CMB that are more than a few degrees apart should never have been in causal contact (due to the expansion of the Universe and the speed of light, some regions of space can never exchange information or reach thermal equilibrium), making the similarity of their temperatures difficult to explain. This is known as the horizon problem.

- The Universe has been measured to be geometrically flat (the density parameter $\Omega = 1$, see Section 1.5) even though this is an unstable state and there has been ample time and conditions for Ω to deviate from one. This implies that there must be some fine-tuning in place. This is referred to as the flatness problem.
- Grand unified theories predict that the Big Bang should have led to the creation of an abundant amount of exotic particles, such as magnetic monopoles, which are not observed.

The theory of Inflation (proposed by Guth (1981) [24] and more recently discussed by Vazquez, Padilla, and Matos (2020) [16]) is an enhancement of the Big Bang theory. It proposed a short period of exponential expansion of the Universe shortly after the Big Bang ($t = 1 \times 10^{-36}$ s, illustrated in Fig. 1.1). The superluminal expansion of the Universe during inflation means that regions which were in casual contact before (and so could be in thermal equilibrium) were no longer so, explaining the horizon problem. The expansion also causes the dilution of the curvature of space-time, making the observable universe appear flat, solving the flatness problem, and the exotic particles could only form during the very brief time before Inflation.

The theory of Inflation is an attractive one and cosmologists are now searching for observational proof. One key prediction of the theory is the production of gravitational waves which propagate through the universe as it expands and cools. The gravitational waves would leave behind a signature in the form of faint B-mode polarisation anisotropies. The goal of many contemporary CMB experiments is to measure this B-mode polarisation.

1.5 ΛCDM

The current concordance Big Bang model (the standard cosmological model) is known as the ΛCDM model. It describes a Universe that contains three main components: dark energy (described by the cosmological constant Λ), cold dark matter (CDM), and ordinary baryonic matter. The model requires six independent parameters, and derives others from them. A common choice for the independent parameters in shown in Table 1.1. The tensor-to-scalar ratio, r, can be derived

Parameter	Symbol	Measurement
Total matter density	$\Omega_c h^2$	0.1198 ± 0.0012
Baryon density	$\Omega_b h^2$	0.02233 ± 0.00015
Ionization optical depth	τ	0.0540 ± 0.0074
Angular acoustic scale	$100\theta_{MC}$	1.04089 ± 0.00031
Scalar spectral index	n_s	0.9652 ± 0.0042
Marginalized amplitude parameter	$ln(10^{10}A_s)$	3.043 ± 0.014
Tensor-to-scalar ratio	r	<0.036 @ 95%CL

Table 1.1: The six independent cosmological parameters as measured by the Planck satellite. These data are based on the Planck TT, TE, EE+lowE+lensing results from the 2018 release (Aghanim et al., (2020) [20]). The last parameter, r, is a derived quantity and the latest measurement is from BICEP/Keck Collaboration (2021) [25].

from these and the current best upper limit is given in Table 1.1. The aim of experiments such as QUBIC is to measure r (which depends on the energy scale of Inflation), a non-zero value which is a key predictor of Inflation.

1.6 Polarised Foregrounds

The B-mode signal is extremely faint and detecting the primordial B-modes is complicated by the contribution of B-mode polarisation from foreground sources. In the case of temperature anisotropies, the foregrounds have been well studied and contributions as a function of frequency are shown in Fig. 1.9. In the case of polarised foregrounds, much work remains to be done.

When cosmic ray electrons interact with the magnetic field of the Galaxy, synchrotron radiation is produced. The electrons rotate around and along the magnetic field lines while emitting photons perpendicular to them. The contribution of synchrotron contamination is dependent on initial cosmic ray energy and spatial location and high spatial latitudes contribute more polarisation contamination (up to 40%). The study of Galactic synchrotron radiation is an active field of study and further details are provided by Orlando and Strong (2013) [27].

Another strong contributor to B-mode contamination is thermal dust. Some dust particles have an asymmetric shape and orientate themselves along the magnetic

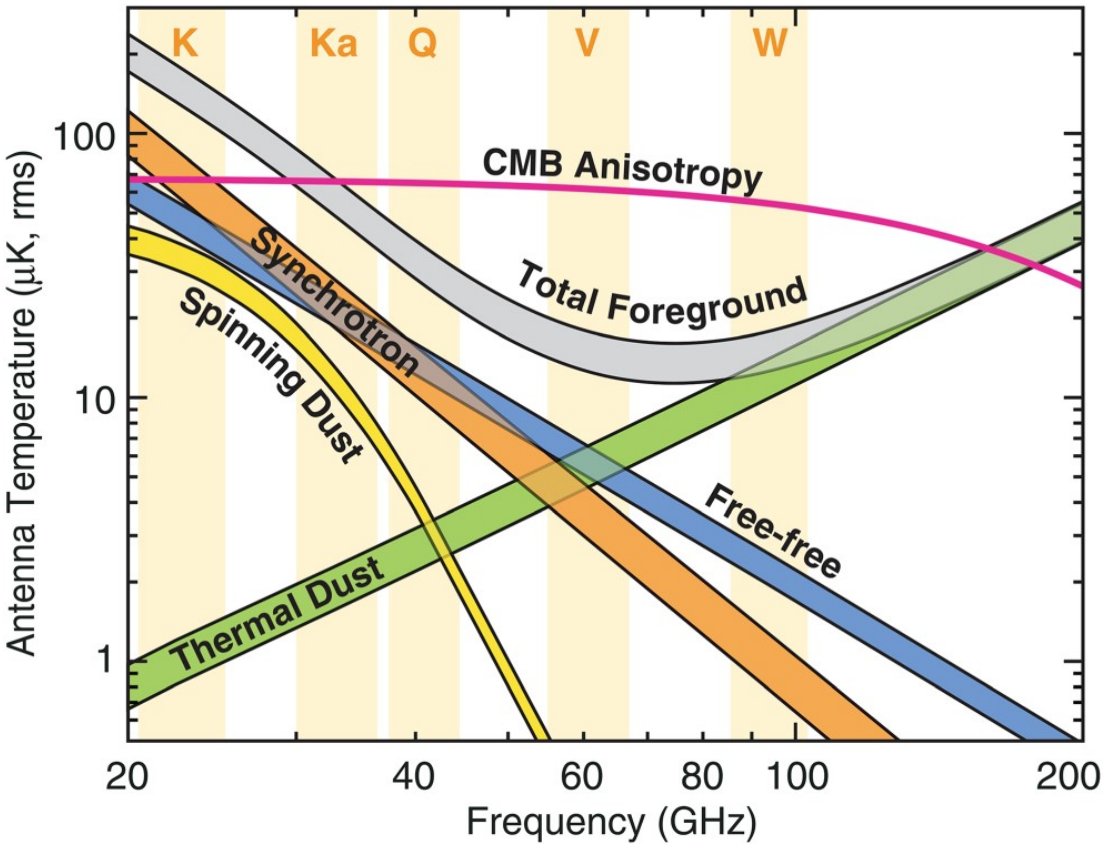

Figure 1.9: The two strongest temperature foreground contributors to CMB observations are galactic synchrotron and thermal galactic dust. Other foregrounds from Table 1.2 are also included. The grey bar shows the summation of the foregrounds. Reproduced from Bennett et al., (2013) [19].

field lines of the Galaxy. Due to this, the thermal radiation from this dust has a polarisation (up to 6%) and has a spatial distribution in accordance with magnetic field lines.

As CMB photons are travelling from the surface of last scattering to the observing telescope, the photons propagate through regions of over and under-densities. The effects of gravity will deflect the course of the photons. This gravitational lensing of photons is expected from Newtonian mechanics and General Relativity. This lensing can induce a B-mode polarisation on the photons up to the 6% level (Lewis and Challinor (2006) [28]) and the effect is even stronger at higher multipoles ($\ell > 1000$), which is evident in Fig. 1.6.

Synchrotron radiation and thermal dust are the strongest emission foregrounds. B-mode lensing is a weaker effect but is still a major concern for B-mode detection. There are numerous other effects which need to be considered, as shown by Table 1.2. Some other notable CMB foreground types are the Integrated Sachs-Wolfe

Foreground contribution	Polarization	Angular scales
Atmosphere	≃0%	Large scales
Ground	Varies	Large scales
Radio Freq. Interference (RFI)	0-100%	All
Sun/Moon	Low	All
Planets/solar system objects	Low	Small scales
Zodiacal light	Low	Large scales
Galactic synchrotron radiation	≃10-40%	Large scales
Galactic free-free radiation	Low	Large scales
Galactic thermal dust radiation	≃2-20%	Large scales
Galactic spinning dust radiation	Low	Large scales
Galactic magnetic dust radiation	0-35%	Large scales
Galactic line emission (e.g. CO)	Low	Large scales
Radio galaxies	Few %	Small scales
Sub-mm/IR galaxies	Low	Small scales
Infrared Background (CIB)	Low	Small/interm. scales
Secondary Anisotropies	Low	All

Table 1.2: The contributions of different kinds of CMB foregrounds. Their effects on polarisation measurements are shown with the angular scale on the sky where the effects occur. Reproduced from Dickinson (2016) [26].

effect, as shown by Sachs and Wolfe (1967) [17] and the Sunyaev-Zeldovich effect as described by Sunyaev and Zeldovich (1980) [29] and Carlstrom, Holder, and Reese (2002) [30]. Useful discussions of foreground contributions are provided by Ichiki (2014) [31] and by Dickinson (2016) [26]. These foregrounds are complex in nature and the process of subtracting them in order to detect the faint B-mode is the subject of on-going research. This has influenced QUBICs design so that 150 GHz and 220 GHz bands are observed simultaneously in order to observe and characterise the CMB and foregrounds together.

1.7 Current and Future CMB Experiments

Theoretical and experimental cosmology are both reaching an apex regarding Inflation theory where current experiments keep lowering the tensor-to-scalar ratio

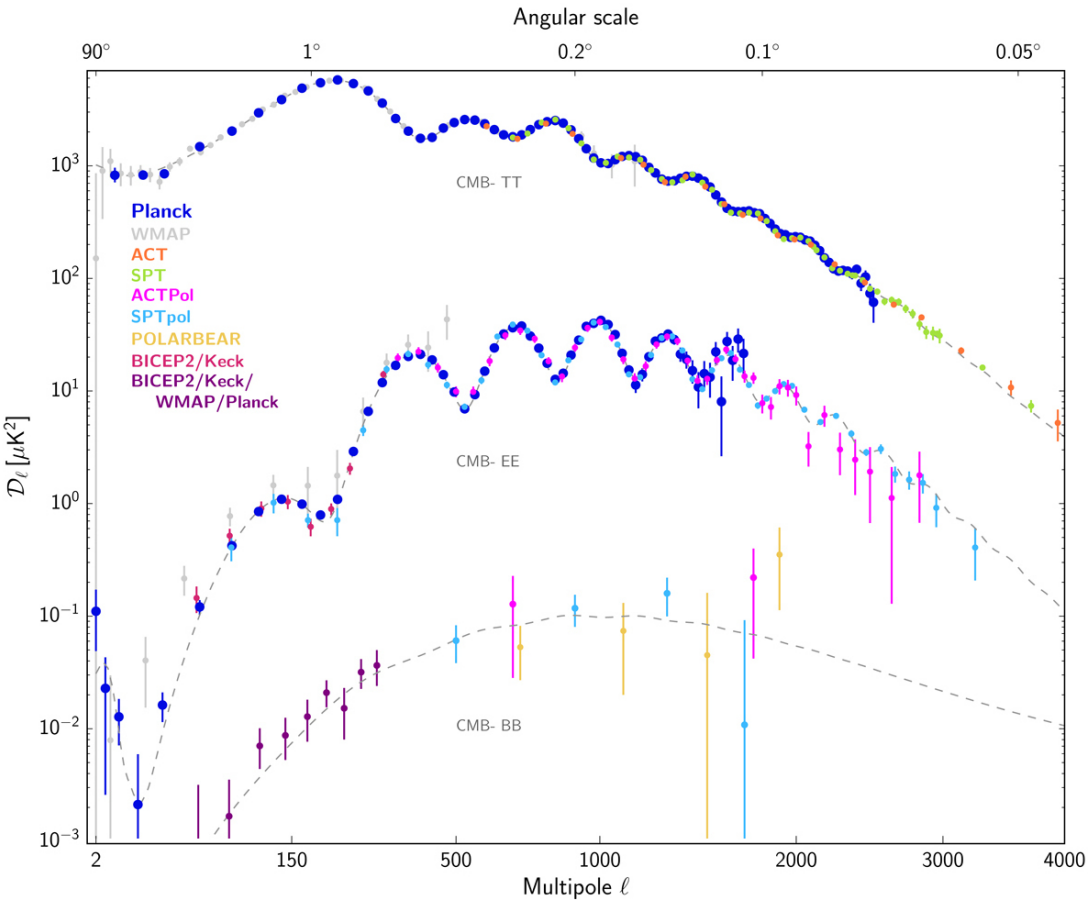

Figure 1.10: Here the angular power spectrum from recent experiments and joint analyses are shown for temperature, E-mode, and B-mode measurements. Each colour corresponds to a different experiment or joint analysis. The Planck temperature, polarization, and lensing data best-fit to the ΛCDM model is shown by the dashed lines. Adapted from the Planck Collaboration (2020) [20].

constraints. This enables theoreticians to rule out certain ΛCDM models and focuses efforts on theories in line with experimental observations. Inflation is a very exciting idea with universal appeal so there are large number of active research groups running experiments aiming to detect this B-mode polarisation. Some notable examples are: SPTPol [32], POLARBEAR [33], ACTPol [34], BICEP2 [35], CLASS [36], POLARBEAR 2 + Simons Array [37], advanced ACT [38], and the upgrade of the BICEP3/Keck array [39]. The measurements of these landmark experiments are summarised in Fig. 1.10. The various groups have produced excellent results measuring and characterising temperature anisotropies, E-mode polarisation anisotropies, and lowering the tensor-to-scalar ratio constraints. At the same time they have shown that systematics and foreground contamination are major hurdles in making observations of the B-mode polarisation.

In response to this, the *fourth generation* of cosmology experiments have been

designed with systematics and foregrounds as primary concerns. One example highlighting this importance came from the 'false' B-mode detection by BICEP which was later shown to be likely due to foreground dust as highlighted by the BICEP2/Keck and Planck Collaborations (2015) [40]. Some of these new examples are: Simons Observatory [41], PIPER [42], LSPE [43], CMB-S4 [44], LiteBIRD [45], and PICO [46]. Missions have even been proposed with the sole purpose of mapping and characterising B-mode foregrounds (BFORE [47]).

The current state of the art is shown by two recent articles lowering the constraints on the tensor-to-scalar ratio, Tristram et el., (2021) [48] and BICEP/Keck Collaboration et al., (2021) [25]. There are numerous other joint dataset analyses such as the BICEP2/Keck and Planck Collaborations (2015) [40] as mentioned previously. These publications show that the best constraints on the tensor-to-scalar ratio or actual measurements of a B-mode will likely come from the joint analysis of datasets from different experiments. The current upper limit is set by BICEP/Keck Collaboration (2021) [25] with the tensor-to-scalar ratio at $\sigma(r) < 0.036$.

1.8 The QUBIC Collaboration

In the last twenty years bolometric interferometry has been thought of as a design solution to detecting the B-mode polarisation of the CMB. Around this time a number of independent research groups were developing instruments with a similar design, they were: the Millimeter-wave Bolometric Interferometry (MBI) (Korotkov et al., (2006) [49]), Tucker et al., (2003) [4]) and the Background RAdiation INterferometer (BRAIN) (Polenta et al., (2007) [5]). These groups joined and formed the QUBIC collaboration (Kaplan (2009) [50], Battistelli et al., (2011) [51]) in 2009, and began work on a new instrument.

A design review of the QUBIC instrument was completed in 2016 (Aumont et al., (2016) [52]). Components have been manufactured, integrated, and calibrated in APC in Paris as summarised by Torchinsky et al., (2020) [53]. QUBIC has been shipped to an integration laboratory in Salta, Argentina and at the time of writing is undergoing acceptance tests before final deployment on site in Alto Chorrillo for sky observations.

1.9 Thesis Aims

This thesis has two broad aims. These are framed by the Experimental Physics Department's history and expertise in general quasi-optical modelling and quasi-optical modelling for experiments at the forefront of cosmological observations (e.g. QUAD and Planck). QUBIC is part of the next generation of cosmology experiments and the department has been contributing fundamental research to the QUBIC project since the merging of the original projects that went on to form QUBIC. Therefore, the first aim of this thesis is to continue this effort by continuing quasi-optical modelling for the QUBIC experiment.

The second aim comes as a result of the timing of the beginning of this research work with the stage of QUBIC's lifecycle. Integration and calibration of QUBIC began in APC at the start of this thesis. Therefore a significant amount of calibration data were being produced which required analysis. This is naturally a complex task for an entirely bespoke instrument like QUBIC. This thesis aims to contribute to the calibration and validation of the instrument via data analysis.

In order to best leverage the expertise of the Department's capability and expertise, the calibration data analysis projects worked on were chosen to make best use of them. In other words, the types of data analysis conducted in this thesis often used predictions from optical models with real instrument detector data to validate the instrument.

The general philosophy of this thesis was to contribute to the calibration, validation, and the successful deployment of QUBIC in the most efficient way possible. This work was largely conducted remotely from Maynooth in Ireland with instrument data generated in APC in Paris. Many visits to APC were made for various measurement campaigns and collaboration meetings and travel to Argentina for commissioning were planned. Once COVID-19 lockdowns began, this travel aspect of the research ended and the remote work further intensified. These thesis aims inform the logic and nature of the chapter contents in the following section.

1.10 Thesis Overview

With the broad aims and general philosophy of this thesis described above, a more narrow and focused description of the work carried out will now be given. Each

chapter has its own individual aims which intend to contribute to QUBIC largely through quasi-optical modelling, data-analysis, or a fusion of the two.

After this introduction chapter, a description of the QUBIC instrument will be provided in Chapter 2. Almost all aspects of the instrument are referenced throughout the thesis, so a general overview is given including a justification for the QUBIC design. Bespoke software, which is pivotal to controlling the instrument, as well as producing, and analysing the data is described.

Since quasi-optical modelling is a cornerstone of most chapters presented in this thesis (and other chapters rely on data produced from these models), Chapter 3 describes the fundamentals of quasi-optical modelling and Physical Optics (PO). GRASP is a commercially available PO modelling software which is used for many of the models developed in this thesis. MODAL, an in-house software, and Zemax, a commercially available package, were also used and are described.

The next chapters focus on developing quasi-optical models of QUBIC for different configurations. Chapter 4 models QUBIC in its scaled-back demonstrator configuration with internal calibration sources. The data produced in this model were used to compare with QUBIC's first laboratory measurements, a major milestone for the QUBIC collaboration.

Chapter 5 develops a PO model of QUBIC in its full instrument configuration and with the most up-to-date and realistic optical elements. The effects of manufacturing defects and additional optical elements were studied. The data produced by this model were used in the following chapters to validate the performance of the instrument with laboratory measurement data.

Chapter 6 shows a measurement of QUBIC's synthesized beam maps as a function of frequency. This was a core and milestone measurement for QUBIC due to the importance of its spectro-imaging wide-band performance. This chapter also explains the optimising of the data demodulation required to accomplish the measurement and the subsequent instrument validation by comparison with modelling predictions.

A dataset analysed in January 2020 contained anomalous artefacts referred to as 'ghosts'. The cause of the ghosting is investigated in Chapter 7 in addition to a study that uses Zemax to test possible optical causes. The resolution of the problem is discussed and results from the subsequent dataset are given.

Chapter 8 introduces a study on redundant baseline self-calibration. The ability to carry out this type of calibration is what drove the interferometric design of QUBIC. The author noted an aspect of QUBICs design that may have significant systematic implications for QUBIC's self-calibration scheme. The effect of aberrations and how they may effect the redundancy of baselines is investigated. The analysis in this chapter was based on PO data produced in Chapter 5.

Finally, a summary of the main conclusions from this thesis are given in Chapter 9.

Chapter 2

The QUBIC Instrument

2.1 Introduction

This chapter concerns the QUBIC instrument, which is the basis of all the work presented in this thesis. Two configurations of QUBIC are used and referred to throughout the thesis, the Technical Demonstrator (TD) and the Full Instrument (FI). First, the concepts driving the design will be described. These concepts are those of Bolometric Interferometry (BI), systematic effects, self-calibration, and spectro-imaging. These factors drives QUBIC's bolometric interferometer design. Following, descriptions of the instrument integration, calibration, and observation methods will also be given. Software is a key aspect of QUBIC's functionality and the QUBIC collaboration has been developing a bank of code to manage data acquisition and data analysis. These will be described. It may be useful to refer back to different parts of this chapter while reading later chapters to understand the operation and integration of the various sub-systems.

2.2 Instrument Design Philosophy

2.2.1 Bolometric Interferometry

Bolometric Interferometry (BI) refers to a technique that uses bolometer detectors that are highly sensitive at millimetre wavelengths to image an interference pattern and to take advantage of the systematic capabilities of interferometers. These

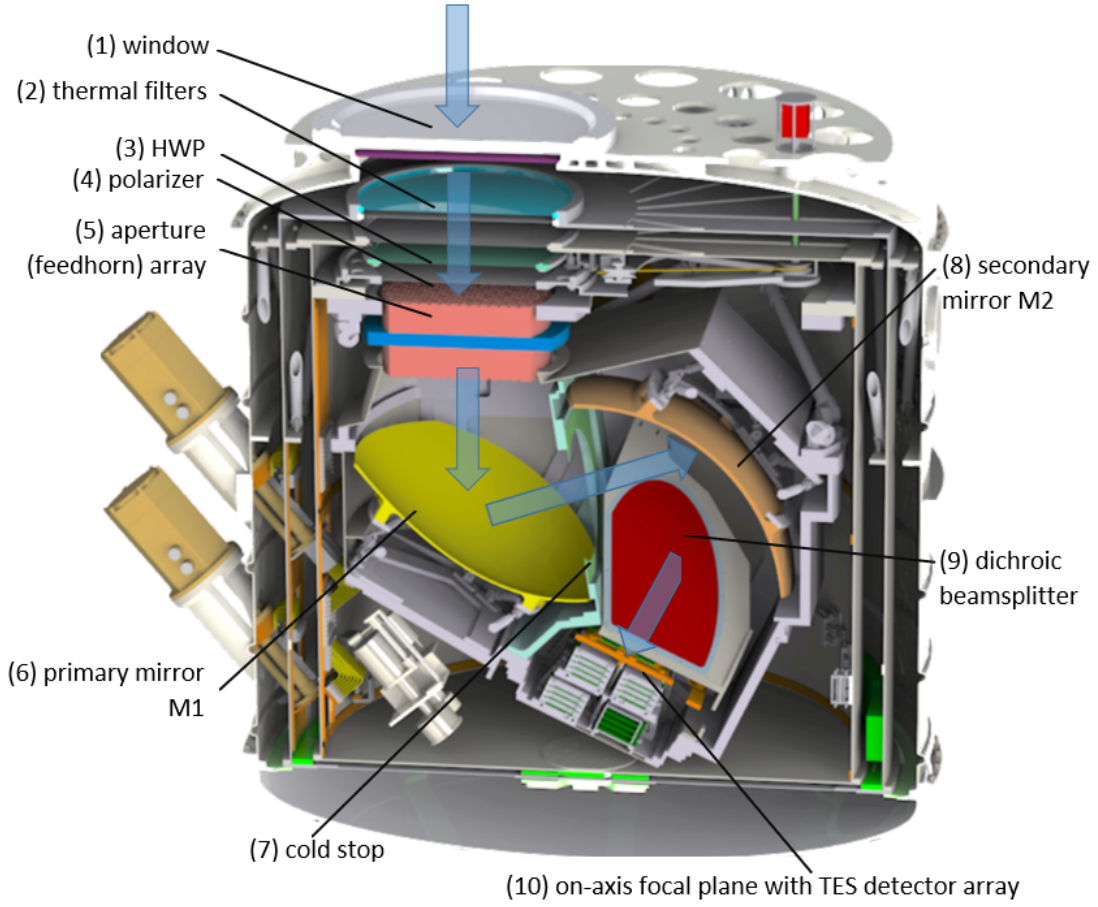

Figure 2.1: An internal cut of QUBIC's cryostat and optical elements reproduced from Mousset et al., (2020) [56]. The detectors and mirrors are mounted inside cryostats at various temperatures.

instruments have been known in the past as omniscopes. The BI technique has been developed over the last twenty years (Tucker et al., (2003) [4]) (Polenta et al., (2007) [5]) (Hamilton et al., (2008) [54]), and (Ghribi (2009) [55]) in response to the precision measurements of the CMB temperature anisotropies by experiments such as Planck, COBE, and WMAP. Measuring the B-mode polarisation of the CMB requires an even higher sensitivity and systematic control than these already highly precise experiments and the BI design is highly capable of this.

A bolometric interferometer, like QUBIC in Fig. 2.1, observes the sky as a Fizeau interferometer with an array of horns and re-emits the sky signal through back-to-back horns into the optical combiner. The beams from the horns form an interference pattern on the focal plane. The focal plane has an array of TES bolometer detectors that images the interference pattern. Hence, QUBIC is an interferometer with the sensitivity of an imager.

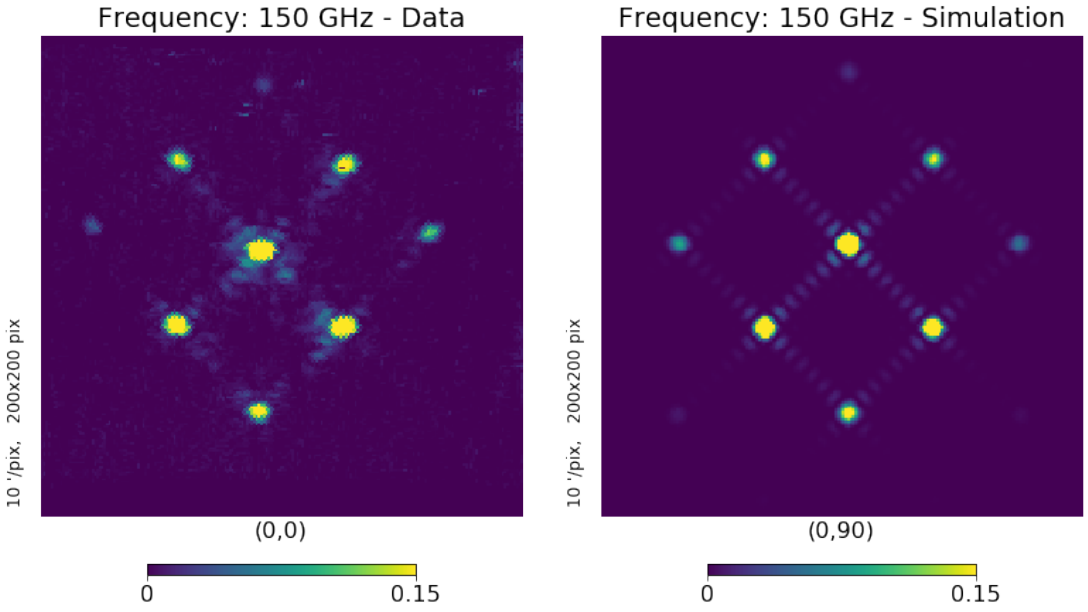

Figure 2.2: QUBIC's synthetsized beam. On the left is the synthesized beam from laboratory measurements. On the right is the predicted synthesized beam from optical simulations. These data are for 150 GHz data. The location of the peaks varies as a function of frequency, as will be shown in this thesis. The color-scale is in arbitrary data units.

Switches in the horn array can control which horns are open so that equivalent baselines from two horns can be compared on the focal plane. This enables QUBIC to take advantage of redundant baseline self-calibration by comparing the interference patterns of equivalent baseline horn pairs. This self-calibration scheme is used to minimise systematic effects. QUBIC will observe with all horns simultaneously so the observed pattern on the focal plane is the convolution of the image of the sky (*the real sky brightness visibility*) with the synthesized beam (*dirty beam*) of the instrument. For QUBIC, the synthesized beam is analogous to the dirty beam described by Section 8.2.3. It is the Fourier transform of the horn array aperture field (analogous to the $S(u, v)$ antenna visibilities, Section 8.2.3). An example of QUBIC's synthesized beam is shown in Fig. 2.2 for an array of 64 'open' horns where the pattern is governed by the horn array. The FWHM of the peaks in the synthesized beam are given by the width of the largest baseline and the field-of-view of the instrument is determined by the beam of the individual horns. The pattern of the synthesized beam, as shown in Fig. 2.2, has spectral dependence which is a key feature for in band spectral performance and spectro-imaging.

Bolometric interferometers are designed for CMB polarisation experiments. Traditionally, CMB experiments use polarised detectors or polarised horns coupled

to the detectors. These configurations are sensitive to polarisation systematics, which reduces the instruments sensitivity the CMB polarisation. Instead QUBIC will use a rotating half-wave plate (HWP) and polariser in the entrance aperture. The future LiteBird experiment (Hazumi et al., (2021) [57]) will use a similar polarisation apparatus. Sky signals enter the aperture, and pass through a series of frequency and Infra-red filters before reaching the rotating HWP and polariser as can be seen in Fig. 2.1. The incoming signal to the HWP (S_{HWP}) is described with polarised E_x and E_y electric fields as:

$$S_{\mathrm{HWP}} = \begin{pmatrix} E_x \cos 2\phi(t) + E_y \sin 2\phi(t) \\ E_x \sin 2\phi(t) - E_y \cos 2\phi(t) \end{pmatrix}. \tag{2.1}$$

The HWP is rotating in time as ϕt. The polariser rejects linear polarisation so the signal outgoing from the polariser is now

$$S_{\mathrm{HWP}} = \begin{pmatrix} E_x \cos 2\phi(t) + E_y \sin 2\phi(t) \\ 0 \end{pmatrix}. \tag{2.2}$$

The signal can be written in terms of the stokes parameters as

$$S = I + Q \cos 4\phi(t) + U \sin 4\phi(t). \tag{2.3}$$

From here the modulated polarisation CMB signal enters the horn array and the optical combiner where it is focused on the focal plane. The polarised signal can be reconstructed from the Stokes I, Q, and U parameters from the detector time ordered data. The downside is that half of the incoming sky signal is immediately rejected by the HWP and polariser. This disadvantage is compensated by the sensitivity of the imaging bolometer detectors. The advantage of this configuration is the inherent polarisation certainty and reduced cross-polarisation recorded by the detectors. This is highly advantageous for detecting the CMB B-mode polarisation anisotropy.

Effect	**Source**
White noise correlation	Phase switch imbalance
1/f noise	RF amplifiers
Bias fluctuation	RF amplifiers, back-end electronics
Thermal fluctuations	Cooling system stages
1 Hz spikes	Back-end electronics
Side-lobe pickup	Main and sub-reflector spillovers
Bandpass asymmetries	Differential OMT and receiver bandpass response
ADC non-linearity	Back-end ADC
Imperfect photometric calibration	Side-lobe pickup, radiometer noise temperature changes and other non-idealities
Pointing	Uncertainties in pointing reconstruction, thermal changes affecting focal plane geometry

Table 2.1: This table summarises the systematic effects studied for Planck in the 2013 data release. These effects will generally apply to all CMB experiments. This table is summarised from Planck Collaboration III (2013) [61].

2.2.2 Systematic effects

Systematic effects are errors, usually due to the design or construction, of a telescope that reduce the quality of the data. A common error to most telescopes is pointing uncertainty. This arises from misalignments or manufacturing defects that cause the telescope to point offset from where it is directed and assumed to be pointing. Another common example is detector location error. If the detector is placed offset from where it was intended to be mounted, a systematic error is induced in the data. Related to this, a systematic error common to CMB polarisation experiments with polarised detectors occurs when the polarised detector (or polarising horn coupled to the detector) has a misalignment which introduces a false polarisation detection. A general description of systematic effects is given by Nagata and Namikawa (2021) [58] and a thorough summary and description of these effects is provided by Su, Yadav, and Zaldarriaga (2009) [59].

Fig. 2.3 shows how systematic contributions are summed for the Planck satellite with reference to the temperature anisotropy. An list of systematic effects (and noise) for Planck is given in Table 2.1.

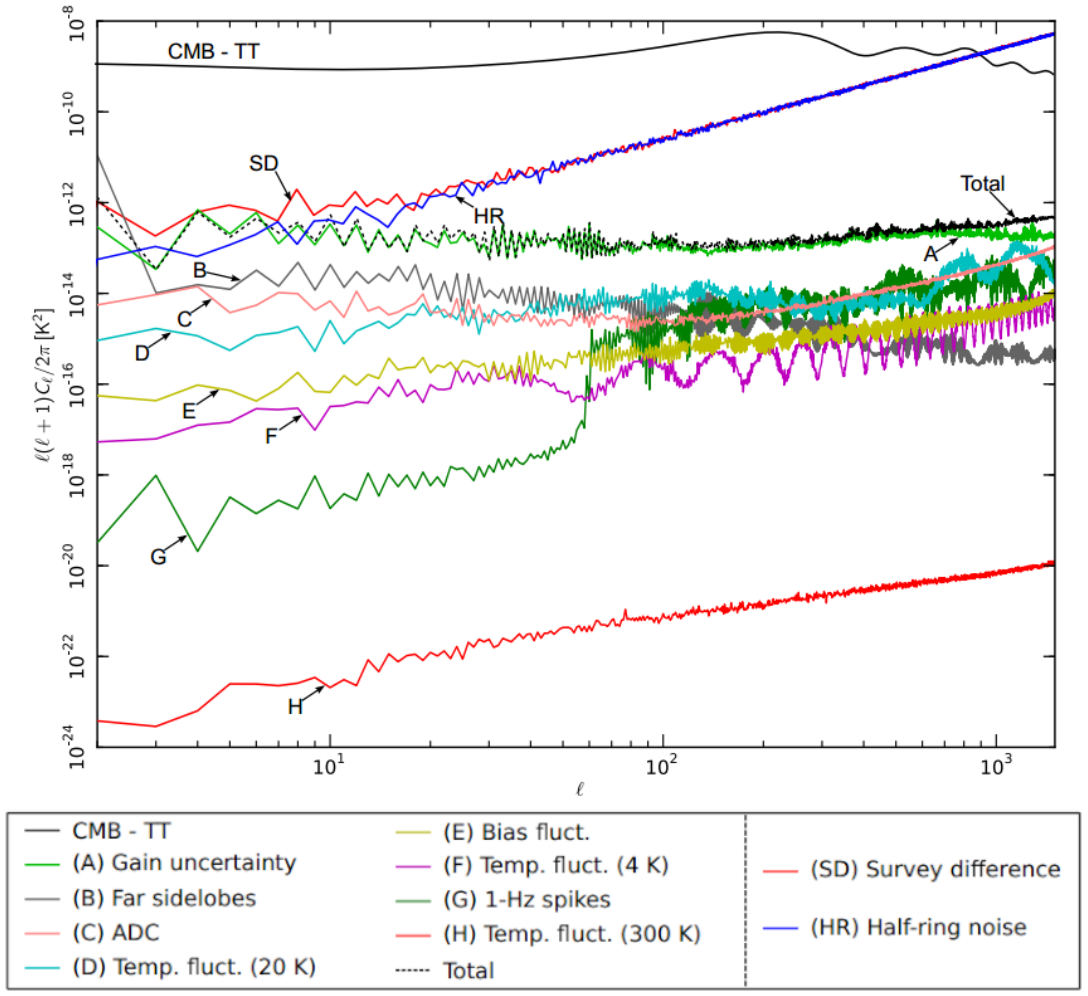

Figure 2.3: Angular power spectra of the various systematic effects compared to the Planck temperature anisotropy spectrum. The black dashed curve, representing the total contribution, has been derived from a map where all the systematic effects have been summed. The CMB curve corresponds to the Planck best-fit model presented in Planck Collaboration XV (2014) [60].

While experiments like Planck and BICEP have made extraordinary progress observing the CMB anisotropies, the faint B-mode anisotropy remains undetected. Minimising CMB instrument systematics is an active field of study towards B-mode detection as evidenced by Wallis, Brown, and Battye (2016) [62] and Hivon, Mottet, and Ponthieu (2017) [63]. The next generation of CMB experiments will require extreme control of systematics in order to detect the faint B-mode. This is why QUBIC has been designed with systematic control via bolometric interferometry and self-calibration as driving design requirements. QUBIC, as a bolometric interferometer, will be particularly sensitive to systematic effects due to:

Horn location systematics: the horns in the horn array may be installed with a positional or directional offset.

Detector location systematics: the exact position of the detectors on the focal plane may be offset from where they are intended to be.

Detector gain: there may be uncertainty in the gain calibration for detectors.

Horn systematics: the manufacturing precision of the horn and its corrugations maybe effect the beams of individual horns.

Rotating half wave plate and polariser systematics: the mechanical alignment of half wave plate and polariser or performance the metal mesh metamaterials may induce systematics.

Pointing uncertainty: misalignments or manufacturing defects that cause the telescope to point offset from where it is directed and assumed to be pointing.

2.2.3 Self-Calibration

QUBIC's bolometric interferometer design is also motivated by the ability to take advantage of aperture synthesis self-calibration techniques developed historically for radio telescope arrays (Pearson and Readhead (1984) [64]). The back-to-back horns in QUBIC's entrance aperture (Fig. 2.1) have switches that can mechanically open and close individual horns. When only two horns are open, an interferometric pattern on the focal plane is formed by illuminating the instrument with an external calibration source[1]. A redundant baseline is another two horns from the horn array that have the same distance and orientation in the focal plane. This equivalent baseline should form the exact same visibility. Any difference measured between the two visibilities can only come from instrument systematics. This principle is exploited by measuring and comparing the redundant baseline horn pair visibilities from QUBIC's horn array. For QUBIC's array of 400 horns there are 79,800 unique baselines ($N(N-1)/2$, where N is the number of horns), each with their own set of matching equivalent baselines. Combined with the number

[1]Rather than comparing baselines from two horns at a time, QUBIC will observe the full horn array minus one horn, then minus another, and the fringe pattern can be determined. It is a technically equivalent way of measuring a baseline pattern. This is done to maintain a more constant thermal load on the detectors and is closer to the observation configuration with 400 horns open.

of detectors and instrument pointings, there are 1×10^{10} unknowns and 1×10^{20} constraints. Therefore, the problem is overdetermined and can be solved by a least squares algorithm. This method effectively solves the systematic effects described above. These details, as well as a description of QUBIC's self-calibration method, are given by Bigot-Sazy et al., (2013) [65].

2.2.4 Spectro-Imaging

Spectro-imaging is a novel technique being developed for QUBIC (Mousset et al., (2020) [56]). The idea of spectro-imaging is to observe the whole of the bandpasses (130 - 170 GHz and 200 - 240 GHz) on a single focal plane and exploit the fact that the synthesized beam of the instrument contains multiple peaks whose angular separation depends on frequency. The wide band observation is split into several narrower frequency sub-bands in post-processing. The spectral distribution of the Galactic and inter-Galactic foreground B-mode polarisation is different to that of the CMB and observations in the higher sub-bands are used to subtract the foreground from the lower frequency sub-bands.

2.3 QUBIC Full Instrument

2.3.1 Instrument Overview

QUBIC is comprised of a number of separate systems and technologies integrated together to form a millimetre-wave telescope. These systems are shown together with a slice through a 3D render in Fig. 2.1. This figure shows how the electronics and optical components are encapsulated in layers of cooled cryostats. Following the cryostat window, there is the optical aperture with filters, a rotating HWP, polariser, and back-to-back horns with switches. There are off-axis mirrors which focus the beams from the horns onto the focal plane detectors. This optical combiner also has a cold-stop (CS) to reduce stray light leakage and a dichroic to split the higher frequency (220 GHz) light onto the secondary off-axis focal plane. The detectors are TES bolometers which require cryogenic cooling to operate at 320 mK. There are both cold and warm electronics comprised of ASICS and SQUID arrays to read the data from the detectors.

The following sections will give an overview of each element with particular attention given to parts pertinent to this thesis. The QUBIC TD was built in order to prove and demonstrate the novel technologies in QUBIC before funding for the FI would be made available. This thesis concerns work on the current TD and the planned FI upgrade in the future so both will be described. The FI overview will be given first and then the TD will be described by highlighting the differences between the FI and the TD. They are similar except for a small number of parts which were reduced in scope for the TD. The FI is the instrument as planned in its fully operational form. This configuration of QUBIC is projected to achieve a tensor-to-scalar ratio of $\sigma(r) = 0.015$, after which will detect or constrain the B-mode level.

The QUBIC instrument is summarised by Aumont et al., (2016) [52] and more details on recent developments, installation, and testing of QUBIC's systems will be available in a special edition of the Journal of Cosmology and Astroparticle Physics (JCAP) [66][56][53][67][68][69][70][71].

2.3.2 Cryogenics

QUBIC has stringent thermal cooling requirements. Other optical elements are also cooled (e.g. filters, horns, mirrors, etc.) in order to reduce background thermal load on the detectors and thereby improve the detector performance. Recent measurements and characterisation of QUBIC's cryogenic system is described by Masi et al., (2021) [68] and additional descriptions are given by May et al., (2018) [72], and Aumont et al., (2016) [52].

There are interconnected cooling systems placed within one another, analogous to a 'Russian doll'. The schematic layout is shown Fig. 2.4 where 40 K, 4 K, pulse tube cryocoolers (PTC), sorption coolers, and vacuum vessel are labelled (the physical layout is evident in Fig. 2.1). Table 2.2 also shows a summary of the components and their cooling stages.

The outer cryostat is a cylinder with a diameter of 1.4 m and a length of 1.5 m. There are two 2-stage 1 W PTCs which service the 40 K and 4 K stages shown in Fig. 2.4 and this enables the condensation of liquid helium in the evaporation refrigerators. A ^{4}He refrigerator cools the optical combiner and filters to 4 K while the ^{3}He cools the detector arrays to 0.3 K.

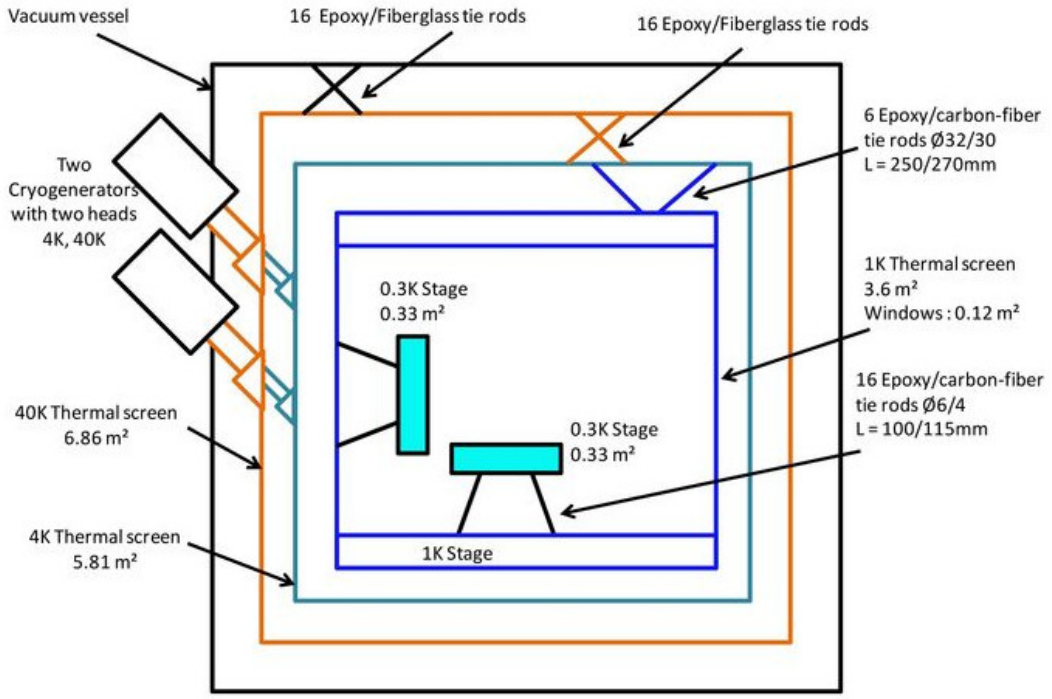

Figure 2.4: Schematic representation of the cooling stages, cryostats, pulse tubes, and sub-system temperatures. *Image credit: Thermeau and Piat, QUBIC Collaboration Meeting.*

2.3.3 Optical Elements

The optical system will be described from the sky to the detectors in the following subsections.

2.3.3.1 Ground Shield and Forebaffle

QUBIC's aperture is protected from radiation leakage from the Sun, Moon, and ground by a forebaffle (FB) and ground shield (GS). These are shown in Fig. 2.5 in a drawing of QUBIC's observatory building with the dome open and QUBIC on its mount. The FB is fixed to the cryostat window while the GS is fixed to the roof of the observatory building.

The FB has a 14° semi-aperture angle with a curved flare of radius $R = 50\,\text{mm}$ and is lined with an absorbing material (ECCOSORB® HR-10) on its inner surface. The GS has an aperture angle of 90°. Combined, the FB and GS are effective at reducing the side-lobe from beams on the sky at angles greater than 25°, as shown

Element	Cooling Stage	Optical z-axis location (GRF)	Diameter TD/FI (mm)
UHMW-PE Window	Outer Cryostat	480.00	560/560
IR blocker 1	Outer Cryostat	460.00	278/435
IR blocker 2	Outer Cryostat	452.55	278/435
IR blocker 3	40 K stage	342.10	225/430
IR blocker 4	40 K stage	335.00	225/430
IR blocker 5	40 K stage	327.10	225/430
IR blocker 6	4 K stage	285.50	200/410
LPE	4 K stage	276.30	200/410
HWP	4 K stage	237.80	180/370
Polariser	4 K stage	183.60	170/360
Horn array & Switches	4 K stage	0.00	120/300
Primary Mirror	1 K		400/594
Cold-stop LPE	1 K		200
Secondary Mirror	1 K		380/607
Dichroic	1 K		
2x 150 GHz edge	0.3 K		
2x 220 GHz edge	0.3 K		

Table 2.2: Table of the optical elements, their temperature stages, sizes, and location relative to the Global Reference Frame (GRF). The GRF refers to the standard coordinate system from which QUBICs components are defined. A document with definitions for QUBIC's reference frames is included in Appendix D.

in Fig. 2.6. Further details of the optical modelling for the FB and GS are given by O'Sullivan et al., (2020) [71].

2.3.3.2 Window, IR Blockers, & Filters

QUBIC's optical chain includes the cryostat window, a number of infrared (IR) radiation blockers, and frequency filters which combine to reduce thermal loading on the detectors and ensure the correct bandpass of CMB radiation is incident on them. The filters were designed carefully to be integrated with the cryogenic apparatus for optimal instrument efficiency. These elements are summarised in Tab. 2.2 and examples shown as installed in QUBIC in Fig. 2.7.

The primary aperture is a 560 mm diameter Ultra High Molecular Weight Polyethylene (UHMW-PE) window. This material is chosen as it is transparent to millimetre-wave radiation while having high structural strength. The window is required to withstand the extreme vacuum pressure ($\sim$100 kPa) from the cooling system. It is shown installed in the cryostat without the FB in Fig. 2.7a.

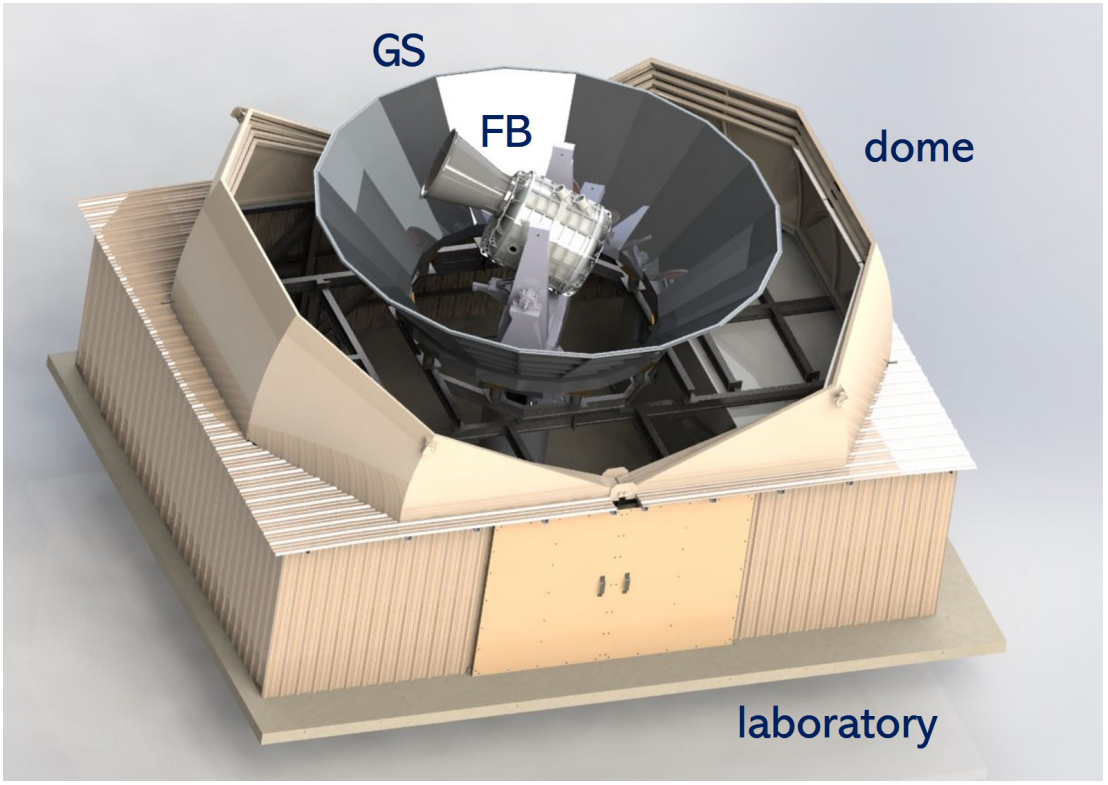

Figure 2.5: 3D render (reproduced from O'Sullivan et al., (2020) [71]) of QUBIC observation building with the cryostat, forebaffle and ground shield shown. *Image credit: Dr M. De Petris.*

The IR blockers are single-layer metal mesh devices and are 4 µm thick. There are six individual blockers mounted at different points between the window and horn array at the interfaces between different cooling temperatures. Each IR blocker reflects the majority of the incident IR radiation while a small fraction is absorbed as heat (which is cooled via the layered cooling stages). These IR thermal filters are produced by the Astronomy Instrumentation Group (AIG) in Cardiff and have been used regularly in similar cosmology experiments. Manufacturing and performance details are provided by Tucker and Ade (2006) [73].

The Low Pass Edge (LPE) filters are also produced by AIG. The design and characteristics are described by Ade, Pisano, Tucker, and Weaver (2006) [74]. These filters ensure the QUBIC passband requirements are met for correct operational performance. The IR filters, band defining filters, polariser and dichroic are all manufactured using the same metal-mesh technique, one such example is shown installed in QUBIC in Fig. 2.7b.

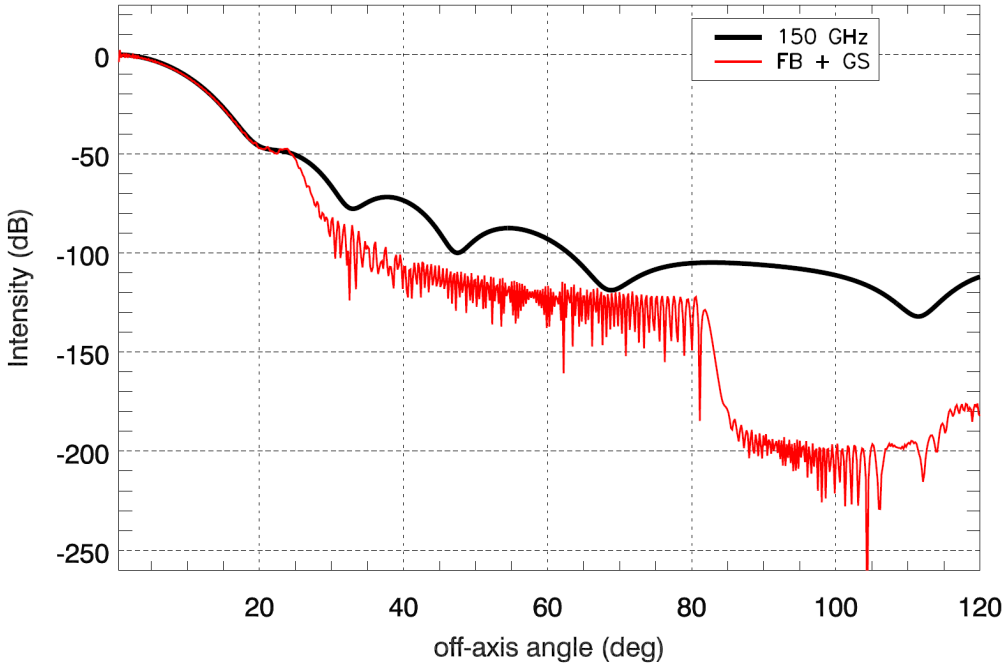

Figure 2.6: The side-lobe from the beam on the sky is reduced with the addition on the GS and FB (red). The black line shows the beam from the sky with no GS or FB at 150 GHz. Reproduced from O'Sullivan et al., (2020) [71]. *Image credit: Dr M. De Petris.*

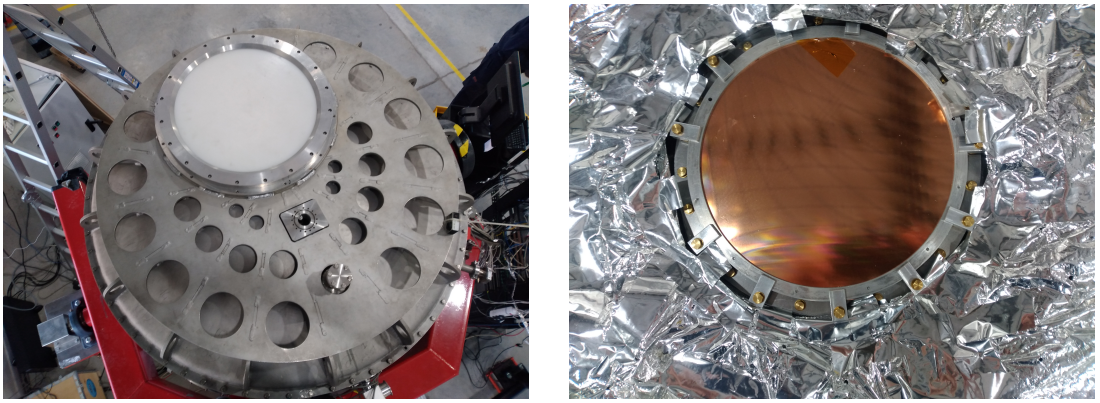

(a) UHMW-PE window mounted on the lid of the aperture. The window transmits millimetre-wavelength radiation while maintaining the cryostat pressure inside.

(b) A filter is shown with the cryostat lid and UHMW-PE window removed.

Figure 2.7: Photographs of the cryostat window and an example of a filter produced by AIG Cardiff (photo credit: Dr C. Kristukat).

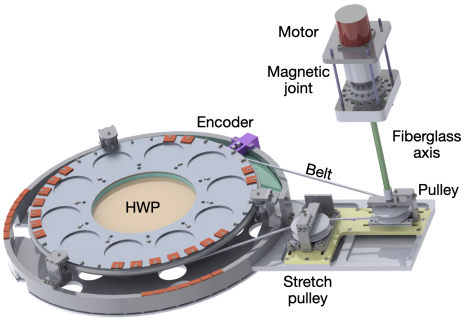

(a) Rotating HWP mechanism (reproduced from D'Alessandro et al., (2020) [69]).

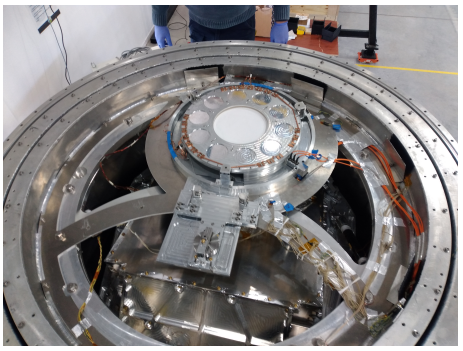

(b) Photograph of the rotating HWP installed in QUBIC (photo credit: Dr. Christian Kristukat).

Figure 2.8: The rotating HWP as (a) a 3D render and (b) a photograph of the mechanism as installed in the instrument.

2.3.3.3 Rotating HWP and Polariser

QUBIC requires strict control of polarisation to detect the CMB B-modes. As such, QUBIC is designed as a Stokes polarimeter using a HWP (Fig. 2.8) and polariser (the same construction as Fig. 2.7b) to measure the polarisation of the CMB signal reaching the detectors.

The HWP is located between the band defining LPE filter and the polariser. This is shown in Fig. 2.1. The HWP material itself is a dielectric meta-material produced by AIG in Cardiff and mounted on a pulley-driven rotating platform (shown in Fig. 2.8a). The installation of the rotating HWP in the cryostat is shown in Fig. 2.8.

The polariser is made from the same metal mesh dielectric material as the filters and are also made by AIG Cardiff (Fig. 2.7). The polariser is located between the HWP and the horn array.

The HWP can rotate in a step-wise fashion and in combination with the linear polariser this modulates the CMB polarisation entering the optical combiner. The design an integration of these components is technically challenging due to the thermal and mechanical requirements. The rotating mechanism has been designed so that it produces minimal thermal loading and is maintained at 4 K. This design of rotating HWP and polariser rejects 50% of incoming light but minimises the cross-polarisation of the CMB sky signal which is key for systematic control and B-mode detection. Laboratory tests show that QUBIC can achieve a residual

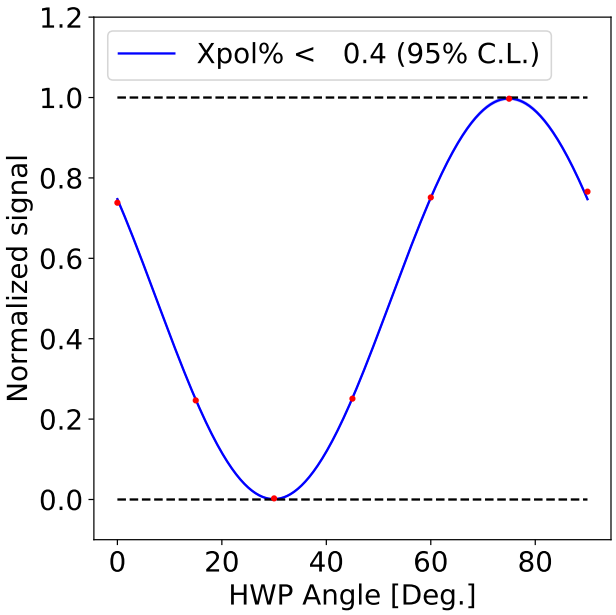

Figure 2.9: Amplitude of the detected power from the polarised calibration source as a function of HWP position, fitted to a sine curve. A linear polariser selects one polarisation direction after the HWP. (This plot is reproduced from Torchinsky et al., (2020) [53].)

cross-polarisation level of 0.5% as shown by Torchinsky et al., (2020) [53]. This is shown in a plot from that article in Fig. 2.9.

2.3.3.4 Horn Array and Switches

QUBIC has an array of back-to-back horns separated by switches that open and close. This array is located below the polariser and in front of the primary mirror (see left in Fig. 2.10). The array is comprised of 400 horns for the FI and 64 for the TD. The FI horn array is shown in Fig. 2.11. In Fig. 2.10 (right) the structure of the back-to-back horns is shown with the switch in between the horns.

Each switch is a metal shutter that blocks or unblocks an open aperture between the back-to-back horns. It is controlled by a coil (manufactured by Line Electric, model TO-5S). The left of Fig. 2.12 shows a diagram of the coil. The central figure shows a 3D render of a shutter blocking the aperture in the closed position. The image on the right shows a photograph of shutters in an open position revealing four unblocked apertures. The switches are used to control which horns allow a beam to propagate (from the sky or a calibration source) onto the focal plane.

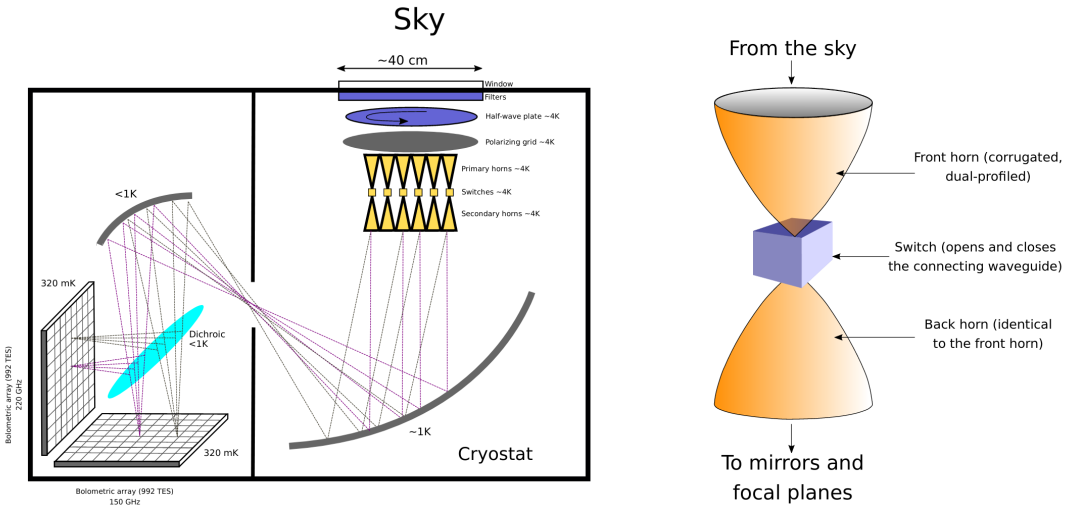

Figure 2.10: Schematic (left) of the QUBIC instrument showing the location of the back-to-back horn array and switches with respect to the other optical components and detectors. Diagram (right) showing the back-to-back horn and switch configuration. Reproduced from Cavaliere et al., (2020) [70].

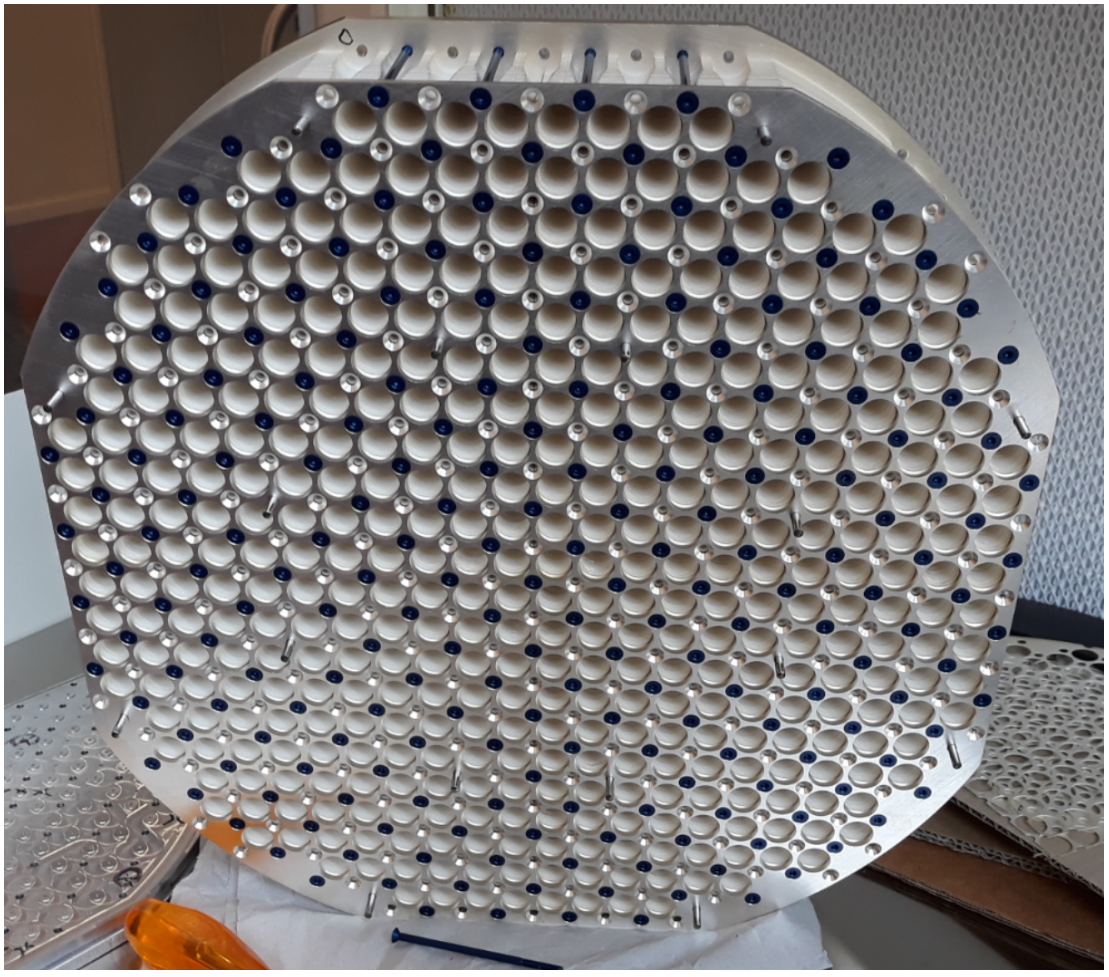

Figure 2.11: The FI horn array with 400 corrugated horns. Reproduced from Cavaliere et al., (2020) [70].

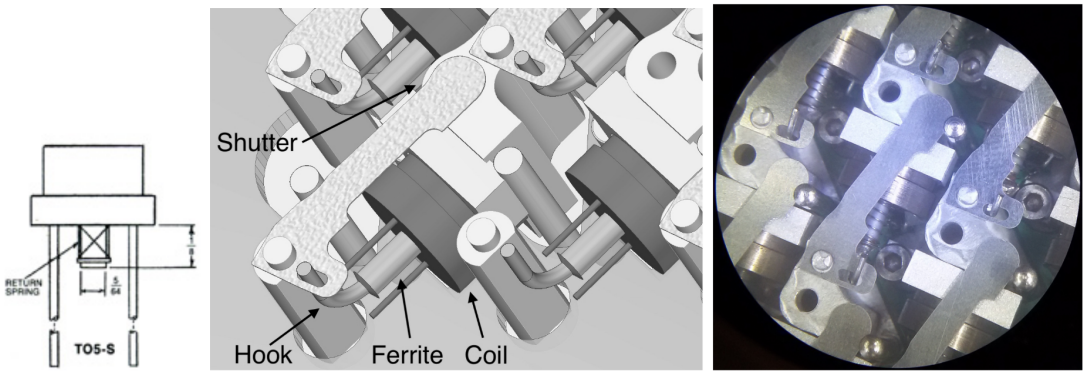

Figure 2.12: A schematic diagram of a horn switch is shown on the left. 3D Computer Aided Design (CAD) render (centre) of the switch mechanism with the shutter blocking an aperture. Photograph (right) of the switching mechanism in the open position with the horns unblocked. Reproduced from Cavaliere et al., (2020) [70].

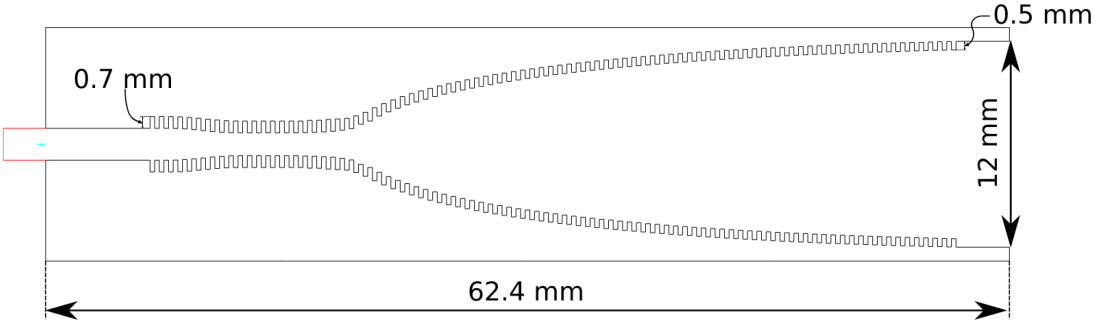

Figure 2.13: The profile and dimensions of a corrugated QUBIC horn. Reproduced from Cavaliere et al., (2020) [70].

This is an essential mechanism for systematic error control using QUBIC's self-calibration technique as described by Bigot-Sazy et al., (2013) [65]. The PSF pattern on the focal plane is dependent on the configuration of horns that are open and closed via the switching mechanism.

2.3.3.5 Horns

The horns are corrugated conical horns with a profile as shown in Fig. 2.13. Each horn is 62.4 mm in length and 12.0 mm in diameter at the aperture. The depth of the corrugations varies from 0.5 mm to 0.7 mm. This design is based on the ultra-Gaussian horn designed for the Clover experiment (Piccirillo et al., (2008) [75]) and produces Gaussian-like beams (FWHM = 12.9° at 150 GHz) with low cross-polarisation and low side-lobe level. The use of these types of horns for CMB experiments is discussed by Ade, Wylde and Zhang (2009) [76].

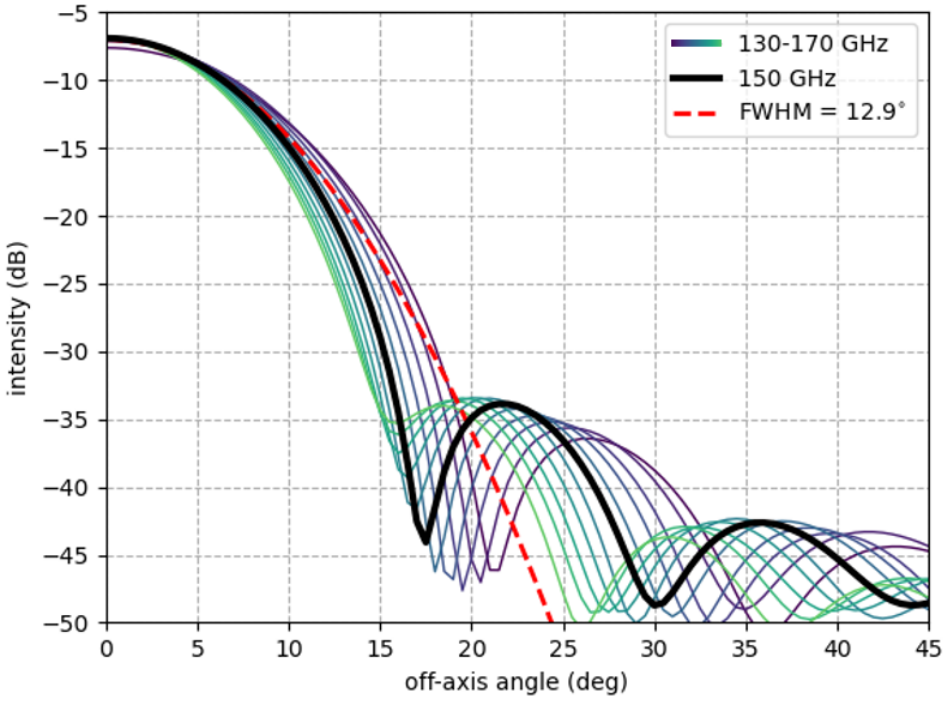

(a) QUBIC horn beam pattern for a selection of single-moded frequencies centred at 150 GHz. A Gaussian approximation with a 12.9° FWHM is also included.

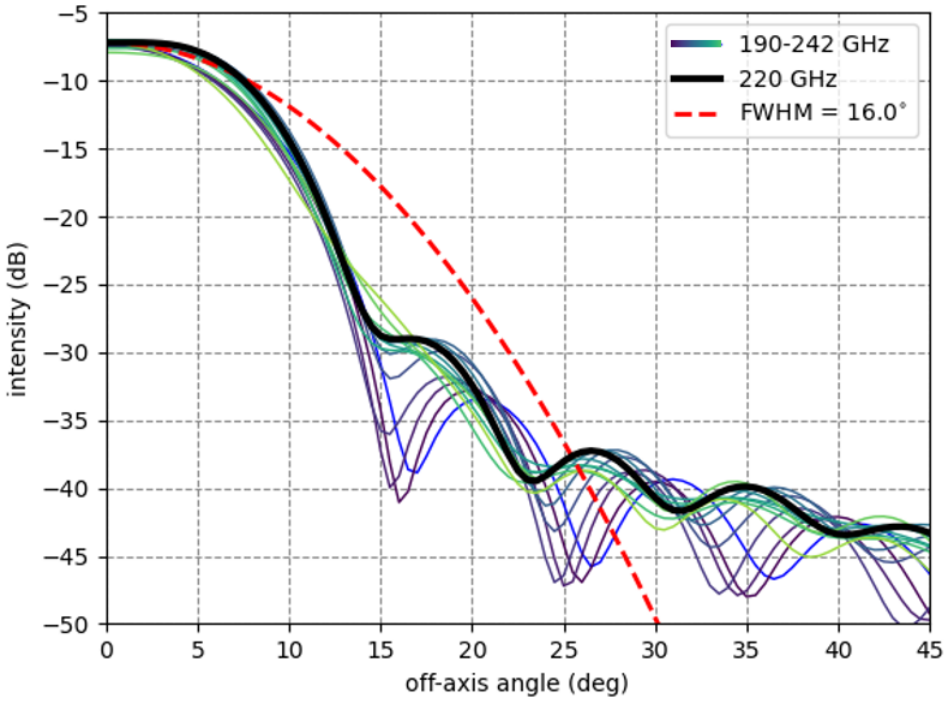

(b) QUBIC horn beam pattern for a selection of multi-moded frequencies centred at 220 GHz. A Gaussian approximation with a 16.0° FWHM is also included.

Figure 2.14: QUBIC horn beams as a function of frequency. The central frequency and a Gaussian approximation are also shown. Figures reproduced from O'Sullivan et al., (2020) [71]. These beams are common to both sky and detector facing horns as they are identical.

The horns are designed to operate single-moded in the 150 GHz band (130 - 170 GHz, Fig. 2.14a) and multi-moded in the 220 GHz band (200 - 240 GHz, Fig. 2.14b). The back-to-back horns are located after the rotating half-wave-plate and polariser. This means that incoming light onto the horns is linearly polarised. As a result, orthogonal modes are not active in the horn. Unless otherwise stated, simulations shown in this thesis were carried out at 150 GHz. The far-field beams shown in Fig. 2.14 apply to both sky and detector facing horns as all horns are identical.

2.3.3.6 Optical Combiner

QUBIC uses an off-axis Gregorian imager as its optical combiner (see Fig. 2.15). The difference between an ideal on-axis setup and the off-axis implementation is shown in Fig. 2.15a. The off-axis nature of the combiner gives rise to aberrations which are extensively studied in this thesis. The effective focal length of the combiner is 300 mm. The primary mirror is a paraboloid with a diameter of 480 mm $\times$ 600 mm and a focal length of 231 mm. The secondary mirror is elliptical with focal point separation of 289 mm and vertex separation of 800 mm. The justification for and the design of this combiner is given by Scully (2016) [77].

The mirrors were manufactured by milling and polishing aluminium blocks. These are shown in Fig. 2.15b. For the FI, flanges were added at four corners of each mirror which are visible in the figure. These were added to aid in mounting and aligning the mirrors in the cryostat.

A cold-stop is located at the common focal point of the primary and secondary mirrors. The cold-stop has an open circular aperture and restricts stray light and thermal radiation from the horn array from reaching the focal plane. The cold-stop aperture in some calibration measurements has a Neutral Density Filter (NDF) to reduce the calibration source power on the focal as it causes saturation of the detectors. This will not be present for scientific sky observations. Its position is shown in Fig. 2.1.

A dichroic is planned to be placed in between the secondary mirror and the focal planes (also shown in Fig. 2.1). The dichroic will split the 150 GHz and 220 GHz beams from the horns onto two focal planes. This layout is shown in Fig. 2.10 (left). Spectro-imaging can work with one focal plane and both

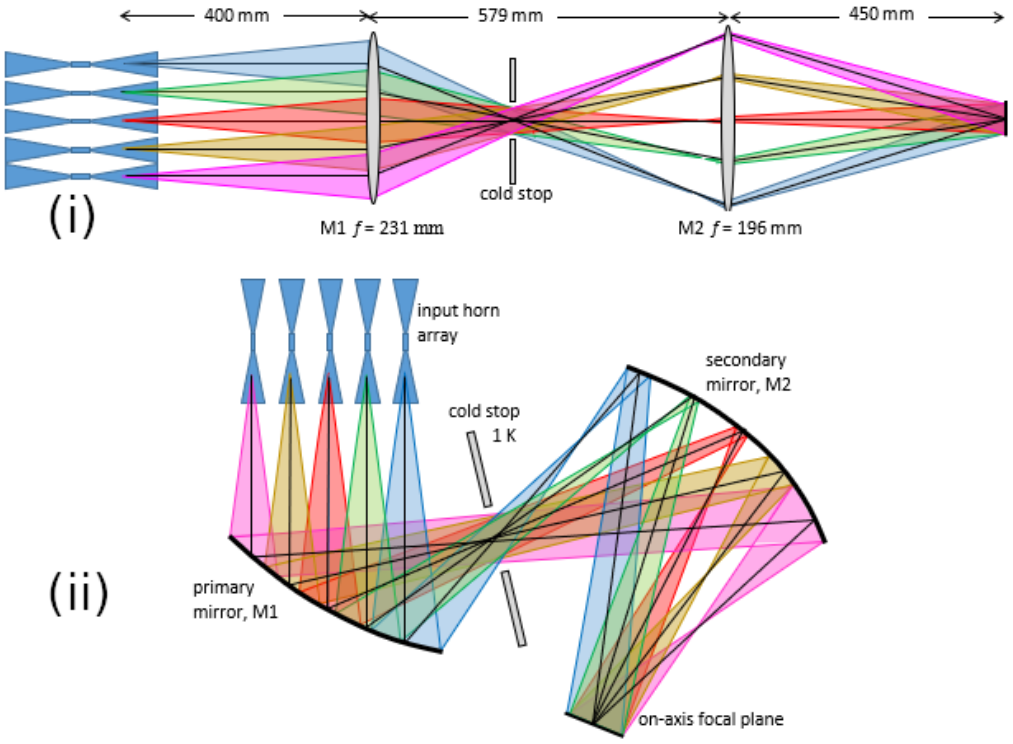

(a) (i) The equivalent ideal optical combiner is shown as an on-axis lensed system. (ii) The real off-axis mirrored optical combiner.

(b) Photograph of the FI mirrors. The four flanges on each mirror are mounting points to aid alignment. The mirrors do not need to be highly polished at QUBIC's operational frequencies.

Figure 2.15: The optical setup and mirrors of the QUBIC optical beam combiner. Figures reproduced from O'Sullivan et al., (2020) [71].

frequency bands but the dichroic and a second off-axis focal plane would boost overall instrument sensitivity. The QUBIC collaboration is focusing on developing the spectro-imaging technique while deciding on the inclusion of the dichroic and second focal plane.

2.3.4 Detectors

QUBIC uses TES bolometers as its detectors (Fig. 2.16). The FI will have two arrays with 992 detectors each. One FI array (Fig. 2.16a) will be directly on-axis with IV-curves tuned for the 150 GHz frequency band. Another array is located off-axis and will be sensitive to the 220 GHz band. Each detector has a sensitive area of 2.7 mm × 2.7 mm square and they are separated by 3 mm. The detectors in the focal plane are arranged into a circular shape with a radius of 57.16 mm. A photograph of one quarter of a focal plane (TD configuration) is shown in Fig. 2.16b. This photo includes wiring from the detectors to the readout electronics.

TES detectors work on the principle of low temperature superconductivity where a material (for QUBIC this is an Nb_xSi_{1-x} amorphous thin film with a critical temperature of 410 mK) is biased to operate in the narrow temperature range where they transition from the normal to superconducting state. When radiation is incident on the detector, the temperature increases as does the resistance (due to the loss of superconductivity). This change in resistance is measured to give the bolometer signal. This in turn reduces the Joule power in the detector circuit which allows the detector to cool (this is called negative Electro-Thermal Feedback (ETF)). The functionality of TES detectors is described by Enss (2005) [78] while the integration and characterisation of QUBIC's detector array is given by Piat et al., (2021) [67]. Fig. 2.16c shows the IV-curves for QUBIC's TD detectors operating at their critical temperature.

2.3.5 Readout Electronics

QUBIC's electronic readout system connects the detectors using aluminium wires to Superconducting QUantum Interface Devices (SQUIDs), Application-Specific Integrated Circuits (ASICs), Field-Programmable Gate Array (FPGA) boards, and finally to desktop PCs recording the detector data. The main components are highlighted in Fig. 2.17. Fig. 2.17a shows the FI TES array wired to the SQUID

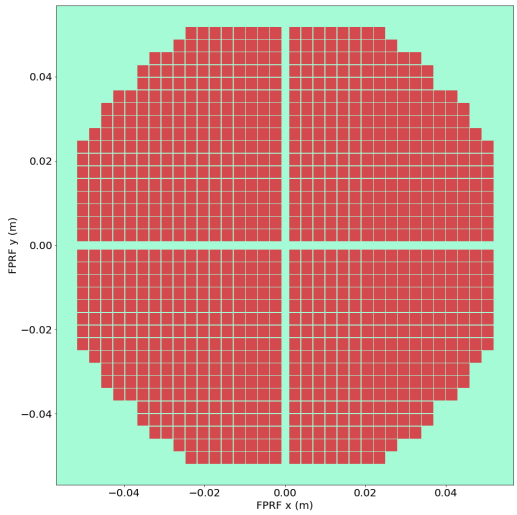

(a) The 992 TES bolometer layout for the FI. The bolometers are arranged into a roughly circular shape. The FPRF axis labels refer to the *focal plane reference frame*.

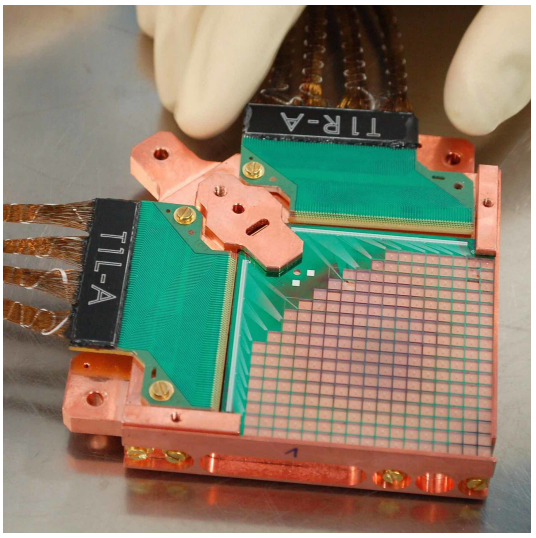

(b) A photograph of one quarter (248 detectors) of the focal plane used for the TD. The wiring to the readout electronics is also shown. Reproduced from Piat et al., (2021) [67].

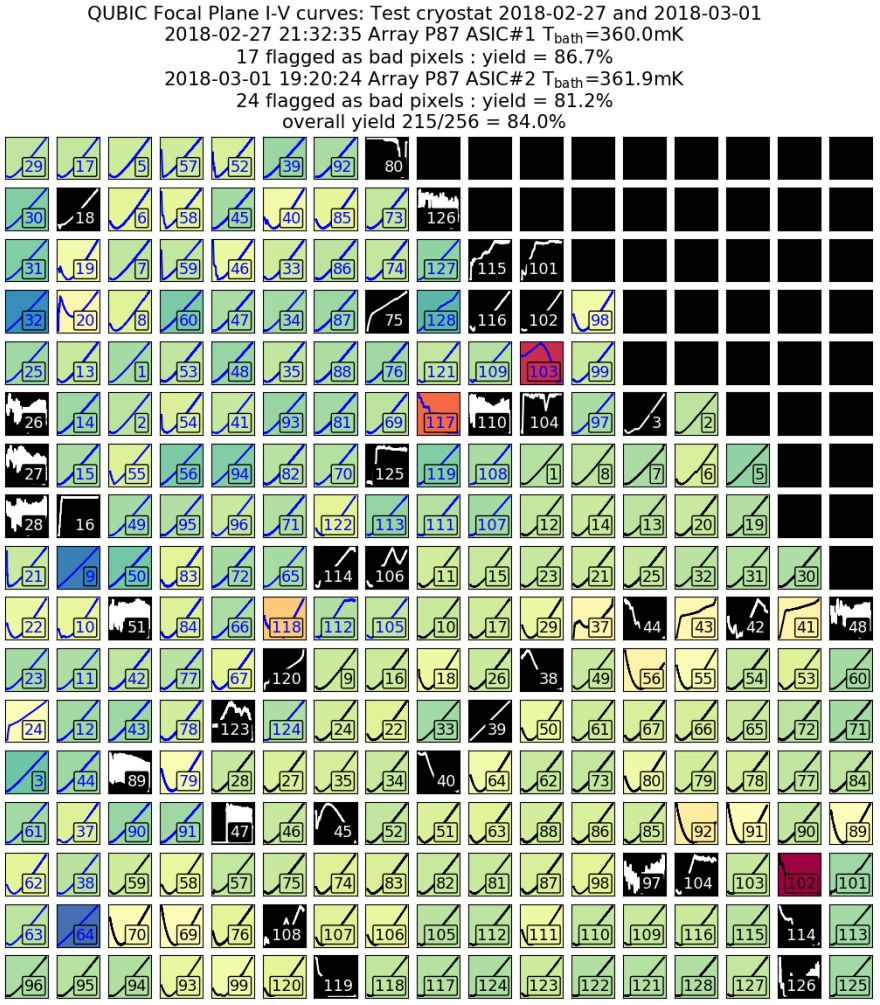

(c) IV-curves for the TD show the detectors operating within the critical temperature. Reproduced from Piat et al., (2021) [67].

Figure 2.16: Examples of QUBIC's focal plane setup for the TD and FI.

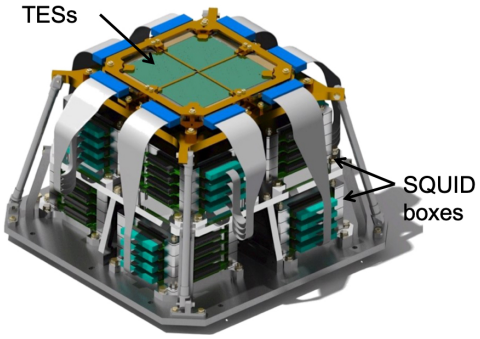

(a) The TES array is shown mounted on the SQUID boxes which are connected via wire columns.

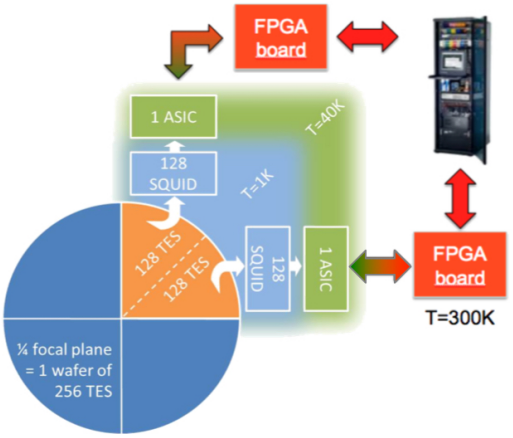

(b) A diagram showing how the focal plane is split into two ASICs. Each ASIC reads 128 detectors through SQUID multiplexing SQUID boxes. The ASICs are connected to room temperature computers. The temperature stages where the electronics are housed are also highlighted.

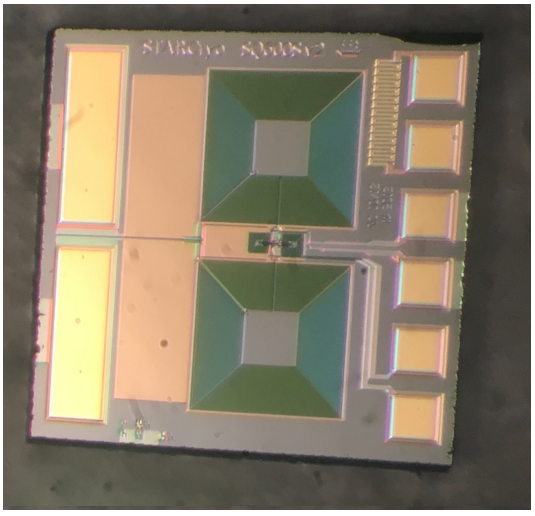

(c) A SQUID die.

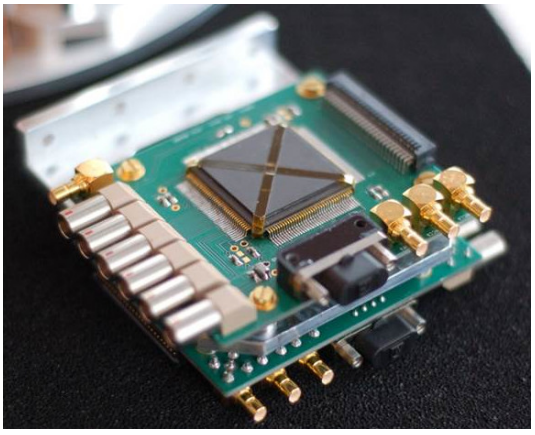

(d) A photograph of an ASIC.

Figure 2.17: Key elements of QUBIC's readout electronics are shown. Reproduced from Piat et al., (2021) [67].

boxes. Each of these components is located in a different cooling stage of the cryostat. This is shown in Fig. 2.17b. Full details of the of the readout electronics integration and characterisation are provided by Piat et al., (2021) [67].

The SQUIDs are cryogenic amplifiers and are held at 1 K for correct operation. The SQUIDs used in QUBIC are a modified off-the-shelf model provided by Star-Cryoelectronics[2]. They also provide a detector multiplexing function, with each SQUID processing data from 32 TES detectors. A photo of one SQUID die is shown in Fig. 2.17c. These SQUIDs are stacked under the focal plane as shown in Fig. 2.17a.

The ASICs (Fig. 2.17d) are kept at 40 K. Each ASIC is capable of processing 4 SQUIDS. This creates a final multiplex factor of 128:1 and this means there are 8 ASICs for one focal plane array for the FI. The ASICs are connected to FPGAs and in turn desktop PCs at room temperature.

2.3.6 FI External Calibration Source

Redundant baseline self-calibration is a key aspect of the QUBIC instrument in terms of minimising systematic effects and detecting the B-mode polarisation. As part of the self-calibration procedure, two external calibration sources (Fig. 2.18) for the 150 GHz and 220 GHz bands will be directed at QUBIC. QUBIC will scan the sources while opening and closing horns in the horn array. This procedure, with special reference to QUBIC, is described by Bigot-Sazy et al., 2013 [65] and later in this thesis in Chapter 8.

The external calibration sources will be mounted on a large tower 52 m above the ground level. This structure is shown in Fig. 2.18a. The structure is located 40 m from the QUBIC instrument itself to ensure the source is in the far-field of the instrument aperture. Fig. 2.18b is a zoomed in image of the top of Fig. 2.18a. It shows two external calibration sources, the associated electronics, and the housing mounted on top of the tower structure. These components are estimated to weigh approximately 50 kg when realised. These details, and drawings shown in Fig. 2.18a, are currently provisional and the exact design is currently being finalised.

[2] starcryo.com

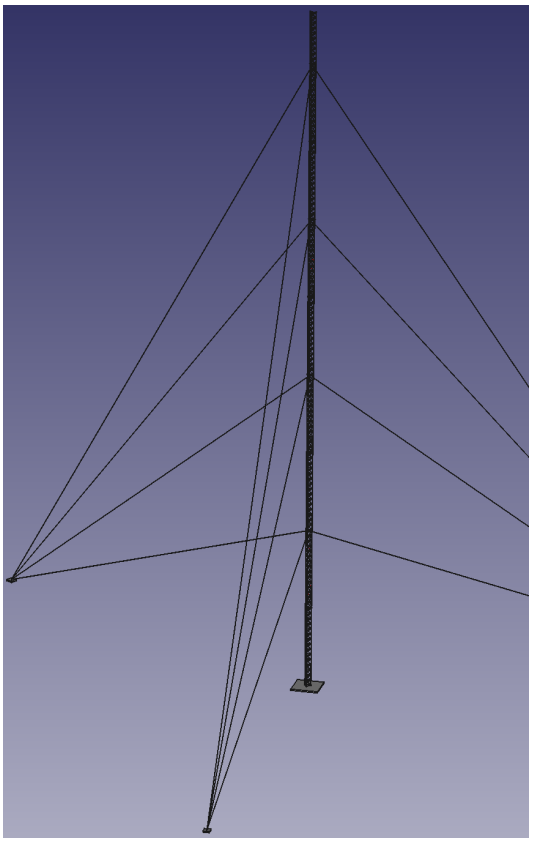

(a) The 52 m tower. The calibration source box and electronics will be mounted near the top.

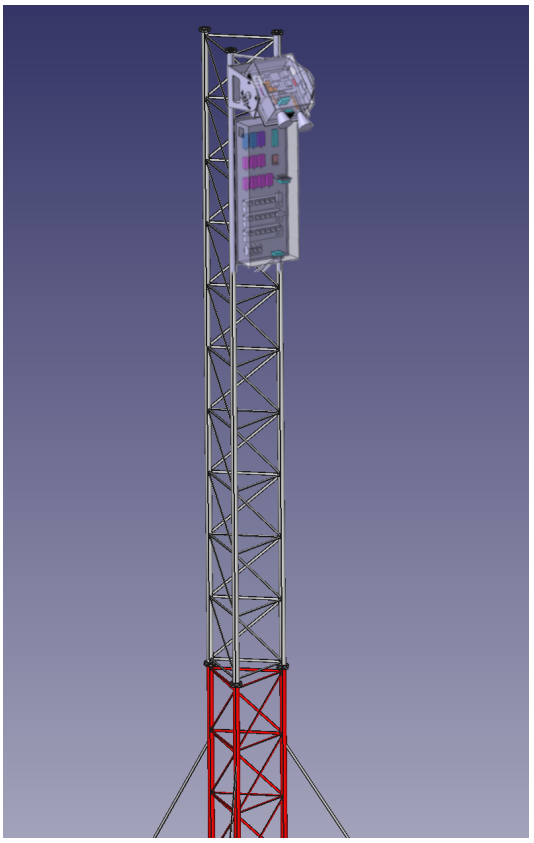

(b) A zoom of the top of the tower to show the calibration source box and electronics. It will be directed at the QUBIC instrument. QUBIC will scan the modulated source in order to perform calibrations.

Figure 2.18: 3D CAD drawings of the calibration tower and calibration source box. These are provisional drawings.

2.4 QUBIC Technical Demonstrator

2.4.1 Motivation for a Technical Demonstrator

The QUBIC TD is a specific configuration of QUBIC used to test and validate the operation and integration of QUBIC and its novel technologies. It has done this through integration campaigns in Paris and Salta and finally sky observations are due to begin soon on-site in Alto Chorillo. The TD will observe the intensity and polarisation of the sky around the Galactic centre. The initial TD sky observations will also test the self-calibration and spectro-imaging functionalities in addition to the hardware. With the technology proved, QUBIC will be upgraded to the FI.

	Horns & Switches	ICFCS	Mirrors	CS	Dichroic	Focal Plane Detectors
TD	64	2	Reduced size	✓(NDF)	✗	248
FI	400	✗	Full size	✓	✓	2x992

Table 2.3: Here the differences between the TD and FI are highlighted. All other components are identical. The Internal Carbon Fibre Calibration Sources (ICFCS) are mounted on the TD horn array. The TD as a Neutral Density Filter (NDF) manufactured by Ecosorb added to reduce the calibration external calibration source power. One-quarter of one focal plane (248) detectors and associated electronics are installed in the TD.

2.4.2 Comparison Between TD and FI

The cryostat, cooling mechanisms, filters, HWP, polariser and many other components in the TD are the same as those that will be used for the FI. The components that are different are listed in Table 2.3. The key differences are in the horn array, mirror size, and number of detectors.

The TD has 64 horns whereas the FI will have 400. The horns will be identical in individual performance. Using 64 horns will affect the PSF and synthesized beam on the sky in terms of FWHM but the peak positions will be the same since the inter-horn spacing is the same. The smaller number of horns also means that the number of redundant baselines is reduced. Even with fewer baselines, self-calibration can be used to constrain and solve the systematics for the TD.

The reduced physical size of the aperture plane horn array makes space for two Internal Carbon Fibre Calibration Sources (ICFCS) that are attached to the side of the horn array. These are wide flat field sources that are used in the detector calibration. They will not be present in the FI.

The TD primary and secondary mirrors have reduced diameters compared with the FI (see Table 2.2). Using smaller mirrors meant that they could be manufactured in-house by our collaborators in Milan. The surface shapes are identical to the FI except for their diameter and that the FI mirrors have flanges added. These flanges were added to aid in alignment of the mirrors.

The TD detector array has one quarter of one focal plane giving 248 TES detectors in total. The FI will have two full focal planes of giving a total of 1984 detectors.

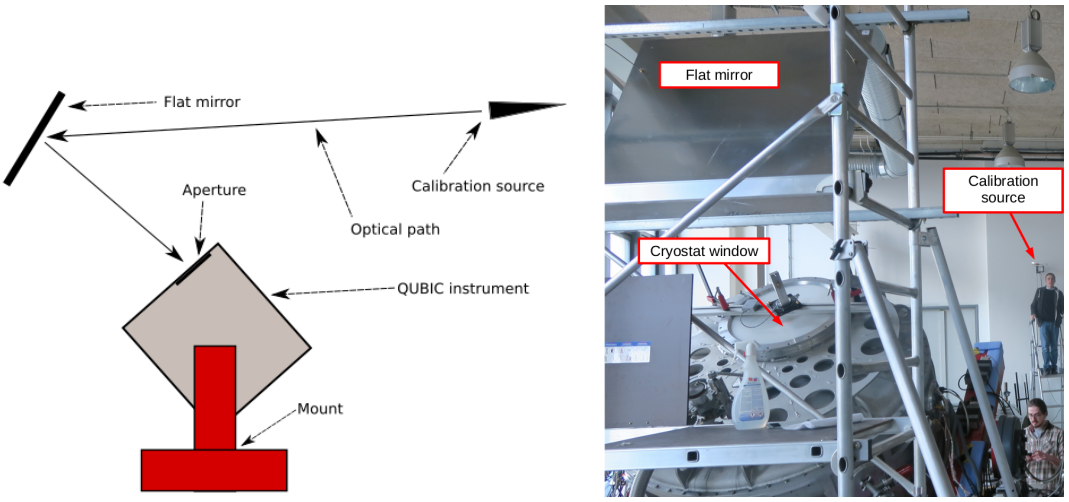

(a) Set-up of the external calibration source and instrument in APC, Paris. The mount moves in azimuth and elevation and effectively scans the source.

(b) Photograph of the external calibration source setup in APC.

Figure 2.19: The calibration source setup. A similar setup will be implemented in Salta. The full tower will be used on-site at Alto Chorillo.

2.4.3 TD External Calibration Source

The external calibration source (Fig. 2.19) for the TD is similar in purpose and setup to the FI external calibrators. The FI external calibration will be primarily used for self-calibration during scientific observations while the TD external calibration source is used for validation and calibration measurements such as testing the rotating HWP and polariser, switches, synthesized beams, TES inter-calibration, etc. within the integration laboratories in APC and Salta.

The calibrator is a 10-GHz Gunn oscillator followed by two multipliers to give a frequency-tunable 130 - 170 GHz source fed by a 10° scalar feed-horn. Fig. 2.19a shows a schematic of the calibration source being reflected off a mirror and illuminating the aperture and subsequently the detectors in the instrument. Fig. 2.19b shows the same calibration setup in a photograph. Chapters 6 and 7 rely heavily on data produced in APC with this calibration source and it is described in more detail in Section 6.2 and by Torchinsky et al., (2020) [53].

2.4.4 TD Internal Carbon Fibre Calibration Lamps

Unlike the FI, the TD has two internal calibration sources (Fig. 2.20) mounted on the TD horn array. The locations of the sources on the horn array are shown

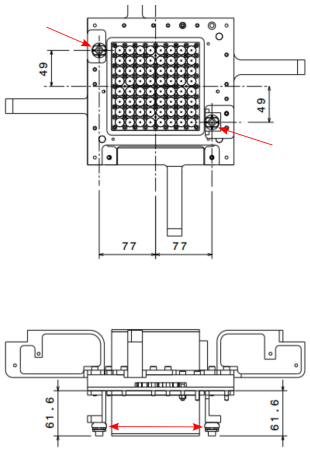

(a) Diagram of the TD horn array. The internal calibration source locations are indicated by the red arrows.

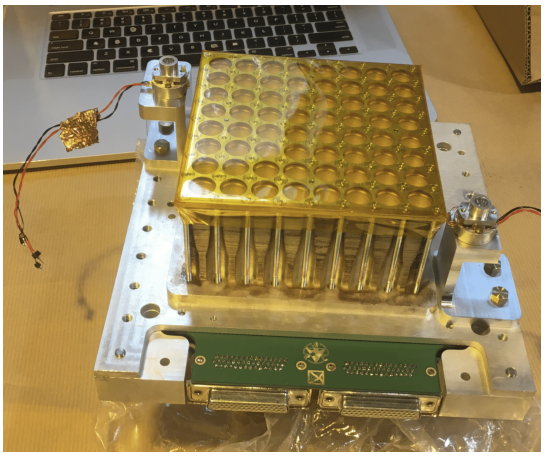

(b) A photo of the TD horn array. The internal calibration sources are mounted on the corners of the array.

Figure 2.20: Details of the internal carbon fibre calibration sources are shown here.

in Fig. 2.20a and in a photograph in Fig. 2.20b. The calibration sources produce 48° beams via thermal carbon fibres. They are intended to produce a flat field on the focal plane for the inter-calibration of the detectors.

These sources have been repurposed from the High Frequency Instrument (HFI) instrument on the Planck satellite and the same units are now installed in QUBIC (the pre launch calibration is detailed by Pajot et al., (2010) [79]). The sources used for calibrating the HFI are described by Henrot-Versillé, Cizeron, and Couchet (2009) [80]. An optical model of these sources for the calibration of QUBIC is the subject of Chapter 4 of this thesis which includes a more detailed description.

2.5 QUBIC Software

All of the hardware described above has been controlled, integrated, calibrated, and analysed through a range of custom software and code packages. QubicStudio, pystudio, qubicsoft, qubicpack, pyoperators, pysimulators, and mypy are integral to QUBIC and this thesis. This thesis relied, in particular, on qubicsoft and qubicpack. The author made contributions to qubicsoft during the course of the thesis and delivered training to new collaborators on how to use the software to analyse data.

- **QubicStudio** is a custom and bespoke software developed by the QUBIC collaboration. QubicStudio operates on a PC connected to the instrument and other ancillary control devices for operating the instrument (cryo heaters, calibration source, detector readout electronics, and mount control). It provides the primary control of the instrument and records all data produced. It also controls the mount movements for calibration and sky observations. It controls cooling and thermometer readouts. During calibration it controls the calibration source settings and records them. It also controls the detector settings (e.g. I-V curve tuning) during an acquisition as well as recording the data produced by the detectors in an acquisition. The data for each acquisition is stored in two types of data file, science and housekeeping. The science files refer to the detector data and HWP position while housekeeping refers to information about the acquisition such as calibration source settings (voltage, offset, amplitude, etc.) and thermometer data.

- **pystudio** [3] is an interface and library for the QubicStudio software.

- **qubicsoft** [4] has simulation and map-making tools for the QUBIC experiment. It has tools for end-to-end simulations, cosmological analysis functions, data reduction and analysis tools, as well as a large array of other useful tools for QUBIC applications.

- **qubicpack** [5] is a package for reading the instrument data, visualization, and data analysis.

- **pyoperators** [6] has high performance computational tools forked from Chanial (2012) [81].

- **pysimulators** [7] has tools for simulating the instrument.

- **mypy** [8] has data and timing tools.

[3] github.com/satorchi/pystudio
[4] github.com/qubicsoft/qubic
[5] github.com/satorchi/qubicpack
[6] github.com/qubicsoft/pyoperators
[7] github.com/qubicsoft/pysimulators
[8] github.com/satorchi/mypy

2.6 Summary

QUBIC has a novel and unique design for a cosmology instrument. It is the only bolometric interferometer of its kind and it is designed to minimise the systematic contamination of B-mode observations. This is made possible via a self-calibration procedure. QUBIC further increases its observational powers by a software technique called spectro-imaging that recovers images at several frequency sub-bands. These features were briefly described at the start of this chapter.

The components were then described in the order they are encountered by a beam propagating from the sky, through the entrance aperture, and to the detectors. The optical components of the beam combiner (for example, the horns, horn array, HWP, polariser, mirrors, and calibration sources) and detector layout are especially important for the work carried out for this thesis. The motivation for having a TD configuration was given and the differences between the two configurations of QUBIC, the TD and the FI, were also discussed.

Chapter 3

Quasi-Optical Modelling Techniques

3.1 Introduction

Typically in radio astronomy the wavelength of radiation is comparable to the size of components and so diffraction is an important effect. Complex modelling techniques such as Physical Optics (PO) and the Physical Theory of Diffraction (PTD) are needed to design and test systems at these wavelengths. In the optical regime, the wavelengths are small compared to the size of the optical components and diffraction effects are reasonably small. Geometric Optics (GO ray-tracing) has low computational requirements and is often sufficient for most optical wavelength needs. QUBIC operates at frequencies between 130 and 240 GHz (corresponding to wavelengths between 1.3 and 2.3 mm). These millimetre wavelengths occur between the radio and optical bands and require the modelling techniques of both long and short wavelength optics and hybrids of the two (quasi-optics such as Gaussian Beam Mode (GBM) analysis).

In this thesis, PO and PTD are used extensively, and to a lesser extent GO. GRASP, a commercially available software, is the main PO and PTD software used (Fig. 3.1). MODAL, an MU in-house PO and PTD software, and Zemax, a commercially available GO software, are also used. This chapter will describe the relevant optical theories and software used throughout the thesis.

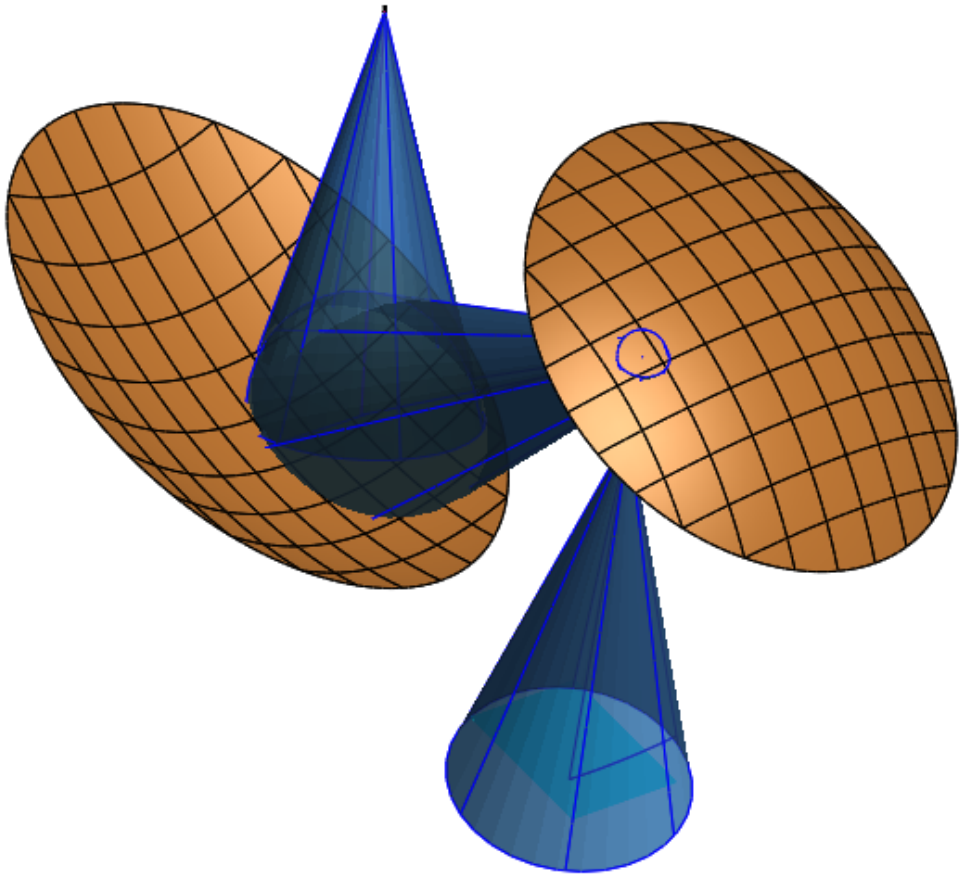

Figure 3.1: A simple model of the QUBIC optical combiner is shown with a Gaussian beam (blue) from the GRASP software. The beam illuminates the mirror near the rim so diffraction and truncation should be considered. The mirrors (orange) reflect the source onto a focal plane grid (light blue).

3.2 Physical Optics

PO implemented in GRASP forms the basis of nearly all modelling in this thesis. It works by calculating the currents that are induced on a surface when an electric field is incident on it. In Fig. 3.1 the beam illuminates a region of the QUBIC primary mirror with an electric field. At a point on the surface where the electric field is incident, the current is calculated for an infinite plane of perfect conductance. This will be computed for a number of points on the surface so that it is adequately sampled. The electric field radiated by these currents is then propagated to the next surface where the total field is the source field plus the reflected field and is written as $E_{PTD} = E_I + E_R$.

Two general assumptions are made in PO. The first is that the scatterer (mirror)

surface is a perfect conductor. The second is that the current induced on a scatter surface is the same as would be induced on a flat plane infinite in size and located at the point on the real surface and tangent to it. There are two ways to calculate the radiated fields, a direct one-step and an indirect two-step method using vector potentials (**A** and **F**). The two-step vector potential method is generally preferred (Balanis (2016) [82]) where the intermediary potentials are:

$$\mathbf{F} = \frac{\epsilon}{4\pi}\iint_S \mathbf{M}(\mathrm{r})\frac{e^{-ikR}}{R}ds \text{ and } \mathbf{A} = \frac{\mu}{4\pi}\iint_S \mathbf{J}(\mathrm{r})\frac{e^{-ikR}}{R}ds \tag{3.1}$$

where **F** is the electric vector potential, **M** is the induced magnetic current in the surface (S) (for a perfect conductor $\bar{M} = 0$), **A** is the magnetic vector potential, and **J** is the induced electric current on the surface, μ is the magnetic permittivity of the surface, ϵ is the permeability of free space, k is the frequency dependent wave number, and R is the radial distance from the source at which the vector is calculated. The electric current that is induced by an incident field on a planar and perfectly conducting surface is

$$\mathbf{J} = 2\hat{n} \times H \tag{3.2}$$

where $\hat{n}$ is the surface normal at the point of intersection of the real surface and the tangential plane.

The full derivation of the fields from these potentials is given by Balanis (2016) [82] and in summary:

$$\begin{aligned}
\mathbf{H}_A &= \frac{1}{\mu}\boldsymbol{\nabla} \times \mathbf{A} \\
\mathbf{H}_F &= -j\omega\mathbf{F} - \frac{j}{\omega\mu\varepsilon}\nabla(\nabla \cdot \mathbf{F}) \\
\mathbf{E}_A &= -j\omega\mathbf{A} - j\frac{1}{\omega\mu\varepsilon}\nabla(\boldsymbol{\nabla} \cdot \mathbf{A}) \\
\mathbf{E}_F &= -\frac{1}{\varepsilon}\boldsymbol{\nabla} \times \mathbf{F}.
\end{aligned} \tag{3.3}$$

By combining these results to find the total electric and magnetic fields it is found that:

$$\begin{aligned}\mathbf{E} &= \mathbf{E}_A + \mathbf{E}_F = -j\omega\mathbf{A} - j\frac{1}{\omega\mu\varepsilon}\nabla(\boldsymbol{\nabla}\cdot\mathbf{A}) - \frac{1}{\varepsilon}\boldsymbol{\nabla}\times\mathbf{F} \\ \mathbf{H} &= \mathbf{H}_A + \mathbf{H}_F = \frac{1}{\mu}\nabla\times\mathbf{A} - j\omega\mathbf{F} - j\frac{1}{\omega\mu\varepsilon}\nabla(\boldsymbol{\nabla}\cdot\mathbf{F}).\end{aligned} \tag{3.4}$$

3.3 Physical Theory of Diffraction

The Physical Theory of Diffraction (PTD) is a correction to PO calculations near the edges of surfaces where diffraction occurs. In PO, currents are calculated for an infinite plane surface. Near the edge of a surface, this assumption is not physical. The final corrected result is:

$$E_{scattered} \approx E_{PTD} + E_{PO}. \tag{3.5}$$

E_{PTD} is calculated by assuming an infinite perfectly conducting half-plane (or canonical edge), rather than 'full'-plane for PO. E_{PTD} integrates edge currents of the main scatterer face and the half-plane face along the edges of the scatterer. GRASP implements PTD based on the method described by Johansen (1996) [83] and [84] and by Shore and Yaghjian (1988) [85].

3.4 GRASP

GRASP (Fig. 3.2) is an antenna design and analysis software package by TICRA[1]. It is a particularly powerful tool due to the range of analysis methods that are implemented such as: PO, PTD, GO, geometric theory of diffraction, spherical wave expansion, plane wave expansion, and method of moments. It is based on object orientated Fortran 90 code and has a useful Graphical User Interface (GUI) for design (Fig. 3.2a) and analysis (Fig. 3.2b). A key feature of GRASP, and one of the reasons it was selected for modelling QUBIC, is that GRASP can model surfaces as tabulated points. This allows real measured mirror points to be analysed and not just an idealised mirror surface equation. General information on GRASP is available in the user guide by TICRA (2015) [86] and technical

[1] www.ticra.com

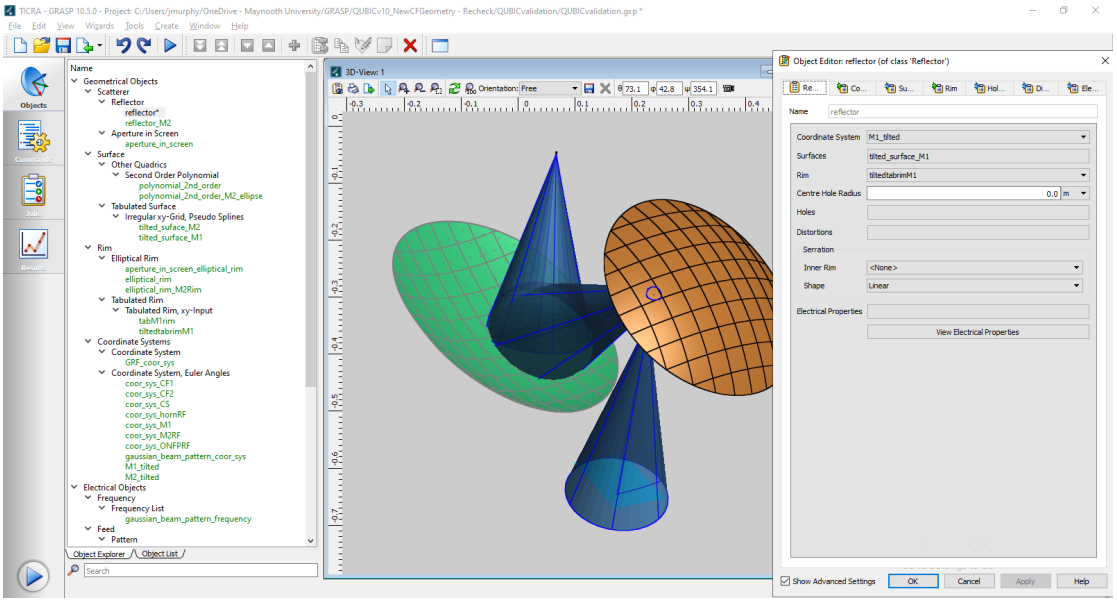

(a) The 'objects' pane is used to design and build the models. It features a CAD illustration and options for geometrical, electrical, and analysis objects.

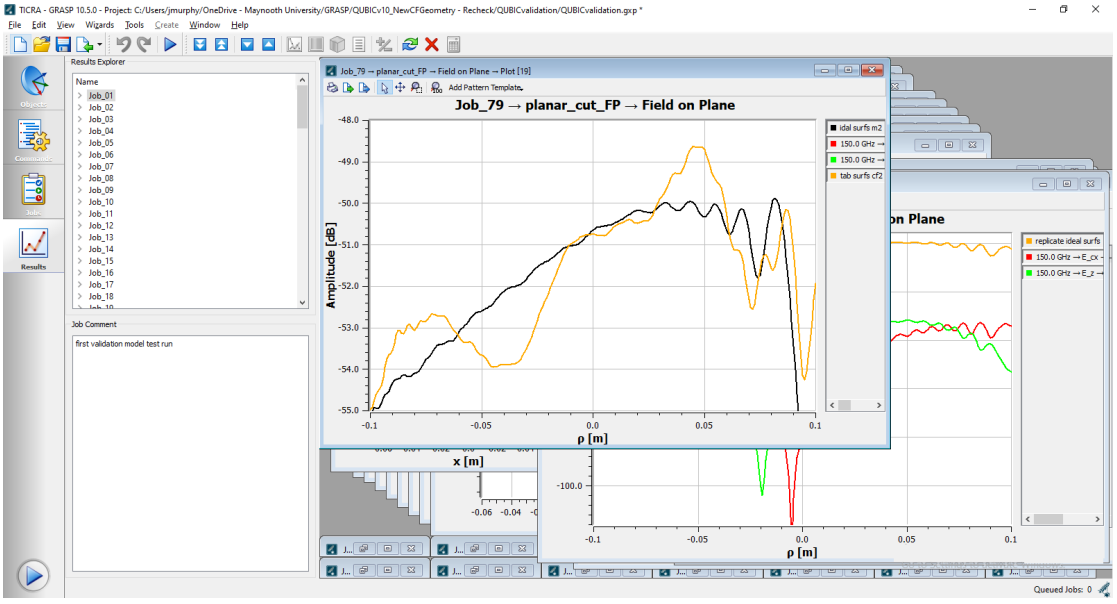

(b) Once the model is setup and simulation data are stored in grids or cuts, the 'results' pane is used for analysis. Cuts and grids can be compared and analysed. The raw data can be exported for further analysis.

Figure 3.2: The 'objects' and 'results' panes from the GRASP GUI are shown.

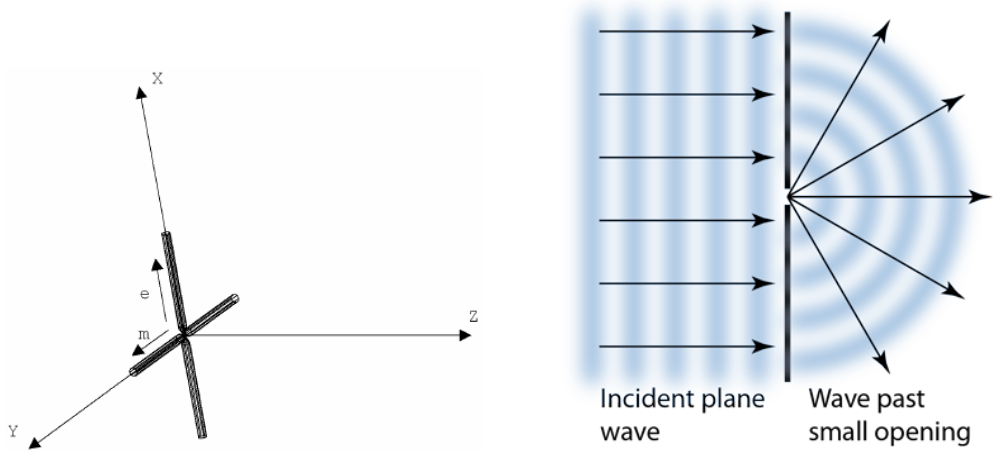

(a) A Hertz dipole in GRASP generates a Huygens source. This consists of both an electric and magnetic dipole along the x and y axes, respectively. Image is reproduced from Pontoppidan (2015) [87].

(b) A Huygens source is the spherical wavefront arising from a plane wave illuminating a small aperture. *Image credit: HyperPhysics [88].*

Figure 3.3: Illustrations showing GRASP's method of defining a Gaussian source.

implementation details are available in the technical description by Pontoppidan (2015) [87]. Some features of GRASP used in this thesis are described next.

3.4.1 Sources

For QUBIC, many simulations begin with a beam from a corrugated horn. Two types of sources are used to model this.

3.4.1.1 Gaussian Sources

A Hertz dipole model is used to generate a Gaussian Beam in the near and far fields. In this set-up, a Hertz Dipole (Fig. 3.3a) is considered as a complex point source that launches a Huygens style (Fig. 3.3b) spherical wave-front with a Gaussian amplitude distribution. In GRASP, the user specifies the frequency of the source, its location (in x, y, and z coordinates), the beam waist radius, radius of curvature of the phase front, and polarisation direction.

3.4.1.2 Tabulated Sources

The Gaussian beam source is useful when setting up and validating instrument models due to its simplicity. However, since the goal of the modelling is to develop a realistic simulation of the optical elements, a more sophisticated model of QUBIC's horn is often required. QUBIC's horn is an 'ultra-Gaussian' hybrid horn. It is single-moded at 150 GHz and multi-moded at 220 GHz (as discussed previously in Section 2.3.3.5). GRASP cannot simulate the feed-horns without the CHAMP add-on. It can, however, read in a tabulated aperture field calculated elsewhere. The tabulated aperture field is propagated as a source using a spherical wave expansion. The tabulated aperture field and Gaussian approximation are compared in Section 5.3 of this thesis.

3.4.2 PO Convergence & Field Accuracy

In PO it is of critical importance to choose the number of points on the scatterer, at which the current is calculated, correctly. If too few PO points are calculated inaccurate fields will result. If too many points are chosen, time is wasted. In GRASP there are two PO point variables ($po1$ and $po2$) for a surface. These PO points can be on a Cartesian or polar grid depending on the geometry of the scatterer and $po1$ and $po2$ determine the sampling rate along each coordinate.

A first order estimation of the number of PO points for a source field on a scatter is given as:

$$po1 = \frac{z}{2.4} \text{ and } po2 = z \tag{3.6}$$

where

$$z = 1.09\pi\frac{D}{\lambda}\sin\theta_0 + 10 \tag{3.7}$$

and D is the reflector diameter, λ is the radiation wavelength and θ_0 is the maximum angle from the beam on the scatter. A rule of thumb that can be used as a first order estimation is that the separation between PO points should be no larger than half a wavelength ($\Delta l < \frac{\lambda}{2}$).

GRASP has an auto-convergence function that is capable of finding the correct number of PO points in a given simulation. It starts by setting $po1 = po2 = 10$. $po1$ is doubled until the resulting fields for subsequent PO point sampling is less than $10^{\frac{\text{field accuracy}}{20}}$. "Field accuracy" sets the acceptable error for the calculated

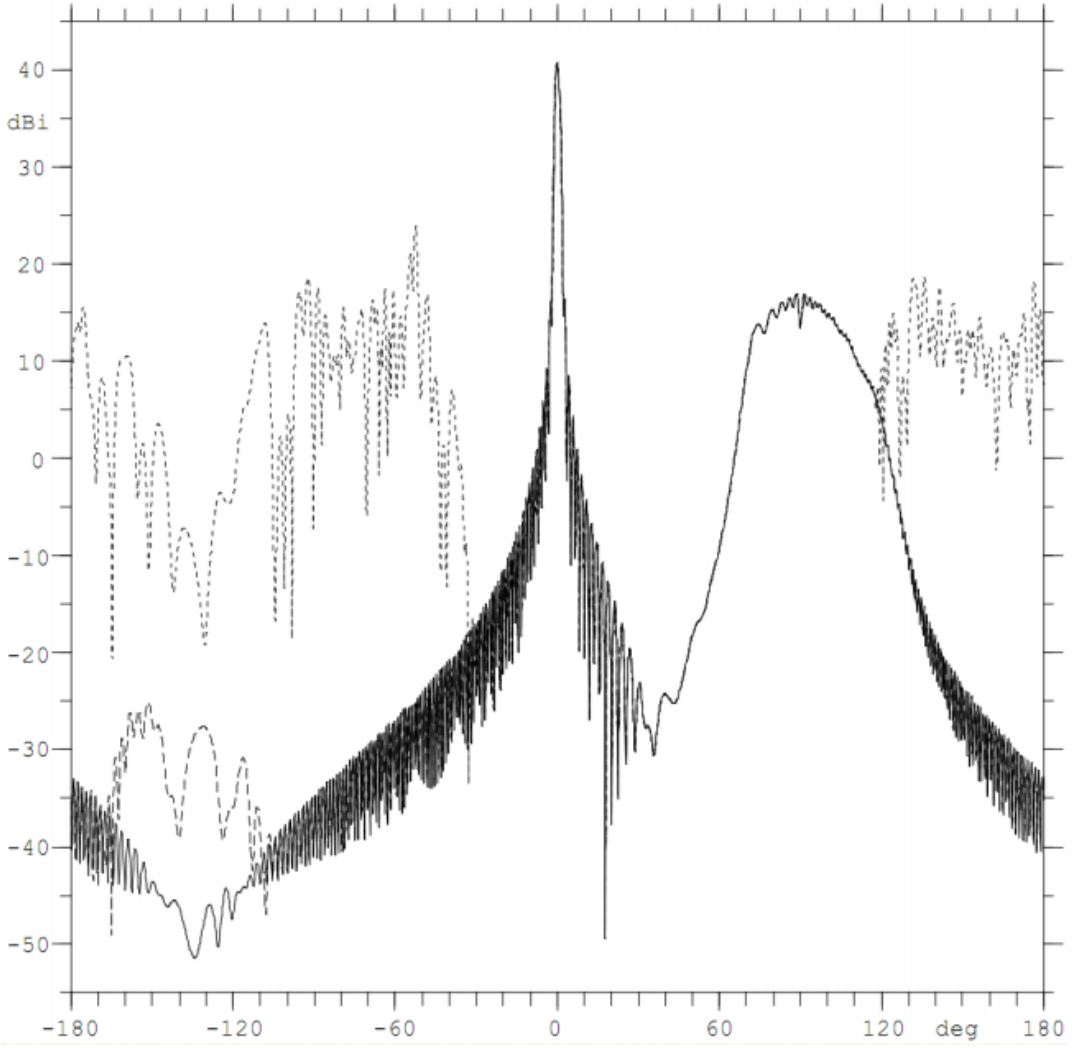

Figure 3.4: An example of the effect of field accuracy for an antenna pattern reflected off a mirror. For the solid line, the field accuracy is set at −100 dB with 31,500 PO points, for the dashes set at −60 dB with 27,435 points, and for the dots it is set at −20 dB with 3,255 points. Reproduced from Pontoppidan (2015) [87].

field. For example, if the field accuracy is set to −60 dB, the field error is −60 dB lower than the maximum value in the field. Typically, the default value of the field accuracy is −80 dB. Once convergence is found for $po1$, $po2$ is found by setting $po1 = po2 = 10$ again and repeating the doubling of sampling for $po2$.

The effects of PO convergence and field accuracy are shown by example in Fig. 3.4. The data are for an antenna pattern after reflection of a horn beam from a mirror. The figure shows that increasing the precision of the field accuracy (setting it lower), increases the accuracy of the pattern at lower power levels by increasing

the number of PO points through auto convergence. The effect of field accuracy while modelling QUBIC is tested in Section 5.3.1 of this thesis.

3.4.3 Mirrors

3.4.3.1 Ideal Mirror Equation

QUBIC's mirrors are ellipsoidal and paraboloidal in shape and are most simply described as a second order polynomial surface in GRASP. The surface equation in GRASP is defined by:

$$Ax^2 + Axy + Ay^2 + Ax + Ay + A_c = Az^2 + Az + Axz + Ayz \tag{3.8}$$

while an equivalent and more standard convention is:

$$\mathrm{Ax^2 + By^2 + Cz^2 + Dxy + Exz + Fyz + Gx + Hy + Iz + J = 0,} \tag{3.9}$$

as is the case with QUBIC documentation. The 3D CAD visualisation of an ideal surface equation is shown by the secondary mirror in Fig. 3.5.

3.4.3.2 Tabulated Mirror Surface

Naturally, the manufactured mirror is likely to have some surface imperfections from the manufacturing process. QUBIC's mirrors were milled from an aluminium block. While the tolerances for mirror surfaces are not extreme at millimetre-wavelengths it is still important to measure the manufactured mirrors and prove they have sufficient optical performance. GRASP has a feature so the x, y, and z Cartesian coordinates of mirror surface points can be loaded as a mirror surface. This way a realistic surface can be modelled. The 3D CAD view of this is shown with the primary mirror in Fig. 3.5. This is an important feature since no other software was available with this feature.

3.4.4 GRASP Files

GRASP's GUI is powerful enough so that simpler optical models can be simulated completely using only the interface. However, with QUBIC, it is necessary to

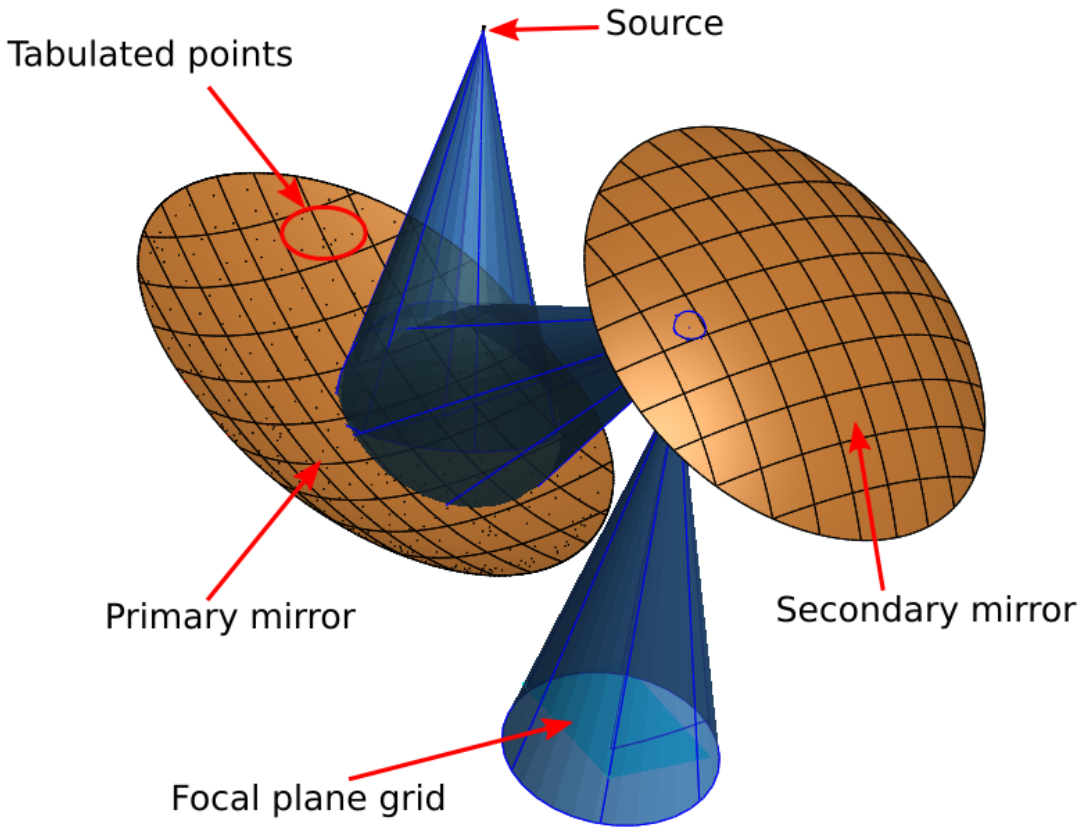

Figure 3.5: Tabulated primary mirror with measured points. The tabulated measured x, y, and z points are shown as black dots on the primary mirror surface and a subset is highlighted with a red circle. In this figure, the secondary mirror is defined by an ideal equation (no tabulated points, perfectly smooth definition). A sample source and the focal plane grid are also shown for context.

produce a large amount of simulation data for each horn at a range of frequencies. In this case, batch mode is used (described below) and .tor, and .tci files should be considered. These files describe the optical elements and control the optical calculations.

The .tor file contains the physical object definitions for each element in the model e.g. the mirror locations and shapes, the focal plane geometry, and horn location definitions. An example is shown in Fig. 3.6.

The .tci file contains a list of commands for each simulation. For example, the first command will typically (for QUBIC) carry out the calculation of the current induced by the source on the primary mirror. Fig. 3.7 shows blocks of commands. Each block is an identical set of commands for each horn defined in the .tor file.

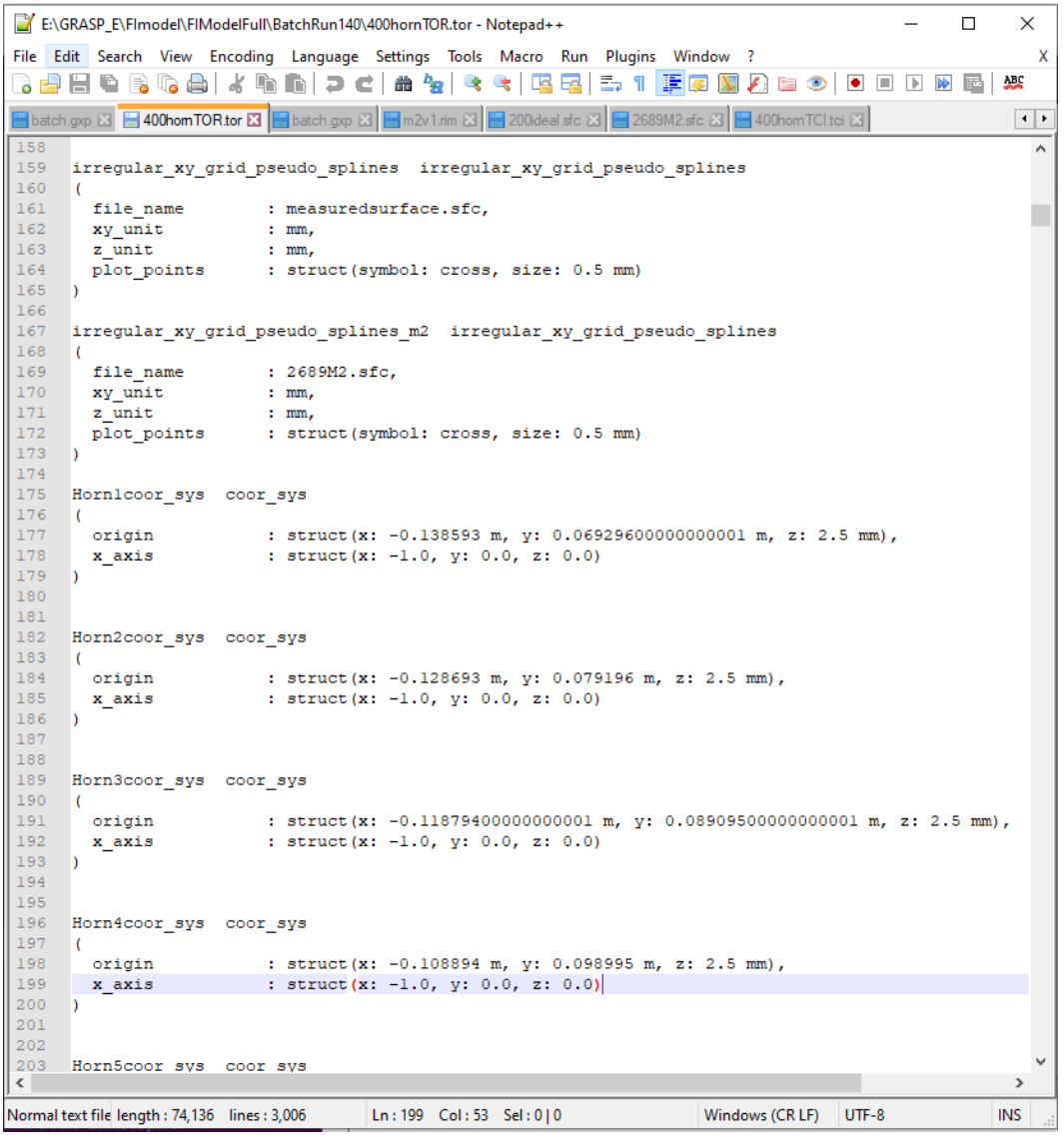

Figure 3.6: An example of a .tor file used. Object definitions for tabulated mirrors are shown before the list of 400 horn definitions. Each object type has its own parameters. For example, in this figure, lines 159 - 165 show a tabulated surface definition. The raw data file is specified, as are the units for the data points, and a graphical plotting parameter.

3.4.5 Batch Mode Operation

GRASP has a feature that allows the user to control and launch multiple simulations and modify the configuration between each run. This is useful for models of QUBIC as the beam pattern on the focal plane needs to be calculated for each of the 400 different horn locations and repeated for different frequencies. Batch-mode enables this kind of simulation to be run automatically.

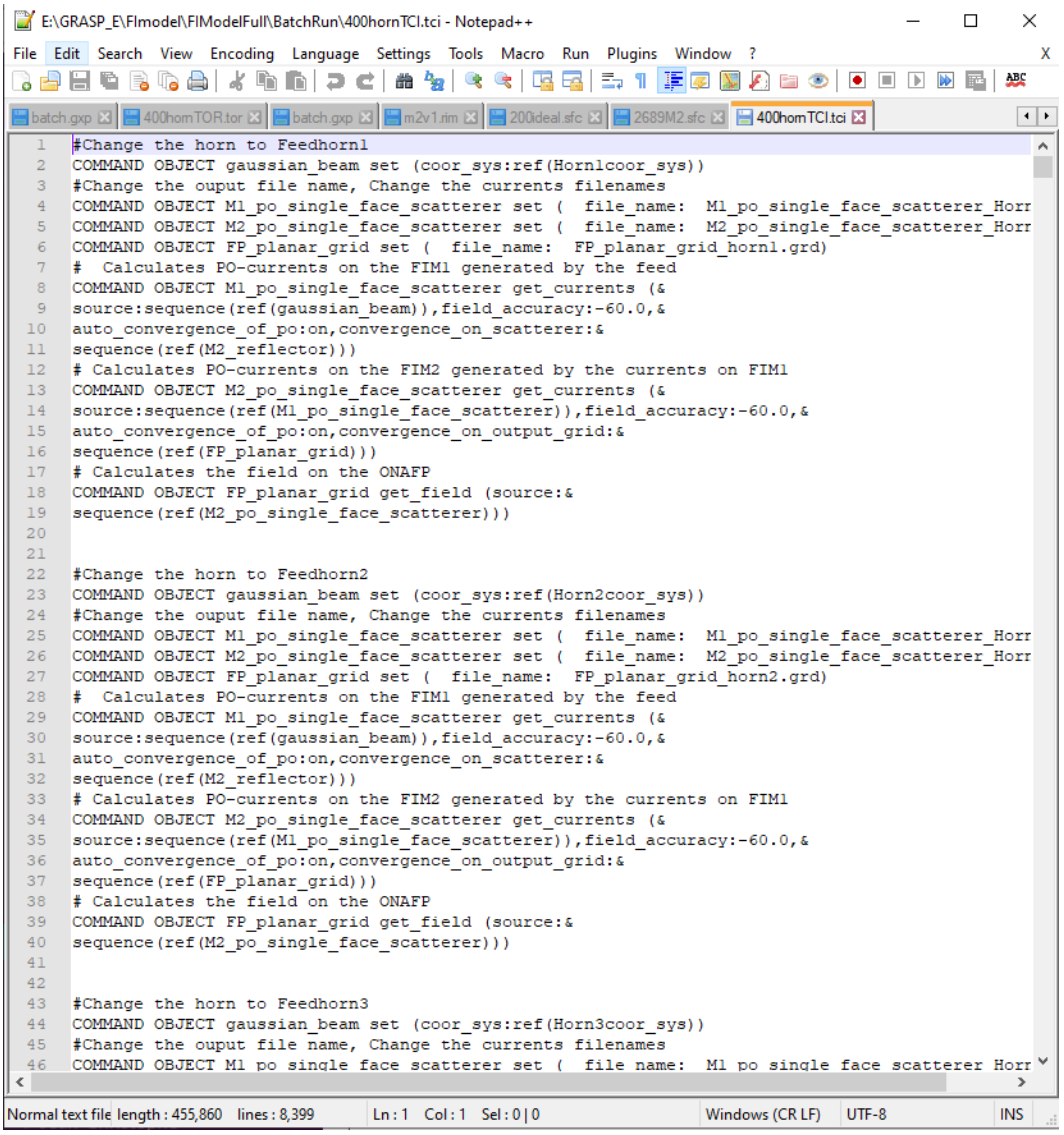

Figure 3.7: The .tci file contains a list of the commands used for a 400 horn batch mode simulation. Lines 1 - 19 show the simulation commands for one batch at one horn location. They are repeated for each horn location throughout the file. The comment lines (#) describe the simulation commands. The commands are carried out on the specified objects defined in the .tor file.

3.4.5.1 Set-Up Run

A batch mode simulation is first initialised with a 'set-up run'. The simulation is first run for, in this case, one horn specifying the optical components and simulation commands in the GUI. The simulation produces .tor, .tci, and a .gxp files (the .gxp file simply states the .tor and .tci file names when batch mode is used). The .tor, .tci, and .gxp files are used as the basis for the more complex batch mode simulation. The .tci file is modified to change objects between each simulation.

This can be done using a script that duplicates the commands but with updated .tor object references.

3.4.5.2 Batch Run

The batch run is now ready. A windows command interface must be used to run a command in the batch folder. For example, "grasp-analysis batch.gxp 400gaussFI150.out 400gausFI150.log" uses the .tor and .tci files specified in batch.gxp file and saves the output data to new .grd files within the '*/working*' folder. Additional information about the batch run are output to the 400gaussFI150.out and 400gausFI150.log files.

Simulations are run for each horn and the data are saved in the 'batch run' folder. There is a file of focal plane data for each horn. The .tor file can be modified to specify other frequencies and the process can be repeated to produce batch mode simulations for a range of frequencies in QUBIC's band-pass.

3.5 MODAL

MODAL (Fig. 3.8) is a PO modelling software (similar to GRASP) developed and maintained in Maynooth University for millimetre and sub-millimetre applications (Gradziel et al., (2007) [89]). MODAL's ability to model corrugated horns is a key feature for this application. MODAL can couple an input field to the back-to-back horns and calculate the resulting aperture field, it does not have to start with the horns as a source. It uses an electromagnetic mode-matching technique to calculate the aperture field of a horn once its geometry is known. In QUBIC, the horns are designed to work single-moded at 150 GHz and multi-moded at 220 GHz and this can also be handled by MODAL. Since the QUBIC horn field is not a pure Gaussian at 150 GHz, it is necessary to test the real beams at 150 GHz in QUBIC's optical combiner rather than simply approximating the beams as a Gaussian beam.

An example of the MODAL GUI is shown in Fig. 3.8a. The GUI is used to load the geometry file, in this case the QUBIC horn geometry file (Fig. 3.8b). The GUI is also used to set the other parameters of the simulation such as the input horn illumination and description of the optics.

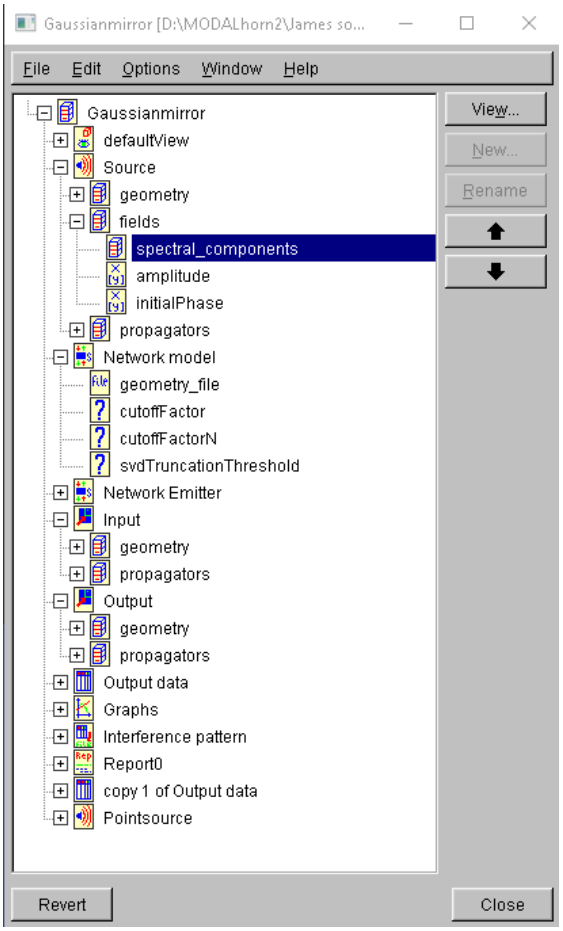

(a) MODAL's GUI interface. The model parameters and geometry are set using the interface e.g. selecting horn geometry file and setting aperture field location and geometry.

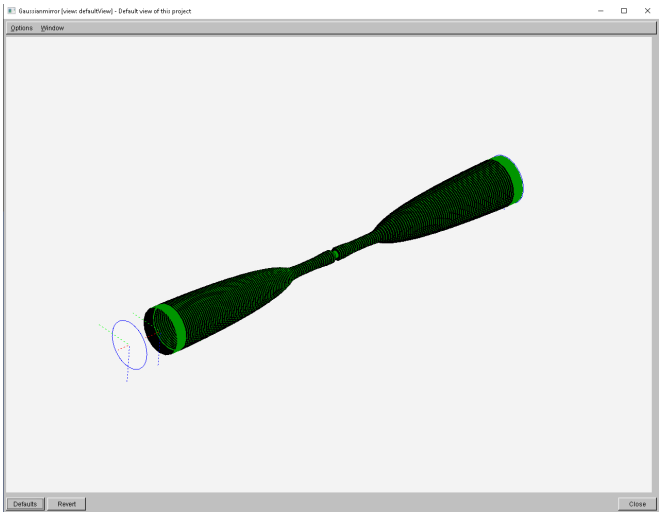

(b) 3D model of the horn geometry selected in the GUI. This image shows one of QUBIC's 400 corrugated back-to-back horns.

Figure 3.8: The model and fields are defined so that outputs can be produced in the MODAL GUI.

3.6 GRASP and MODAL Capabilities

GRASP and MODAL are very similar software packages that make the same PO calculations on scattering surfaces. There are some differences that means it is sometimes necessary to choose one over the other:

- **MODAL** is an in-house software package, it is a powerful tool capable of full end-to-end optical simulations. In this case, it can take a far-field source distribution, propagate it to and through the back-to-back horns, through the mirrors and apertures of the optical combiner and onto the focal plane. However, MODAL must use an analytical description of the mirror surfaces, it cannot as yet describe them using a set of x, y, and z surface coordinates.
- **GRASP** is an industry standard software package for PO optical modelling. This is an intrinsic advantage since it makes it easy to share models and data with colleagues. In GRASP, a realistic source beam must be modelled (externally or with an add-on package) and propagated directly through the optics onto the focal plane (while MODAL can have a source in the sky illuminating all of the horns and then the horns illuminating the subsequent optical elements). GRASP can define mirror surfaces and rims as x, y, and z points.

To take advantage of these individual features, the software packages are used in conjunction with each other. In this case, GRASP is required for its ability to model accurate surfaces. MODAL can calculate and produce a tabulated aperture field that can be given as an input to GRASP. GRASP can subsequently be used to propagate the tabulated aperture field (generated in MODAL) through the accurate optics and onto the focal plane.

3.7 Geometric Optics

Geometric Optics (GO, or ray optics) is the modelling of radiation as rays. The rays typically propagate in straight line paths from a source and reflect off surfaces. Bending of light through media of differing refractive index, e.g. lenses, is commonly modelled by GO. PO is necessary for complete analysis in systems like

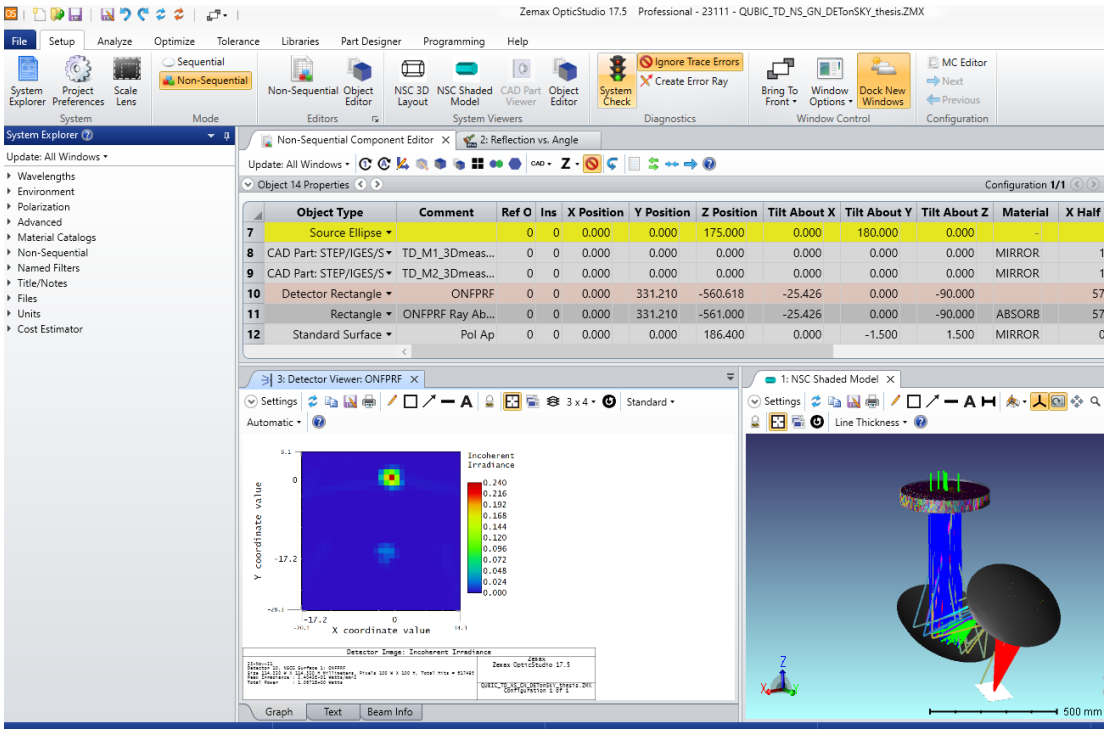

Figure 3.9: The Zemax GUI for its non-sequential mode. In the lower left a focal plane plot shows rays focusing at two points. The lower right shows the 3D model. The central interface has the object definitions.

QUBIC; however, in certain applications, e.g. stray-light analysis, GO is preferable.

3.7.1 Zemax

Zemax Optic Studio[2] is a commercially available GO modelling software. The Zemax GUI is shown in Fig. 3.9. It is primarily used for lens design and high frequency applications. While QUBIC's optics are already designed and manufactured, Zemax has powerful features that were used during this thesis. It has two design modes: sequential and non-sequential. Sequential mode is usually used for lens and optical design and considers rays as propagating from one optical component to the next, in sequence. Non-sequential mode is more suited to other tasks such as stray light analysis where rays reflect off surfaces multiple times and in different order.

Ray-tracing is still useful for many millimetre-wave and sub-millimetre applications. With QUBIC, Zemax has been used, for example, in the alignment of the

[2] www.zemax.com

mirrors (which was done using visible wavelength lasers) and stray light analysis by the author as shown by O'Sullivan et al., (2018) [22]. In this thesis, Zemax GO software is used to test for possible optical causes anomalous measurement data (Chapter 7).

3.8 Conclusion

This chapter describes the main optical modelling techniques and software that have been employed in this thesis for modelling QUBIC.

GRASP PO is the main software used in Chapters 4 and 5. The PO FI optical model data generated in Chapter 5 is then used as a basis for the analysis carried out in Chapter 8. The data from Chapter 5 were also used to validate the orientation of the horn array, described by Torchinsky et al., (2021) [53]. Chapter 5 uses an aperture field model generated in MODAL, developed by Burke (2021) [90] and extended to a range of frequencies, and integrates it into GRASP to model a realistic horn source.

Zemax GO is used for a part of the analysis in Chapter 7, for the stray light analysis in O'Sullivan et al., (2018) [22], and was also used for an analysis of incident angles on the QUBIC dichroic, which is still under development and not reported here.

Chapter 4

Technical Demonstrator Calibration Optical Model

4.1 Introduction

QUBIC's primary goal is to detect the faint B-mode polarisation anisotropies of the CMB. QUBIC, like other contemporary CMB experiments, was designed with systematic error minimisation as a primary concern because of the faintness of the B-mode signal. This is the reason for QUBIC's interferometer-imager design that uses arrays of TES detectors on the focal planes and it is the calibration of these detectors that is the subject of this chapter.

When QUBIC is cooled to its operational temperature ($T = 320$ mK) the TESs are in a superconducting state. Small differences, for example as a result of manufacturing variations, means that each bolometer will have differences in sensitivity and calibration is required to tune and bias each bolometer correctly. The configuration of the horn array in the TD made it possible to fit in internal carbon fibre calibration sources at the edges of the horn array. Ideally, these sources would produce a flat field on the focal plane, illuminating all detectors with equal power so they can be inter-calibrated. Inter-calibration will be carried out regularly during normal operations.

The calibration is carried out in several stages. During the integration phase the instrument is operated in a 'blind' cryostat configuration where a metal plate is used to close the cryostat window and block external radiation from entering the

optics. Measurements are then used to provide an initial inter-calibration of TES sensitivity, linearity, and time-constant as well as providing a check of the cold alignment of the optical components. In order to do this, measurements must be compared with the predicted power on the focal plane and so it is necessary to make an optical model of the sources and QUBICs optical combiner using PO. Models of the QUBIC calibration set-up are made in GRASP (Physical Optics modelling software by TICRA (2015) [86]) and MODAL (in-house software to MU maintained by Gradziel et al., (2007) [89] that was described in Chapter 3).

This chapter will show the model set-up of the internal calibration sources and QUBIC optics in GRASP and validate the model with a similar software (MODAL). As part of this work, realistic elements (e.g. measured mirror surfaces, rims, and a cold-stop) are added to the GRASP model and their effect on the predictions assessed. Since the source is a thermal source and has spectral dependence, this will also be modelled in GRASP.

4.2 Carbon Fibre Sources

The carbon fibre sources available to the QUBIC project (Fig. 4.1) were first used to calibrate Planck's High Frequency Instrument (HFI) (Pajot et al., (2010) [79]). They were successfully characterised and modelled for use with Planck's bolometers and were designed for bolometers operating at 100 - 1000 GHz, incorporating QUBIC's frequency range from 130 - 250 GHz. The sources are thermally stable at the low temperatures inside the cryostat. HFI's bolometers were operating at 100 mK while QUBIC's will be at 320 mK (Pajot et al., (2010) [79]).

The fibres are heated by the Joule effect and radiate thermally. One of the thermal carbon fibres are shown in Fig. 4.1a. The fibre signals are modulated with a square waveform and cool-down on a sufficiently short time-scale ($\tau < 10$ ms) between pulses so that they can be used to measure the time constant of the bolometers (QUBIC requires the bolometers to have a time constant in the 10 - 100 ms range). The radiated power is on a par with QUBIC's requirements in the pW range.

The fibres are installed in the cavities of horns as shown in Fig. 4.1b. The horns are Winston-cone-like concentrators designed to produce a 48° light cone at Planck HFI frequencies (Pajot et al., (2010) [79]). The purpose of the wide beam is to illuminate the whole focal plane with power for the inter-calibration

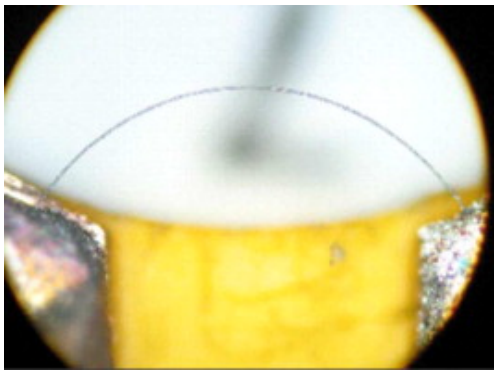

(a) Carbon fibre in a horn cavity, 6 µm diameter, 1 mm in length.

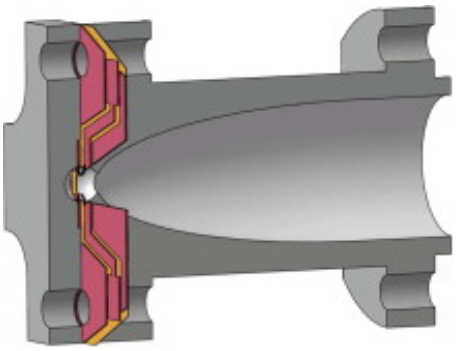

(b) Two fibres in the horn cavity shown in a horn profile cut.

Figure 4.1: Photograph of a carbon fibre and CAD drawing of the fibre in horn cavity. These figures are from Henrot-Versillé, Cizeron, and Couchet (2009) [80].

of the detectors. An over-moded Winston cone produces a top-hat like beam. Since QUBIC observes at the low-frequency end of the Planck band and we are less interested in the parts of the beam that never make it to the QUBIC focal plane, it was decided to approximate the beam by a Gaussian of FWHM of 48° in order to study the likely effects of truncation and diffraction of such a beam by the combiner optics. A photograph of the two sources installed on the corners of the TD horn array is shown in Fig. 4.2. Further details on the development and characterisation of the sources are given by Henrot-Versillé, Cizeron, and Couchet (2009) [80].

4.2.1 Source Installation

The sources are mounted on the edges of the TD horn array as shown by Fig. 4.2. They are installed on the underside of the TD array so that they are facing the primary mirror and can illuminate the detectors while the instrument is in a 'closed' configuration. This way excess radiation from outside the instrument does not interfere with the measurements made with the calibrators. The coordinate locations of the sources in the horn array reference frame are shown in Fig. 4.2.

4.3 Initial GRASP Physical Optics Model

The aim of this analysis is to characterise and provide an optical model of QUBIC's TD for an accurate calibration of the TESs. QUBIC's engineering documents are

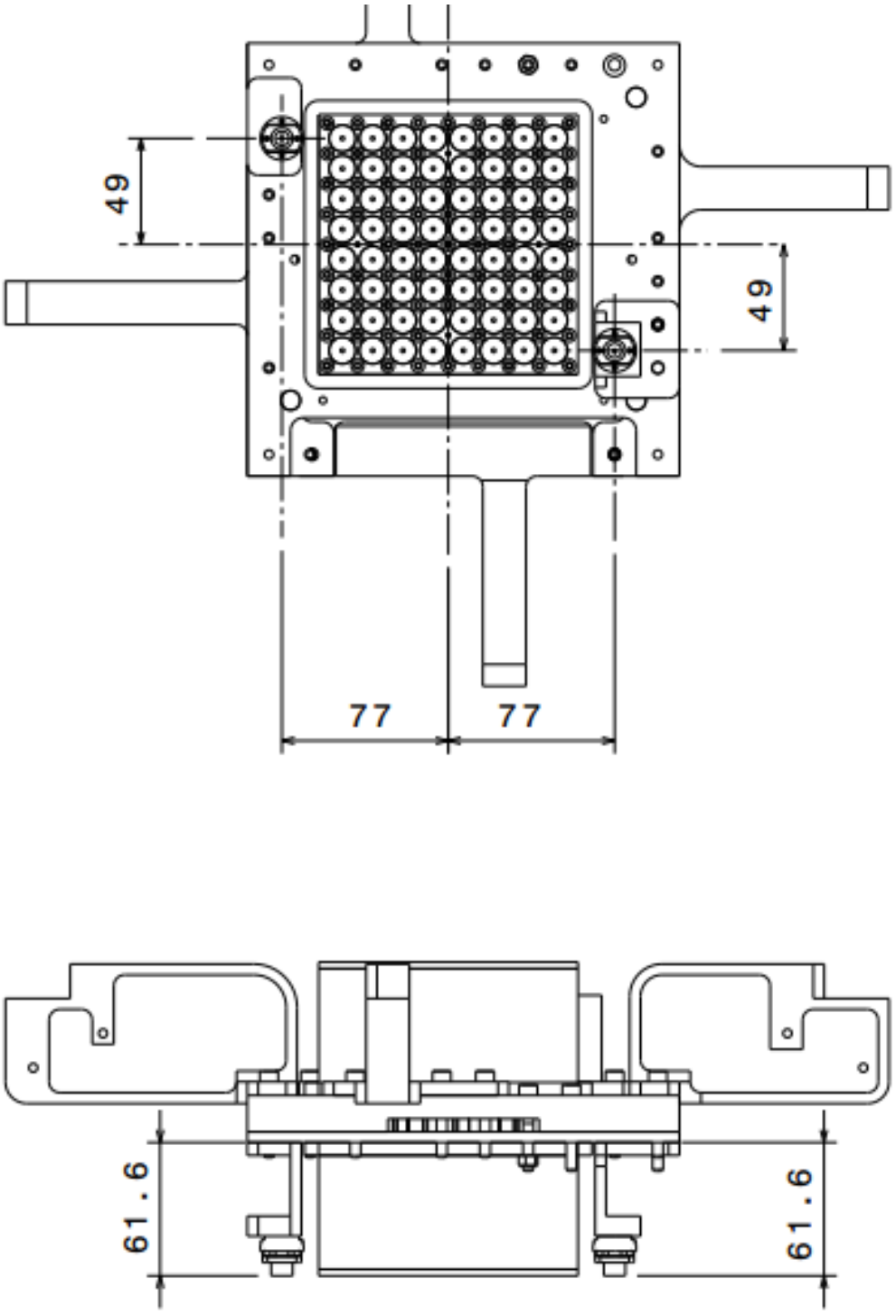

Figure 4.2: Diagram of the TD horn array. The internal calibration source locations are shown here. The measurements are shown in mm.

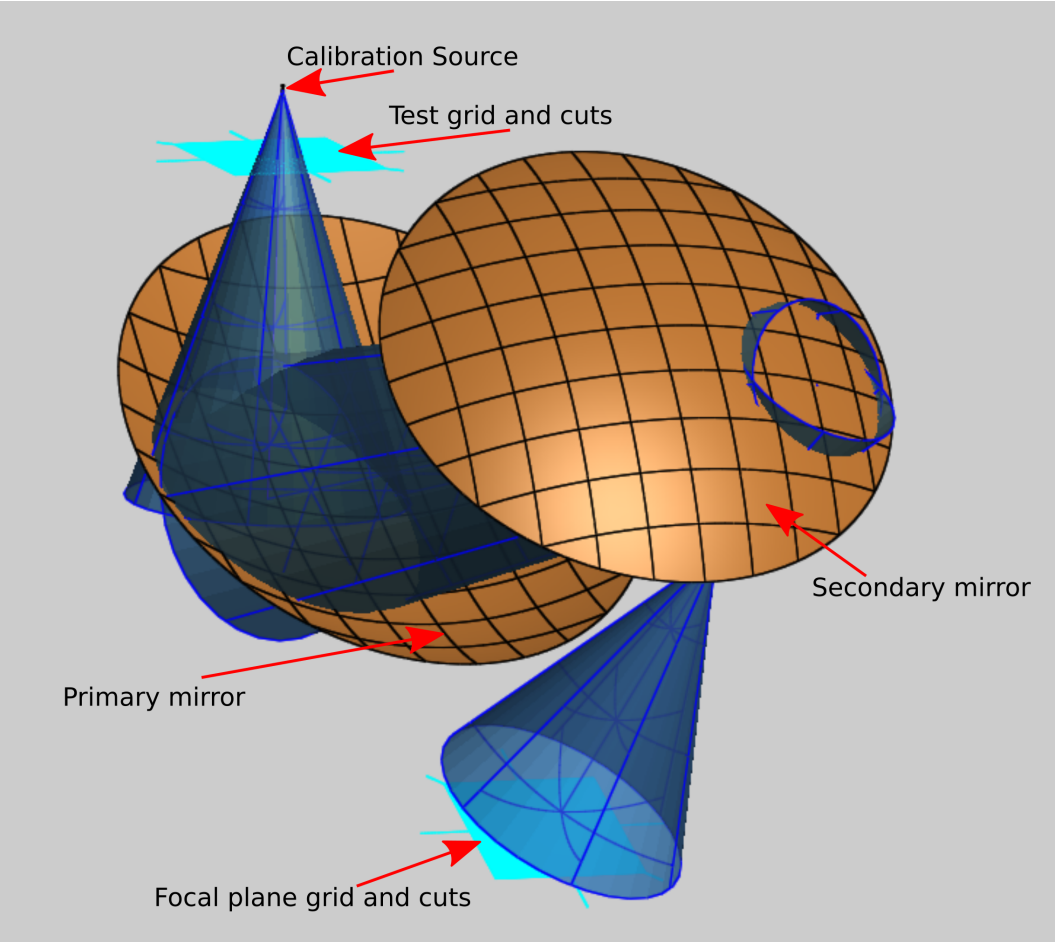

Figure 4.3: Basic GRASP model setup and source. The blue beam represents an internal calibrator beam. The bronze/orange surfaces are the primary and secondary mirrors. The light blue grid at the end of the beam path is a detector grid with QUBIC's focal pane geometry. A grid and cuts are also placed below the calibrator beam for validation.

used to create a model in GRASP. The GRASP software is described in Chapter 3 of this thesis. In the initial model, simplified rims and perfect mirror surfaces are used, the cold-stop, HWP, polariser, and filters are excluded, and the carbon fibre sources are modelled with a Gaussian beam. This is done so it can be directly compared with a MODAL model that was developed by Burke (2021) [90]. Only optical elements after the back-to-back horns need to be modelled since the carbon fibre beams face the primary mirror from the horn array location. As such, the back-to-back horns, polariser, HWP, and filters are not considered in the model. A 3D view of this set-up is shown in Fig. 4.3 with a simple Gaussian source, the real calibration source will be wider (48°). Once the model is validated in this configuration, it will be updated with measured component surfaces to more accurately model the realistic QUBIC instrument. This couldn't be done with the

MODAL software.

4.3.1 Model Set-up

The model geometry parameters (reference frames, horn, mirror, and focal plane locations) were given in an internal QUBIC document (Brossard et al., (2017) [91]). The mirror surfaces are defined by Scully (2016) [77] using the coefficients of a second order polynomial surface equation and shown in Appendix C. In the validation model, the ideal mirrors are described by the surface equation but are later replaced with the measured data of the manufactured surface. The sources are set at their real locations and detector grids are set according to QUBIC's focal plane definition. This set-up in GRASP is shown in Fig. 4.3. The blue beam is emitted from the source location, reflects off the mirrors and illuminates the focal plane. The same set-up is used in MODAL. Both models should produce identical results as the same PO modelling approximations are used by both.

4.3.2 Calibration Source Set-up

The calibration source beams were each defined to be a 48° FWHM Gaussian beam. The equivalent waist radius of such a 150 GHz beam was calculated as ω_0 = 0.8578 mm using Eqs. 4.1a, 4.1b, and 4.1c given in Goldsmith (1998) [92].

$$\theta_0 = \frac{\lambda}{\pi\omega_0} \tag{4.1a}$$

$$\theta_{fwhm} = 1.18\theta_0 \tag{4.1b}$$

$$\omega_0 = \frac{1.18\lambda}{\pi\theta_{fwhm}}. \tag{4.1c}$$

The grid below the calibration source (CF1), as shown in Fig. 4.4, is used to compare these beams in both GRASP and MODAL. CF2 data will later be shown for the focal plane only since, at this point, CF1 and CF2 produce identical data on test grids just below the sources. The cut is taken 50 mm directly below CF1. The results are shown in Fig. 4.5[1]. The GRASP cut is shown in purple and the MODAL cut is shown in green. In both cases, the Gaussians are set with a

[1]This plot, as well as the majority shown throughout this thesis, are plotted with a central frequency of 150 GHz unless stated otherwise.

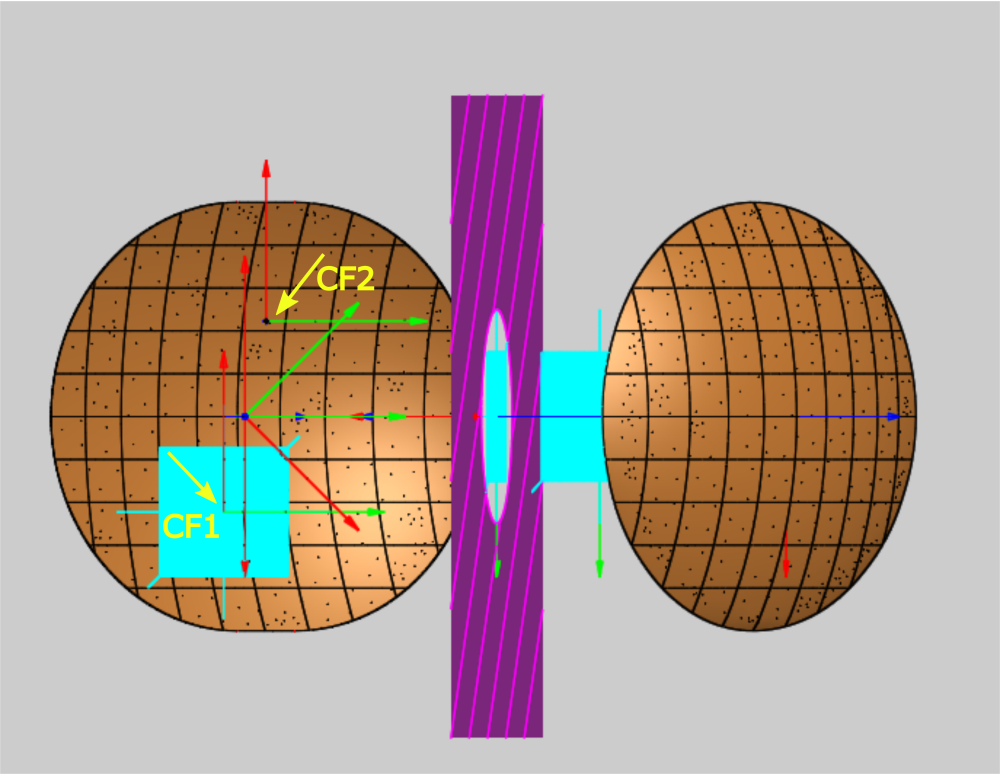

Figure 4.4: A top-down view of the QUBIC model in GRASP shows the locations of the calibrators (CF1 and CF2). The cold-stop, in pink, is included in this figure. The mirrors in this figure are defined with tabulated surfaces representing accurate cooled and measured surfaces. The black dots on the surfaces show the points where the surfaces were measured.

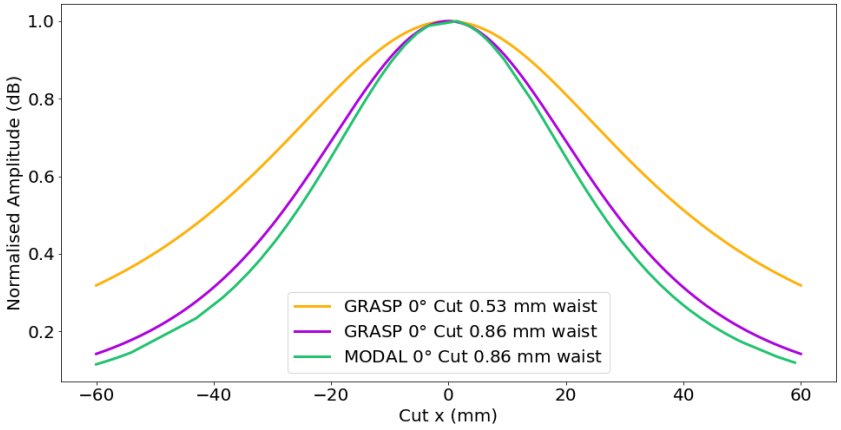

Figure 4.5: Cuts taken 50 mm the calibration source. The purple line is for GRASP with a Gaussian beam waist radius of $\omega_0 = 0.8578$ mm. The green line shows data the same set-up in MODAL. When a beam waist radius of $\omega_0 = 0.53$ mm is defined in GRASP, the orange line is produced.

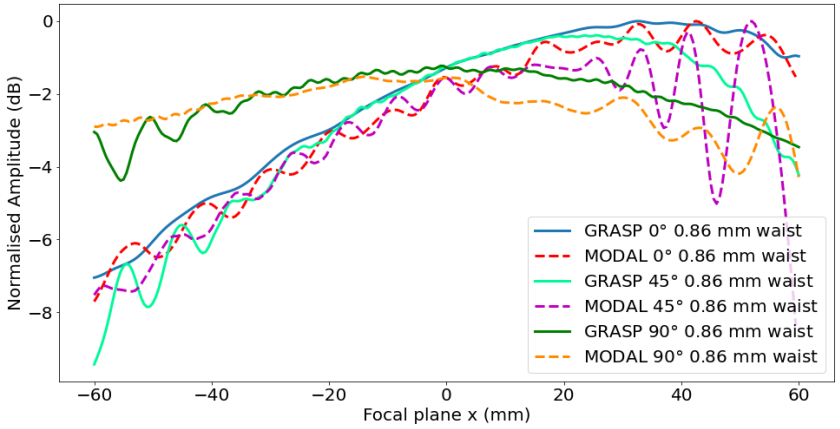

Figure 4.6: Cuts taken at the focal plane with both software packages defining Gaussian beams at the CF1 location with a beam waist radius of $\omega_0 = 0.8578$ mm. 0°, 45°, and 90° focal plane cuts are shown.

beam waist radius of $\omega_0 = 0.8578$ mm. There is a small difference in these data with GRASP producing a wider beam. This is an unexpected difference. The two software packages should produce the same data. Slight differences in the software implementations account for this and is investigated and corrected by setting the beam waist radius to $\omega_0 = 0.53$ mm in GRASP.

The data are then compared at the focal plane. The focal plane is at the end of the beam path in Fig. 4.4. These data are shown in Fig. 4.6 for GRASP and MODAL cuts on the focal plane at 0°, 45°, and 90°. By comparing the blue line and red dashes, cyan line and purple dashes, and the green line with yellow dashes, it is clear these data are not in agreement as was expected. The reasons for this unexpected difference in data for identical models are investigated below.

4.3.2.1 GBM Paraxial Limit

Another effect to consider as a result of the large beam radius of the source is the paraxial limit of Gaussian beam approximations. The initial calculation of the beam waist, $\omega_0 = 0.8578$ mm, was calculated with Eqs. 4.1a, 4.1b, and 4.1c. This works for a well collimated beam. However, the carbon fibre source is not a well collimated beam at 48°. A beam is considered well collimated when its full-width, half-maximum (FWHM) is less than 20° ($\omega_0/\lambda > 0.9$) as shown by Goldsmith (1998) [92]. In fact, the carbon fibre source has a beam waist to wavelength ratio $\omega_0/\lambda = 0.4$, far below what is considered well-collimated. Since the same

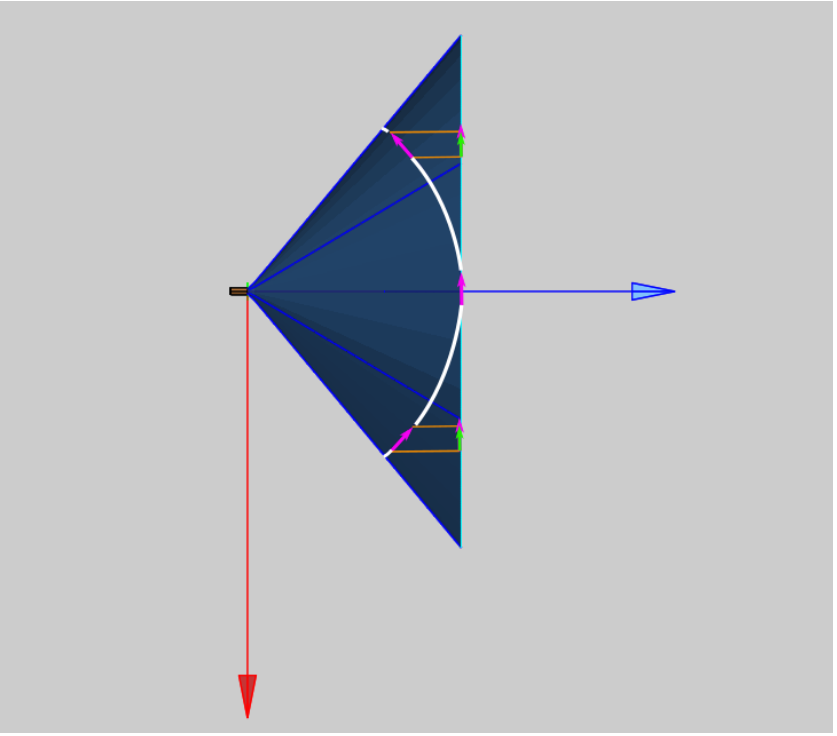

Figure 4.7: This figure shows the near field projection effect in GRASP. The pink vectors are the electric field that is projected onto a planar grid to give the smaller green vectors.

ω_0 value is used for defining Gaussian beams in both MODAL and GRASP, this definition is not in itself problematic when comparing the software packages, but, as discussed next, how each software package defines a Gaussian beam. Given the same parameters, the profile is different in a way that becomes apparent for wide beams.

4.3.2.2 GRASP Near-Field Projection

GRASP defines its Gaussian Beam and calculates electric fields on grids and cuts differently to MODAL. The carbon fibre emits a 48° FWHM Gaussian beam and so the radius of curvature of the spherical wavefront of the beam will have significant curvature within the combiner. GRASP defines this beam amplitude as being Gaussian on a spherical surface rather than on a plane grid like in MODAL.

There is a projection effect that occurs because of the source and analysis set-up. GRASP calculates the field values from projected vectors. When the curvature of the spherical wavefront is sufficiently large (due to the wide beam) and the grid is sufficiently near to the source, the electric field is projected onto the grid.

In Fig. 4.7, the pink vectors show the electric field vectors. When they are projected to the grid or cut, the smaller green projected values are calculated in the output .grd file. The resulting electric field values (projected onto a flat plane) are slightly smaller for the GRASP definition as compared with the MODAL definition of Gaussian distribution on a plane. This explains the difference in otherwise identical set-ups in GRASP and MODAL seen in Fig. 4.6.

4.3.2.3 Correction Factor

Due to this technical difference in how each software calculates fields on grids and cuts, the GRASP model is modified to correct for the projection effect. By modifying the beam waist radius in GRASP, the beam can be tuned to match the pattern on the focal plane produced by MODAL. This new beam waist is found to be $\omega_0 = 0.53$ mm. This is very different to the $\omega_0 = 0.86$ mm Gaussian definitions as shown by the orange line in Fig. 4.5. However, when the data are compared on the focal plane (after propagation), excellent agreement is found between GRASP and MODAL models for the simulation. These data are shown in Fig. 4.8a. Using the same correction factor, agreement between GRASP and MODAL is found for CF2 as well. These data are shown in Fig. 4.8b. For both of the calibration sources, there is excellent agreement between GRASP and MODAL for all cuts. The normalised powers match for all cuts as well as the diffraction fringes along the cuts. It is important to state here that the 'correction factor' is used to reconcile the native definition of a Gaussian beam in the two different software packages and does not imply that either one is more correct than the other, in fact they are both likely to be an approximation of a real beam. The difference only became apparent for the wide beam of the CF sources. Both software packages also allow a source to be defined using a table of field values on a plane and, in this case, the definitions would be the same.

This work shows that care must be taken about how the source is defined but the agreement between the two software packages gives confidence that the new GRASP model has been set-up correctly and the MODAL work of D. Burke can be progressed using the additional features available in GRASP.

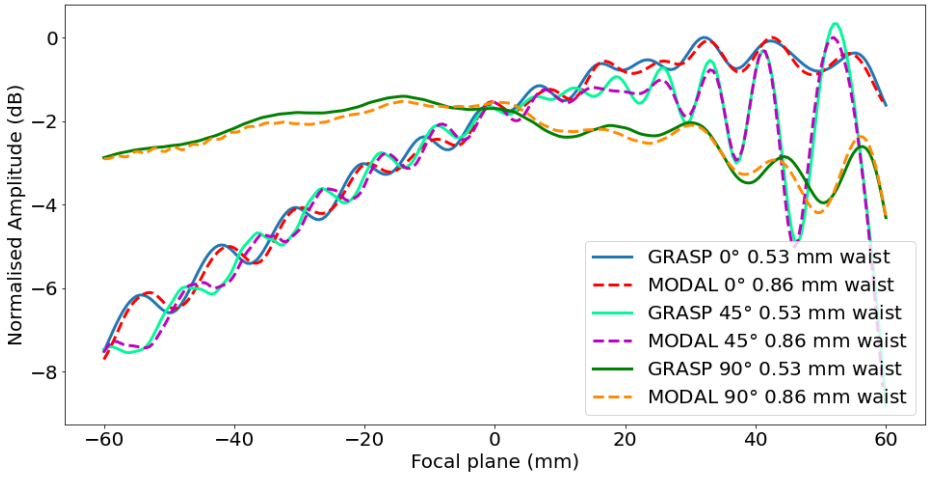

(a) Cuts taken at the focal plane with MODAL defining Gaussian beams at the CF1 location with a beam waist radius of $\omega_0 = 0.8578$ mm. In GRASP the corrected waist of $\omega_0 = 0.53$ mm is applied. The cuts are taken at 0°, 45°, and 90° on the focal plane.

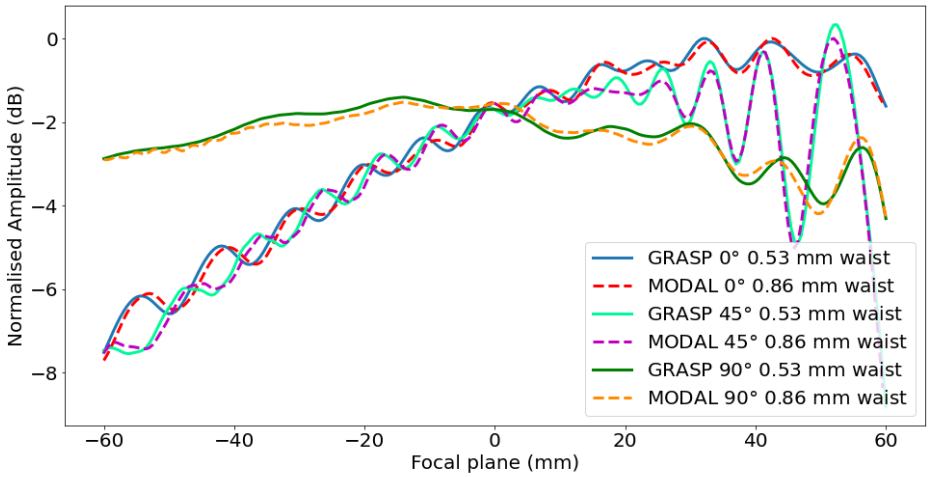

(b) Cuts taken at the focal plane with MODAL defining Gaussian beams at the CF2 location with a beam waist radius of $\omega_0 = 0.8578$ mm. In GRASP the corrected waist of $\omega_0 = 0.53$ mm is applied. The cuts are taken at 0°, 45°, and 90° on the focal plane.

Figure 4.8: Cuts at the focal plane for CF1 and CF2 with the correction applied in GRASP.

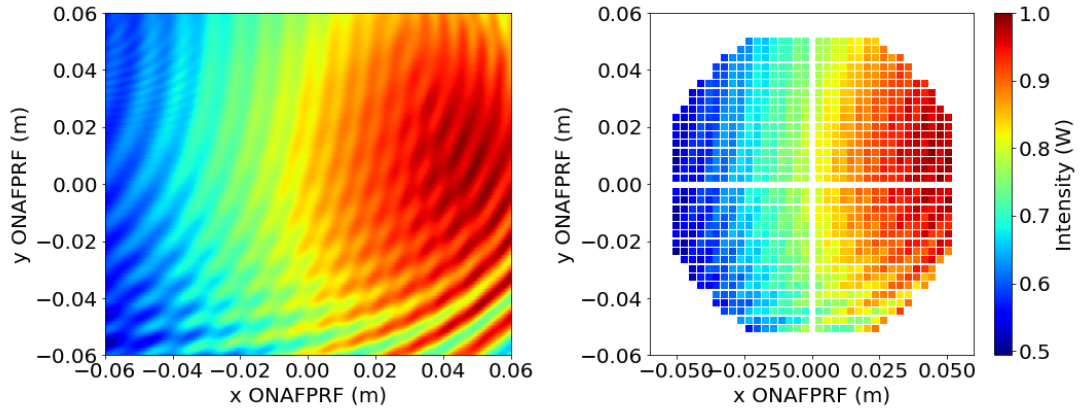

(a) (left) Focal plane power (normalised to 1 W) and (right) power on each TES in the array from the GRASP model for CF1.

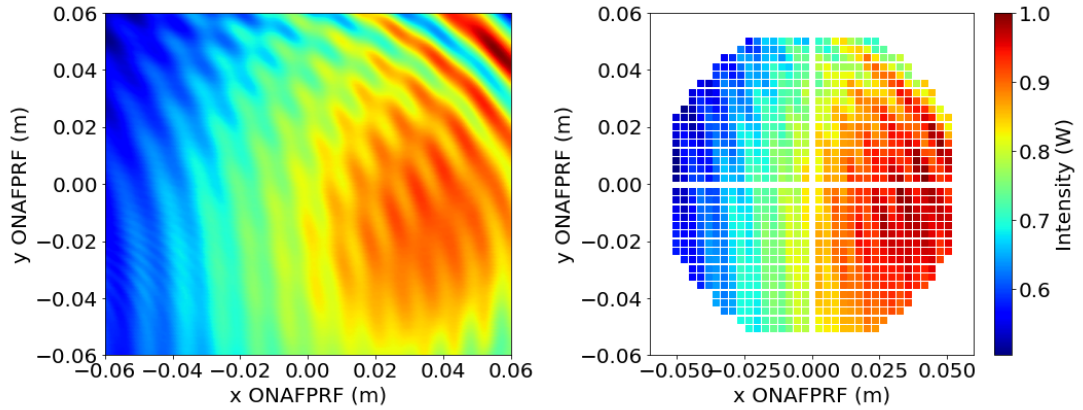

(b) (left) Focal plane power (normalised to 1 W) and (right) power on each TES in the array from the GRASP model for CF2.

Figure 4.9: Power for each TES bolometer and the data used to calculate the power.

4.3.3 Focal Plane Pattern

Using the validated model of the simplified optical combiner and the carbon fibres as sources, a plot was made of the power distribution on the focal plane. These will be used for the calibration of the TD. The left hand side of Figs. 4.9a and 4.9b show the full grids from which the cuts were taken in Figs. 4.8a and 4.8b. The cuts are more useful for analysis but the grid plots make visualisation of the carbon fibre beams more intuitive and gives insights into understanding the shape and behaviour of the cuts.

The right hand side plots of Figs. 4.9a and 4.9b show how the power would be averaged over the TES bolometers. Further information on QUBIC's detector

layout is provided by Brossard, Piat, Grandsire, and Hamilton (2015) [93]. The plot of power on the bolometers are normalised to the maximum value.

A range in power can be observed in the plots of Fig. 4.9 with low power in blue on the left and the power increases towards the right side of the focal plane. Diffraction fringes and aberration are also observable. This is likely caused by the mirror shapes and the mirror edges. The unusual patterns are due to the fact that the beam from the calibrators is so wide that the mirrors, which were designed for the much narrower horn array beams, cause a high level of truncation. Although the original idea was to have a uniform beam on the focal plane, the sources available made this impossible and, in fact, having some features in the focal plane pattern may allow additional checks on the optical alignment and detector linearity.

4.4 Adding a Cold-Stop

The cold-stop (CS) is a 200 mm aperture (QUBIC Collaboration (2017) [94]) in a screen placed between the primary and secondary mirrors. Its primary function is to minimise unwanted thermal radiation and stray light from reaching the focal plane. It is mounted inside the cryostat at 4 K, which is why it is named the 'cold' stop.

The cold-stop is added to the GRASP model as an electrical object "aperture in screen" and the commands are modified accordingly to include its effect. The rim is defined with a diameter of 200 mm to match the physical cold-stop geometry. A 3D image of this set-up is shown in Fig. 4.10.

The effect of adding the cold-stop to the basic validated model is shown with 45° cuts of the focal plane pattern in Fig. 4.11. The cut with a cold-stop has a smoother focal plane pattern compared to the cut without the cold-stop. A smoother power distribution on the focal plane might be a preferable outcome for the TES calibration. Other than the improved smoothness with the cold-stop, the beam profiles are in agreement.

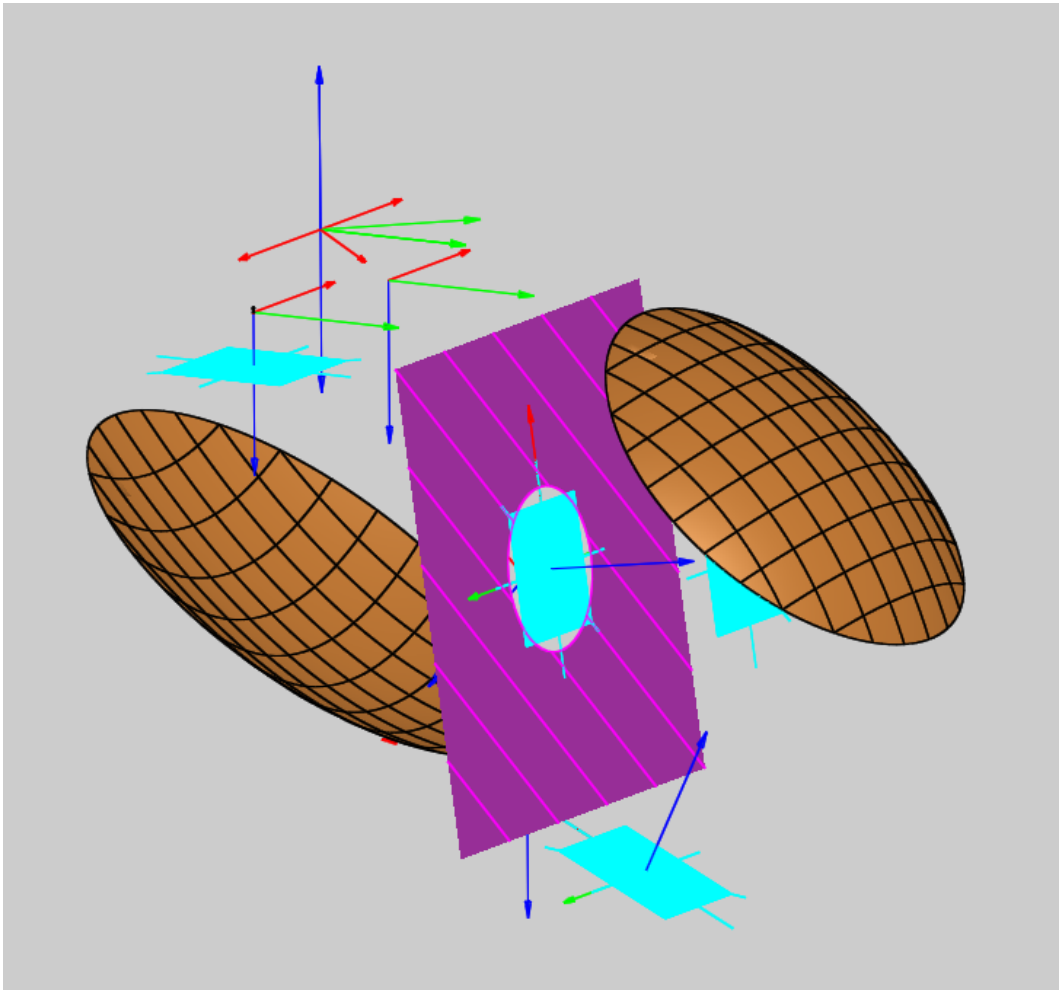

Figure 4.10: 3D image from GRASP showing an 'aperture in screen' used to model QUBIC's cold-stop (pink). Additional cuts and grids are shown at the aperture, prior to the secondary mirror. These additional cuts and grids are useful for studying the beam shape at different points as it propagates through the optical combiner.

4.4.1 The Size of the Cold-Stop

Considering the size of the carbon fibre beam relative to the size of the aperture, it is unexpected to see that the effect of adding the cold-stop to the model is negligible. Because of this, the importance of cold-stop size on the model is investigated. The size of the beam in the combiner is shown in Fig. 4.12a. With this visualisation, one might expect diffraction to occur due to the beam width relative to the aperture size. After reflecting off the primary mirror, the beam is large compared to the size of the cold-stop aperture. However, by visualising the source as rays (Fig. 4.12b), it is seen that the majority of reflected rays from the primary mirror have largely collimated paths through the cold-stop. A small

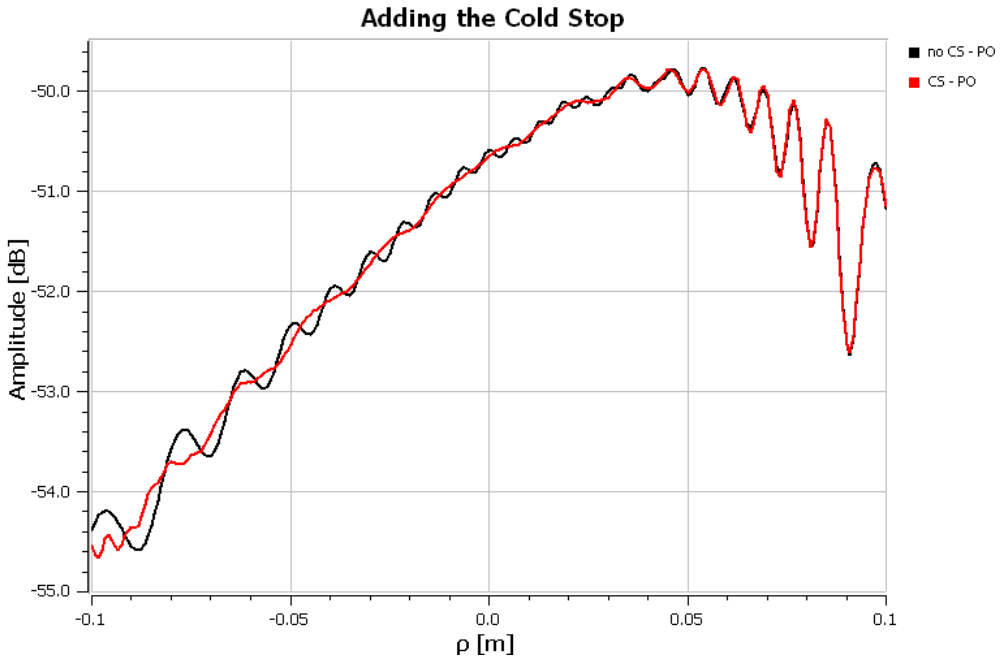

Figure 4.11: PO cuts of the focal plane pattern at 45° with (black) and without (red) the cold-stop. The data were similar for all cut angles and 45° is shown as a representative sample.

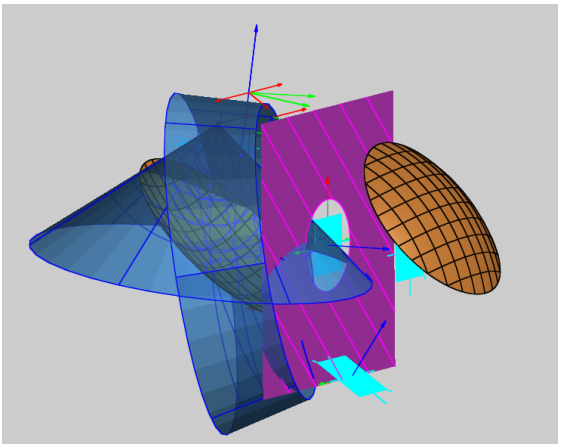

(a) 48° beam visualised at the cold-stop. The GRASP 3D viewer fails to propagate the Gaussian beam through the cold-stop.

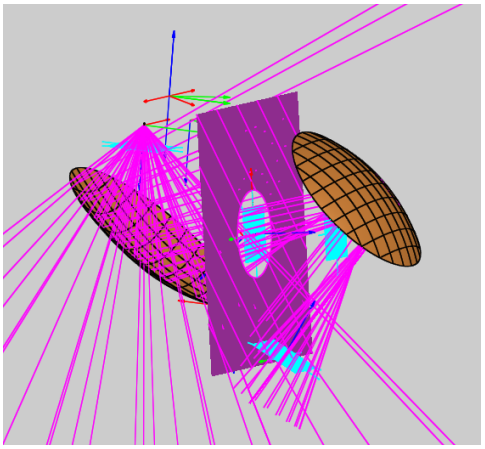

(b) 48° beam as rays propagated to the focal plane. Only the low power edge rays are affected.

Figure 4.12: 3D visualisation in GRASP of 48° beam in QUBICs optical combiner as a Gaussian beam and as rays. The cold-stop can be seen to block the edges of the beam and rays.

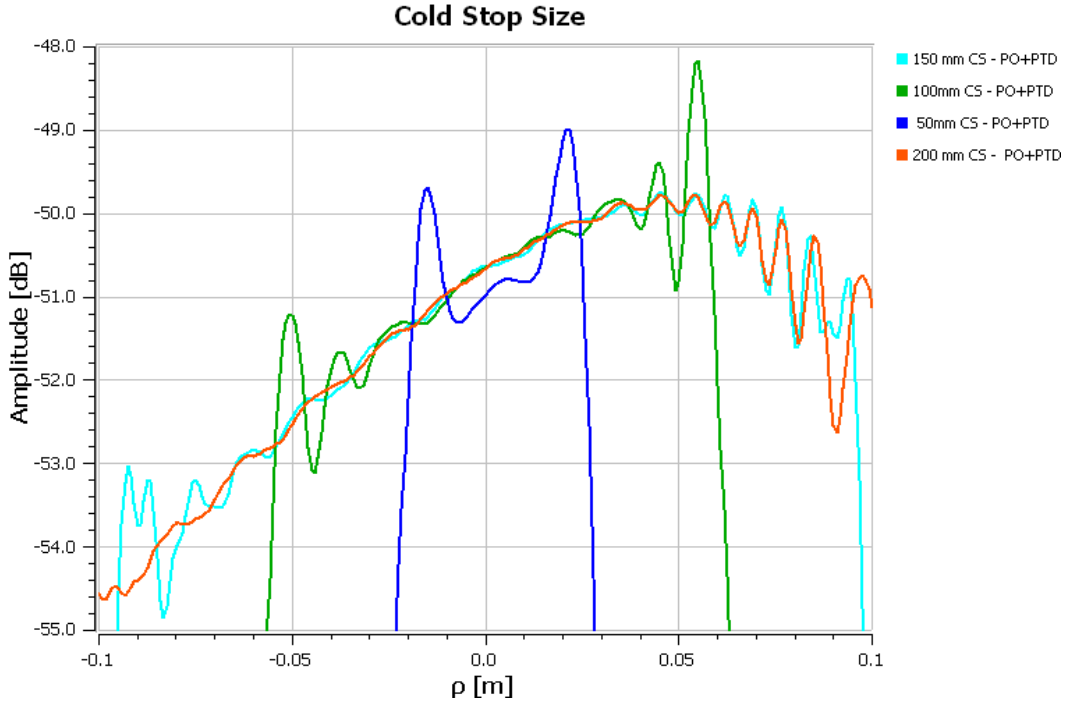

Figure 4.13: Cuts comparing the focal plane pattern with a cold-stop aperture of different sizes.

fraction of the edge rays are blocked by the cold-stop. This helps to explain why the cold-stop has such a small affect on the focal plane field for the carbon fibre source.

To find out the focal plane patterns sensitivity to cold-stop aperture size, different cold-stop diameters were tested. The results are shown in Fig. 4.13. The sizes tested are diameters of 50 mm, 100 mm, 150 mm, and the actual 200 mm aperture. It should also be noted here that the actual focal plane size is 120 mm so the range of interest is from -60 mm to 60 mm.

These results show that the 200 mm cold-stop has a useful smoothing effect on the focal plane for the CF1 source and causes no significant additional distortion. Distortions become apparent for a 150 mm cold-stop but this is likely still an acceptable size considering the focal plane size. These distortions occur outside the focal plane area. The 100 mm and 50 mm diameter cold-stops cause serious distortions to the focal plane cuts and would have considerable effects if the cold-stop was so small for the TES calibration.

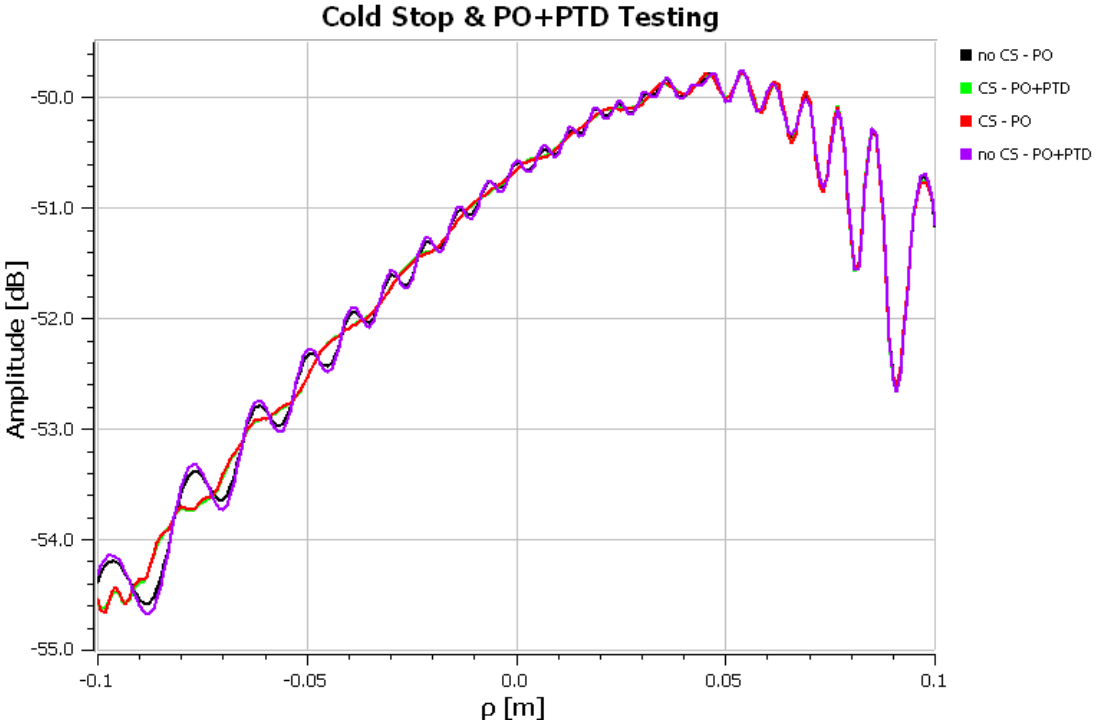

Figure 4.14: Plots comparing PO+PTD against just PO for two cases, with and without the cold-stop for CF1. The actual focal plane area ranges from -0.06 to 0.06 m. MODAL data for this set-up were not available for comparison.

4.4.2 Cold-Stop: PO vs PTD

With the cold-stop added to the model, it is an excellent opportunity to analyse the effect of adding PTD to the calculations. It is useful to test PTD at this point since all the significant rims are now present in the model. PTD provides more accurate calculations due to edge and rim effects compared to PO alone. These rims are from the mirror edges and the cold-stop aperture.

Another reason to test PTD at this point is because the carbon fibre beam at 48° is wider than the beams from the array of 64 horns of the TD. So if PTD calculations do have significant effects on the focal plane pattern then using the carbon fibre set-up is the most useful 'worst-case-scenario' for PTD calculations.

By comparing the black and purple lines in Fig. 4.14, minor differences can be seen by adding PTD to the PO calculations when the cold-stop is not present in the model. These minor differences are not present in the high power part of the focal plane and in fact, the differences are only evident outside the focal plane area.

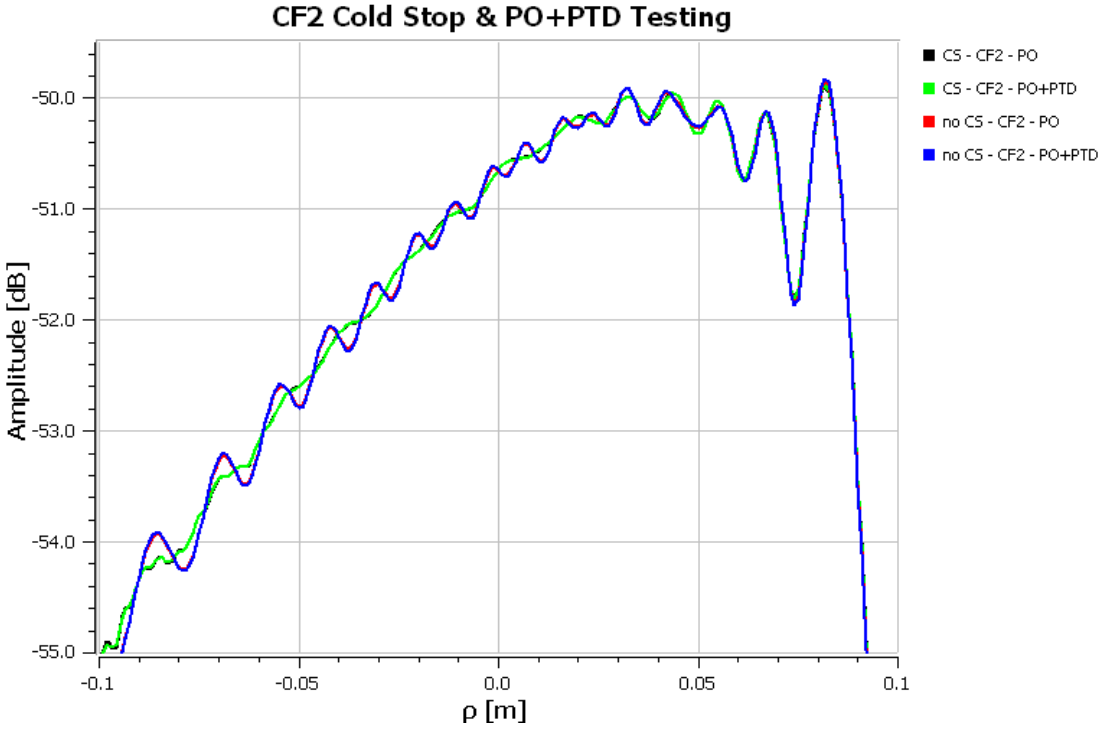

Figure 4.15: Plots comparing PO+PTD against just PO for two cases; with and without the cold-stop for CF2. The actual focal plane area ranges from -0.06 to 0.06 m. MODAL data for this set-up were not available for comparison.

The same is true when the cold-stop is added to the model. This plot shows again the smoothing effect that adding the cold-stop has to the model. It can be concluded that for both cases (with and without the cold-stop), that adding PTD to the PO calculations has a small measurable but insignificant effect. Naturally PTD effects will be considered and checked when realistic mirrors and rims are added to the model. PTD effects are not expected to be significant and they are not computationally expensive to include in simulations.

The same conclusions can be drawn for the CF2 calibration source. These results are summarised in Fig. 4.15. As with CF1, the results for CF2 show that adding the cold-stop has the beneficial effect of smoothing the beam profile on the focal plane. In addition, only a negligible change to the results occurs when PTD is added to the calculations.

4.5 Modelling Realistic Optical Elements

4.5.1 Realistic Rims and Surfaces

With the CF source model in GRASP validated against the MODAL model, it is now possible to add more realistic elements[2] to the model and analyse their effects on the focal plane pattern. The measured mirror surfaces and measured mirror rims will be added. There will also be discussion on the effects of using PTD and PO in the calculations. For the simplified model that was used for the validation against MODAL, perfect mirror surfaces were used as they were designed in software for QUBIC's TD. Naturally, the manufacturing process introduces errors on the surface of the machined mirror. This is due to the inherent tolerances of the machines and tooling used to mill QUBIC's mirrors from aluminium blocks. The mirror designs were for the operating temperature of 4 K, and thermal models were used to convert these designs to 300 K, the room temperature at which they were manufactured.

Once the mirrors were manufactured, the mirrors were measured with a coordinate measuring machine to characterise the surface roughness introduced by the manufacturing process. The uncertainty on these measurements is 5 µm, which is sufficient for all analysis with these data. When the measured data are compared to the ideal surface points, the uncertainty on the measured data is, therefore, negligible. As such, a 3D model of the measured TD mirror surface was produced to be used for the optical analysis and calibration. This model is output in a text file which lists the 3D measured x, y, and z coordinate points over the mirror surfaces. This can be loaded into GRASP as a tabulated surface in place of the ideal equation describing the surface.

The QUBIC combiner will be cooled to 4 K and be under low vacuum pressure so the surface measurements were transformed to this temperature with CATIA[3] by QUBIC collaborators. These are the most realistic mirror surfaces that can be used to predict the power from the horn array and calibration sources on the QUBIC TD focal plane.

[2] A realistic surface is a measured surface profile from mirror surface measurements. A realistic rim considered the best real world model of a mirror rim, measured or modelled.

[3] www.3ds.com

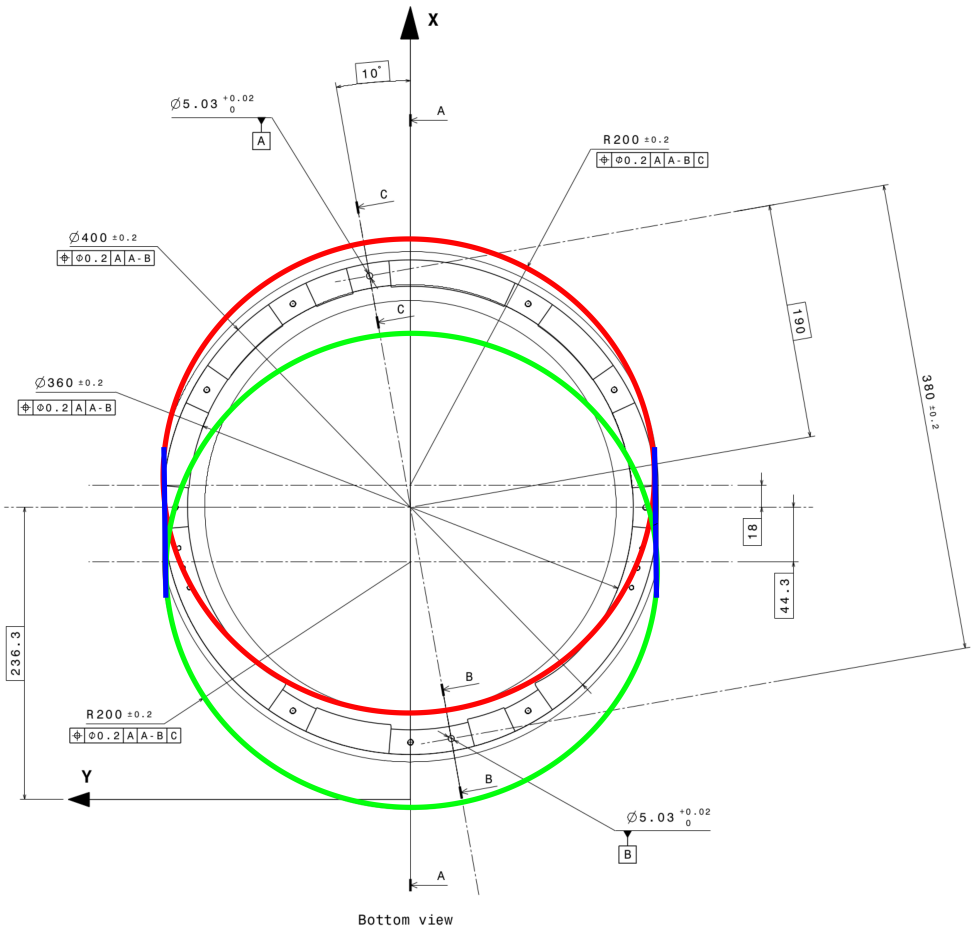

Figure 4.16: This drawing describes the realistic geometry of the TD rim. The rim is composed of the outer elements of two intersecting circles (red and green). Two common tangents of the circles are connected by straight lines (blue).

As with the mirror surfaces, a simplified circular rim was used for the primary mirror in the validation process. In reality, QUBIC's primary mirror has a more complicated shape. The primary mirror rim is comprised of two circles offset from each other with the outer points joined by two straight lines. This is shown in Fig. 4.16. The circles and the lines that make up the mirror rim are shown in red, green, and blue. Two of these rims (simple and realistic) were tested for the primary mirror. A circular rim is used for the secondary mirror. When the effect of the realistic rim versus a simple circular rim was tested on the focal plane, no difference was found. The realistic rims are included in the model from this point on as in Figs. 4.17 and 4.18.

Figs. 4.17 and 4.18 compare the different optical elements tested in the GRASP model, including the rims. The 'elliptical rim', as described in the figure label, is a rim type definition used by GRASP. In this simple case, the elliptical rim

is used to define a circular rim (0.2 m × 0.2 m) that approximates the realistic primary mirror rim. The 'tabrim' stands for tabulated rim. The tabulation refers to the rim that was measured and tabulated in a 3D CAD file of the real rim as manufactured. The 'tilted tabrim' is the same as 'tabrim' but defined in a different coordinate system necessary for the tabulated surface. The results for these should match exactly and this is seen in Figs. 4.17 and 4.18 (blue and pink) for CF1 and CF2 respectively. This indicates that the coordinate system definitions are working properly for 'tabrim' and 'tilted tabrim'. The tabulated surface refers to the measured surface that has been deformed to 4 K to replicate QUBIC's operational parameters. It requires a new reference frame which is 'tilted'. The reason is that a small angular tilt had to be accounted for when measuring the surface and the mirror was measured in a difference reference frame than the one described in QUBIC's reference frame documentation.

'CS' refers to the cold-stop, described previously, being included in the model data. With these terms explained, results of Figs. 4.17 and 4.18 can be described properly.

4.5.2 Realistic Model: CF1 Results

The results for the first carbon fibre source start with the model used for the cold-stop analysis (Section 4.4.2) as a baseline reference (black line - Fig. 4.17). Then, elements are changed incrementally until the desired model is achieved.

The realistic rim for the primary mirror (shown by the red line in Fig. 4.17) is added first. This updated rim has a beneficial smoothing effect on the focal plane data. This is observed by comparing the red line with that for the basic set-up described by the black line. Note that the red data are obscured by the pink line.

Since the beam is wide and rims can cause large diffraction, PTD is also tested. This is seen in the same figure by a blue line (also obscured by the pink line) and shows little to no effect on the focal plane cut. Since computation time is negligible for the model and PTD could have significant effects in another model configuration, PTD is included for subsequent models. As mentioned previously 'tabrim' is plotted in two reference frames (blue and pink lines in Fig. 4.17). These are the same rim but in different reference frames. The matching results are seen with the pink line completely obscuring the blue line.

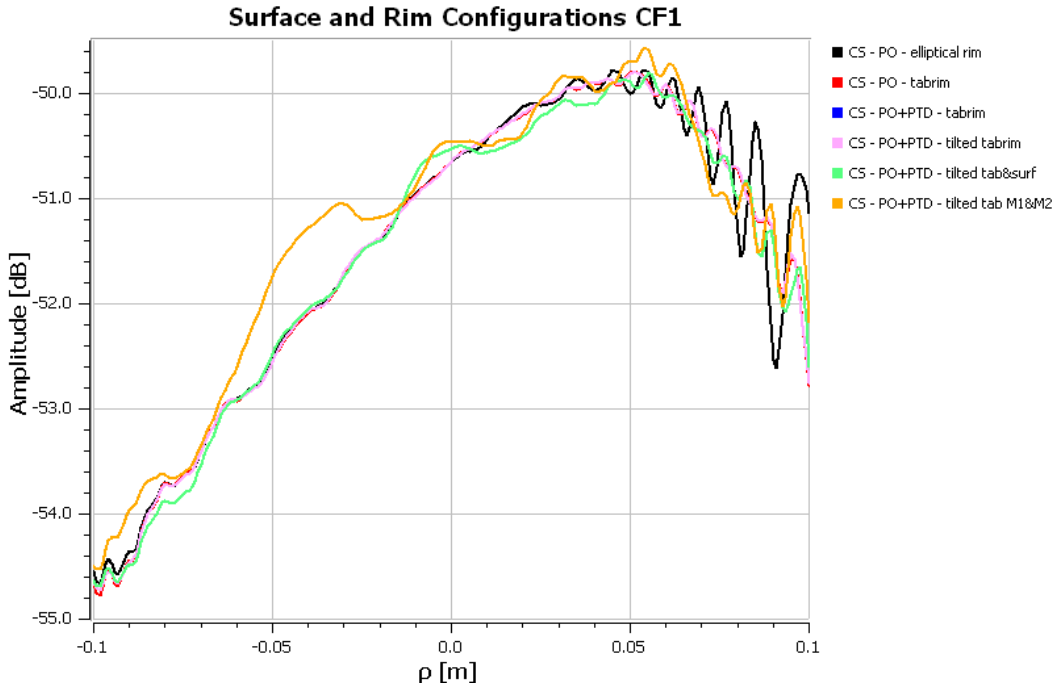

Figure 4.17: Cuts with various model configurations for CF1 with the cold-stop included. The black line shows the basic elliptical rim model of the primary mirror. The tabulated rim is in red. The blue line includes PTD and is obscured by the pink line. The pink line shows the 'tilted tabrim', which is equivalent to 'tabrim' in another reference frame. The green line shows the measured points used for the primary mirror surface. The orange line shows data for measured surface data for both mirrors.

The green cut in Fig. 4.17 represents the model with a realistic primary mirror. This means the measured and cooled primary mirror model is used (in the modified reference frame) with the realistic rim as well as the cold-stop aperture. The secondary mirror is still defined by the ideal equation. This configuration starts to show noticeable aberrations on the focal plane. At -0.015 m on the cut there is increased power in comparison to previous models. Around 0.02 m on the same cut, there is decreased power. This variations show the realistic mirror surface introduces power variations of $\sim$ 0.2 dB.

Using the realistic measured and cooled secondary mirror model, an even more notable distortion is introduced to the focal plane. At -0.05 m the cut deviates by $\sim$ 0.9 dB. This can be considered an edge region since the focal plane extends to -0.06 m and is a 'low power' region from the source on the focal plane. However in a 'high-power' region (0.025 - 0.06 m), this model has increased power relative to previous iterations of the analysis ($\sim$ 0.02 dB). These variations introduced by using the realistic versions of the mirrors are measurable but are not

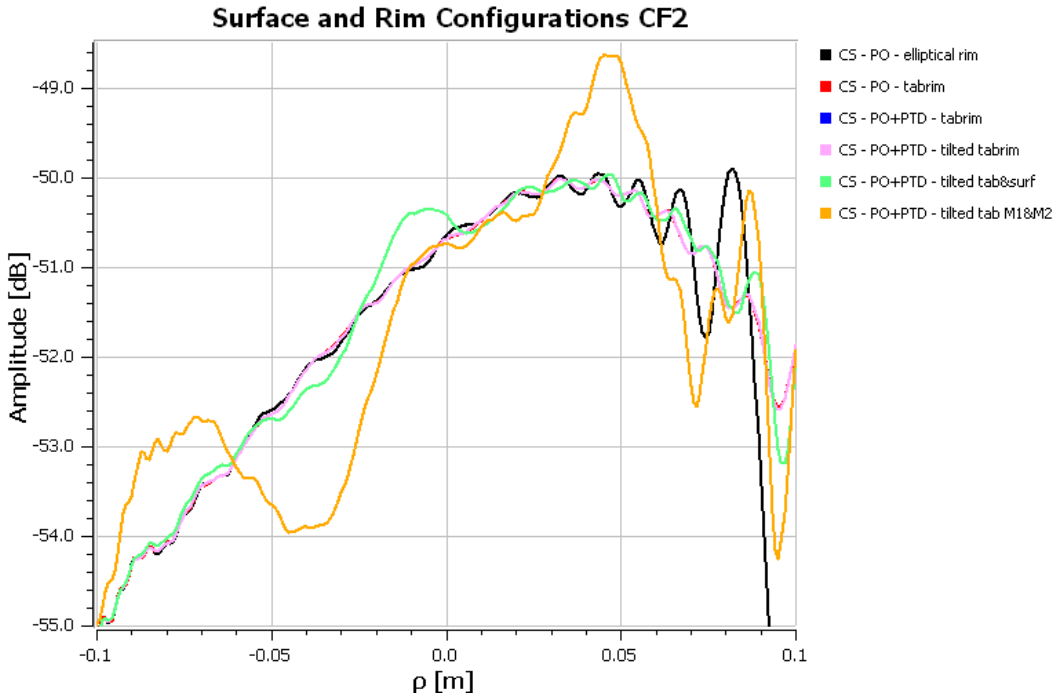

Figure 4.18: Cuts with various model configurations for CF2 with the cold-stop included. The black line shows the basic elliptical rim model. The tabulated rim is in red. The blue line includes PTD and is obscured by the pink line. The pink line shows the 'tilted tabrim', which is equivalent to 'tabrim' in another reference frame. The green line shows the measured points used for the primary mirror surface. The orange line shows data for measured surface data for both mirrors.

necessarily considered problematic. The aberrations can be accounted for in the inter-calibration of the detectors.

4.5.3 Realistic Model: CF2 Results

The same analysis was repeated for the second carbon fibre source (CF2). The only change was the location of the source to reflect where it is located on QUBIC's TD horn array (see Fig. 4.4). The analysis provided for CF1 applies to the CF2 results shown in Fig. 4.18.

However, when the realistic model for the secondary mirror is introduced, much larger variations are seen. These are on the order of 1.2 dB in some locations (-0.04 m and 0.045). Again, this is not necessarily a problematic result since the model is an accurate representation of QUBIC's calibration set-up and it can be used for the calibration. It is worth noting that the first carbon fibre source is less sensitive to surface and rim variations caused by the machining process.

4.5.4 Realistic Focal Plane Results

Figs. 4.17 and 4.18 show the preferred realistic models (yellow) of the carbon fibre beams on the focal plane as cuts for both CF1 and CF2. These models include PO+PTD, measured mirror surfaces, representative model of the rim, and the cold-stop.

The updated focal plane power plots are shown in Figs. 4.19a and 4.19b for the realistic optical model of the QUBIC TD. Visually these are different to the results from the basic configuration used in the ideal validation scenario (Figs. 4.9a and 4.9b). The power levels in both cases are normalised so it is only the shape and spatial distribution of the power that is different. These data show that using a realistic model of the surfaces, rims, and cold-stop is important for the detector calibration since the width of the beam is subject to truncation as evidenced by Figs. 4.17 and 4.18. The effects of realistic mirror surfaces and rims for the horn array beams are investigated in detail with the FI instrument model in Chapter 5.

4.6 Carbon Fibre Source Spectrum

4.6.1 Frequency Modelling

Since the carbon fibres are frequency tunable, simulations are made with the realistic model for a range of frequencies. The simulations are made for the lower band: 130 - 170 GHz at 5 GHz intervals. For the CF calibrator horns, the published geometrical light cone half angle of $\approx 24^\circ$ was used for all frequencies in the band (for an over-moded Winston cone the angular pattern is well predicted by geometric optics theory, i.e. approximately constant out to an angle determined by the ratio of input to throat diameters). These data are summarised as 45° cuts in Fig. 4.20. The spectral data are normalised across all frequencies to the maximum value. This way the relative power as a function of frequencies is observable. The full grid patterns for each frequency and for each carbon fibre source are given in Appendix A.

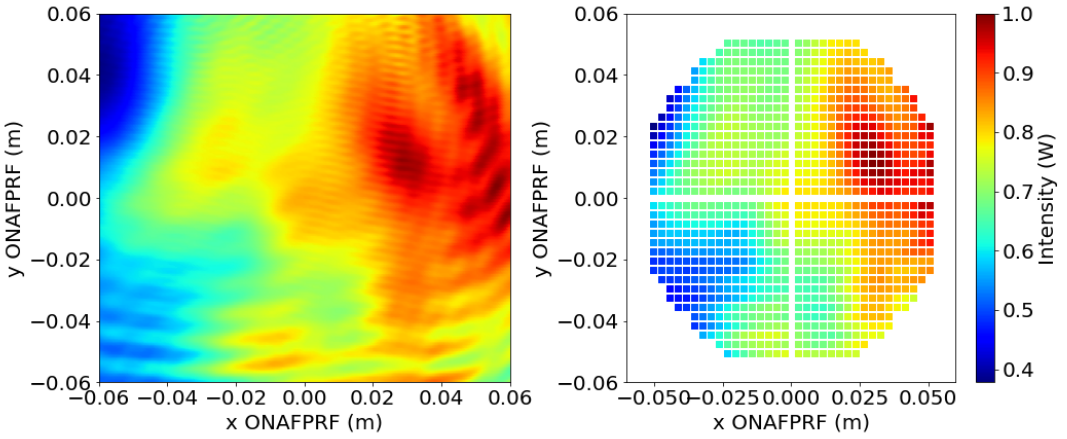

(a) (left) Realistic focal plane power (normalised to 1 W) and (right) power on each TES in the array from the GRASP model for CF1.

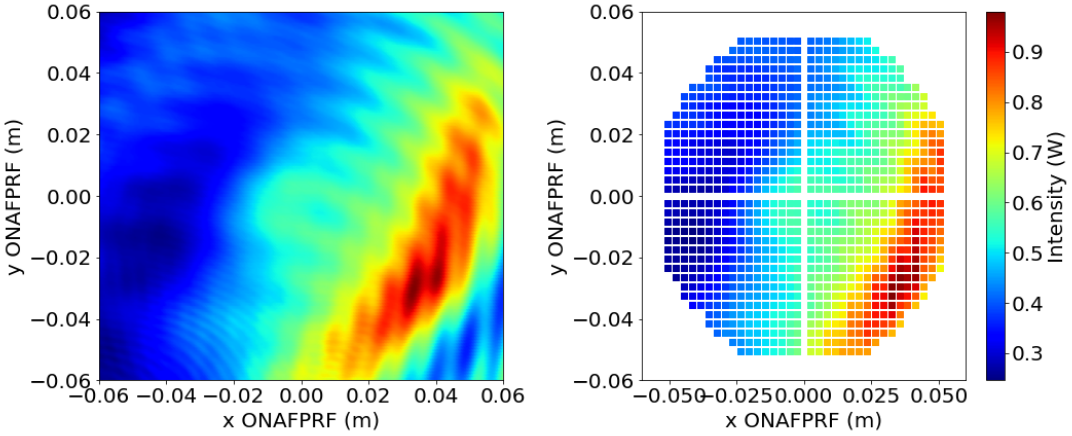

(b) (left) Realistic focal plane power (normalised to 1 W) and (right) power on each TES in the array from the GRASP model for CF2.

Figure 4.19: The focal plane data for CF1 and CF2 are shown for the realistic optical model with the cold-stop, realistic rims, and realistic mirror surfaces included. The left side show the data for the whole focal plane area. The right shows that data integrated into the detector geometry. Each square is a detector. 'ONAFPRF' refers to the on-axis focal plane reference frame.

Fig. 4.20a shows the cuts for CF1. The data show that in the GRASP software, higher power is transmitted to the focal plane for lower frequencies. The general shape of the profiles are similar for all frequencies.

A similar trend is evident in Fig. 4.20b for CF2 with less power difference observed between the frequencies. Fig. 4.20b has a $-45°$ cut to highlight the high power region of the focal plane grid (see the focal plane grid pattern in Fig. 4.19b for reference).

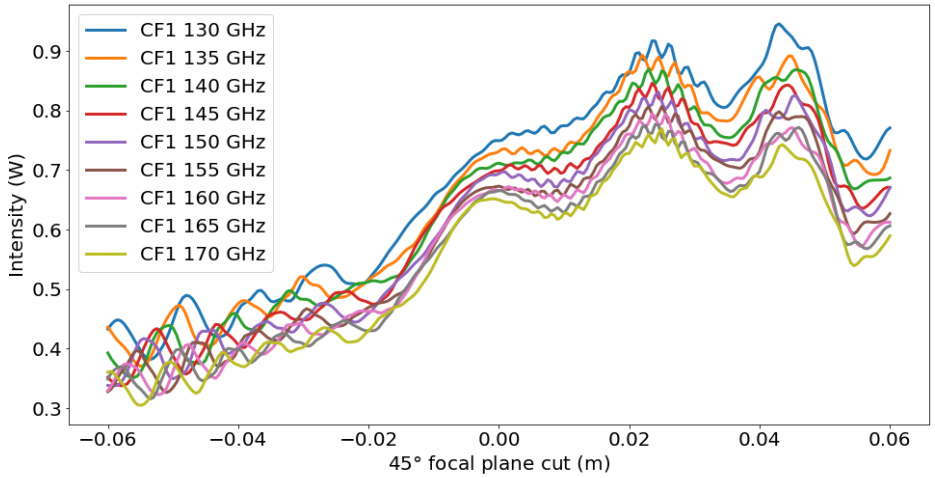

(a) CF1.

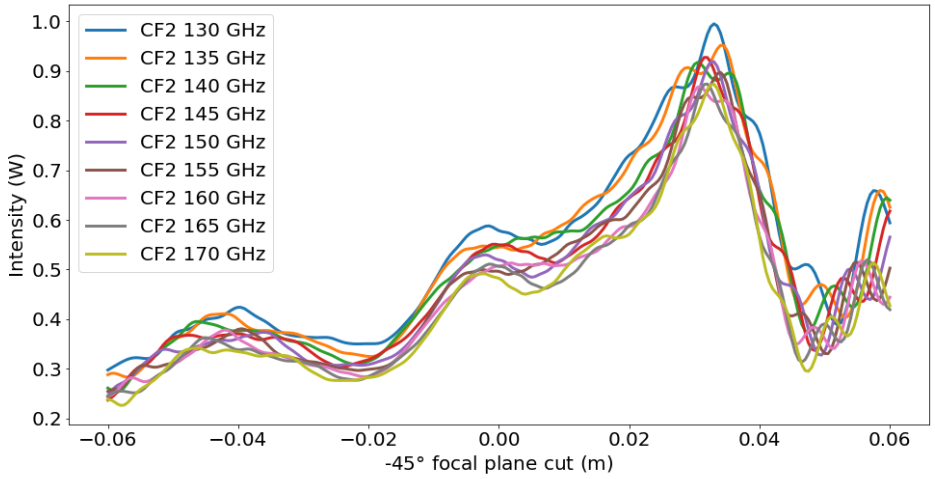

(b) CF2.

Figure 4.20: Cut of power on the focal plane (normalised) from the calibration source and a range of frequencies in the lower QUBIC band.

4.6.2 Spectral Weighting

Due to the thermal nature of the carbon fibre source, it is useful to include its spectral behaviour in the model. This is done using data provided in the PhD thesis by Henrot-Versillé (2006) [95] and shown in Fig. 4.21. This figure shows the intensity of the fibre output measured at different frequencies. The yellow line for the 1 mm fibre is of particular interest since this is the fibre installed in QUBIC. This plot shows that at 170 GHz there is an arbitrary flux value of 6.2 while 130 GHz has a value of 3. This indicates that the carbon fibre source will

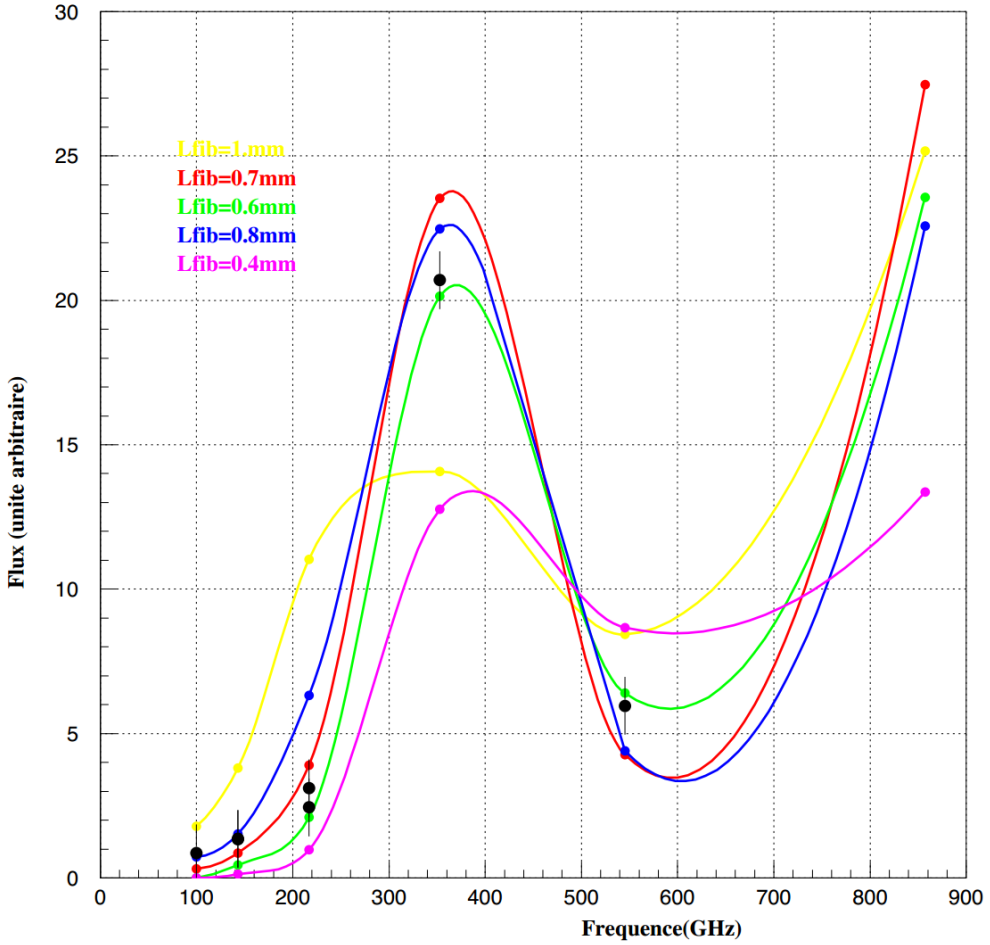

Figure 4.21: Carbon fibre flux measurements for fibres of different lengths (Henrot-Versillé (2006) [95]). The y-axis shows arbitrary flux. The x-axis shows the frequency at which the flux was measured. A 1 mm fibre was used for QUBIC.

Frequency (GHz)	130	135	140	145	150	155	160	165	170
Weighting	0.65	0.74	0.83	0.91	1	1.09	1.17	1.26	1.34

Table 4.1: Carbon fibre flux weighting for frequencies across the QUBIC band. These were calculated from an interpolation of the 1 mm data in Fig. 4.21 and are normalised to one at 150 GHz.

have a higher contribution of power at higher frequencies compared to the lower frequencies. The resolution of the data is low so an interpolation is made so that a weighting can be applied to the spectral data from the optical modelling. This interpolation is shown in Table 4.1. The interpolated data are used to apply a weighting to data at each frequency.

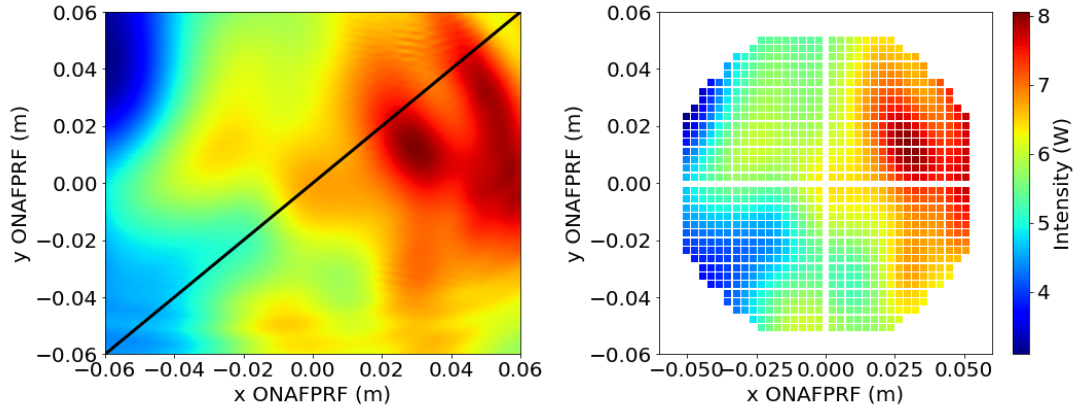

(a) The simple normalisation where all frequencies are normalised to one.

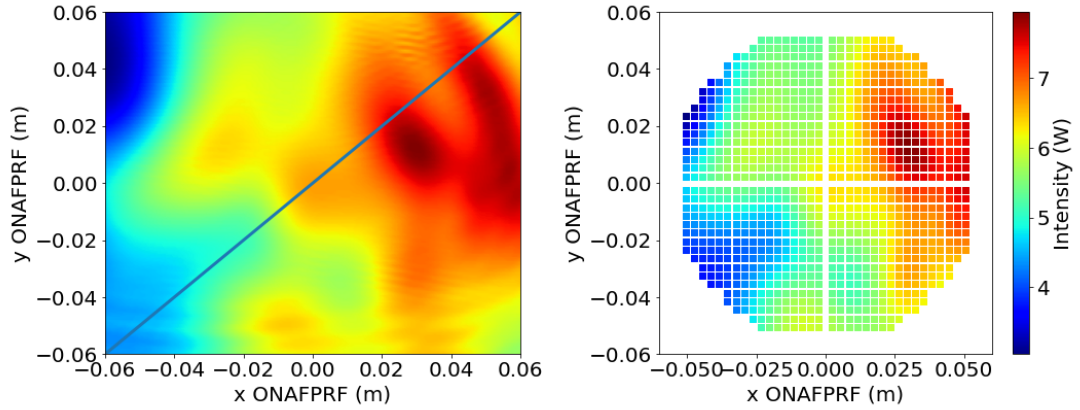

(b) The weighted model based on the interpolation in Table 4.1.

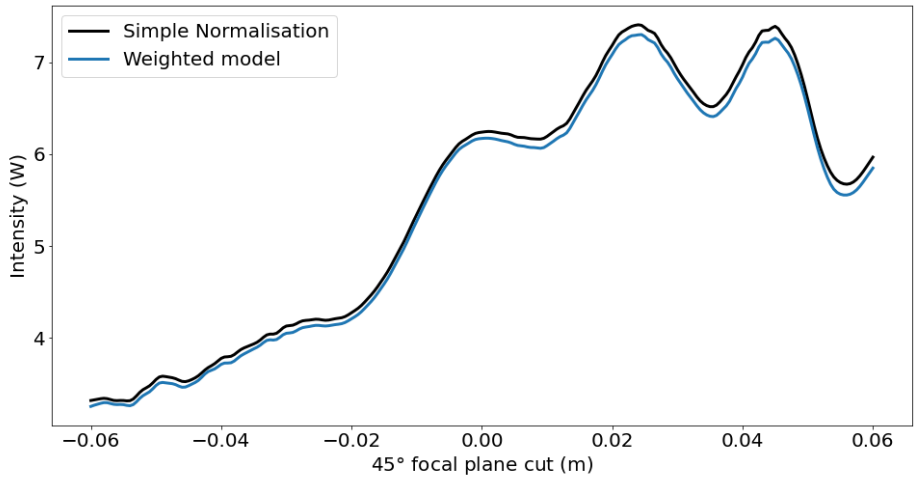

(c) The two weighting methods are compared with 45° cuts. The two methods are in agreement.

Figure 4.22: The spectrally weighted models for CF1 are shown on the focal plane. The entire focal plane is shown on the left. The right shows that data integrated into the detector geometry. Cuts along the black and blue lines on the left plots are shown in (c).

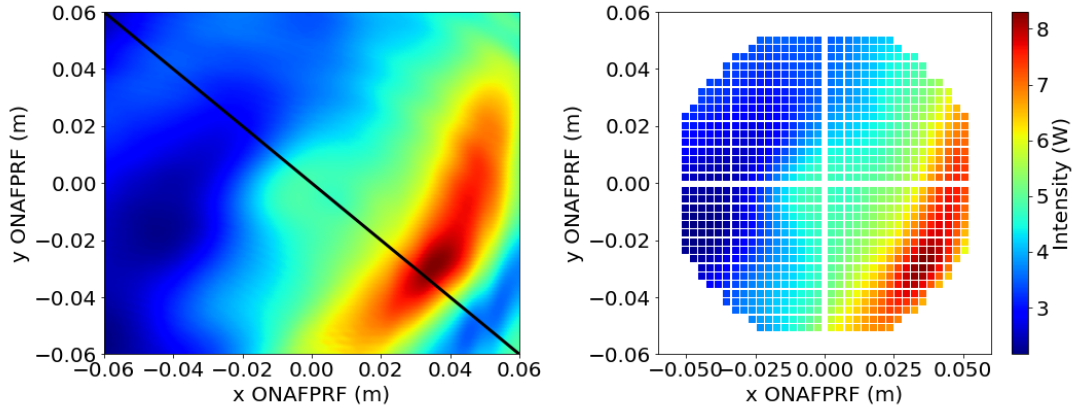

(a) The simple normalisation where all frequencies are normalised to one.

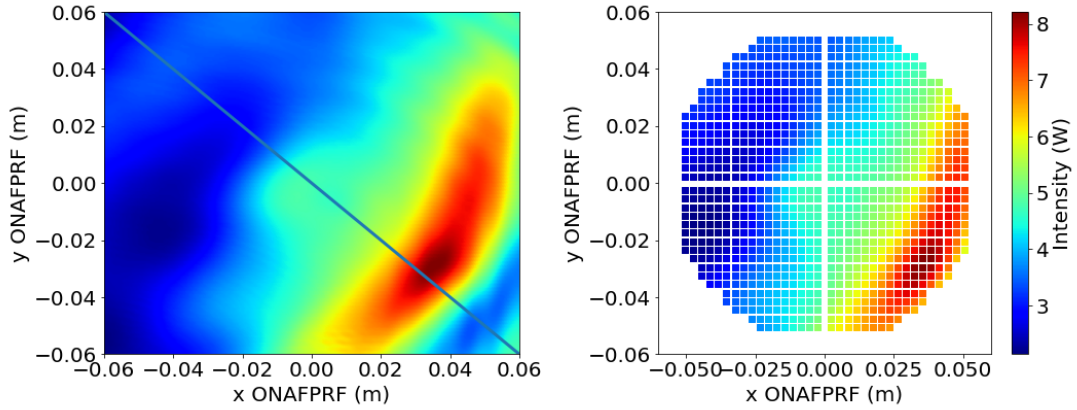

(b) The weighted model based on the interpolation in Table 4.1.

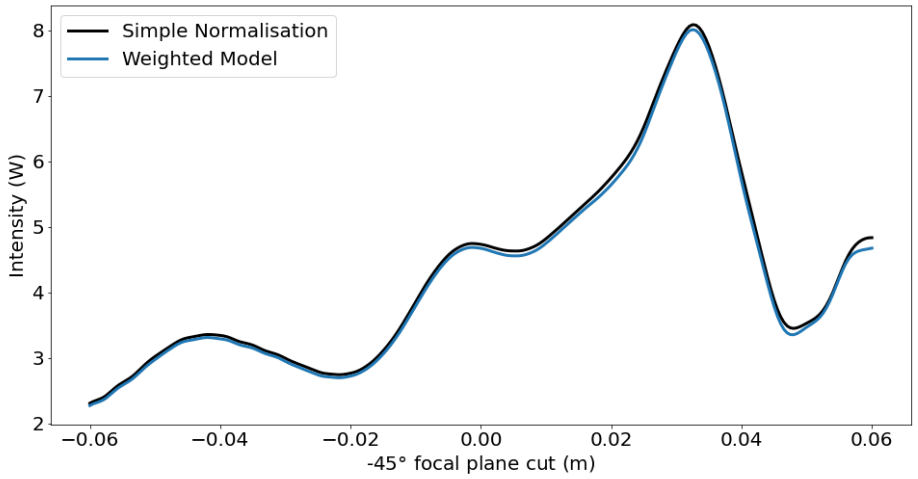

(c) The two weighting methods are compared with -45° cuts. The two methods are in perfect agreement.

Figure 4.23: The spectrally weighted models for CF2 are shown on the focal plane. The entire focal plane is shown on the left. The right shows that data integrated into the detector geometry. The black and blue lines show the cuts used to analyse and compare the data.

The results of these weighting schemes for the spectral data are summarised for CF1 in Fig. 4.22. Fig. 4.22a shows the data for the simple weighting where the initial power at all frequencies was set to 1. The results for the realistic weighting are shown in Fig. 4.22b. Cuts across the data are shown in Fig. 4.22c. The cuts are near identical in shape. There is a small difference in power of 1.4% at the peaks. A reduction in power is expected since the input power at some frequencies is reduced below 1 but it is an insignificant difference and either model may be used. The data are interesting since the broadband data appears smoothed when compared to single frequency data, for example in Fig. 4.20a where the data are variable with more peaks, troughs, and fringe-like patterns.

Fig. 4.23 shows the data comparing the two weighting schemes for CF2. Fig. 4.23a is the grid data for 130 - 170 GHz where all intensities are given the same weighting of 1. Fig. 4.23b shows the data when the weighting of Fig. 4.21 and Table 4.1 is used. The two weightings are compared in Fig. 4.23c. These data show that the two weighting methods give almost the same results, with a difference of only 1.1% at 0.0375 m on the focal plane. Similarly to CF1, the broadband data appears smoothed when compared to single frequency data, for example in Fig. 4.20b. This gives confidence that a more detailed knowledge of the data in Fig. 4.21 is not required.

4.7 Conclusion

Two internal calibrators are installed on QUBIC's TD horn array so that they illuminate the whole focal plane and can be used for the inter-calibration of the TES detectors.

This chapter has used GRASP to model the beams from thermal carbon fibre sources through QUBIC's optical combiner. The model was validated against a simple model in MODAL. Near field effects were observed and studied in the GRASP model and a correction factor was applied (due to the Gaussian beam mode paraxial limit) to ensure the proper 48° FWHM beam is propagating from the source. This model also showed that the source does not illuminate the focal plane with equal power due to truncation by the mirror surfaces and edge.

After validation, the GRASP TD model was upgraded to include a cold-stop and realistic optical elements such as measured and cooled mirrors and rims. The effect

of the size of cold-stop was studied and found not to be significant until it was made unfeasibly small.

The inclusion of PTD in the PO model was also studied and found to be negligible. PTD was still included due to its low computational cost. A final single frequency realistic model for both carbon fibre sources was realised and showed that realistic elements modify the beam on the focal plane when compared to the simple model with ideal elements. The data show the necessity of modelling of realistic elements for the internal calibrator model on the focal plane.

The model was then extended to a range of frequencies from 130 to 170 GHz to match QUBICs single-moded bandpass. The intensity of the focal plane patterns at these frequencies were added due to the thermal nature of the sources. Two incoherent source weighting schemes were tested: a uniform normalisation and a normalisation based on measurements made when the sources were tested for the Planck project. The latter spectral weighing method is a more realistic model of the expected source behaviour. It is interesting that only a small difference between the models was found and choosing the spectrally weighted model should provide higher fidelity results when the data is used for QUBIC data-analysis and calibration.

The data produced were also shown integrated into the bolometer detector areas for single frequencies and for the wide-band models. These data will be integral to the inter-calibration of the TES detectors. These data are especially important since the modelling has shown that the illumination is not flat across the focal plane as was originally hoped.

Chapter 5

Full Instrument Optical Model

5.1 Introduction

After initial observations the QUBIC instrument will be upgraded from the TD to the FI configuration in Argentina as described in Chapter 2. The FI will have the full array of 400 horns (instead of 64), full sized mirrors (increasing from a diameter of 462 mm to 594 mm), and two full focal plane arrays. This chapter discusses the development of an optical model of the QUBIC FI in GRASP. An accurate optical model of the FI is essential for spectro-imaging and systematics minimisation.

GRASP is again the most useful tool for this modelling since it has a feature that allows custom surfaces to be defined from x, y, and z point coordinates. After the manufacturing of the FI mirrors, the surfaces were measured. These data are used in GRASP to define the mirror surfaces and produce the most accurate predictions for the focal plane intensity pattern that account for manufacturing imperfections.

The implementation of the mirror rims and surfaces are discussed and analysed in detail. A tabulated source from MODAL is implemented for the horn beams as discussed in Chapter 3. The beam on the focal plane is simulated for each horn as a method for finding the PSF of the instrument. The simulations are then extended to cover QUBIC's single-moded band-pass from 130 - 170 GHz. Finally, the focal plane data are integrated over the detector array geometry to be made useful for spectro-imaging and calibration purposes.

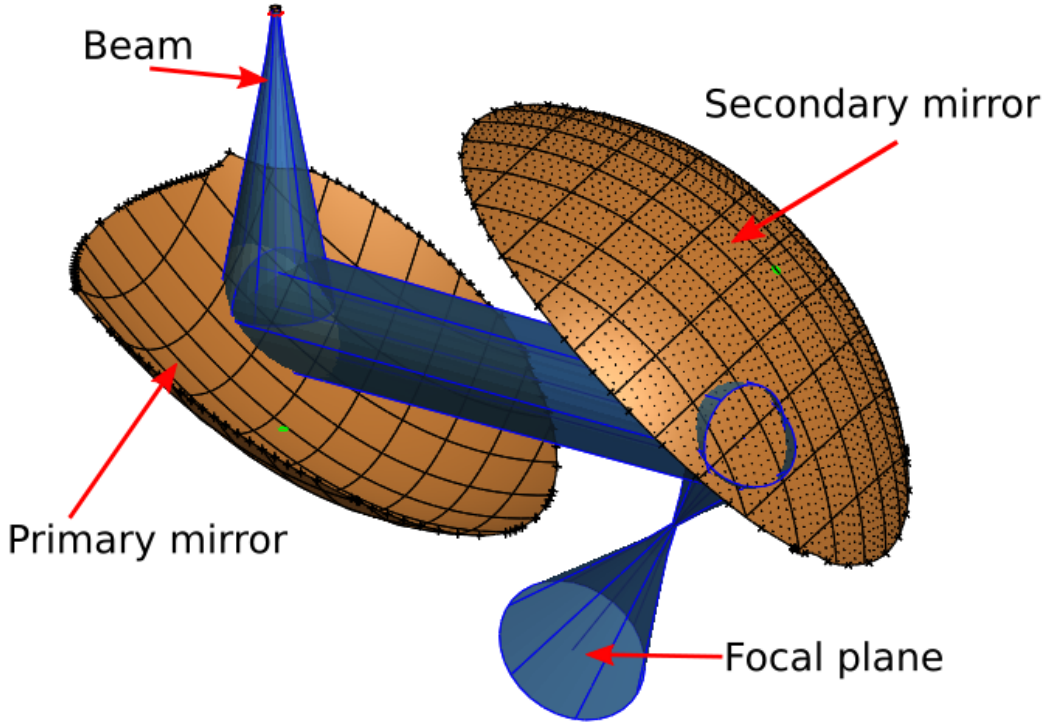

Figure 5.1: A simplified optical model of QUBIC from the GRASP software. One beam is propagated. The beam reflects off the primary and secondary mirrors and is incident on the focal plane.

5.2 Model Configuration for the FI

The starting point for this model is the validated TD model used in Chapter 4. The cold-stop and focal plane in this model are the same as for the TD. The source is changed from a carbon fibre test source to a Gaussian model of the horns initially, and then updated to a more accurate tabulated source. The horn array is changed from an 8×8 array to a 400 element array with the horns arranged in a circular pattern (Fig. 2.11). The mirrors are changed to their full sized versions. A simplified setup (no cold-stop) is shown in Fig. 5.1 with the larger FI mirrors and the path of one horn beam propagated through the combiner onto the focal plane.

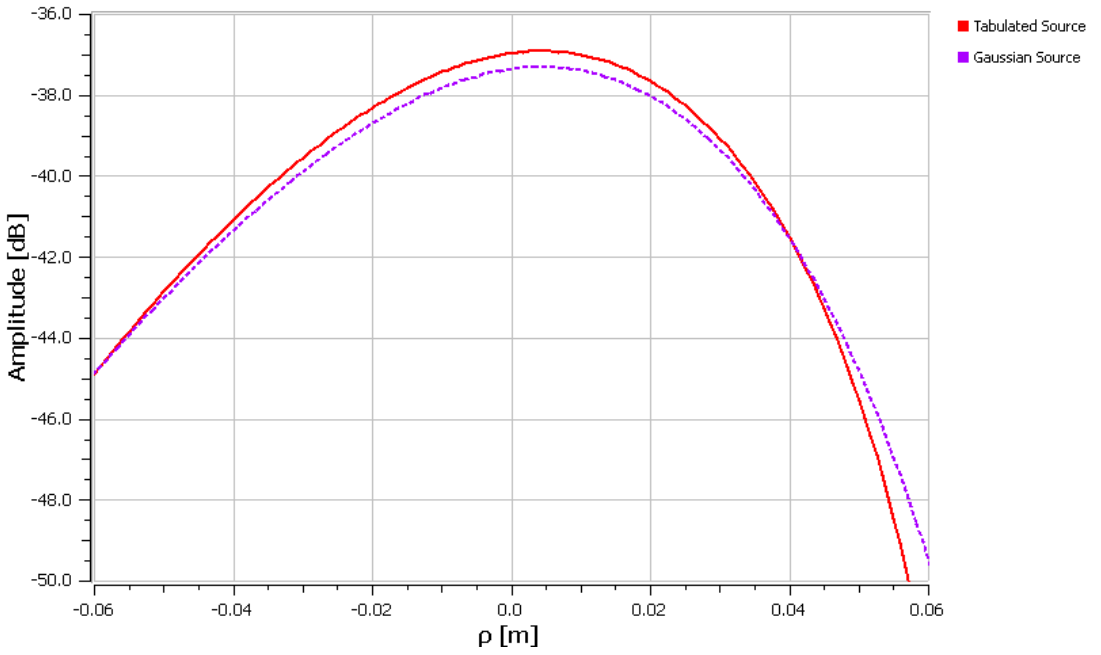

Figure 5.2: The test horn beam (horn 113) on the focal plane (after propagation through the combiner) for a Gaussian source (red) and the true modelled and tabulated horn source (purple dashes), both at 150 GHz. While not an exact match, the Gaussian is a useful approximation of the real beam. The specific location of horn 113 is given in Appendix B.

5.3 Horn Beam Profile

QUBIC's corrugated horns are designed to propagate sky signals with frequencies from 130 - 170 GHz as single-moded beams through to the optical combiner. The same horns will propagate multi-moded sky signals through the optical combiner at 200 - 240 GHz. At the lower single-moded frequencies, the beam profile is close to a Gaussian as shown in Fig. 5.2. Fig. 5.2 shows two horn beams incident on the focal plane. The purple dashed line shows a model of the corrugated horn propagated through the optical combiner. The solid red line shows the same for a Gaussian approximation of that horn beam. While the tabulated source model carries more on-axis power ($\sim$ 0.4 dB), the beam shapes are very similar and results calculated for the Gaussian approximation are likely to be very close for the exact horn beam.

The computation time required by GRASP to run a simulation with the real tabulated source is significantly longer when compared to a Gaussian model. Considering the computational limitation and the similarity of the beam profiles, it is sensible to test and model the optical set-up with the Gaussian source to streamline the process. Once the model is complete, the exact source can be included

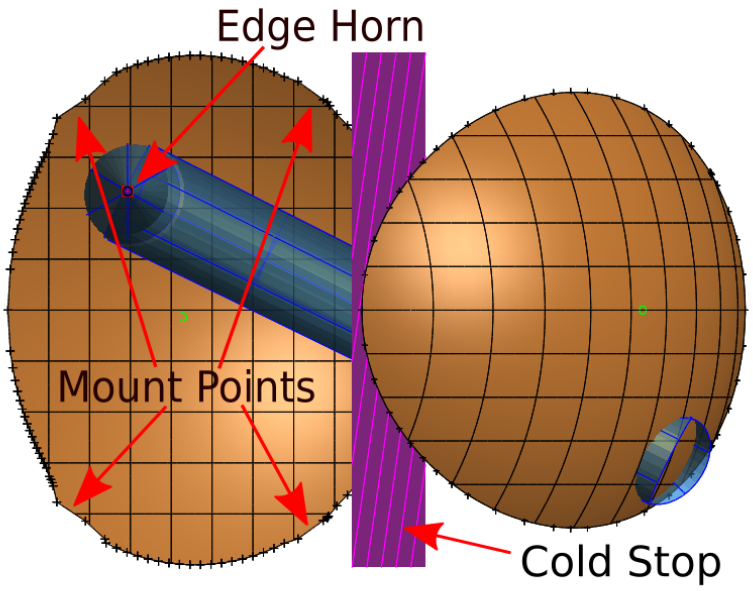

Figure 5.3: A top down view of the QUBIC optical model. The edge horn (labelled) used in testing propagates the beam (blue). The rim cat-ears near the mount points are also shown. The cold-stop (pink) is also included in this model.

for the final run of simulations. As such, this chapter will contain models and simulations using both the simplified Gaussian model source and a realistic model of the horn beam.

The FI requires the beams from an array of 400 of these horns to be combined on the focal plane. Before combining 400 horns it is simpler to build the model and test with only one horn. The single test horn is chosen as one horn from the FI array, the exact choice depends on what aspect is being studied. As will be described in Section 5.4, a significant effort was put into the correct definition of the mirror rims and so a horn closest the rim and mirror mounts was chosen. The test horn's proximity to the mounts is useful since mirror rims are a source of beam aberration due to truncation and diffraction. A beam from this horn is also incident on the mirror with a large angle of incidence. In this sense, it can be considered a 'worst-case-scenario'. If there are problems with the surfaces or rims in the model, this horn beam will show up those model issues. Fig. 5.3 shows the rim edges near the mount points and the horn (113) whose beam propagates nearest one of the mount points.

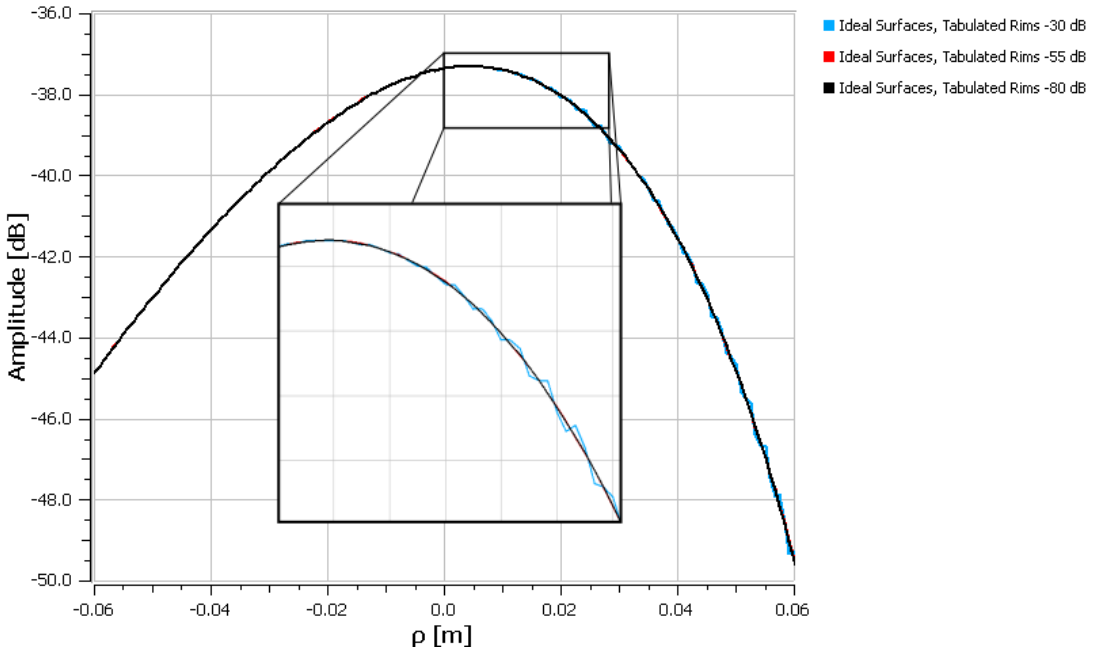

Figure 5.4: Error in the field due to PO convergence and field accuracy. The zoom inset shows variations of ∼0.1 dB at a field accuracy of -30 dB (blue line). The red (-55 dB) and black (-80 dB) lines are in perfect agreement.

5.3.1 Field Accuracy

By setting automatic PO convergence in GRASP the field accuracy can be set to the users requirements (summarised in Section 3.4.2). If the field accuracy is set too low, this can result in a ripple on the field data.

An example of the effect of field accuracy level can be seen in Fig. 5.4. Different field accuracy levels are tested for the same test set-up as in Fig. 5.3. At -30 dB a ripple of ± 0.1 dB is present on the inset plot. A field accuracy of -55 dB is already convergent when compared with -80 dB as shown in the figure. Plots in this section will have at least a -55 dB field accuracy unless otherwise stated.

5.3.2 Near Field Effects

Near field effects and distortions to the tabulated beam before the primary mirror are important to study. Goldsmith (1998) [92] provides Eq. 5.1 to describe the near field region (or confocal distance) of a Gaussian source as:

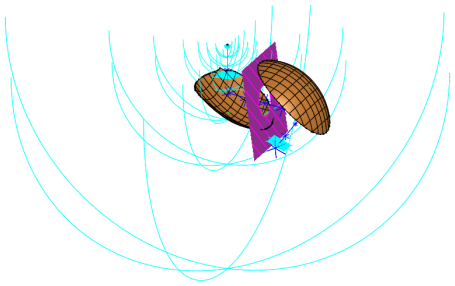

(a) Spherical cuts at set distances ranging from $z = 8\,\text{mm}$ ($z < z_c$) to the far field as calculated by GRASP ($z >> z_c$).

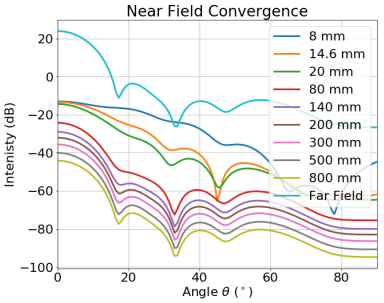

(b) Here the cuts are plotted for near field calculations at set distances from the tabulated source on the horn array. The far field calculation is also incuded. Naturally the peak power decreases as distance increases (GRASP uses a different normalisation for far-field calculations).

Figure 5.5: Experimental set-up used to find near field convergence for the tabulated source with the results plotted.

$$z_c = \frac{\pi {\omega_0}^2}{\lambda} \tag{5.1}$$

where ω_0 is the beam waist radius of the Gaussian beam approximating the horn ($\omega_0 = 3.329\,\text{mm}$[1] for the QUBIC horns at 150 GHz) and λ is the wavelength of the source. With this set-up, the confocal distance is $z_0 = 14.6\,\text{mm}$. If the GRASP output cuts were defined within 14.6 mm of the horn array, near-field effects would be expected on the beam profile. The tabulated source is a bespoke design so naturally this Gaussian equation does not give an exact value for the confocal distance for the QUBIC horn.

Fig. 5.5a shows the locations of a series of spherical cuts relative to the tabulated source. These are chosen to experimentally find far field convergence by testing near field cuts at greater and greater distances from the source. Eventually, the near field calculations should match the far field result. These are plotted in Fig. 5.5b. It is normal to find the peak power is different for different values of z. As such, normalised cuts are shown in Fig. 5.6.

The cut data show the far-field convergence clearly. Only at distances of $z > 300\,\text{mm}$ is the side lobe null (at 17°) sharply resolved. Defining the far-field is subjective and in the case of $z = 200\,\text{mm}$, the side lobe null is still clearly evident.

[1] ω_0 is calculated as per Eq. 4.1c.

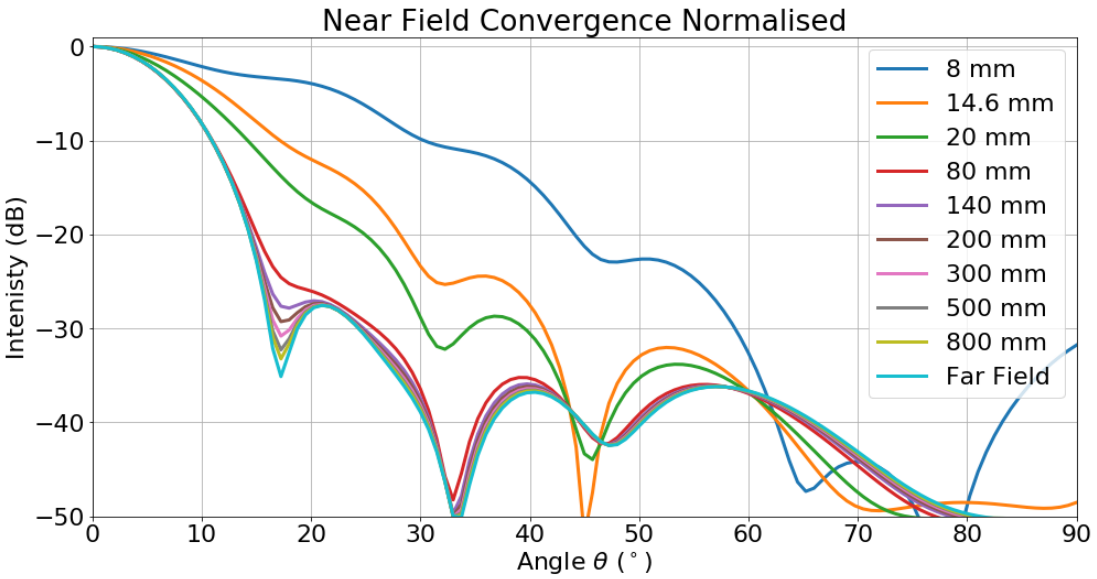

Figure 5.6: Normalised beams from Fig. 5.5b. Normalisation is required to compare the beam profiles as peak power decreases with distance from the source.

In practical terms, at $z = 80\,\text{mm}$ the beam has no near-field features at angles less than 12.9° and the approximate FWHM of the horn beam is 12.9°.

Fig. 5.6 does show that some near-field effects from the tabulated source are present near the primary mirror and will have some, albeit likely unmeasurable, effects on the points spread function on the focal plane. GRASP, of course, can accurately calculate currents on the primary mirror for a tabulated source.

5.4 Rim Model

Quasi-optical beams can be truncated and therefore distorted by the rim or edge of a surface. Usually a mirror surface should be sufficiently large in comparison to the beam that it reflects so that they are not affected by the rim and diffraction. QUBIC has an array of 400 horns so the outer horn beams are most likely to be affected by rims. The beams have a FWHM of 12.9° but the wider side lobes might spread onto the rim. Fig. 5.3 shows one of these outer horns. Horn 113 (as defined by Brossard and Chanial (2014) [96] and summarised in Appendix B) and its beam path illustrate its proximity to the rim of the primary mirror (M1) and the secondary mirror (M2). The effects of the rims can be examined by testing if the beam of horn 113 on the focal plane changes with the rim definition.

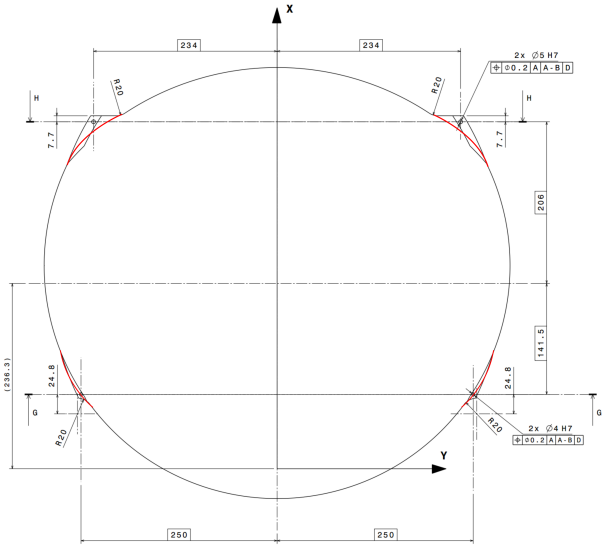

(a) The primary mirror, M1.

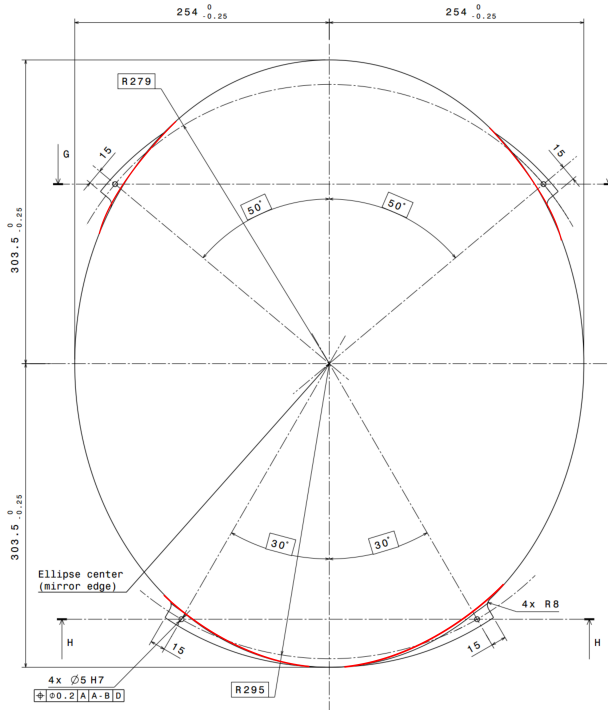

(b) The secondary mirror, M2.

Figure 5.7: Schematic view of the final design of the mirror surfaces. The red lines show the old and simplified configuration. The final design has "cat-ear" like mount points to help with mirror alignment.

QUBIC's rims were initially designed with ideal ellipses as shown by Scully (2016) [77], but space and manufacturing requirements led to a more complex shape for the rim. The rim for the primary mirror as manufactured is comprised of the union of two circles with "cat-ear like" regions near the mount points (Chapron (2018) [97] and shown in Appendix C). These cat ears are evident in Figs. 5.7a and 5.7b for the primary and secondary mirrors respectively. The red lines drawn on the rims in Fig 5.7 show the old simple design. The mount points were added to the FI mirrors to help with the alignment of the mirrors in the cryostat. This was motivated by difficulties in the alignment procedure of the TD mirrors (Gayer (2021) [98]).

It is necessary to test the most realistic and representative rim possible to ensure an accurate model is made for the FI, for example by including relevant components such as the CS. A number of methods were used to find an accurate rim that can be defined appropriately in GRASP. The methods are: using a convex hull approach, drawing and fitting circles from the technical drawing, and by selecting points from the CAD models of the mirrors.

The primary question to be answered concerning the rim definition in GRASP is with regards to the effect of the mirror rim on the beam and in particular, if the cat-ear like modification to the rim near mount points would affect the beam. A file did not exist with the rim points so one was created for use in GRASP. The methods are described in the following sections.

5.4.1 Simple Ellipse

A simple ellipse can be used as a rim based on the geometry from the technical drawing used for manufacturing (Chapron (2018) [97] and shown in Appendix C). From this, the semi-minor axis is 200 mm and the semi-major is 297 mm. This rim can be used as a baseline for comparison against more representative rim models. The ellipse model is simple to define in GRASP and it is computationally efficient which is beneficial for simulation time. With the ellipse defined in GRASP, the edge horn (horn 113) beam is propagated onto the focal plane and is measured along a cut across the focal plane in Fig. 5.8 (blue line). This is the baseline against which other models will be compared.

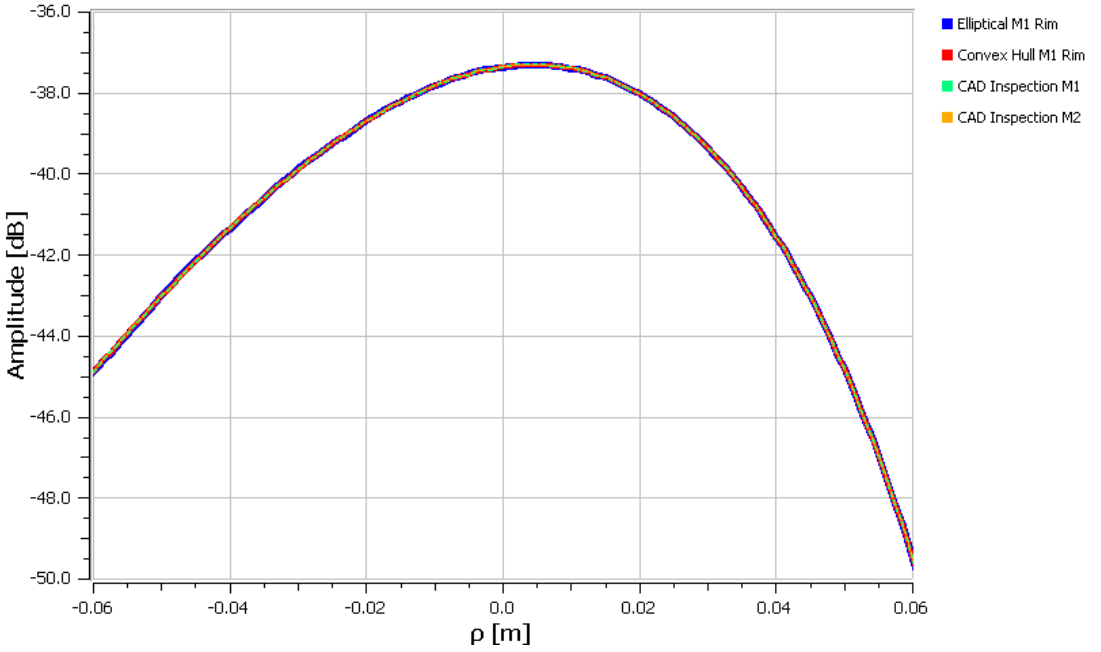

Figure 5.8: The edge horn beam profile on the focal plane for a simple elliptical rim (blue line) and for the rim made from the convex hull approach (red line). The rim made from the CAD points is plotted with green dashes. The beam when the same method is applied to the secondary mirror is plotted with an orange line. The data match for the four models with -80 dB field accuracy.

5.4.2 Convex Hull Approach

The convex hull method finds the smallest possible polygon around a set of points. As the name implies, the polygon edges are always convex, never concave. A set of x, y, z data exists for QUBIC's mirrors at 300 K as described in Section 3.4.3.2. Later, data became available for the mirror deformations at 4 K (Section 5.5.7). When the primary mirror was manufactured it was measured in x, y, z coordinates to check against design specifications. Naturally the manufacturing process will cause slight imperfections on the surface of the mirror. These measured points will be used in a later section to test the surface accuracy but the file is also useful for defining the rim in GRASP.

The Qhull library from SciPy by Virtanen et al., (2020) [99] is based on the quickhull algorithm by Barber, Dobkin, and Huhdanpaa (1996) [100] commonly used in the field of computational mathematics. Here, this method is used to define a rim model for QUBIC's mirror and tested against other rim models in GRASP.

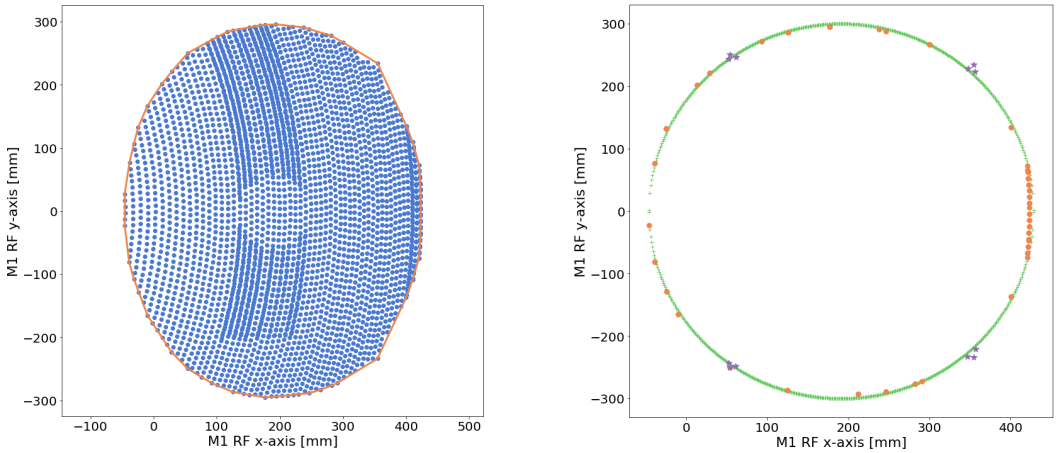

(a) The measured x, y, z mirror points in blue have their outer points fitted (orange) using the convex hull method. Note that this plot's x-axis is reversed in comparison to Fig. 5.3 due to a different reference frame of the measured mirror data. This figure also shows an interesting feature regarding the measured surface points that is discussed later in this chapter. There are mixed samplings of x and y points

(b) The convex hull points are shown in orange (orange lines in left panel). The green dots are points fitted to an ellipse based on the convex hull points. The purple stars are the measured points nearest the mount points.

Figure 5.9: Examples of the method used to create the primary mirror rim model using the convex hull approach.

The measured surface data file was used for the convex hull approach to defining the mirror rim. For the rim in GRASP, only the x and y coordinates are needed. The smallest polygon found by the algorithm for the primary mirror rim has 69 sides and shown in Fig. 5.9a. The output (with 69 x, y points) does not clearly resolve the rim lips. As a result, the points are added manually to the rim model. With the coordinates output to a text file, they can be loaded as a rim file in GRASP (Fig. 5.9b). The resolution around the rim visually appeared too low. Points were interpolated to fill in the rim as shown in Fig. 5.10. This figure shows how GRASP interpolates the points in the cat-ear regions. As can happen when interpolating, the line deviates from the points in places, here near the cat-ear regions.

The result of this approach is also shown in Fig. 5.8. The data shown compare a simple elliptical model (blue line) of the rim compared to the convex hull (red line) approach. The data from the focal plane pattern of a horn from the two models agree exactly with a field accuracy of -80 dB. This means there is no difference between using the two models in terms of the output on the focal plane. There

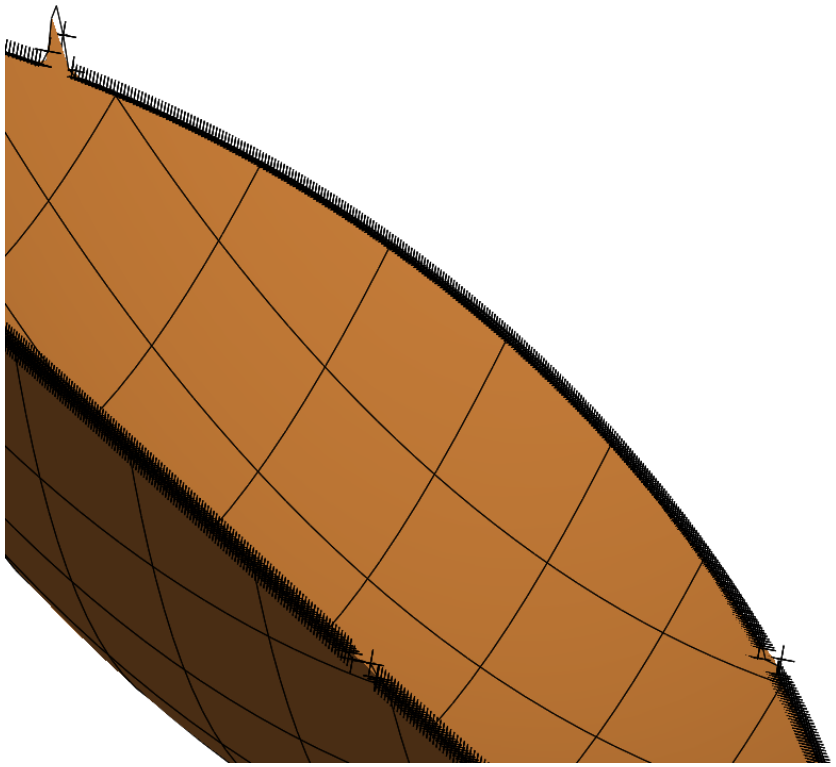

Figure 5.10: Graphical representation of the convex hull rim in GRASP. Also shown here is the interpolated line between the points that GRASP generates from the input data. The interpolated line is evident in the top left in the cat ear region.

would be an advantage to using the elliptical model in terms of computation time over the convex hull rim.

Even though the data are in perfect agreement for the two models, it is clear the convex hull approach is not a good visual representation of the mirror rim when compared to the engineering documentation as shown in Fig. 5.10. There is an unrealistic ridge effect from GRASP's interpolation. GRASP's interpolation methods combined with the input data from the model fail to model the mount point cat-ears to a satisfactory degree. Another reason for this is due to the fact that the convex hull was based on the measured mirror data which do not fully reach the edge of the rim. So, other methods need to be investigated to determine if the mount points will have an effect on the focal plane data.

It is evident from looking at the x, y, z data near the mount points that the data require some degree of a concave fitting so the convex hull fit does not suit this particular mirror and the measured data. However, for another mirror or design, this

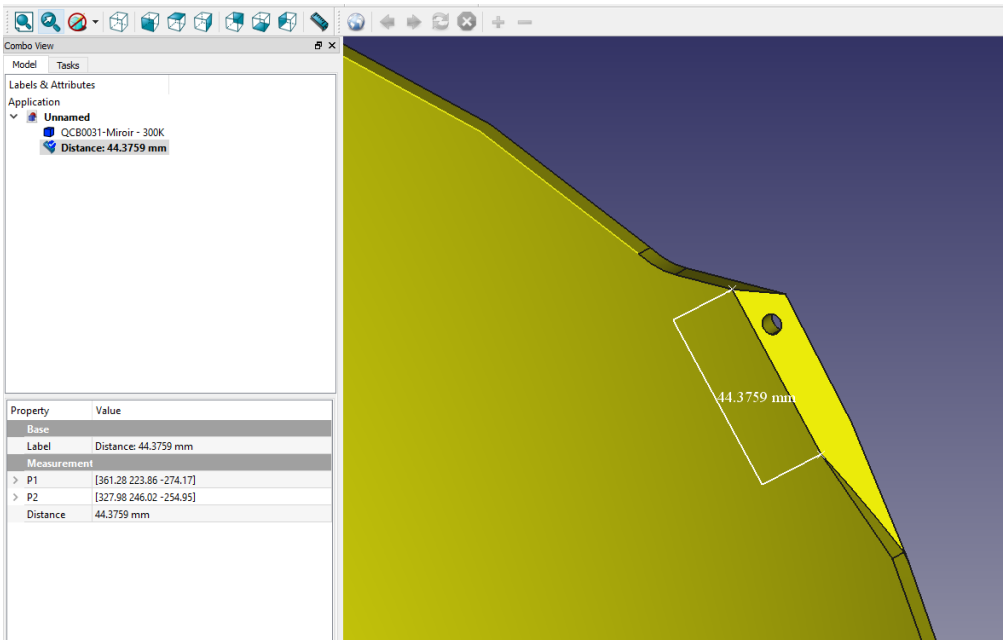

Figure 5.11: The CAD model for primary mirror is shown here in FreeCAD. In the bottom left, it is shown how points can be found to find accurate rim edges near the mount points.

method could indeed prove useful for determining the rim of a surface. Regardless, as shown in Fig. 5.8 the rim does provide an excellent and well performing result on the focal plane in comparison to other methods despite the lack of visual agreement. It is still interesting to see how these elliptical and convex rim models compare with a realistic and accurate model of the rim. This is discussed next.

5.4.3 CAD Model Inspection

Another method for finding realistic rim points is to manually inspect the CAD file for the mirror and select the rim points in CAD software. These points can be chosen with sufficient precision ($<1\,\mu m$) and added to a rim file in GRASP. This way, the highest possible resolution of the rim near the mount points is achieved.

Here, this was accomplished by loading a CAD file for the mirror into FreeCAD[2] and selecting the points to accurately represent the rim. The points are then prepared in a rim file for analysis in GRASP. Using this method the rim was found as shown in Fig. 5.11.

[2]www.freecadweb.org

The results for this rim are shown in Fig. 5.8, along with the results for the ellipse rim and convex hull rim. By inspecting the points from the CAD model, the beam on the focal plane matches the data from the other two models.

5.4.4 Rim Models Summary

Fig. 5.8 shows that the three different methods of modelling the rims result in the same beam on the focal plane. The results of the rim modelling show that the FI optical model is not sensitive to the exact rim definition. In fact, it is even acceptable to use the simple elliptical rim in the model. If computation time becomes problematic for the 400 horn simulation, this is an element that could be simplified to save on computation time.

It is shown that the convex hull approach did not model the cat-ear like mount points on the primary mirror with adequate resolution (at least visually) but the results proved it was effective for the main rim shape. It is likely even the basic convex hull rim with 69 points (and no external interpolation) would have produced identical results in Fig. 5.8. This method could prove useful for similar applications.

The CAD inspection method resolved the cat-ear mount points appropriately and the predicted beam on the focal plane matched both other models which is satisfactory evidence the cat-ear shapes added to the manufactured mirror should not affect QUBIC's PSF on the focal plane for the full horn array.

5.4.5 Secondary Mirror Rim Definition

The details of the rim modelling have been described in detail for the primary mirror. Based on findings from the primary mirror rim, the CAD inspection method is used to make a model of the rim for the secondary mirror. The secondary mirror has a much simpler profile, as evidenced Fig. 5.7b (and Appendix C), with less prominent mount points added to the designed rim shape.

By adding the modelled rim for the secondary mirror in the GRASP model, the effect of modifying the rim is assessed as shown in Fig. 5.8 with the orange line (obscured by an identical beam). No difference is observed in the data when using the modelled secondary mirror rim in comparison to a simple elliptical rim.

5.5 Surface Modelling

The manufacturing process for the mirrors may introduce errors on the surface that must be tested against the design requirements. Typically $\lambda/20 - \lambda/4$ is considered to be a sufficient tolerance level with $\lambda \approx 2\,\text{mm}$ for QUBIC at 150 GHz. This is the criterion that will be used to measure surface accuracy in addition to focal plane results.

The surfaces of the mirrors were measured in Cartesian x, y, z coordinates after manufacturing. The measured surface data can be implemented in GRASP to define the mirror surface as a tabulated surface. This can be compared against the ideal mirror equation as defined in the mirror design documents. The measured file for the primary mirror has 3416 coordinate points that can be loaded into GRASP as a tabulated surface. Doing so, the effects of manufacturing defects can be analysed on the focal plane beam for the same test edge horn as used above (horn 113). This section will explain the steps taken to ensure accurate mirror surface modelling in GRASP.

5.5.1 Tabulated Secondary Mirror Surface

As before, this section adds one element to the optical model keeping all other aspects the same. Here, the mirror surface for the secondary mirror is defined in GRASP from the measured coordinate file rather than the ideal equation parameters.

Fig. 5.12 shows the result of this change to the model. The black line is a cut of the focal plane pattern when using the ideal mirror surfaces as in previous versions of the model. The orange line (obscured by the green line) shows the same for the measured secondary mirror surface. The two methods are in good agreement with the maximum difference between the cuts being less than 0.1 dB.

Also shown for comparison in this plot is the beam when using GRASP's triangulation interpolation method for a tabulated surface. The result of this is shown by the green line. GRASPS's pseudo-spline method and triangulation method are in excellent agreement for the secondary mirror. The results are within accepted tolerances and will not affect the final result on the focal plane. As such,

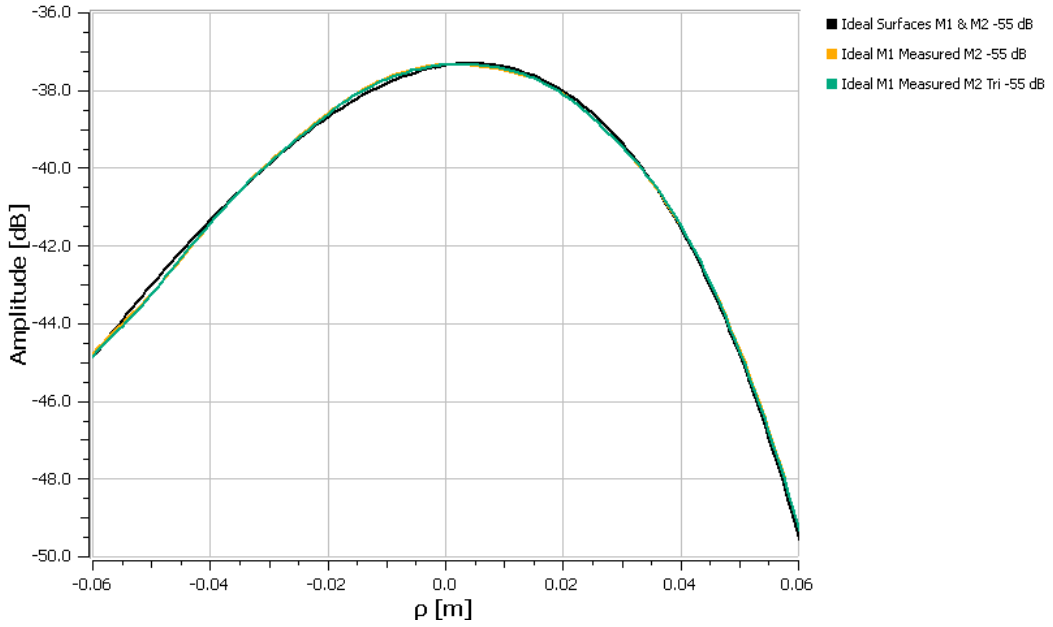

Figure 5.12: Focal plane beam pattern when using different secondary mirror surface definitions. The measured points are implemented in the model for the secondary mirror (yellow line, pseudo-spline interpolation). The y axis shows power in dB. The x axis is in metres. The x-axis ranges from -0.06 to 0.06 which corresponds to the focal plane. The previous configuration with ideal surfaces (black line) is the same as Fig. 5.4. The beam that results from using tabulated points with the triangulation interpolation is in green.

the tabulated secondary mirror could be used in this configuration for the final simulation.

5.5.2 Tabulated Primary Mirror Surface

The same procedure is used to test the measured surface for the primary mirror. The model is kept the same as Fig. 5.4 but the measured file is used to define the surface for the primary mirror. The secondary mirror has the ideal surface defined by the equation parameters from the design specifications (Chapron (2018) [101]). The results of this are shown in Fig. 5.13. This shows that the measured mirror file introduces a significant ripple variation on the beam on the order of 0.7 dB. Pseudo-spline interpolation of the tabulated data is used by GRASP to generate the mirror for Fig. 5.13.

This is especially problematic because the ripples are in the centre of the beam profile where the majority of the power and intensity is present. Such an unexpected result warrants further investigation since it is known that the measured

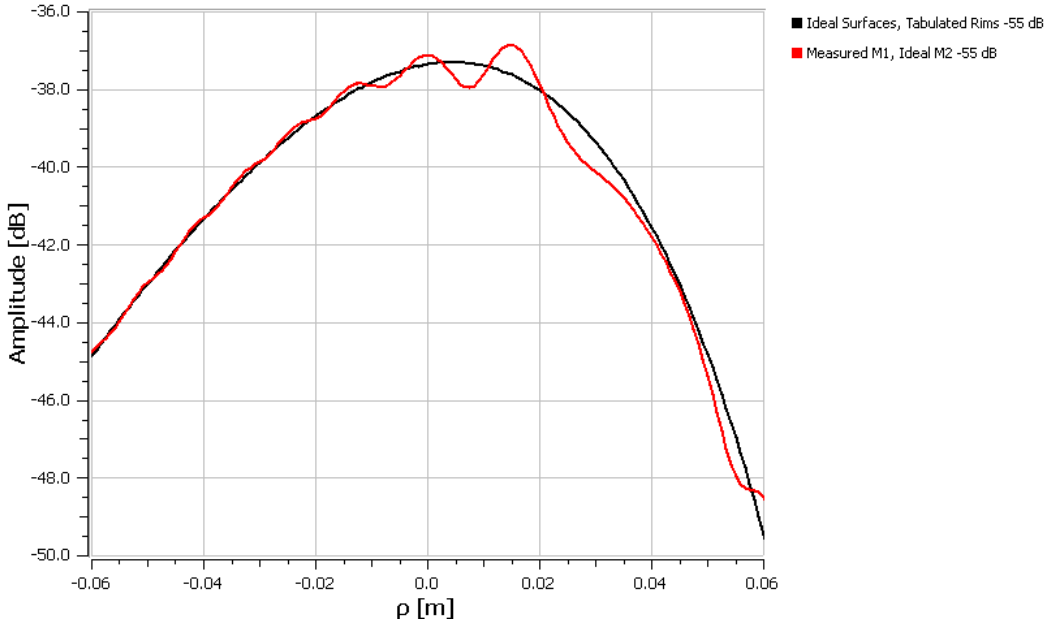

Figure 5.13: Focal plane beam pattern when using different secondary mirror surface definitions. The measured points are implemented in the model for the primary mirror (red line). The black line shows the model with ideal surfaces generated from the mirror equation as in Figs. 5.4 and 5.12.

surface points have been manufactured and tested within tolerances. If there is a variation due to manufacturing defects, the expected variation is less than observed in this analysis. In addition, the shape of the ripples is not dissimilar to what might be expected if there are sampling-related issues.

Other sources of error need to be investigated to prove or disprove the cause of the beam shape in Fig. 5.13. A number of parameters are tested including under-sampling, over-sampling, GRASP's surface interpolation method, PO point convergence calculations, and field accuracy. By investigating all of these possible causes of the ripple, it is possible to understand and resolve the issue.

5.5.3 Testing Sampling Rate

One explanation for the ripple observed in Fig. 5.13 is sampling. If there are too few measured coordinate points used to define the mirror, aberrations or ripples could be observed in the data. Over-sampling is also worthy of consideration and is tested alongside under-sampling.

The sensitivity of the model to sampling can be tested by using identical mirror surfaces but with different sampling rates. The model is kept the same as in Fig.

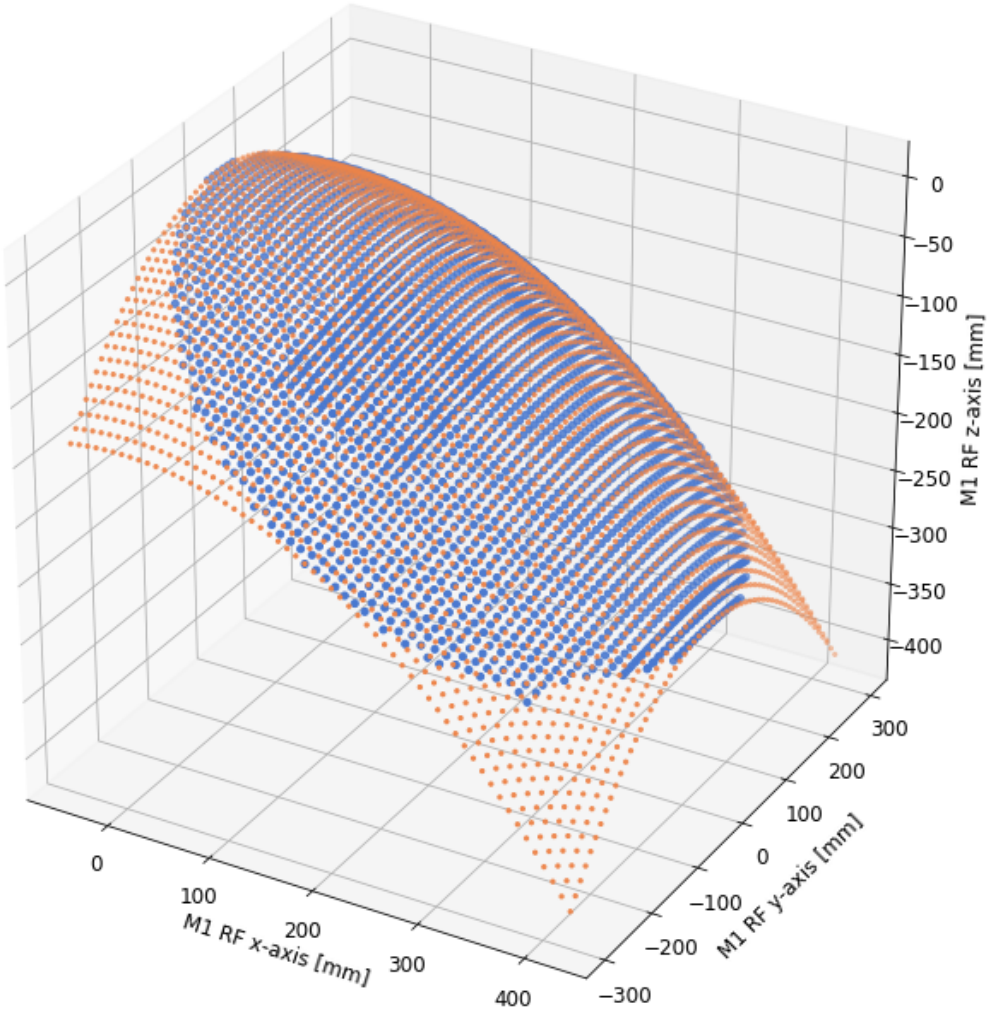

Figure 5.14: An example from the software used generate the sampling files. This plot shows a sampling rate of 3450 points (orange) to match the sampling rate of the measured points file (blue).

5.4 but new files are used to define the primary mirror surface. These new files have different sampling rates associated with them and are generated in python software. A grid of x, y points is generated to cover the area of the FI primary mirror (466×600 mm^2). The number of grid points in this area depends on the sampling being tested. The z values for these x, y points are calculated using the ideal mirror equation:

$$Ax^2 + By^2 + Cz^2 + Dxy + Exz + Fyz + Gx + Hy + Iz + J = 0. \tag{5.2}$$

Solving for z gives

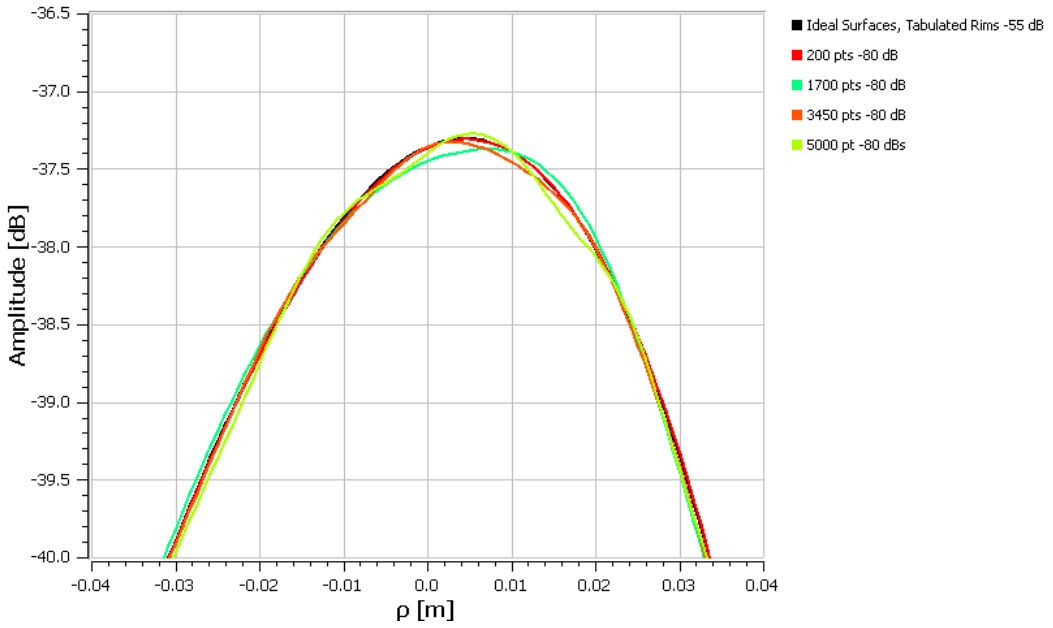

Figure 5.15: This plot shows the focal plane beam profile for different sampling rates applied to the primary mirror. The plot is zoomed in compared to previous plots to show the differences.

$$z = \frac{-(Ex + Fy + I) \pm \sqrt{(Ex + Fy + I)^2 - 4C(Ax^2 + By^2 + Dxy + Gx + Hy + J)}}{2C}. \tag{5.3}$$

An example is shown in Fig. 5.14.

The measured mirror file uses 3416 points to define the surface. Three other sampling rates are tested here to check if the 3416 points from the measured file are appropriate. The mirror equation for the primary mirror is used to generate files with 200, 1700, 3450, and 5000 points in total.

The results are shown in Fig. 5.15. This plot is zoomed in on the horizontal axis to make the differences visible. It is seen that sampling can only have an effect on the order of 0.1 dB. No significant ripples are observed. This rules out under or over-sampling as the cause of the ripples from Fig. 5.13.

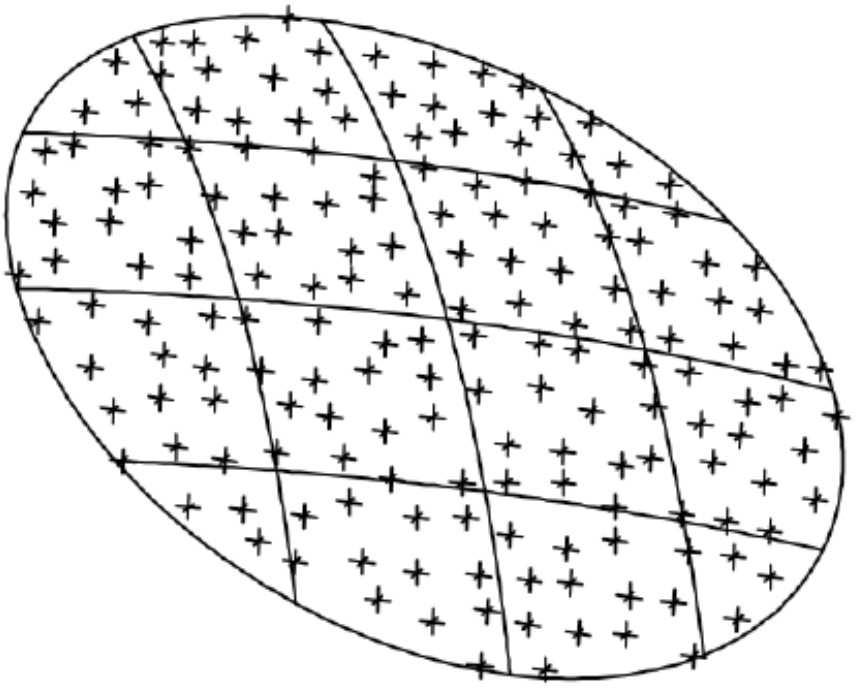

Figure 5.16: Plot reproduced from TICRA (2015) [86]. This figure shows an example of irregularly spaced points for use with the triangulation interpolation.

5.5.4 GRASP Interpolation Methods

GRASP offers two interpolation methods for tabulated surface points (an example from GRASP is shown in Fig. 5.16), pseudo-splines and triangulation. Pseudo-splines are recommended for regularly spaced points and triangulation is recommended for randomly spaced points, the differences for the primary measured mirror file is shown in Fig. 5.17. Both interpolations produce a rippling although they are different. This is relevant to the measured points file used here as the points are not completely regularly spaced as is evident in Figs. 5.9a and 5.14. In these figures there is a region in the centre of the mirror where there is a higher density of regularly spaced points. One might take the view that these measured points are simultaneously regularly spaced with an irregular point density. According to the GRASP documentation, this file could be appropriate for the triangulation interpolation if the points are viewed as irregular.

The difference between these two methods are shown in Fig. 5.17. The pattern when ideal surfaces are used is shown in black. The result for pseudo-spline method is shown in green and for triangulation in orange. This shows that the triangulation method performs significantly better than the pseudo-splines method for the

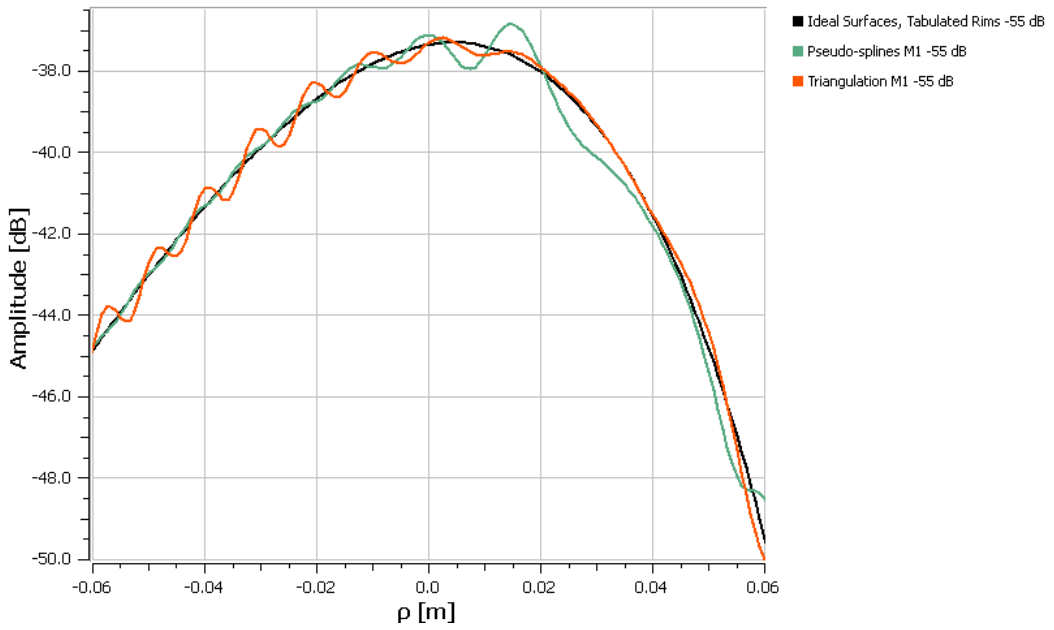

Figure 5.17: This plot shows focal plane beam profile for different interpolation methods applied to the primary mirror measured data. Triangulation interpolation also produces problematic results with the measured data.

measured points file. The amplitude of the ripples is reduced from 0.7 dB to 0.3 dB with the triangulation interpolation method, but this is still too large. This result does give insight to the source of the ripple.

5.5.5 Least Squares Surface Fitting

Since the interpolation of the measured points in GRASP appears to be the cause of the ripples, an alternative approach was tried. A least squares fit was used to get an equation of the form of Eq. 5.3 to fit to the measured data. The best-fit coefficients were then used to define the mirror in GRASP. Table 5.1 shows a comparison of mirror equation coefficients for the 300 K ideal mirror and the 300 K measured points. The fitted equation was also used to generate tabulated data as shown Fig. 5.14 (to test the effect of sampling point density). A grid of x and y points were generated with a density of points to equal the density of the x and y in the measured data. This ensures the sampling rate is the same for both surface models when the method is tested. Fig. 5.15 showed that this PO model is insensitive to sampling rate but it is still good practice to to have the fitted and measured data with equal sampling rates.

Parameters	300 K Ideal	300 K Measured
A	$-2.748\,66 \times 10^{-3}$	$-2.129\,47 \times 10^{3}$
B	$-2.748\,66 \times 10^{-3}$	$-2.147\,53 \times 10^{3}$
C	$-7.089\,29 \times 10^{-5}$	$-2.695\,07 \times 10^{1}$
D	$1.420\,60 \times 10^{-23}$	$1.587\,82$
E	$4.792\,50 \times 10^{-21}$	$4.797\,17 \times 10^{1}$
F	$1.016\,07 \times 10^{-22}$	$-2.300\,44$
G	$5.587\,17 \times 10^{-19}$	$-1.124\,50$
H	$1.709\,07 \times 10^{-20}$	$-5.867\,50 \times 10^{-1}$
I	$-1.834\,04 \times 10^{-3}$	$-1.436\,28 \times 10^{3}$
J	-1×10^{-6}	-1

Table 5.1: Equation coefficients for the primary mirror according to Eq. 5.2. The 300 K ideal mirror and 300 K measured data are shown. The form of the equation is such that very different sets of coefficients can result in a similar surface profile and fitting for coefficients can result in surprisingly large variations. When these surfaces are plotted, the variation of the surface with temperature is reasonable.

5.5.6 Equation Fitting Results

Files are generated in software with regular x, y spacing and their z points calculated for both equations (ideal and fitted). The measured sample spacing, provided by QUBIC collaborators[3], varied from 4 mm to 9 mm and the spacing for the regularly sampled data was 8.5 mm. This is compared to a wavelength of 2 mm. These surfaces are plotted in Fig. 5.18. These coordinate points are then used to define mirror surfaces in GRASP and tested with both pseudo-spline and triangulation interpolations.

The results from these surface definitions on the focal plane are shown in Fig. 5.19. The fitted equation points (orange and purple lines) produce a beam with a 0.2 dB deviation from the ideal equation defined surface. The points fitting the ideal equation (green and blue) produce a beam 0.05 dB from the equation defined surface. This shows that fitting points in software matches the equation definition within about 0.05 dB.

[3]The modelled data were shared by QUBIC collaborators Dr Antonio Zullo, Dr Marco De Petris, and Dr Michele De Leo.

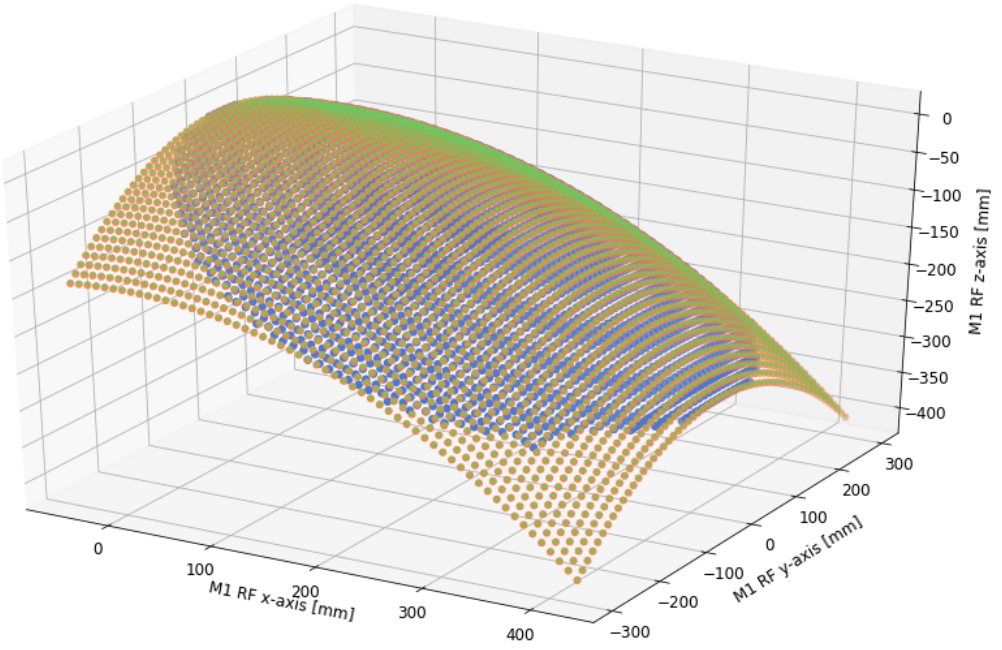

Figure 5.18: The blue points are from the measured data file with irregular spacing. Orange and green are the re-sampled regularly spaced surface points from the ideal and fitted mirrors respectively.

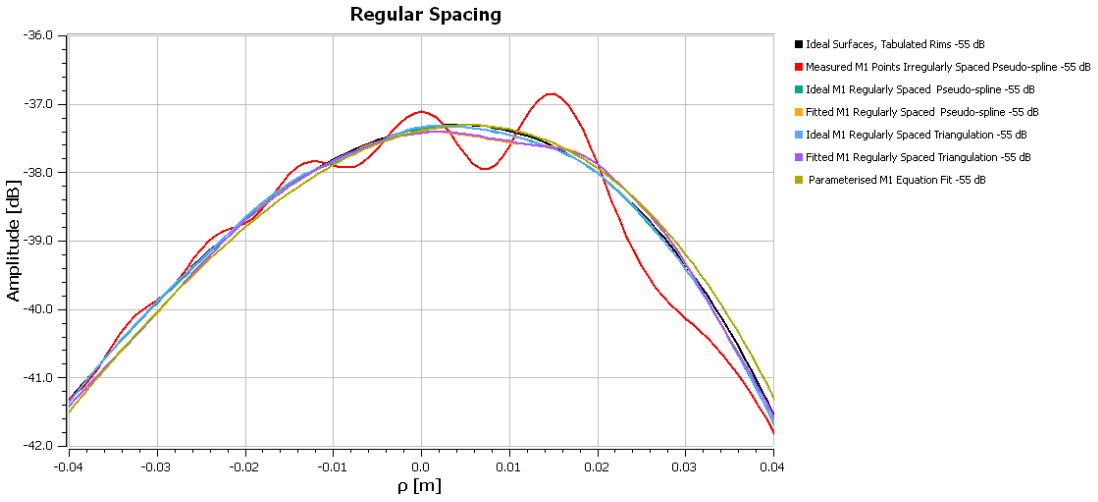

Figure 5.19: The ideal equation surface is shown in black and the measured points (pseudo-spline interpolation) surface in red as in Fig. 5.13. This plot is zoomed in order the show more clearly the effects of using z points generated from surface equations with regular spacing. The green and blue lines both show the ideal mirror equation with regularly spaced points using the pseudo-spline and triangulation interpolations and are in perfect agreement. The fitted surface points with regular spacing are shown by the orange and purple lines and are in perfect agreement for both interpolation methods. The fitted surface defined in GRASP using the equation parameters is shown by the yellow line.

Fig. 5.19 also tests the triangulation and pseudo-spline methods on these same points. The triangulation and pseudo-spline methods were found to agree in this case so there is no performance benefits by using triangulation interpolation with a regularly spaced grid. Pseudo-splines is a marginally better choice since there is a 2 - 10 second simulation time gain on a 6.5 minute simulation.

Fig. 5.19 also shows the fitted equation defined using the surface equation parameters as a yellow line. These data are in good agreement with the ideal mirror definition at the peak with only a small deviation either side of the peak and no observable ripples. This indicates that surfaces defined by the fitted equation parameters and points generated from the equation both improve on the irregularly sampled surface definition and remove the ripples from the beam produced by measured data.

The most interesting result from Fig. 5.19 is that the ripple feature is almost entirely removed. This shows that interpolating irregularly sampled data in GRASP was indeed the cause of the ripple. It is also prudent to test how accurately the equation describes the data.

Fig. 5.20 contains data evaluating the performance of the fitted equation that describes the measured x, y, z points at 300 K. Fig. 5.20a takes irregularly spaced x and y points from the measured data and uses the best-fit equation to generate fitted z values (red) as well as comparing the measured data to the ideal surface (green). The residual difference (red) between the fitted z values and the measured z values are plotted. The RMSE of these residuals is calculated and plotted in terms of wavelength by dashes for each set of residuals. An RMSE of $\lambda/16.02$ is found for the measured and fitted data. An RMSE of $\lambda/17.04$ is found for the measured and ideal surface. These are well within an acceptable range and shows that the equation and the resulting fitted z-points are a useful description of the measured surface. It also shows that the measured data are in good agreement with the ideal surface prediction and manufacturing defects are minimal.

Fig. 5.20b shows the positions of the residual difference points on the mirror surfaces of the ideal z values and the measured z values. The worst results occur for the corner cat-ear points. These can be considered outliers and not optically relevant to the modelling.

The effects of using measured mirror points has been investigated at 300 K as that was the temperature at which the measurements were made. These data, when

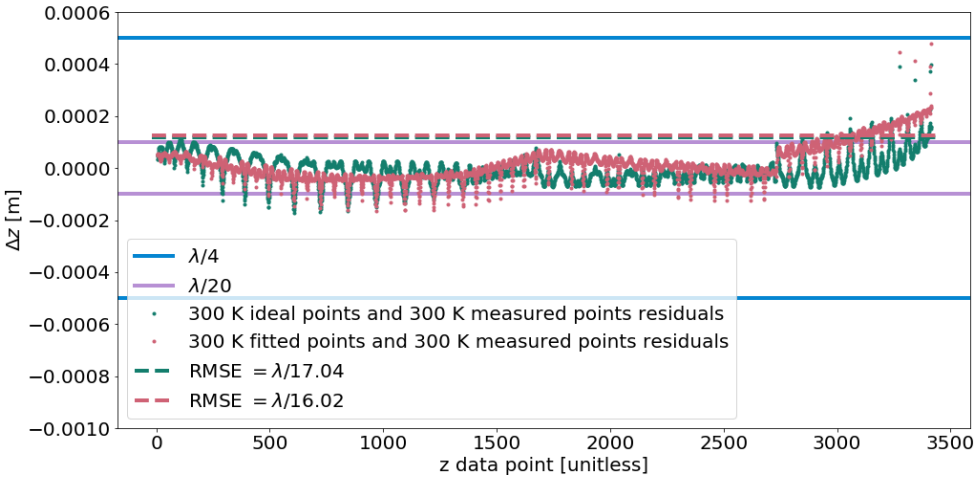

(a) For each x and y point in the 300 K measured data file, a z point is generated from the equation. The horizontal axis shows each of the 3,416 x and y coordinate points. The red data points on the vertical axis are the residual difference (Δz) between the z points from the measured data file and the z points generated from the fitted equation. The green data points show the residual difference between the measured data and the ideal model of the surface. The RMSE of the Δz is plotted as a dashed line. For reference the criteria for an optically 'good' mirror ($\frac{\lambda}{4}$, blue line) and a 'perfect' mirror ($\frac{\lambda}{20}$, pink line) are shown.

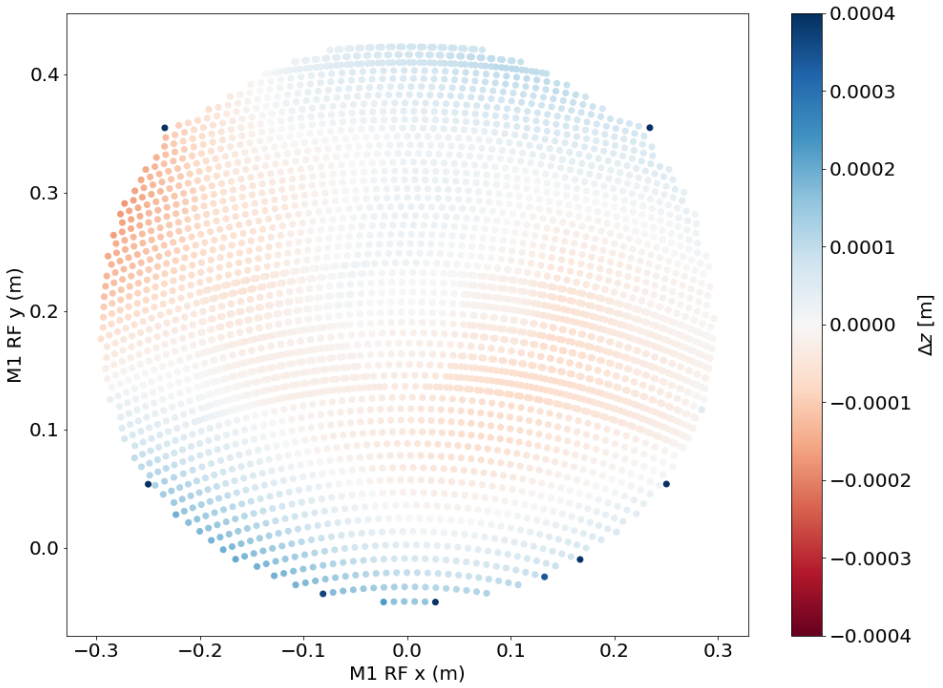

(b) The locations of the residuals (Δz, colourbar) on the mirror surface are shown for the measured data and ideal model of the surface at 300 K.

Figure 5.20: The data here evaluate the goodness of fit of the equation generated to describe the 300 K measured primary mirror.

Parameters	4 K Ideal	4 K Measured
A	$-2.772\,72 \times 10^{-3}$	$-5.907\,55 \times 10^{3}$
B	$-2.772\,72 \times 10^{-3}$	$-5.940\,99 \times 10^{3}$
C	$-7.151\,34 \times 10^{-5}$	$-1.326\,38 \times 10^{2}$
D	$1.433\,03 \times 10^{-23}$	$3.371\,88$
E	$4.834\,45 \times 10^{-21}$	$5.804\,00 \times 10^{1}$
F	$1.024\,96 \times 10^{-22}$	$-2.217\,44$
G	$5.611\,57 \times 10^{-19}$	$-8.385\,36$
H	$1.716\,53 \times 10^{-20}$	$-3.838\,82$
I	$-1.842\,05 \times 10^{-3}$	$-3.968\,65 \times 10^{3}$
J	-1×10^{-6}	-1

Table 5.2: Equation coefficients for the primary mirror according to Eq. 5.2. The 4 K ideal mirror and 4 K measured data are shown.

input to GRASP, returned a sampling error, which was corrected by describing the measured surface from a fitted equation. This resulted in corrected and now useful model of the measured mirror surface as an input for GRASP with pseudo-spline (or triangulation) interpolation. The conclusions will carry over to 4 K, the operating temperature of the optics at which the original design was made.

5.5.7 4 K Cooled Mirror Measurements

The ideal equation description of the mirrors (Table 5.1) used up to now were made for room temperature manufacturing at 300 K. The surfaces were then measured at 300 K. When QUBIC is cooled and taking measurements, the mirrors will be cooled to 4 K, the temperature at which the mirrors should have their designed shape. The mirrors will deform as they cool to this temperature. The measured points were modelled as being on the surface of an aluminium block and the block's deformation with temperature was modelled in CATIA[4] software by 3ds[5] by our Italian collaborators to give a set of "measured" data points at 4 K and a best-fit equation (Table 5.2).

[4]The modelled data were shared by QUBIC collaborators Dr Antonio Zullo, Dr Marco De Petris, and Dr Michele De Leo.

[5]www.3ds.com

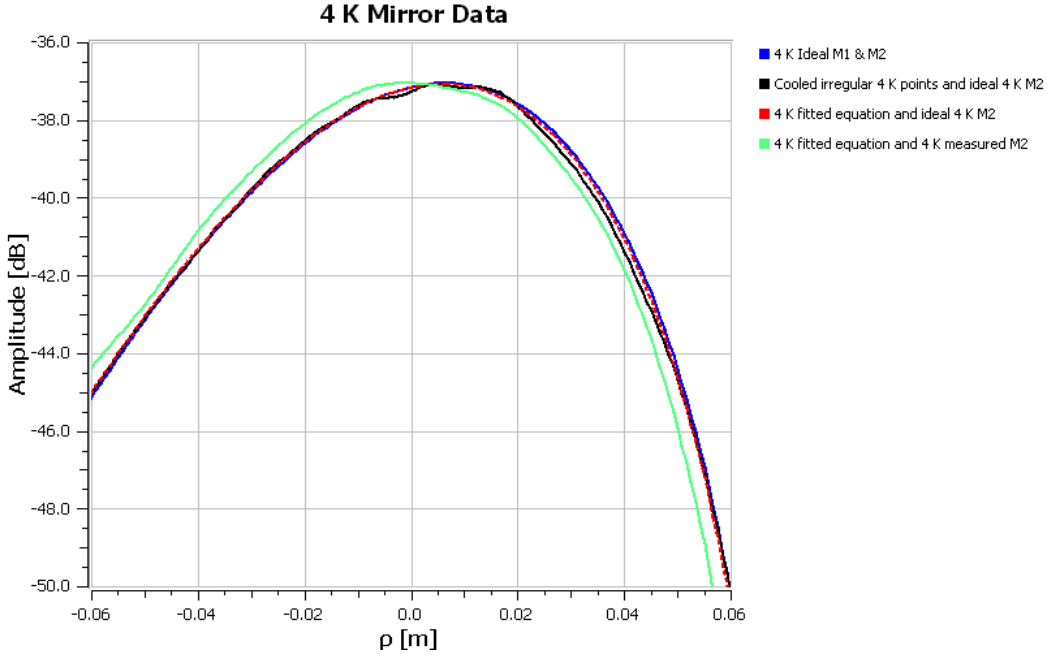

Figure 5.21: Focal plane cuts comparing the different surface models for the mirrors. The blue line shows the model with ideal mirrors. The black line shows the model with an ideal equation secondary mirror and the 4 K measured surface primary mirror with irregular spacing. These data show a variation due to the irregular sampling of x and y points. The equation of the 4 K primary mirror and with an ideal 4 K secondary mirror are shown by the red dashes. The equation of the 4 K primary mirror and 4 K measured points for the secondary mirror are shown by the green line and the peak is shifted to the left by 0.0069 m on the focal plane.

This software works by defining a volume (e.g. the aluminium block that the reflective surface is milled from and is mounted inside the cryostat) at a particular temperature. The software then cools or heats the volume and the volume's deformation as a function of temperature is measured and output. In this case, the surface was measured at 300 K and the software was used to model the surface deformation at 4 K with respect to the starting temperature of 300 K.

These data were also affected (although less severely) by the irregular sampling for the primary mirror as shown in Fig. 5.21 with the black dashes. The blue line shows the data generated using 4 K ideal equations for the primary and secondary mirrors. The rippling is apparent at the peak of the black line for the irregularly spaced measured and cooled data.

The red line in Fig. 5.21 keeps the ideal 4 K secondary mirror and changes the irregularly spaced 4 K points of the primary mirror to a fitted equation of those

points and defined as a parametrised surface equation. The rippling is effectively solved.

Since the measured 4 K data for the secondary mirror have regular spacing they can be directly defined as points using the pseudo-spline interpolation. These data are shown by the green line in Fig. 5.21 with the measured and parametrised model of the primary mirror. This causes the central peak to be shifted by 0.0069 m to the left. Otherwise the beam shape on the focal plane is the same.

Fig. 5.21 summarises the key findings about the modelling so far. The figure shows how the model evolves from an idealised one (blue) to a more representative model of the instrument as it truly exists. When the measured data (measured points cooled to 4 K) for M1 are added (black), the sampling issue is apparent. Using the method validated previously, changing the M1 surface to a fitted equation definition (red), the sampling issue is resolved. When the measured points for M2 are added (green) the peak is shifted in the negative x direction. This shift is not due to sampling but is explained by a phase slope in the measured data, which is discussed and characterised below.

The accuracy of the equation fit to the measured points is shown in Fig. 5.22. This figure shows these residuals as green dots. The RMSE of these z point residuals is taken as before. The RMSE of the residuals is $\frac{\lambda}{132}$ which far exceeds what is considered optically perfect ($\frac{\lambda}{20}$). This shows that the equation fit to the 4 K measured mirrors is a suitable model of the measured points and that this equation is suitable for use in GRASP.

In order to further understand the reason for the 0.0069 m shift in the peak location when the 4 K measured mirrors are considered, additional data analysis is required but it is not considered an issue for QUBIC. It has been shown already that the equation of the measured data is an excellent model of the measured x, y, z points producing an RMSE less than $\frac{\lambda}{132}$.

Fig. 5.23 examines the relationship between the cooled 4 K measured data and the ideal 4 K surface using the regularly spaced x, y points from the measured data file for the primary mirror with orange dots in Fig. 5.23a. Here the measured data are close to being considered optically 'good' ($\frac{\lambda}{4}$) with an RMSE of $\frac{\lambda}{3.02}$. This metric normally refers to diffraction limited visible optic imaging systems. QUBIC is a millimetre wave instrument and does not rely on sharp imaging resolution. As such, it is not a large concern for the RMSE to be out of specification with what is

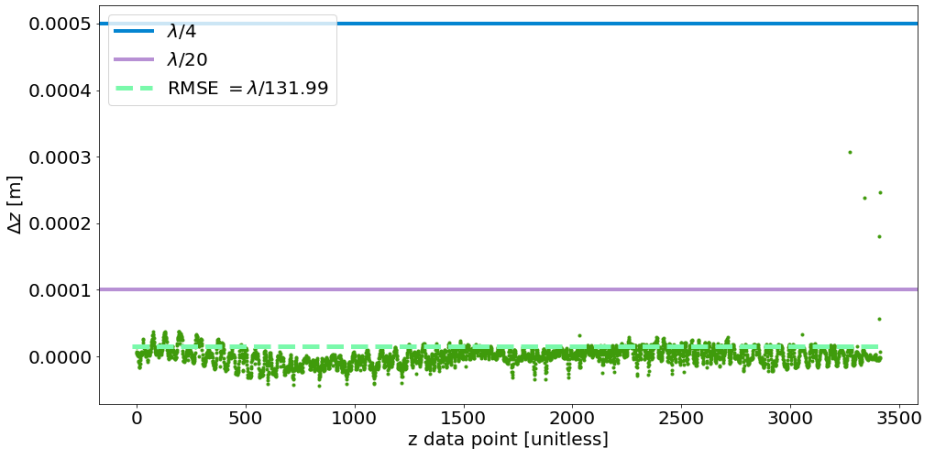

Figure 5.22: For each x and y point in the 4 K measured data file, a z point is generated from the equation. The horizontal axis shows each of the 3,416 x and y coordinate points. The data points on the vertical axis are the residual difference (Δz) between the z points from the measured data file and the z points generated from the equation. The RMSE of the Δz is plotted as a dashed line. For reference, the criteria for an optically 'good' mirror ($\frac{\lambda}{4}$, blue line) and a 'perfect' mirror ($\frac{\lambda}{20}$, pink line) are shown.

normally considered optically good. The best metric for QUBIC, is to analyse the PSF's and check their spectral performance as will be shown later in this chapter and by a proxy method in Chapter 6. Fig. 5.23b shows the distribution of these points on the mirror surface. These data indicate the residuals, or deviation from ideal, are higher in the upper left region of the plot. These data also show that the measured points cooled and deformed to 4 K by the CATIA software is very close to the ideal model of the primary mirror at 4 K and that the manufactured and measured mirror is generally in good agreement with the ideal surface.

Fig. 5.24 shows the same data for the secondary mirror. The difference between the measured points to the ideal equation is evaluated at the same x and y points is shown in Fig. 5.24a by blue dots. The RMSE is has an average of $\frac{\lambda}{0.24}$, which is a significant result. This deviates from what is considered optically 'good' but this is not a roughness but a systematic deviation. When evaluated on the mirror surface, as shown in Fig. 5.24b, there is a gradient of residuals from the lower right towards the upper left. This residual behaviour is unlike that seen in Fig. 5.20b. This gradient in residuals could be the cause of the shift in the beam seen in Fig. 5.21.

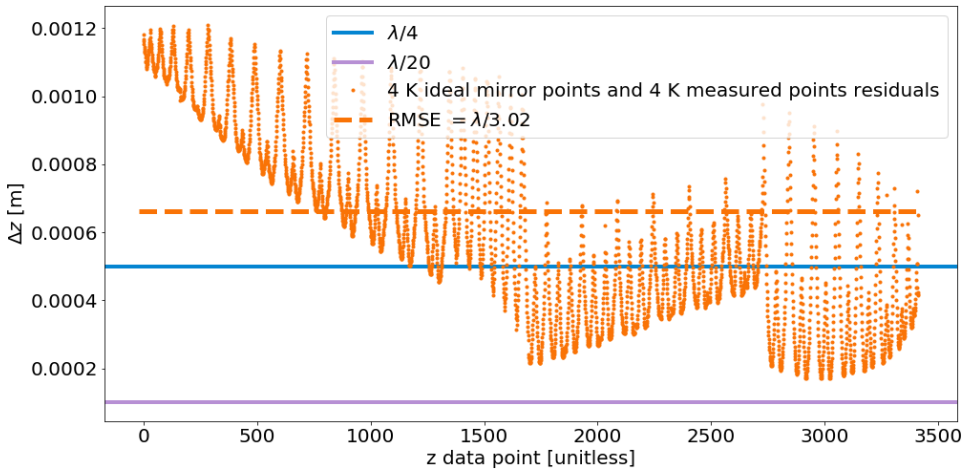

(a) For each x and y point in the 4 K measured data file, a z point is generated from the 4 K ideal equation. The horizontal axis shows each of the 3,416 x and y coordinate points. The data points on the vertical axis are the residual difference (Δz) between the ideal equation z points evaluated at the x and y positions of the measured file and the 4 K measured z points. The RMSE of the Δz is plotted as a dashed line. For reference the criteria for an optically 'good' mirror ($\frac{\lambda}{4}$, blue line) and a 'perfect' mirror ($\frac{\lambda}{20}$, pink line) are shown.

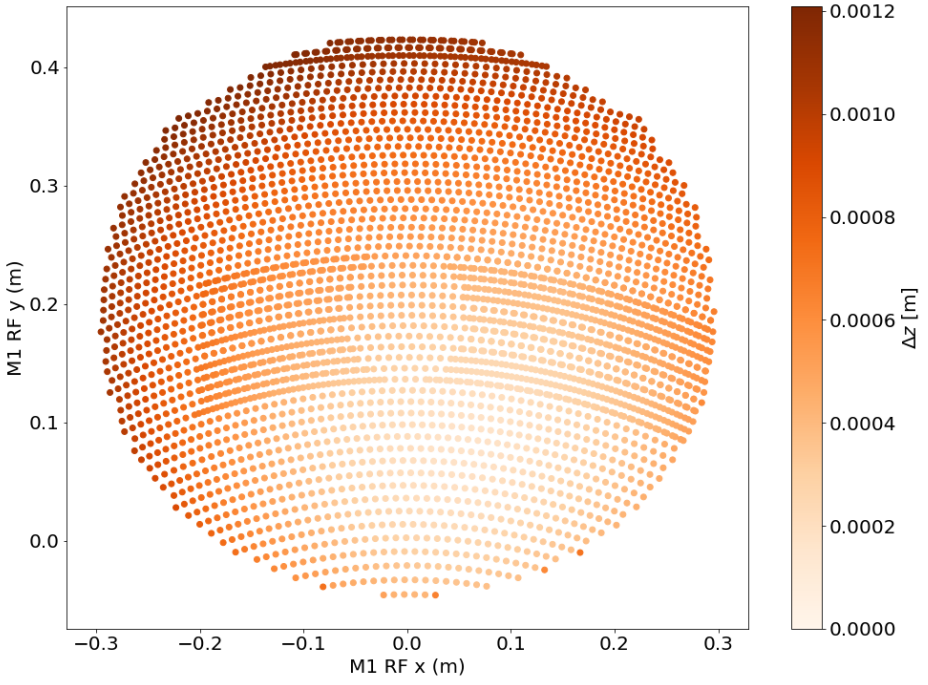

(b) The locations of the residuals (Δz, colourbar) on the mirror surface are shown.

Figure 5.23: These data compare how the 4 K measured primary mirror compares to the ideal equation at 4 K. Of course, they are not expected be an exact match but this is a useful comparison to show in what way the measured and cooled mirrors deviate in shape from a perfect model.

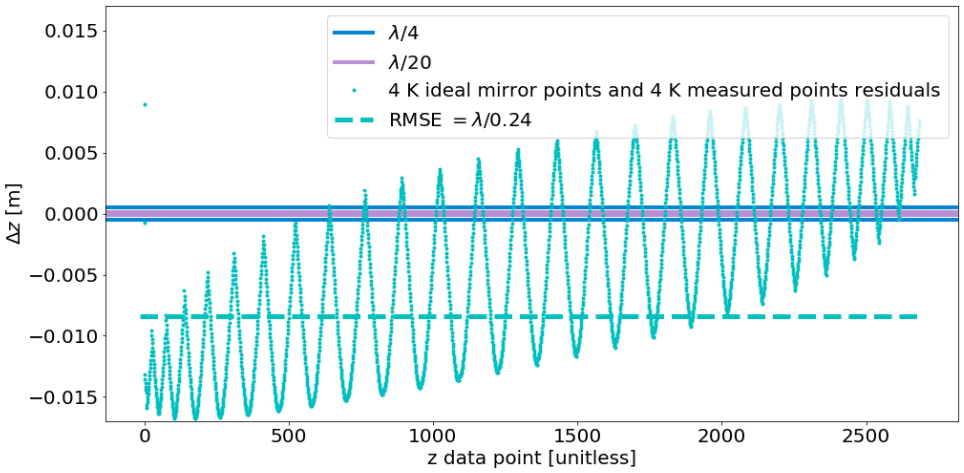

(a) For each x and y point in the 4 K measured data file, a z point is generated from the equation. The horizontal axis shows each of the 3,416 x and y coordinate points. The data points on the vertical axis are the residual difference (Δz) between the ideal equation z points evaluated at the x and y positions of the measured file and the 4 K measured z points. The RMSE of the Δz is plotted as a dashed line. For reference the criteria for an optically 'good' mirror ($\frac{\lambda}{4}$, blue line) and a 'perfect' mirror ($\frac{\lambda}{20}$, pink line) are shown.

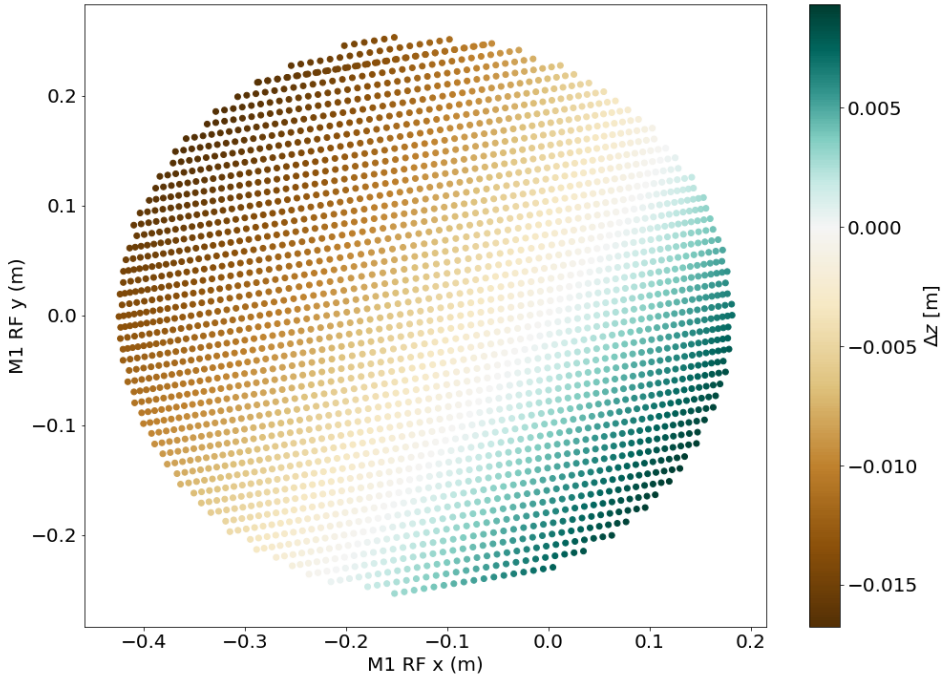

(b) The locations of the residuals (Δz, colourbar) on the mirror surface are shown. Here, a gradient of residuals is evident from the lower right to the upper left.

Figure 5.24: These data compare how the 4 K measured secondary mirror compares to the ideal equation at 4 K. Of course, they are not expected be an exact match but this is a useful comparison to show in what way the measured and cooled mirrors deviate in shape from a perfect model.

5.5.8 Surface Modelling Summary

This section has investigated the most accurate way to model the QUBIC mirror surfaces. Surface measurement data give the best representation of the real surface but incorporating those in the GRASP model requires work.

Generally, GRASP was easily capable of implementing the measured data for the secondary mirror. An unphysical ripple arose when using the measured data for the primary mirror and a number of methods and solutions were found to deal with and solve this. The cause of the effect was determined to be due to the GRASP interpolation of the irregularly sampled x and y points in the measured data for the primary mirror. Instead of reading the data directly into GRASP it was found that using a least squares fit to find the best quadratic surface description of the points, and then using this equation in GRASP, gave the best results.

Data in Fig. 5.20 showed the 300 K measured data were in excellent agreement with the ideal predictions of the mirror surface at 300 K. In contrast, Figs. 5.23a and 5.24a showed the cooled 4 K data were in poorer agreement with 4 K ideal predictions of the measured surface. This likely explains why, in Fig. 5.21, adding the measured secondary mirror to the model shifts the peak to the left. Even though the agreement of the data does not appear ideal, it is still the most up-to date prediction of the mirror surfaces as manufactured. Further efforts investigating the cooling model of these measured data might be insightful. The model is set up using this current and up-to date data and can be easily modified in the future to input newer models of the mirror surfaces if required.

5.6 Realistic Model of the Horn

5.6.1 Aperture Field

The MODAL model of the horn was developed by Burke (2021) [90]. MODAL uses the horn geometry and electro-magnetic mode-matching to produce an aperture field at the exit of QUBIC's back-to-back horns when the entrance of the horn is illuminated by a far-field point source at 150 GHz. Further details and dimensions of QUBIC's horns are given in Section 2.3.3.5 and Fig. 2.13. A model of the horn in MODAL software is shown in Fig. 5.25.

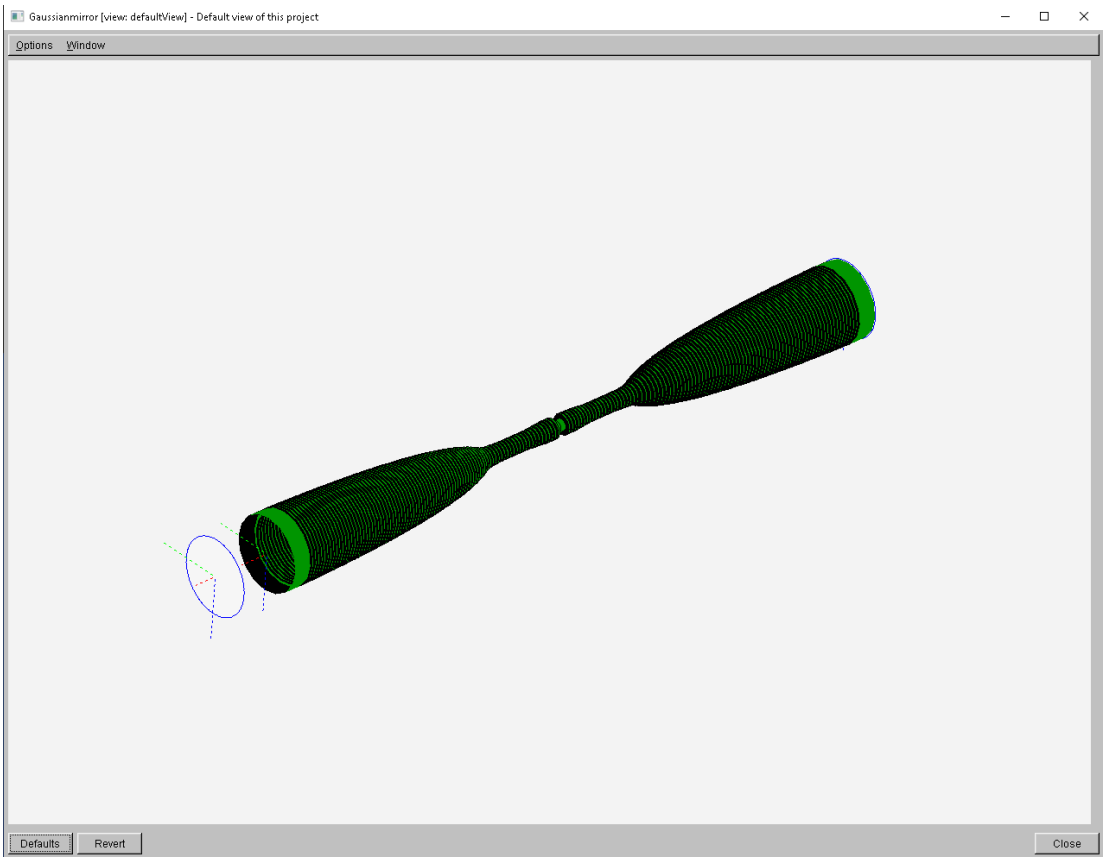

Figure 5.25: QUBIC's corrugated back-to-back horn shown in the MODAL GUI. The aperture field model generated by this horn geometry in MODAL is used as a tabulated source input in GRASP to model the accurate horn beam.

This model was modified to produce aperture fields at 130, 140, 160, and 170 GHz. This gives a broadband range of frequencies centred at 150 GHz to simulate the range of frequencies in QUBIC's lower band. 0°, 45°, and 90° cuts of these aperture fields are shown in Fig. 5.26. Since these data are shown at the horn exit aperture they are considered near-fields.

The data in Fig. 5.26 are in line with expectations and suitable to be implemented in the GRASP model as a tabulated source (Section 3.4.1.2). This is the most accurate method of modelling QUBIC's horn beam (Section 2.3.3.5) in GRASP. The fields are defined at and propagated from the exit aperture of QUBIC's back-to-back horns. As the beam propagates through the optical combiner, the near-field pattern eventually develops into the far-field pattern. If evaluated prior to the primary mirror, the pattern resembles the beam profiles shown in Fig. 2.14.

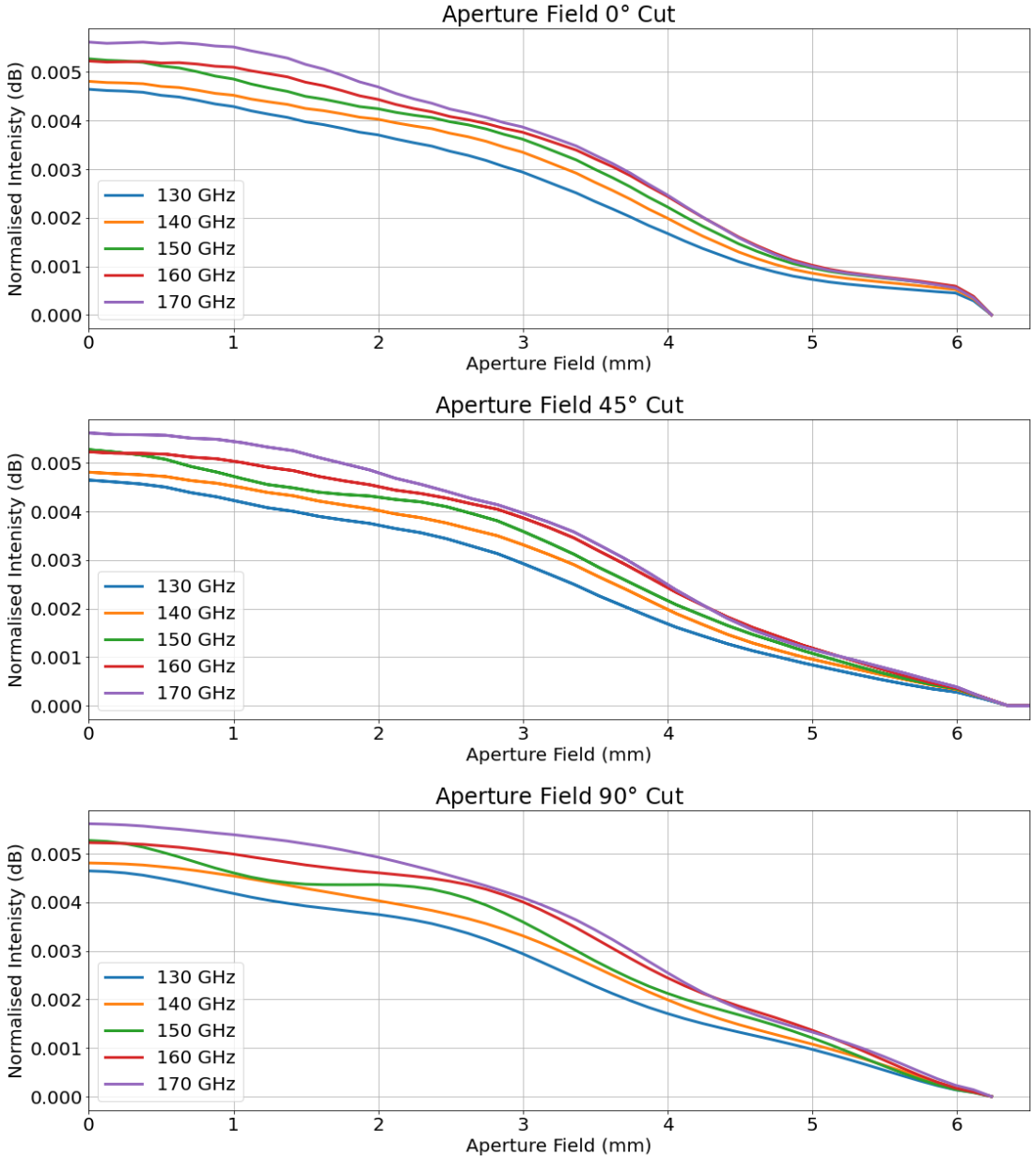

Figure 5.26: Cuts of the horn aperture fields from 130 - 170 GHz. Each colour describes a frequency. The x-axis shows the off-axis distance on the aperture.

5.6.2 Far-Field Spherical Cuts

The aperture fields produced in MODAL are input into GRASP at the horn aperture exit locations for the full array of 400 horns. GRASP can then propagate the accurate aperture fields of the QUBIC horn through the optical combiner. This is done for each horn at each frequency. It is useful to first compare these beams at different frequencies using a spherical cut in the far-field. This method shows how the near-field aperture fields of Fig. 5.26 converge in the far-field in GRASP.

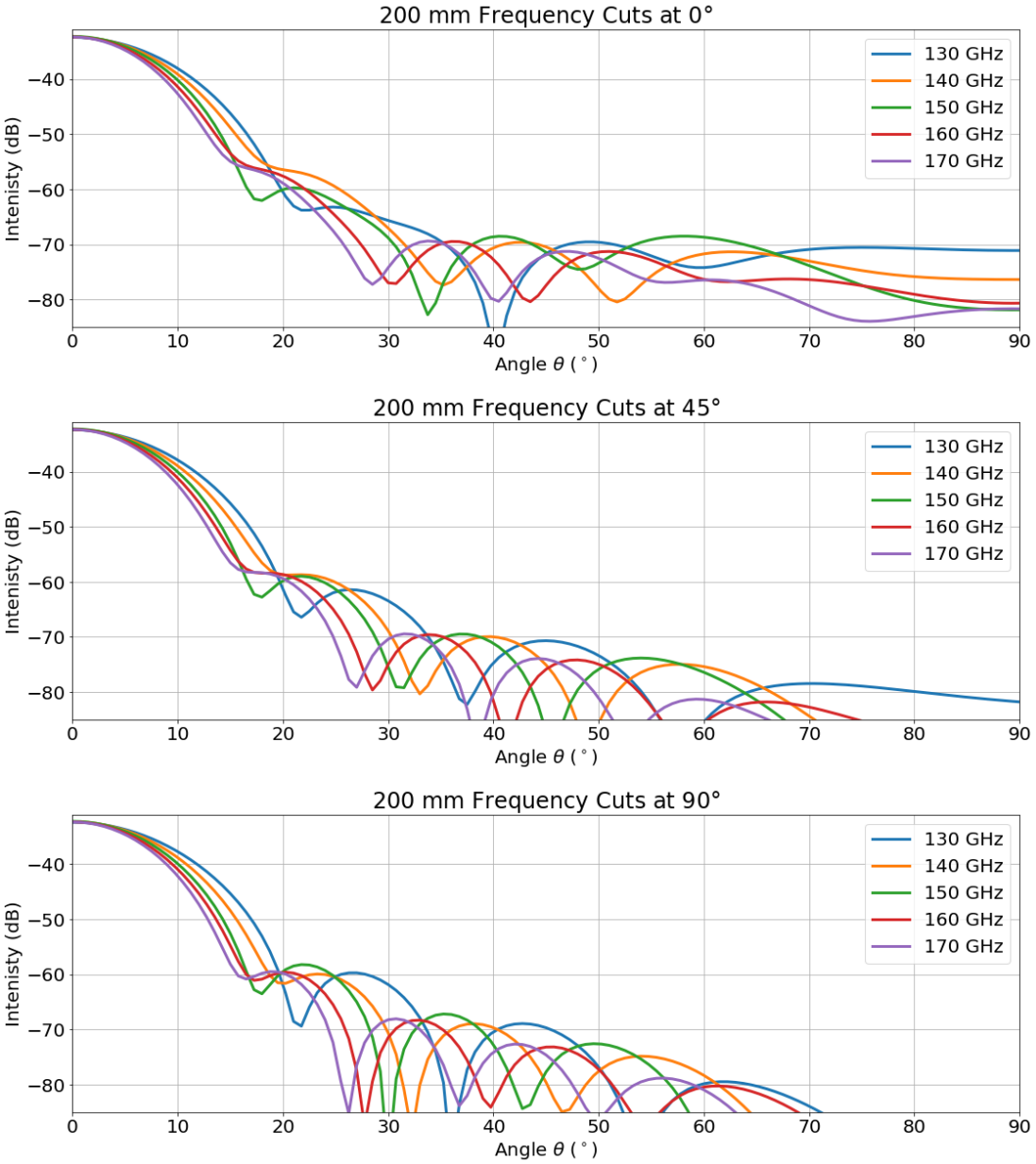

Figure 5.27: Far-field spherical cut (0°, 45°, and 90°) of the horn beam models for 130 - 170 GHz. Each colour refers to a different frequency. The y-axis shows the intensity of the beams in dB. The far-field spherical cut is analysed on-axis and a distance directly after the horn from which the tabulated aperture was defined. This far-field cut is visualised as the largest and furthest cut from the source in Fig. 5.5a.

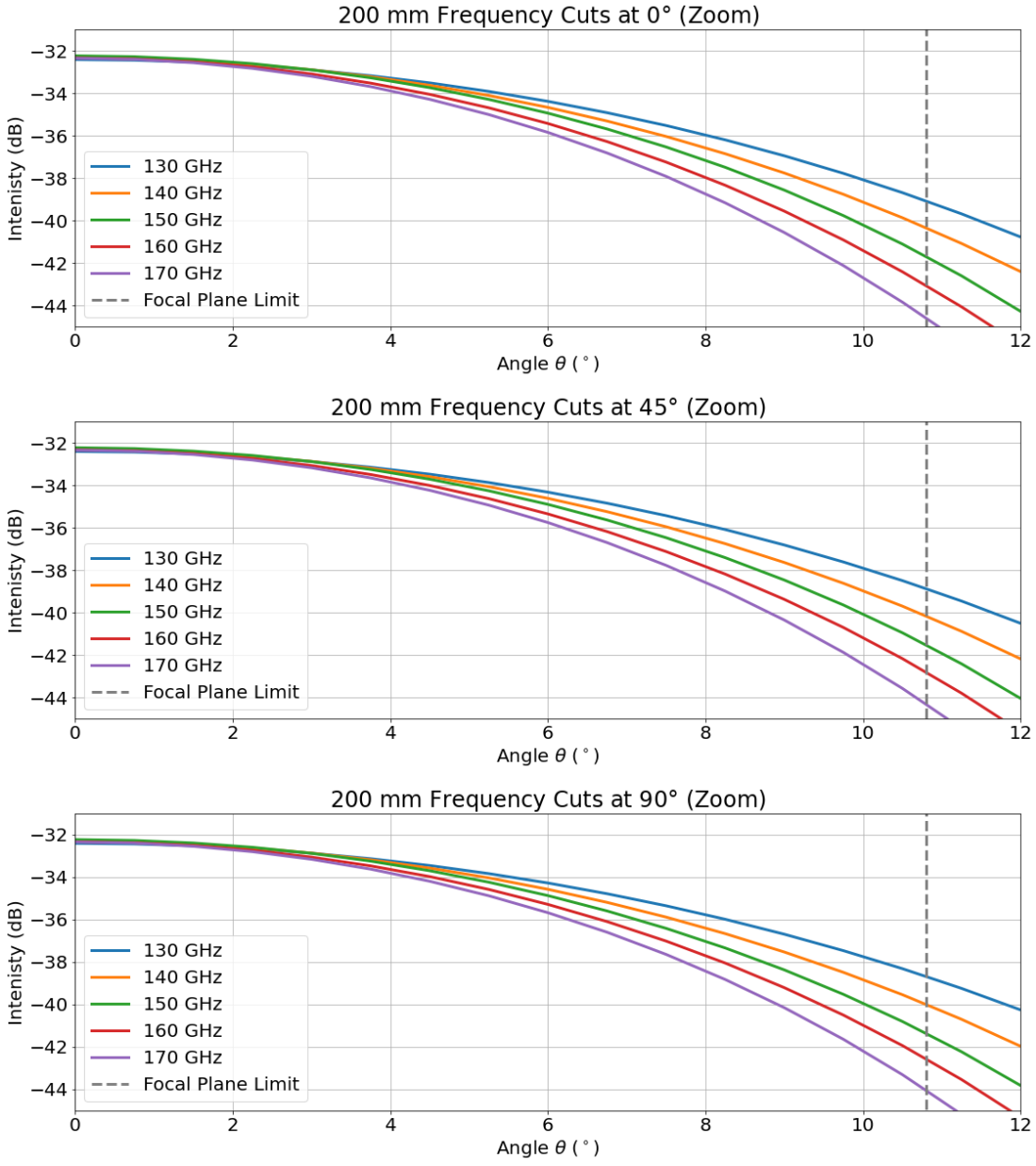

Figure 5.28: A zoomed-in spherical cut (0°, 45°, and 90°) of the far-field horn beam models for 130 - 170 GHz. Each colour refers to a different frequency. The y-axis shows the intensity of the beams in dB. The grey dashes show the region of the beam incident on the focal plane.

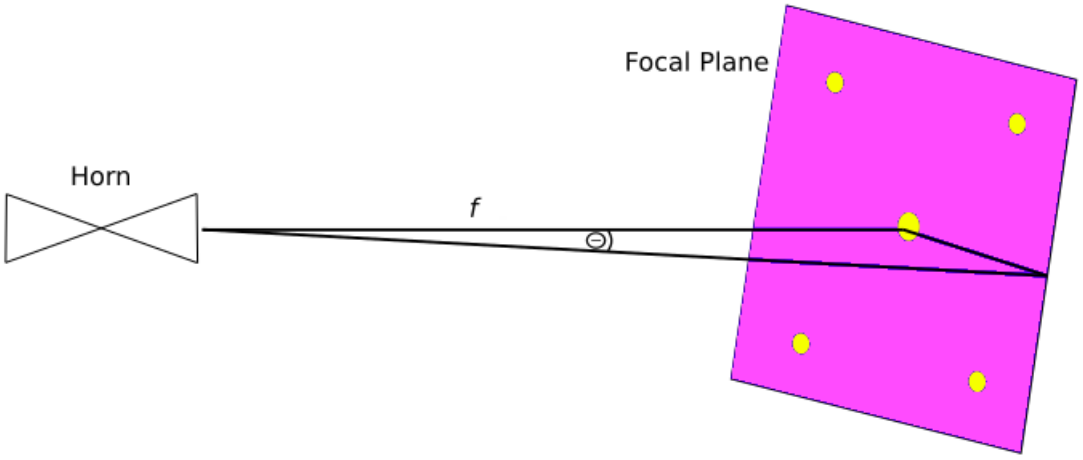

Figure 5.29: This figure shows that only a finite part of the horns beams are incident on the focal plane regardless of the FHWM of the actual beam (12.9°). An on-axis example is shown where the focal length of the combiner is 300 mm and the size of the focal plane is 57.16 × 57.16 mm. Therefore only $< 10.8°$ of the beams are incident on the focal plane.

200 mm was found to be sufficiently in the far-field as was described in Section 5.3.2 and Fig. 5.6.

The 200 mm far-field beams as a function of frequency are shown in Fig. 5.27 with each colour referring a different frequency between 130 and 170 GHz. The lower frequencies produce broader beams compared to higher frequencies. The 150 GHz beam produces the highest peak power by a fraction of a dB. This is clearer in Fig. 5.28 which is a zoomed version of Fig. 5.27. The cuts at 0°, 45°, and 90° are nearly identical for each frequency as expected. The angular size of the focal plane that can be illuminated by a horn is given by Eq. 5.4.

$$\theta = \tan^{-1} \frac{r}{f} \tag{5.4}$$

where f is the focal length of the combiner ($f = 300\,\text{mm}$) and the radius of the focal plane is r ($r = 57.16\,\text{mm}$). The angle θ is the region of the beams from the horns that reach the focal plane (Fig. 5.29). From this calculation, the central 10.8° of the horn beams are found to be incident on the focal plane. The $< 10.8°$ portion of the beams will illuminate the focal plane while the region outside this angle will not be detected. The grey dashed line in Fig. 5.28 is highlighted since it shows the region of the beams that are incident on the focal plane.

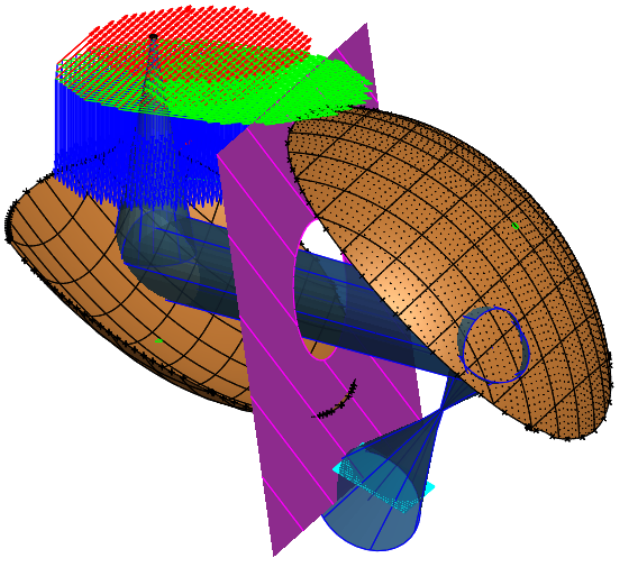

Figure 5.30: An example of the configuration used for the 400 horn simulation from GRASP's GUI. Each of the coordinate axes represents the location of a horn. Only one of the 400 horn beams are shown. The realistic tabulated rims and tabulated secondary surface (4 K) are shown. The primary mirror is an equation described using a fit to the measured data at 4 K. The cold-stop is present.

5.7 Full Instrument Point Spread Function at 150 GHz

5.7.1 Final Model Configuration

Section 5.2 has determined how to best implement the most realistic optical elements in GRASP. This informs the configuration of the model used for the simulation of the full array of 400 horns.

As discussed earlier in this chapter, mirror rim points were taken directly from their CAD model. The primary mirror (M1) surface was described using the best-fit quadratic equation to measured points (4 K). The measured points (and GRASP's pseudo-spine interpolation) were used for the secondary mirror (M2).

The focal plane, cold-stop, and horn array geometry were defined according to the technical engineering documentation. The source was the tabulated aperture field of QUBIC's horn, described in Section 5.6.1 at each location in the horn array.

A graphical representation of this is shown in Fig. 5.30. A beam from each horn location was propagated to the focal plane resulting in 400 files with one focal plane field distribution. The proper method for combining the data on the focal plane is described in the next section as this cannot be done in GRASP.

5.7.2 400 Horn PSF on the Focal Plane

For a given frequency there are 400 files generated by batch processing that need to be added coherently. GRASP files have a header with information about the simulation, then each line of data has the real and imaginary component of the field at a point on the focal plane.

The first line corresponds to the focal plane position with the lowest x and y value in focal plane reference frame. Then the next line corresponds to the point with the same y value and the next highest x value and so on until the x values run from -0.06 to 0.06 m (geometry of the focal plane). Then the y value is incremented and the pattern repeats.

Customised software[6] is used to process, analyse, and plot GRASP output files. The software first converts real and imaginary components of the GRASP data to magnitude and phase and creates an intermediary file that matches the format of MODAL data. The GRASP data are processed like this so that GRASP and MODAL data can easily be processed and analysed by the same software and analysis tools. Magnitudes ($|X|$ and $|Y|$) and phases (Φ_x and Φ_y) are calculated from the real ($\Re_x$ and $\Re_y$) and imaginary ($\Im_x$ and $\Im_y$) components for each data point in the planar grid file as follows:

$$\begin{aligned} |X| &= \sqrt{\Re_x^2 + \Im_x^2} \\ \Phi_x &= \arctan \frac{\Im_x}{\Re_x} \\ |Y| &= \sqrt{\Re_y^2 + \Im_y^2} \\ \Phi_y &= \arctan \frac{\Im_y}{\Re_y}. \end{aligned} \tag{5.5}$$

With this calculated, the data are then formatted to match the MODAL data format and stored in an intermediary '.qb' file for each horn. When fields at

[6] github.com/seamusomurchu/multifrequency

the same frequency are added, their real and imaginary components are summed separately before calculating an over all intensity.

The intensity is calculated from the magnitude and phase for co and cross-polar (x, y direction) data with $I = E^2$:

$$\begin{aligned} I_x &= (|X| \cos \Phi_x)^2 + (|X| \sin \Phi_x)^2 \\ I_y &= (|Y| \cos \Phi_y)^2 + (|Y| \sin \Phi_y)^2. \end{aligned} \tag{5.6}$$

And the I_x and I_y intensity components can simply be added:

$$I = I_x + I_y. \tag{5.7}$$

A final generalised '.pkl' file for each horn is then output. It contains all the information about the simulation such as frequency, horn number, filename, field magnitude, phase, real, imaginary components, and intensity. The processing function also takes the focal plane intensity data and integrates it into the detector geometry (shown later in Section 5.8.3 and used throughout this thesis). The same software can make plots for a given horn input.

The advantage of having individual files for each horn means that a particular horn configuration can later be selected and plotted. For example, with 64 TD horns or 400 FI horns, PSFs can be formed when computed and plotted as described above.

5.7.3 Point Spread Function at 4 K

The combined PSF data from the batch mode simulation for QUBIC's array of 400 horns is shown in Fig. 5.31. Fig. 5.31a shows the focal plane data in arbitrary intensity units for a model of QUBIC with realistic elements such as mirror surfaces, and rims, and the cold-stop which are features not previously modelled. The secondary peaks are more easily seen when a logarithmic scale is applied to the intensity data as shown in Fig. 5.31b. Here, the central peak and subsidiary peaks are evident. The scale is normalised intensity as the power of these simulations is arbitrary. In GRASP each horn source produces 4π watts and should be normalised appropriately. In calibration and scientific acquisitions the power will be

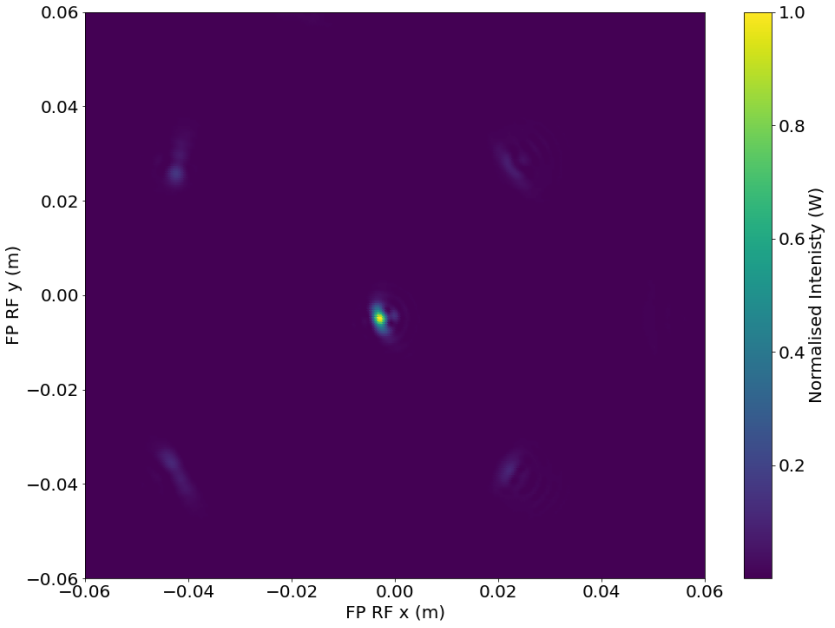

(a) The PSF with the normalised intensity plotted on the colour scale.

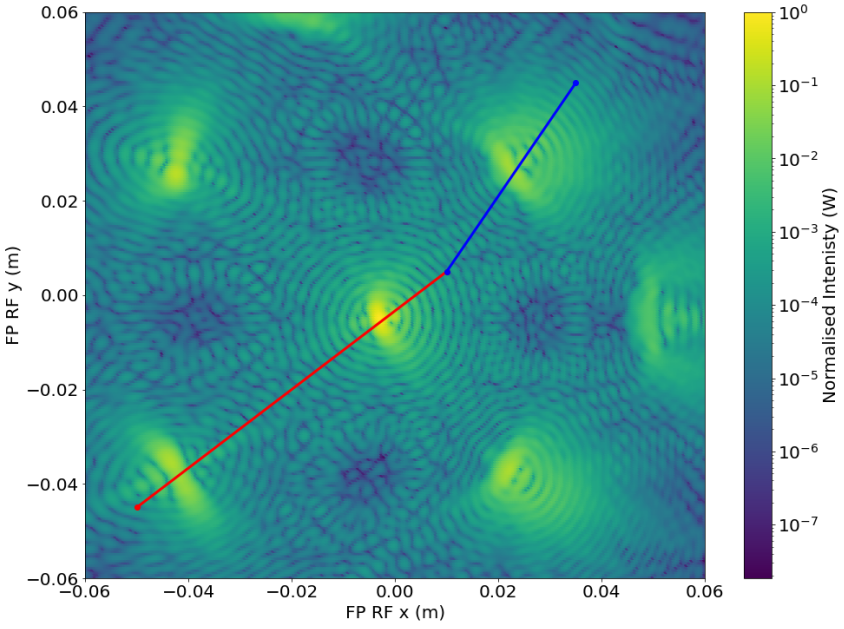

(b) The PSF with the logarithmic and normalised intensity plotted on the colour scale. This figure also shows the PSF analysis cut used. It is made of two lines, red and blue, to account for aberrations so that the full cut passes through two subsidiary peaks and the central main peak. The data from this aberrated cut is compared to the symmetric and un-aberrated on-axis ideal cut in Fig. 5.32.

Figure 5.31: Two forms of the point spread function for 400 horns combined on the focal plane. The data were generated in GRASP using realistic optical elements. Data are shown for 150 GHz.

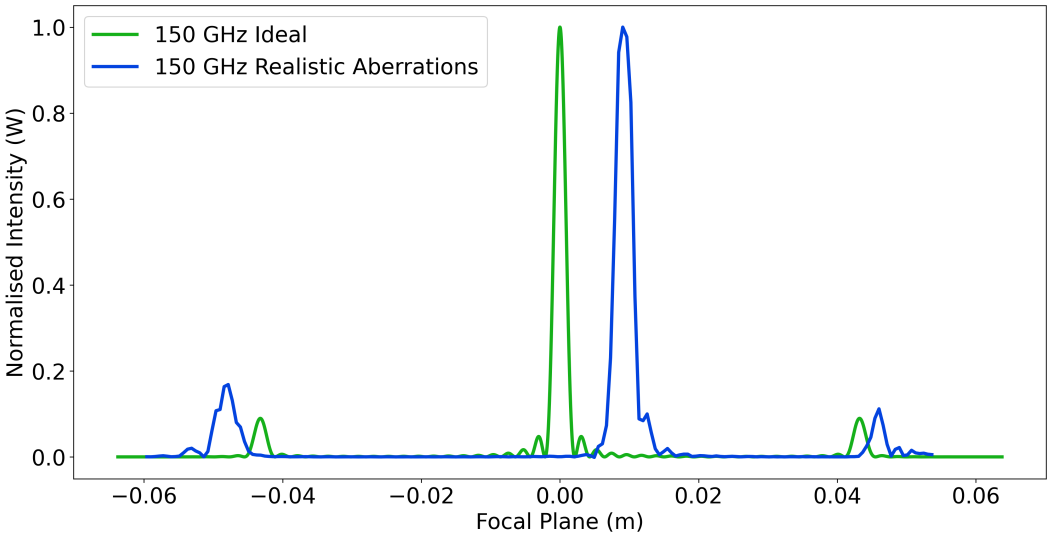

Figure 5.32: These data compare the PSFs (combination of 400 horns on the focal plane) for an idealised model (on-axis components with no aberrations or truncation) and for the most realistic model using the measured surfaces and rims transformed to 4 K as described in Fig. 5.31b.

dependent on the input signal power or sky signal. Note the lack of symmetry due to QUBIC's off-axis optical design. Other effects of off-axis optics are the subject of Chapter 8 of this thesis. In particular, Section 8.3 shows a clear comparison of an ideal and the real off-axis focal plane models. These data show that, when QUBIC is modelled by PO, off-axis aberrations modify the shape of the PSF but the side lobes are still sufficiently strong. This is an especially important aspect in terms of spectro-imaging as the side lobe peak positions should be measured as a function of frequency.

5.7.4 Point Spread Function at 4 K: Comparison to Ideal Mirrors

Fig. 5.21 has shown the effects of realistic optical elements on the focal plane for a single horn. These effects can be shown for the 400 horn PSF as well. They are analysed along a cut of the PSF as shown in Fig. 5.31b (to account for off-axis aberrations) in order to study the relative positions of the main and subsidiary peaks.

The cut is compared with the simplest model of all, assuming on-axis ideal components with no truncation or aberrations in Fig. 5.32. Fig. 5.32 shows the difference in FWHM and peak heights for the main and subsidiary peaks for the ideal and

realistic models. The FWHMs broaden when the realistic 4 K mirrors are considered. The data also shows how the realistic and aberrated optical envelope (see O'Sullivan et al., (2021) [71] and Burke (2021) [90]) modifies the peak positions and relative intensities. The importance of the modelling work described in this chapter is clear.

5.8 PSF Frequency Extension: 130 - 170 GHz

The realistic optical modelling of the QUBIC FI and generation of the PSF has been shown at 150 GHz. This is a useful result on its own but extending the model to a range of frequencies produces the data required for the calibration of the instrument. This is especially so with regards instrument calibration when spectro-imaging is tested on the instrument in the near future. The MODAL aperture field model at 150 GHz is modified to produce 130, 140, 160, and 170 GHz aperture field data.

5.8.1 Focal Plane Data

Batch mode simulations are made for each horn at each frequency. The fields are calculated on a focal plane grid. The PSF is first made for each frequency by adding the fields from each horn as described. This is done for the range of frequencies from 130 - 170 GHz in 10 GHz steps. The individual frequencies are then combined by adding their intensities incoherently.

The focal plane grid data are shown in Fig. 5.33 for each frequency. These data show the secondary peaks closer to the centre at 130 GHz and the peaks move towards the edge of the grid as the frequency increases to 170 GHz. This is the behaviour expected with QUBIC's optical configuration as detailed by O'Sullivan et al., (2020) [71].

The theoretical prediction of the optical combiner's frequency response is shown in Fig. 5.34 for an ideal combiner. In this configuration, QUBIC has on-axis optics and lenses instead of mirrors (while the model for Fig. 5.33 uses the accurate off-axis optics which induces aberrations). There are no aberrations in these theoretical predictions of the PSF spectral behaviour but it is useful to explain

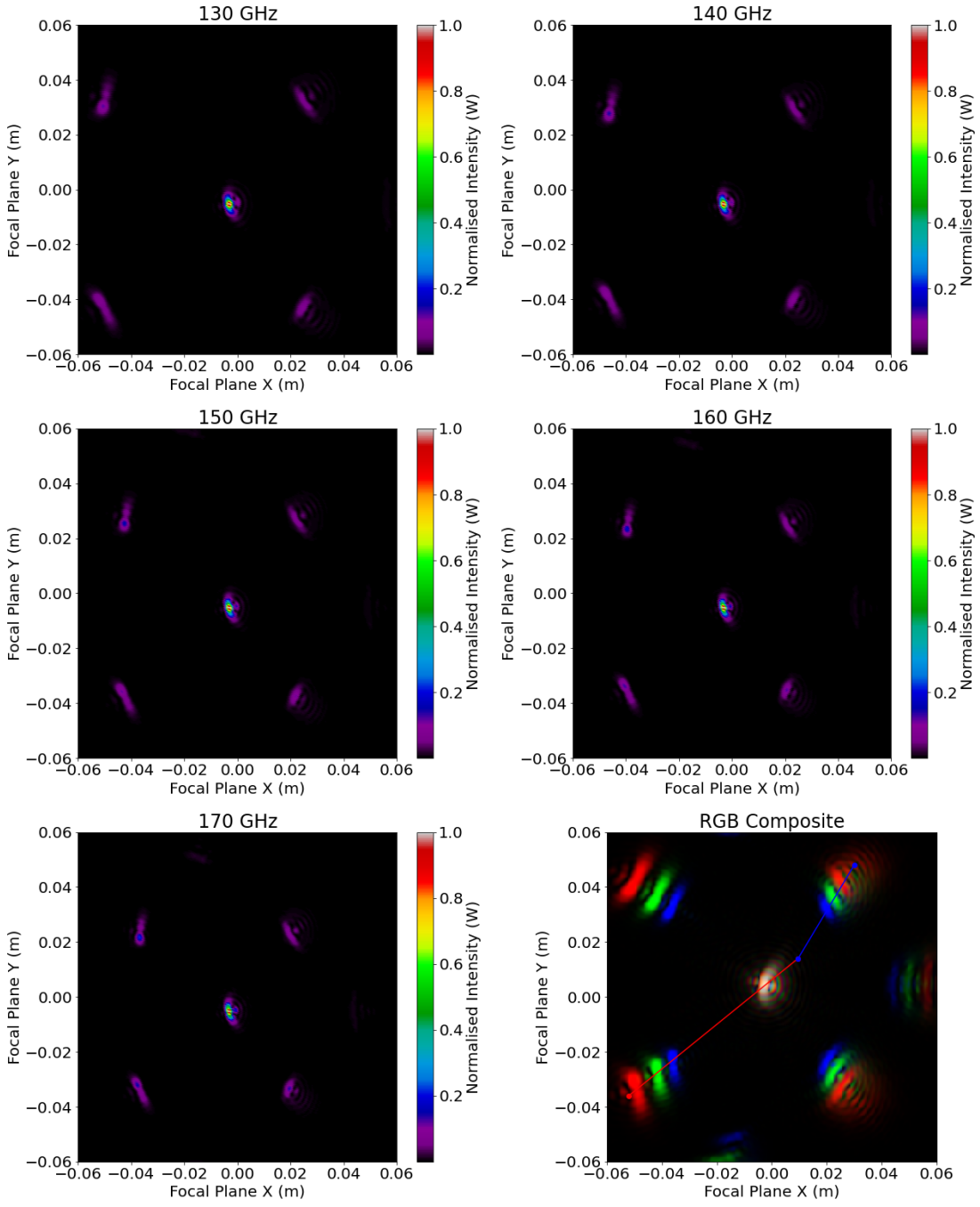

Figure 5.33: Each frequency on the focal plane where the z-axis is an normalised intensity in Watts. The lower right image is an RGB composite of 130, 150, and 170 GHz data. This image also shows a cut comprised of a red and blue line (to account for aberrations) that the data will follow in subsequent figures.

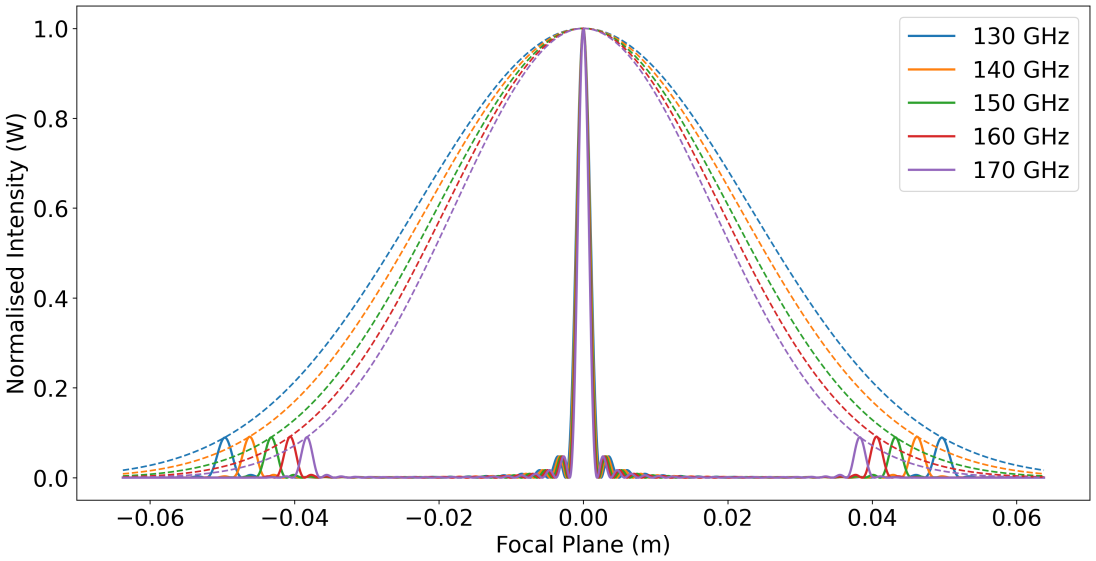

Figure 5.34: Frequency response of QUBIC in an ideal on-axis optical configuration. Here, no aberrations are observed. The lower frequencies have their secondary peaks closer to the center and higher frequencies are closer to the edge of the focal plane. The dashed lines show the PSF envelope for a given frequency.

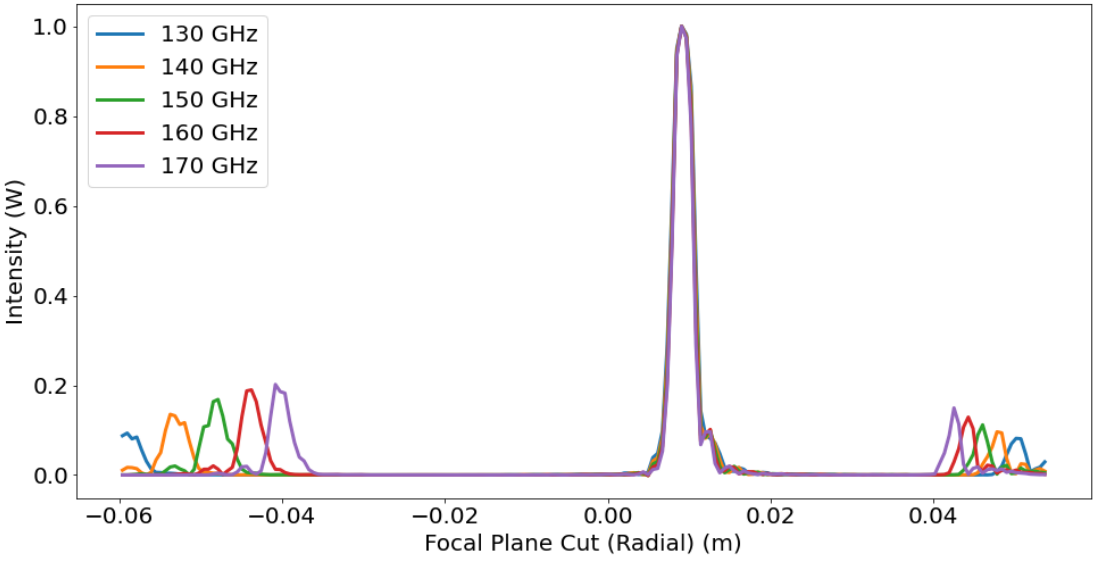

Figure 5.35: Cuts of the focal plane data that show differences with frequency more clearly. The same cut as in the lower right of Fig. 5.33 is used to account for optical aberrations.

the main features seen in the real PSF. (This simple model was also shown at 150 GHz in Fig. 5.32.)

The lower right of Fig. 5.33 shows an RGB composite image made from the 130 (R), 150 (G), and 170 (B) GHz data. This figure shows the side lobes moving and changing shape with frequency. This is an instructive and useful way to visualise QUBIC's spectro-imaging capability on the focal plane.

5.8.2 Frequency Cuts on the Focal Plane

The data from Fig. 5.33 are shown as cuts in Fig. 5.35 along the lines shown in the lower right of Fig. 5.33. The effect of the off-axis optics is clearly visible as the central peak is offset from the centre and the secondary peaks are not symmetrically located around the central peak.

The central peak of each frequency are aligned (and offset from the centre of the focal plane due to optical aberrations). The secondary peaks' positions change with frequency on the focal plane. This is the same behaviour described in the ideal combiner case (shown in Fig. 5.34).

The data of Fig. 5.34 and 5.35 show that the aberrated PO model of QUBIC has strong side lobe strength as a function of frequency. This shows that QUBIC will be able to perform spectro-imaging as detailed by Mousset et al., (2020) [56]. The key difference is that previous studies of spectro-imaging used ideal on-axis models of the PSF (and synthesized beam). The next stage of these studies and the final implementation of spectro-imaging should include optics with off-axis aberrations like those shown here.

It is also natural to consider using this data to validate and check instrument performance in the laboratory. But this is challenging because the SNR for the detectors was low at the time resulting in too few detectors being able to sample the PSF on the focal plane. The other aspect is that QUBIC has a relatively low number of detectors resulting in low imaging resolution. This would make accurate measurements of the peaks difficult. It is better for QUBIC to measure the synthesised beam maps as a calibration method and this is the focus of Chapter 6.

5.8.3 Focal Plane Frequency Patterns Integrated Over Bolometer Area

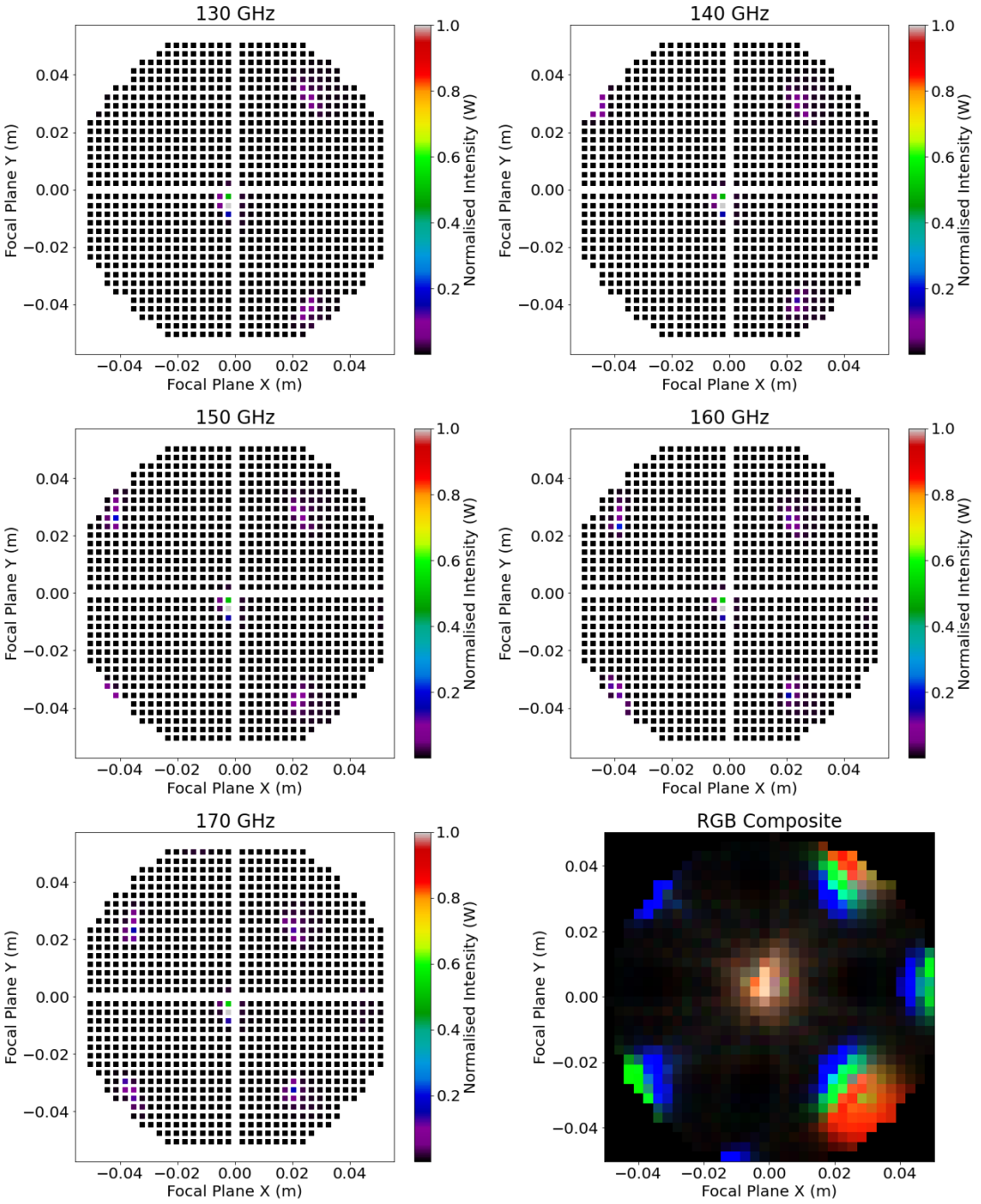

Figure 5.36: Each frequency on the focal plane integrated into the bolometer area where the z-axis is an arbitrary intensity in Watts. The lower right image is an RGB composite of 130, 150, and 170 GHz data.

Fig. 5.36 shows the data from Fig. 5.33 integrated over the bolometers' physical geometry. Each of the 992 bolometers has an area of 6.76 mm^2 and they are separated by a gap of 2 mm. It is naturally useful to use the focal plane data

generated by these simulations to find the point spread function as it would be measured with the real detector geometry and layout.

This was done for each frequency as shown in Fig. 5.36. The lower right of Fig. 5.36 shows an RGB composite from the 130, 150, and 170 GHz data. The same physical behaviour is observed as for the full focal plane area but in this form, the data are shown with a realistic resolution. The data in this form are useful for instrument calibration and spectro-imaging.

5.9 Conclusion

This chapter has shown the development of the most accurate optical model of QUBICs FI, accounting for diffraction effects due to the cold-stop and rims, imperfections in the mirror surface from manufacturing, and cooling deformations to 4 K. The model also uses the most accurate description of the back-to-back horn beam and simulates this beam for each horn in the horn array. The simulations are extended to the single-moded instrument bandpass and integrated into the detector geometry. Data have been produced that are essential to future data-analysis, calibration, spectro-imaging, and systematics minimisation.

In this chapter the model configuration is defined by its particular mirror rim and surface definition. Direct rim data were not available so a number of methods to generate rim data were implemented and tested. The results show that QUBIC is not sensitive to diffraction from the edges of the rim and all tested rims produced essentially identical data on the focal plane.

GRASP's tabulated surface feature was used to test the measured mirror points at 300 K. Later, the temperature deformations (300 K to 4 K) of this mirror surface were modelled and made available. The data could directly be read into GRASP for the secondary mirror and showed only a small effect on the focal plane when compared with the ideal description. The data for the primary mirror was problematic because of the interpolation in GRASP and produced a ripple effect on the focal plane beam. The source of the issue was an unusual sampling of x, y points in the measured data. Once the cause was determined, a solution was found by finding an equation to describe the measured points of the primary mirror and using this in GRASP.

In order to propagate an accurate horn beam in the model, a tabulated aperture field was defined in GRASP. The data for the tabulated aperture field were generated by MODAL. MODAL can simulate the fields in corrugated horns where GRASP, without add-ons, is limited in that regard. These MODAL aperture field data were generated from 130 - 170 GHz.

The 150 GHz field was used first to run a batch mode simulation of all of QUBIC's 400 horn beams propagating through the optical combiner. The method of generating the PSF from custom software was described. These batch mode simulations were then extended from 130 - 170 GHz for each horn. The focal plane data were then integrated over the detector array geometry. The modelling and analysis of the mirror surfaces have shown that the PSF is aberrated and has slightly broader FWHMs for the real primary and secondary mirrors compared to what would be predicted of an ideal on-axis model.

The modelling has included realistic compoents such as measured mirror surfaces and the CS. The spectral PSFs represent the most accurate representation of the QUBIC instrument performance and modelling them has required the unique features of both GRASP and MODAL. Since there is no predefined performance metric for these PSF's (other than having clearly resolved subsidiary peaks), these PSF's instead inform and prescribe QUBIC's future data analysis developments. This means that these data will be necessary to feed into spectro-imaging and systematics minimisation methods during calibration and data analysis.

Chapter 6

Map Production

6.1 Introduction

Synthesized images-on-the-sky maps are a useful probe to analyse QUBIC's measurement data from the calibration campaign in APC. They will also be important for future data analysis and spectro-imaging with real scientific data. These synthesized maps can be made for each detector by scanning a calibration source in azimuth and elevation (Fig. 6.1). This chapter is concerned with the optimisation of the data reduction (demodulation) software to improve the SNR ratio of these maps. This done for a range of frequencies to validate QUBIC's spectral performance.

Some initial maps had been produced prior to the work described here but they were not compared to optical simulations or used to quantitatively validate the instrument. The older maps, made earlier in QUBIC's calibration campaign, showed electronic cross-talk and optical 'ghosting' (this is documented and resolved in Chapter 7 of this thesis). The datasets used in this chapter had a higher SNR due to instrument and operational improvements (for example the cooling was increased which improved the detector performance). As QUBIC's capability improved with every acquisition campaign (QUBIC must be warmed in order to make hardware improvements and cooled again, this takes a number of days), the quality of the data also improved. During the summer of 2020, the quality of the calibration data improved to the point that crucial measurements of the detector maps could be made at a range of frequencies.

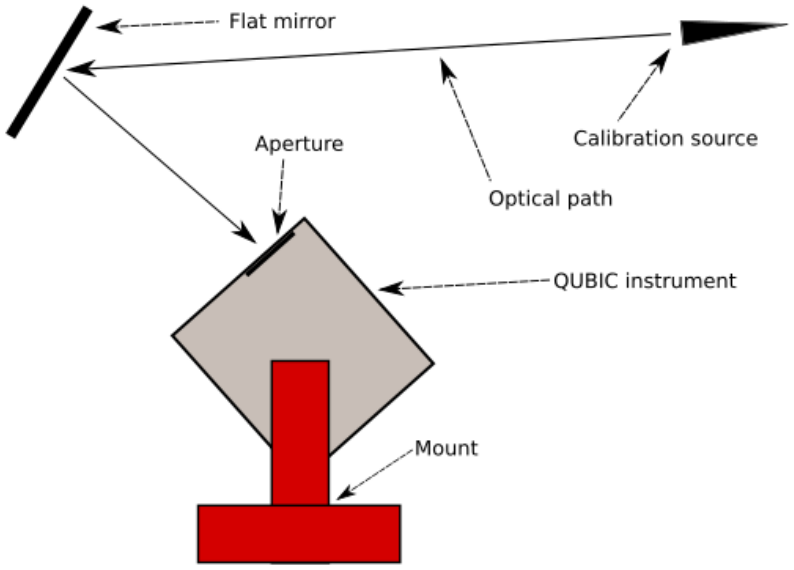

Figure 6.1: The laboratory scan configuration. The calibration source is mounted on a wall. Its signal is reflected off a flat mirror (mounted on an adjustable scaffold rig) and into QUBIC's aperture. The QUBIC mount moves in azimuth and elevation and the source signal is modulated. This is an enlarged version of Fig. 2.19a.

Measurements such as the synthetic map peak FWHM, peak position, and peak separation, all as a function of frequency, are crucial to validate the QUBIC instrument and its key spectro-imaging feature. Spectro-imaging is required for QUBIC to separate galactic foregrounds and dust from the polarised CMB signal, this aspect is described by Mousset et al., (2020) [56]. As such, it was important to prove that QUBIC is capable of spectro-imaging and to develop software to be used in the future with scientific sky data.

This chapter will describe improvements made to QUBIC's software and data processing functionality in order to improve the signal-to-noise ratio of the demodulated map data. It will also show how these maps were made (at several frequencies) and compared them to both idealised theoretical predictions of the synthetic image and simulations from optical models. Finally, these data will show that the QUBIC instrument has spectral performance in line with predictions from optical simulations.

6.2 Data Acquisition for Calibration

6.2.1 Source Set-Up

The calibration source is a 10 GHz Gunn oscillator followed by two frequency chain multipliers that produces a frequency-tunable 130 - 170 GHz source. It is manufactured by Virginia Diodes[1] and is used to excite a scalar feed-horn. The source is controlled by a Raspberry Pi[2] that operates a signal generator (it configures amplitude, frequency, offset, shape, and duty cycle) and sends the resulting signal to the Gunn oscillator. The calibration source signal is typically a modulated 1 Hz sine wave with 0.5 V offset and 0.5 V amplitude (as was the case for these acquisitions). The output of the calibration source is recorded at a rate of approximately 300 samples per second. The Raspberry Pi also monitors and records the power output from the Gunn oscillator using an output port on the feedhorn waveguide. The system is controlled by Python code with a GUI interface called QubicStudio. More details about this calibration source hardware and software are given by Torchinsky et al., (2020) [53].

The calibrator horn[3] is an ultra-Gaussian (99.88% power in the fundamental Gaussian mode) corrugated horn developed by Thomas Keating Ltd. The exact geometry of the horn was not available but D. Burke (2021) [90] showed close agreement between the beam profile provided by the manufacturer and a 10° FWHM Gaussian beam. The manufacturer quotes $w = 0.5a$ (w is beam radius, a is aperture radius) for these horns, independent of frequency. The horn is setup to reflect off an aluminium flat mirror so that the beam is incident on QUBIC's aperture. This arrangement is shown in Fig. 6.1. The total path length is 11.43 m, the maximum distance that can be accommodated in the laboratory. A sufficient distance from the horn to the aperture is necessary so the calibration source beam is flat over the extent of the aperture. This setup was simulated using PO by Burke (2021) [90]. It was determined that 11.43 m is a large enough distance to ensure the calibration source is in the far-field of the QUBIC aperture. This requirement ensures that each horn in the horn array is illuminated with equal power by the calibration source.

[1] vadiodes.com

[2] raspberrypi.org

[3] These horns are a modified version of the one found here - http://www.terahertz.co.uk/tk-instruments/products/corrugatedhorns/ultra.

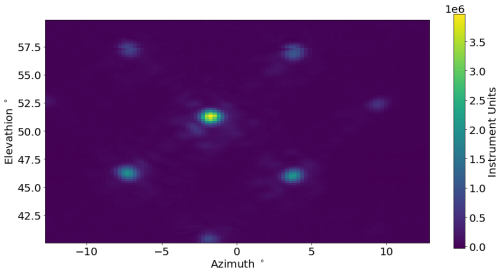

(a) An example of a map made for TES 76. The characteristic synthesized-image pattern is reproduced. The beam intensity, in demodulated instrument units, is plotted as a function of the instrument's azimuth and elevation and the source was centred at 50°.

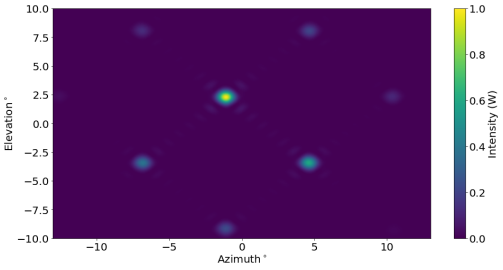

(b) A synthesized image from an optical model by Burke (2021) [90] for TES 76. The normalised intensity is plotted.

Figure 6.2: synthesized-image maps for a single TES detector. They show the image-on-the-sky for a single detector. These figures show real data from the instrument and an optical model. The real instrument data were measured with the source at an elevation of 50° while the simulation was centred at 0°.

6.2.2 Azimuth-Elevation Scans

While the source is illuminating the horn array and the detectors are operating, the mount sweeps the QUBIC instrument in azimuth and elevation to make a scan of the source. The mount and instrument are illustrated in Fig. 6.1. Fig. 6.1 also shows the optical path from the source to the QUBIC TD aperture. From there, beams from the re-emitting back-to-back horns in the combiner propagate through the optics onto the focal plane. Scans are made at 130, 150, and 170 GHz so that the spectral behaviour of the maps can be measured.

An image of the source (i.e. a map of the angles on the sky to which QUBIC is sensitive) can be created for each TES bolometer but the signal must be filtered and demodulated for this map to be made. Fig. 6.2 shows examples of synthesized image maps. They are similar to the focal plane PSF but the peak locations are less affected by aberrations. In a scan, the mount moves the instrument in azimuth before increasing the elevation one step. This is repeated until the scan is complete. Typical parameters for a scan of this type include azimuth angles from $-20°$ to $20°$ and 101 elevation steps from $40°$ to $60°$ (it's practical to have a central elevation of $50°$ so the instrument is aligned with the calibration source in the mid-point of the scan). A scan can take as long as 8 to 22 hours depending on the scanning parameters and resolution. The results of one such scan for a detector is shown in Fig. 6.2a and a prediction from optical simulations is shown in Fig. 6.2b.

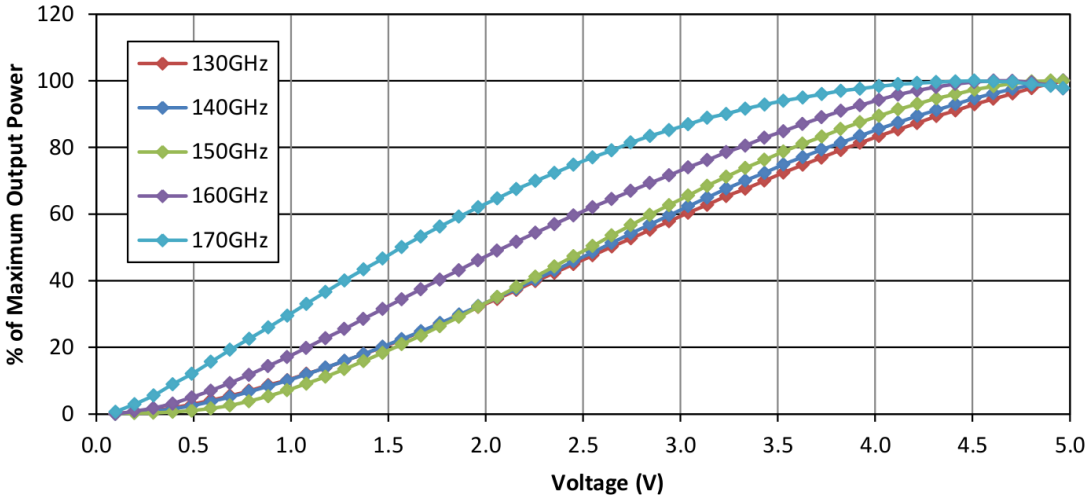

Figure 6.3: Calibration source output power as a function of source voltage in the 130 - 170 GHz range.

The scanning resolution should be considered as it affects the accuracy and precision of the measured results. In the scans shown here, angular range in azimuth and elevation and the step size of the scans result in an angular precision of approximately $\pm 0.10^{\circ}$ and as a result, the maps are made with a 101×101 pixel format. Increasing the scanning resolution and map-making resolution would likely improve the precision of the results but this setup is sufficient for this validation and measurement procedure. Increasing the resolution would also result in impractically time-consuming scans.

6.2.3 Saturation of the Calibration Source Signal at 170 GHz

Keeping the calibration source settings constant for each scan means that the calibration source produces an increased power level at 170 GHz. This is highlighted in the manufacturers datasheet VDI (2017) [102], which is reproduced in Fig. 6.3. 0.5 V was chosen for the calibration source settings for each frequency in the measured datasets. This power level will be shown later to cause saturation in the detectors at 170 GHz.

There is a second effect that contributes to the increase in power level as a function of frequency on the detectors, that is the power coupling to the horns changes as a function of frequency. This is described later in Section 6.5.1.

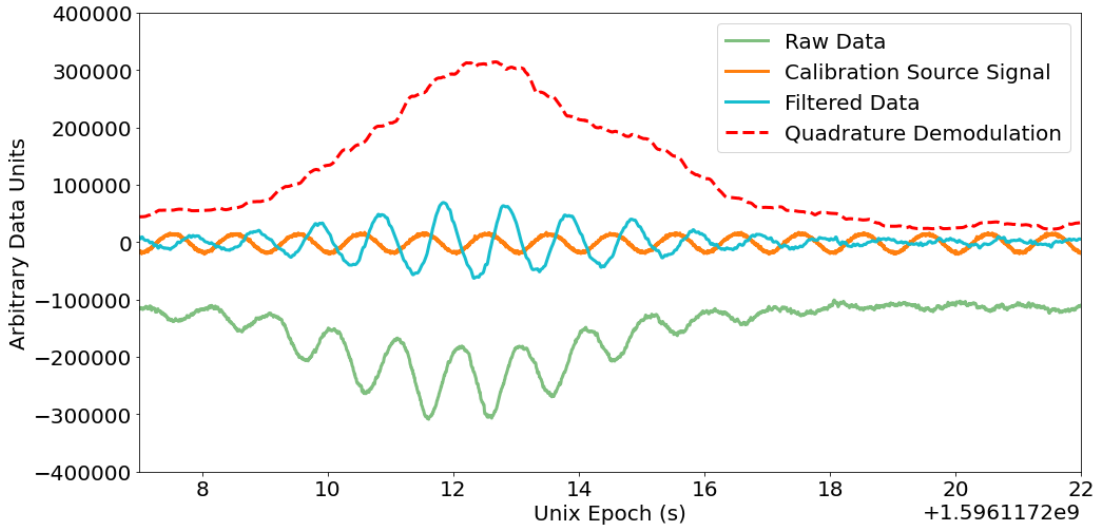

Figure 6.4: This plot demonstrates the different instrument signals when a TES detects a source. In this case, the orange line is the calibration source signal. In green is the raw instrument data, the blue is the filtered instrument data, and the red dashes show an example of a demodulated signal. The data are shown in arbitrary data units and the calibration source is scaled to a visible size in the plot. A shift in time between the source peaks can be seen in the data here which may be explained by an electronic time shift discussed in Sec. 6.3.4. This plot shows 17 seconds from a 9 hour acquisition.

These two effects together cause saturation in the detectors at 170 GHz. This creates an uncertainty when comparing the central peak amplitudes between frequencies. The locations of the central and secondary peaks are unaffected by this saturation effect. Measurements of the FWHM of the peaks is still possible for the 130 and 150 GHz data. For the purpose of this study, measuring the locations of the central peak and secondary peaks (and FWHM, where possible) are sufficient for validating QUBIC's spectral capability.

6.3 Optimising Signal Demodulation

6.3.1 Filtering Data

Each detector produces time ordered data (TOD) during a scan. Scans typically take at least 9 hours for a suitable SNR in the resulting maps. The TESs are heated by the signal from the modulated calibration source, this changes their resistance and a detection is made. The functionality of TES bolometers are explained by Enss (2005) [78] and described in Section 2.3.4. This detection can be seen in Fig.

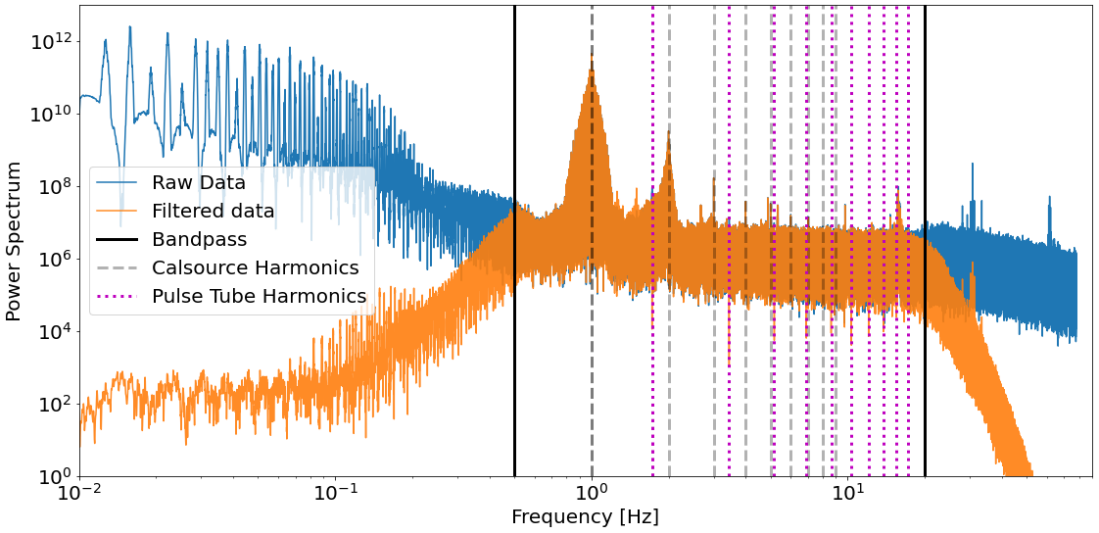

Figure 6.5: A frequency power spectrum with the raw (blue) and filtered (orange) data. The band-pass is shown by the black lines. The frequency of the calibration source and the associated harmonics are shown by the grey dashes. The pulse tube harmonics in pink are removed with a notch filter.

6.4 by the oscillating (at 1 Hz) raw instrument (green) signal. The instrument data must then be filtered (blue) and demodulated (red).

In Fig. 6.5 the filtering methods are illustrated using a frequency power spectrum of the TOD from a detector. A band-pass filter is first applied from 0.5 Hz to 20 Hz because the calibration source modulation frequency is typically 1 Hz (or a value close to 1 Hz, and the bandpass should be modified appropriately if the modulation frequency is different). It is intended to try and preserve the harmonics of the calibration source (grey dashes in the figure) since these are the signal components of interest. The goal is to recover the calibration source signal at 1 Hz (and harmonics) from the other signals. The pink dashes in Fig. 6.5 show the induced noise from the pulse tubes (PT) at 1.724 Hz and harmonic multiples of 1.724 Hz. A notch filter with a width of 0.004 Hz is used to remove noise from the PTs in the signal. A small notch width is preferable since some calibration source harmonics overlap with PT harmonics (for example near 7 Hz).

The filtered data are shown in blue in Fig. 6.4. This is the signal that will be used for optimising the demodulation. Unix epoch is the most convenient measurement of time since the signals come from electronic readouts.

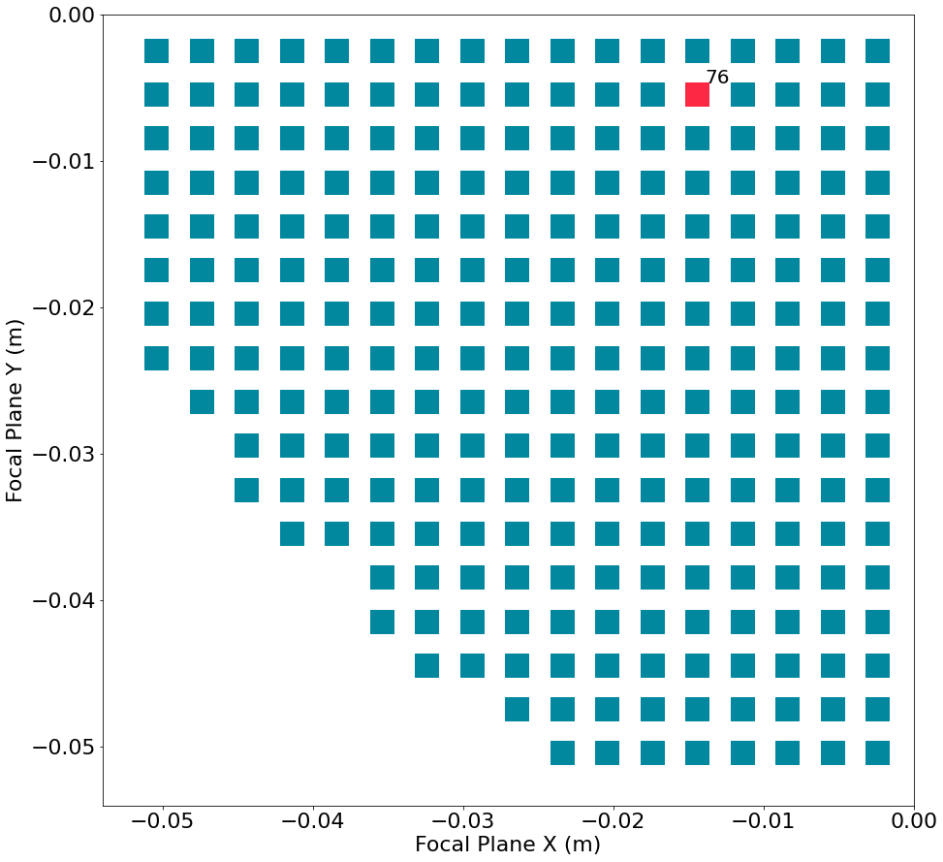

Figure 6.6: As QUBIC is set-up in its TD configuration, one quarter of the focal plane is currently installed. The analysis performed in this chapter mainly relies on data from TES 76 highlighted in red.

6.3.2 TES Selection

Scans were taken over three days at 130, 150, and 170 GHz with one day dedicated to each acquisition. Due to a multitude of factors, choosing a TES for analysis is not trivial. Ideally, every TES would be tested but between datasets different factors mean the TOD for a given TES on a given day might produce bad data. Examples include cross-talk, noise, glitches, detector yield, or changes in cryostat temperature among others. In particular, TESs are sensitive to the intensity level of the source which is different at 170 GHz. The synthesized map peak amplitudes and locations vary for each TES on the focal plane. There is a strong advantage to choosing a TES close to the centre of the focal plane. TESs at the centre of the focal plane have a larger SNR and are subject to less aberration. This is described by O'Sullivan et al., (2020) [71] and by Burke (2020) [90].

There is a benefit in choosing from TESs: 6, 37, 50, 58, 76, 93 because optical simulation data were available for comparison to the instrument data at 150 GHz.

These data were produced by Burke (2021) [90] in MODAL. TES 76 was selected for analysis. Figure 6.6 shows that TES 76 is located near the centre of the focal plane and had good data at 130, 150, and 170 GHz for tests carried out during the campaign. The data were saturated at 170 GHz which has some implications for measurements, which are discussed later.

6.3.3 Demodulation Principles

The experimental procedure described in Section 6.2 allows for synthesized image on sky maps to be made for each of the TES detectors. However, the TOD obtained for each detector is a mix of the calibration source signal and other sources of noise such as $1/f$ noise and noise from the PTs. This TOD must be demodulated to recover the calibration source signal by filtering out the noise. This allows the production of synthesized maps with good SNR. Two types of demodulation techniques are used in this analysis, coherent and quadrature demodulation. These demodulation types are standard in digital signal processing and are described by Haykin (2009) [103].

Both techniques could be used to demodulate the science data but there are some differences between the methods that have operational implications for QUBIC. Quadrature is more robust and works independent of signal synchronisation. The downside is that there is noise added to the demodulated signal. Coherent demodulation requires perfect, or corrected, signal synchronisation and returns a demodulated signal with minimal noise. This method was preferable in the context of this chapter because at the time QUBIC had not achieved full detector performance (due to cooling and temperature). The highest level of SNR was required to analyse the measured calibration data. In the future, for science observations, the B-mode signal is very faint so coherent demodulation is similarly a preferable method for data reduction. QUBIC will be more efficient and collect science data quicker with the coherent demodulation method.

It will be shown that in each case the detected signal is multiplied by the modulating signal ($\sin(\omega t)$), producing a high frequency component ($2\omega t$) which must be filtered with a low pass filter (this is implemented as a standard function in *qubicsoft*). The low pass filter is applied using the convolution theorem (shown in Eq. 6.1) and FFT (fast Fourier transform). This is the principle that convolution in the time domain is equivalent to multiplication in the frequency domain.

$$h(t) = \{f * g\}(t) = \mathcal{F}^{-1}\{\mathcal{F}(f) \cdot \mathcal{F}(g)\} \tag{6.1}$$

If $\mathcal{F}(f)$ is an FFT of the low-pass filter kernel and $\mathcal{F}(g)$ is the FFT of the modulated signal, a low pass filter is applied giving $h(t)$. The implementation used in *qubicsoft* uses a flat window (or "no window") as the filter kernel. A Hann window filter kernel, among others, were also tested and showed no improvement, this could be investigated in the future but the filter kernel is not a limiting factor in this context.

These calculations are implemented in *qubicsoft*, hosted on GitHub (2020) [104]. The demodulation calculations and FFT convolution are functions in the demodulation library which are controlled by Python scripts.

6.3.3.1 Coherent Demodulation

The first type of demodulation for discussion is coherent demodulation (also known as synchronous demodulation). This is the most basic form of demodulation. Eq. 6.2 shows how the detected modulated source signal (X) is mixed with a wave matching the modulation signal (local oscillator, C) to give T. It is the amplitude of the source signal, A, that we want to recover. There may be an unknown phase shift (ϕ) between the signal used to modulate the source and the replicated signal used for demodulation, as was the case in Fig. 6.4. Using trigonometric identities, an expression is obtained with a high frequency $2\omega t$ term.

$$\begin{aligned} X &= A\sin(\omega t + \phi) \\ C &= \sin(\omega t) \\ T &= X.C \\ T &= \frac{A}{2}[\cos(\omega t + \phi - \omega t) - \cos(\omega t + \phi + \omega t)] \\ T &= \frac{A}{2}[\cos(\phi) - \cos(2\omega t + \phi)] \end{aligned} \tag{6.2}$$

A low pass filter ($\mathcal{LPF}$) is applied using the convolution theorem (Eq. 6.1) and this removes the high frequency $2\omega t$ term. This is shown by Eq. 6.3:

$$
\begin{aligned}
T &= \mathcal{LPF}\big(\frac{A}{2}[\cos(\phi) - \cos(2\omega t + \phi)]\big) \\
T &= \frac{A}{2}\cos(\phi).
\end{aligned}
\tag{6.3}
$$

If the X and C were synchronous ($\phi = 0$), or the phase offset is known, then T is an effectively perfect demodulation and A is recovered from T. Unfortunately, this assumption cannot be made for QUBIC even when the Raspberry Pi and *QubicStudio* are both supposedly GPS synchronised. This is an important aspect in this chapter and is discussed later. Eq. 6.3 shows that as ϕ approaches $\pm\pi/2$ the demodulated signal will tend to zero. A trial-and-error approach of demodulating the signal using a range of values of ϕ until the output is maximised could be used. A more robust solution to demodulation is quadrature demodulation which does not require ϕ to be known.

6.3.3.2 Quadrature Demodulation

In quadrature demodulation the modulated signal X is mixed with C_I, a local oscillator wave (sine term), and C_Q, the local oscillator wave shifted by 90° (cosine term), shown in Eq. 6.4. By applying trigonometric identities expressions with sine and cosine terms are produced which both include the high frequency $2\omega t$ term. These can be filtered in the same fashion as with the coherent demodulation using a $\mathcal{LPF}$.

$$
\begin{aligned}
X &= A\sin(\omega t + \phi) \\
C_I &= \sin(\omega t) \quad \text{and} \quad C_Q = \cos(\omega t) \\
T_I &= X.C_I \quad \text{and} \quad T_Q = X.C_Q \\
T_I &= \frac{A}{2}[\cos(\omega t + \phi - \omega t) - \cos(\omega t + \phi + \omega t)] \\
T_Q &= \frac{A}{2}[\sin(\omega t + \phi + \omega) + \sin(\omega t + \phi - \omega t)] \\
T_I &= \mathcal{LPF}\big(\frac{A}{2}[\cos(\phi) - \cos(2\omega t + \phi)]\big) \\
T_Q &= \mathcal{LPF}\big(\frac{A}{2}[\sin(2\omega t + \phi) + \sin(\phi)]\big) \\
T_I &= \frac{A}{2}\cos(\phi) \quad \text{and} \quad T_Q = \frac{A}{2}\sin(\phi) \\
|T| &= \sqrt{T_I^2 + T_Q^2} = \frac{A}{2}
\end{aligned}
\tag{6.4}
$$

In Eq. 6.4, the demodulated signal (T) contains the two components, T_I and T_Q, commonly known as the *in-phase* and *quadrature* components, respectively. $|T|$ returns the quadrature demodulated signal. Since $\sin(\phi)$ and $\cos(\phi)$ are summed and squared, the phase-error ϕ is cancelled. Quadrature demodulation is always better than coherent demodulation when the phase shift is unknown. The drawback is that there is additional noise ($\sqrt{2}$) in a quadrature demodulated signal.

6.3.4 Optimising Demodulation Performance

The success of the coherent demodulation procedure depends on how well the source and detector signals are synchronised (or how well any phase shift is known). It became clear they were not synchronised in the case of QUBIC (as can be seen from the shift between the orange source and blue detector signals in Fig. 6.4). This was a surprising complication as the instrument and the calibration source are both recorded with GPS timing. Since the phase shift was unknown it was decided to carry out coherent demodulation for a series of phase shifts to see which maximised the recovered signal.

The trial and error method mentioned previously was used and demodulations were made for 13 shifts over a 1 second period, since the calibration source frequency is 1 Hz. This is shown in Fig. 6.7 where shifted demodulations (and quadrature

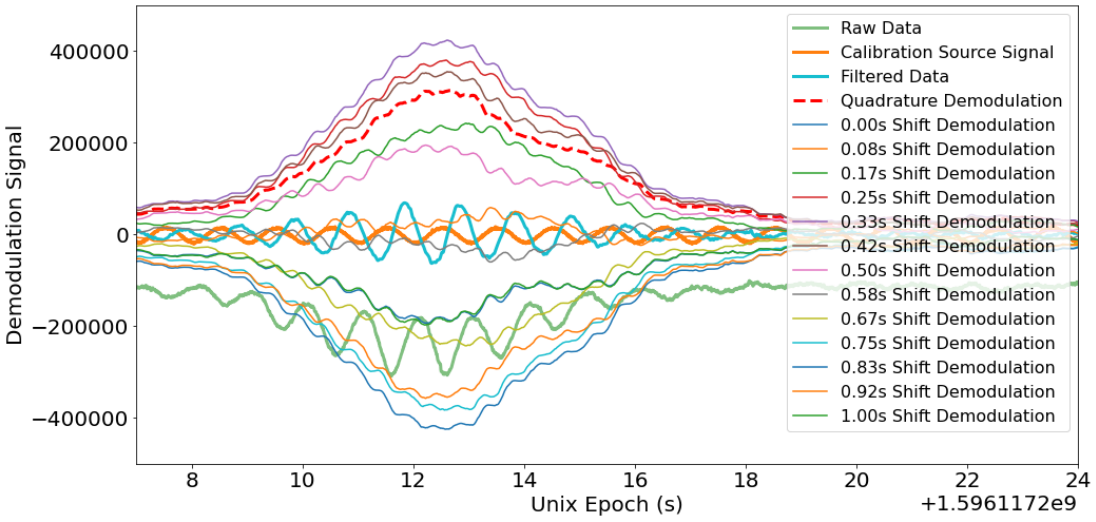

Figure 6.7: The filtered data are shown for a series of different demodulation types and calibration source shifts. Here a demodulation with a calibration source shift of 0.33 s provides the best demodulation with the highest amplitude (purple line). Note that these data show 17 seconds of a 12 hour data-set.

demodulation) are shown for a 17 second time period. The relative performance of the demodulations can be compared this way. Fig. 6.7 shows that the coherent demodulation of 0.33 s returns the highest demodulation while the 0 s shift (raw data) returns a negative amplitude demodulation. This is only for a 17 s snapshot of the whole dataset so a more quantitative description and analysis is necessary.

It was first noted in this analysis that the calibration source and instrument data were unsynchronised. During the analysis, the synchronisation issue was investigated and characterised. For a given acquisition, the phase shift remains constant throughout the measurement. But each acquisition (e.g. each day) may have a different phase shift. As a result of this phase shift difference a solution is being implemented to synchronise the calibration source and instrument.

Quadrature demodulation was also implemented for the same data set and the resulting signal is shown as a dashed red line in Figs. 6.4 and 6.7[4]. The presence of noise in the real signal means the quadrature demodulation does not recover the signal perfectly but nevertheless performs well with no prior knowledge of the phase shift. This shows how quadrature demodulation is a good solution when analysis does not require the highest possible SNRs while analysis requiring high

[4]The quadrature method adds a $\sqrt{2}$ noise factor to the demodulated signal. The quadrature demodulated data in Figs. 6.4, 6.7, and 6.10 are normalised by the $\sqrt{2}$ noise factor in *qubicsoft* and therefore appear lower in amplitude compared to the ideal coherent demodulated data.

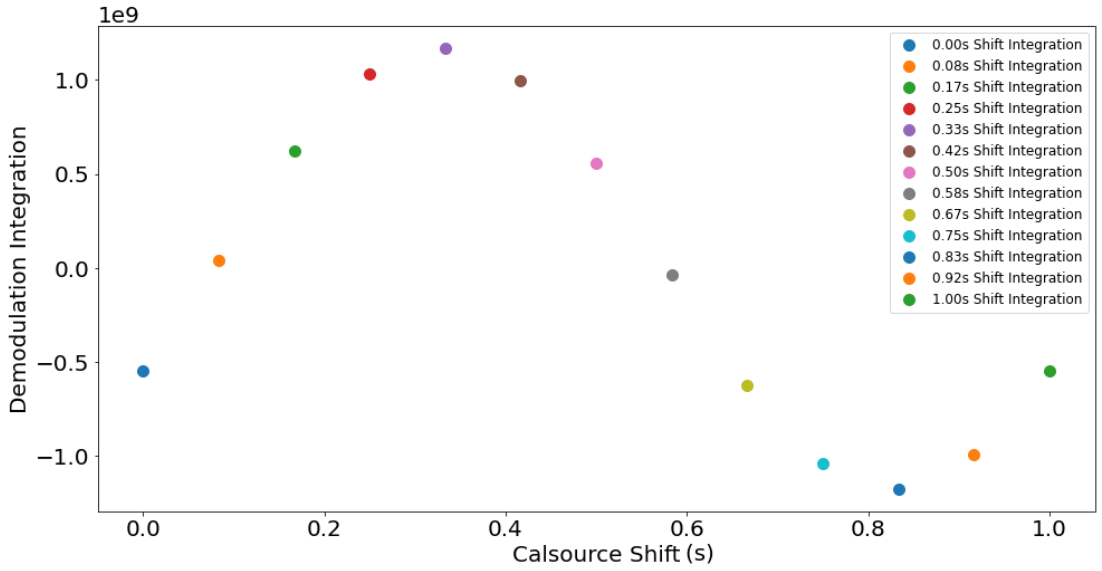

Figure 6.8: The signals from the various demodulation shifts are integrated to get an estimation of their performance. The y-axis data are integrated arbitrary data units.

SNRs should implement a well tested coherent demodulation (until a technical solution is found).

6.3.4.1 Measuring Performance

The relative performance of each demodulation is tested in two ways. The first is by integrating the demodulation amplitudes for each coherent shifted demodulation. Secondly, the maps are made for each demodulation and are compared. Both methods should agree on an optimal demodulation.

The demodulations with the highest amplitude, and therefore highest SNR, will return the highest integrated value. The results of this integration are shown in Fig. 6.8 where each data point shows the integrated value for a demodulation with a given phase shift. From this figure, it is evident again that a shift of 0.33 s applied to the calibration source results in the demodulation with the highest integration making this shift a good candidate for demodulation of the data-set. The integration value for each phase shift shows the cosinusoidal dependence on the phase shift predicted by Eq. 6.3.

For the second method, maps are made for each of the demodulations (as listed in Fig. 6.7) and then analysed (FWHM and peak position, and peak amplitude) using the cut shown in Fig. 6.9. This figure is a replica of Fig. 6.2a except a cut

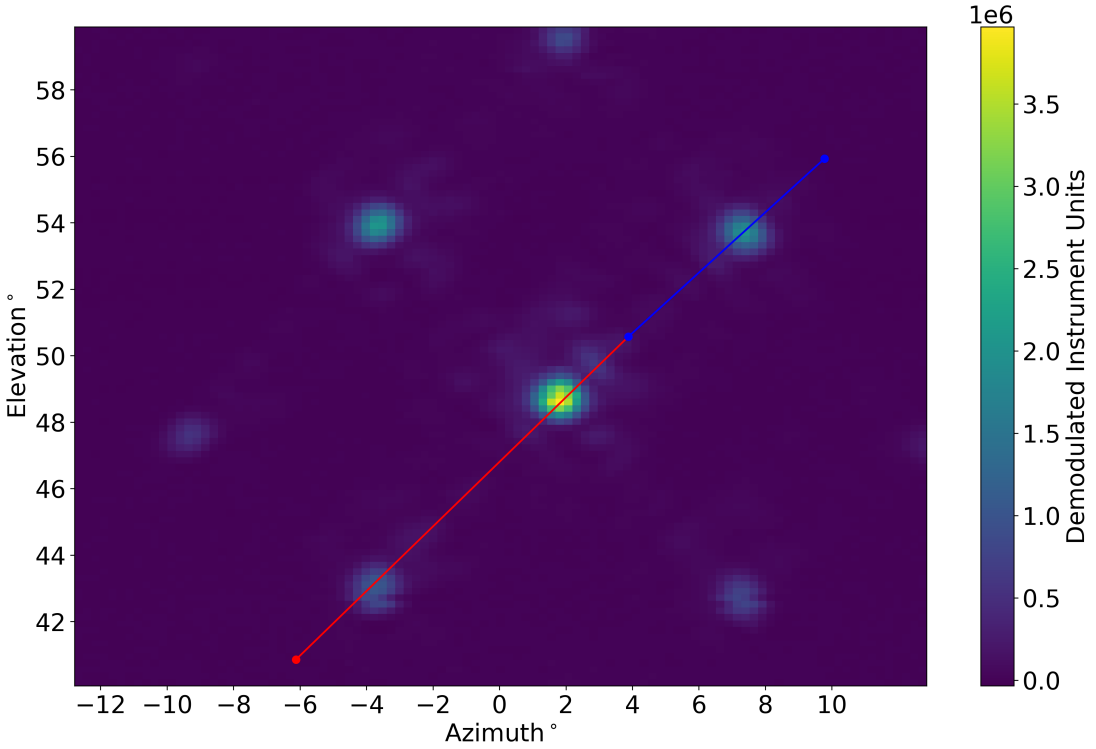

Figure 6.9: A map of the calibration source for a single detector (TES 76) from a 150 GHz scan on 30-07-2020. The characteristic main peak and side lobes are evident. The intensity is in arbitrary demodulated instrument units. Due to optical aberrations the cuts are made along two lines (red and blue).

is overlaid in two parts. This use of two lines is due to the aberrations that have already been described. This means typical 0°, 45°, and 90° degree cuts cannot be made. Instead, the cut is made in two parts so that the final cut includes the central peak and two secondary peaks.

The intensity along the cut for each shift and quadrature demodulation is shown in Fig. 6.10. Note that as the time shift increases, the amplitude of the demodulated peak in Fig. 6.10 increases until a shift of 0.33 s, then, the values decrease. These two methods both show the same cosinusoidal behaviour seen in Fig. 6.8 and that the optimal phase shift is 0.33 s.

This type of analysis provides a high degree of certainty that the demodulation is reliable and near-optimal. There may be some scope for improvement, one way might be to examine different windows/filter kernels, but this initial treatment was considered sufficient for the calibration and testing phase.

From these demodulated data sets, detector maps as a function of frequency were produced. These are especially important to test due to QUBIC's dependence on

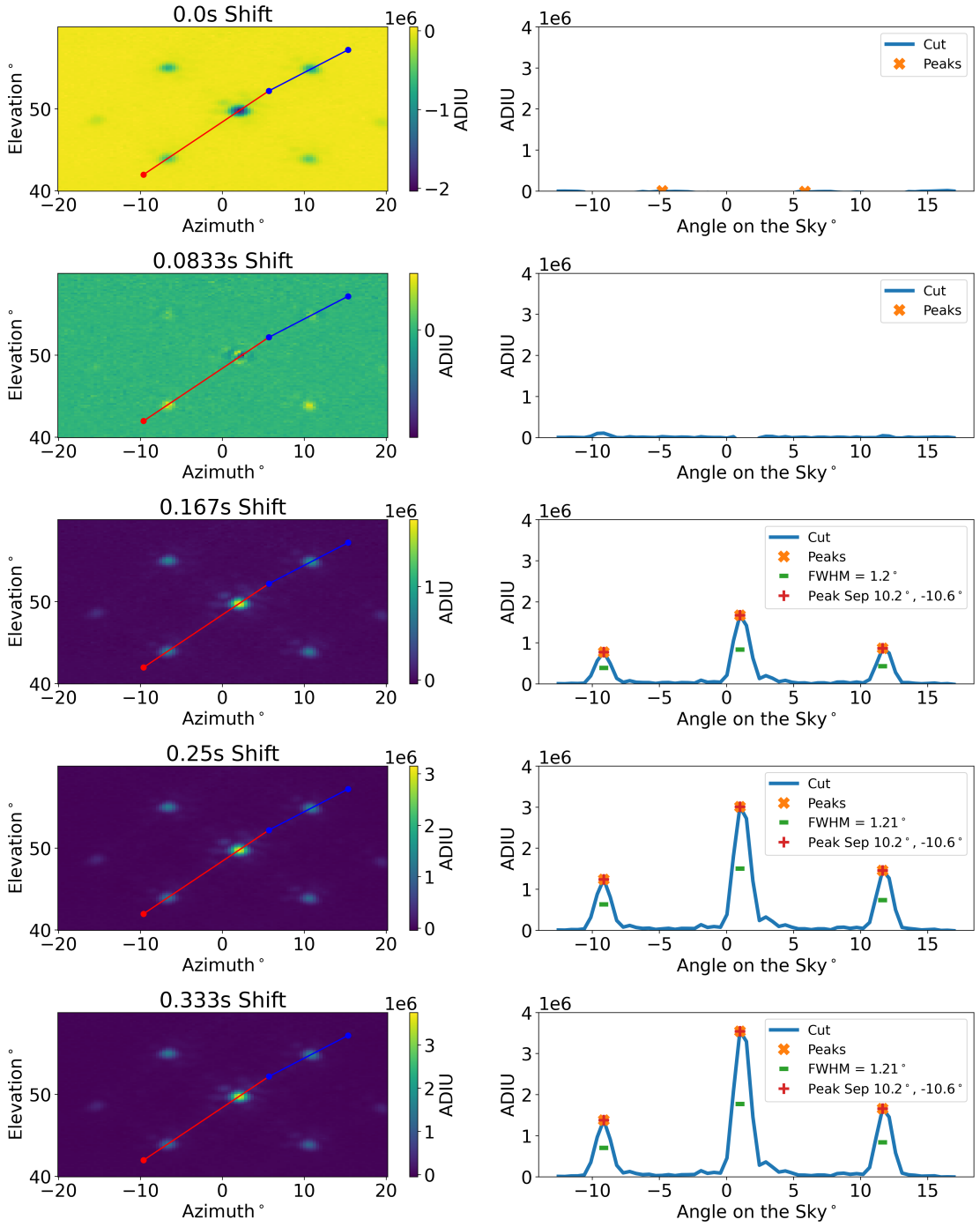

(a) Demodulated maps and cuts of shifts from 0 to 0.33 s. For the 0 second shift, the map returns negative demodulation while the absolute value is shown in the cut for these data.

Figure 6.10: *Image on the sky* maps (left) and cuts (right) for demodulated data from TES 76 with different shifts applied to the demodulation signal. The quadrature demodulation data are also included at the bottom. The sinusoidal behaviour of amplitude with phase shift is expected from Fig. 6.8. It is clear the 0.33 s shift provides the optimal demodulation when looking at the amplitude of the central peak and side lobes. *Continued next page.*

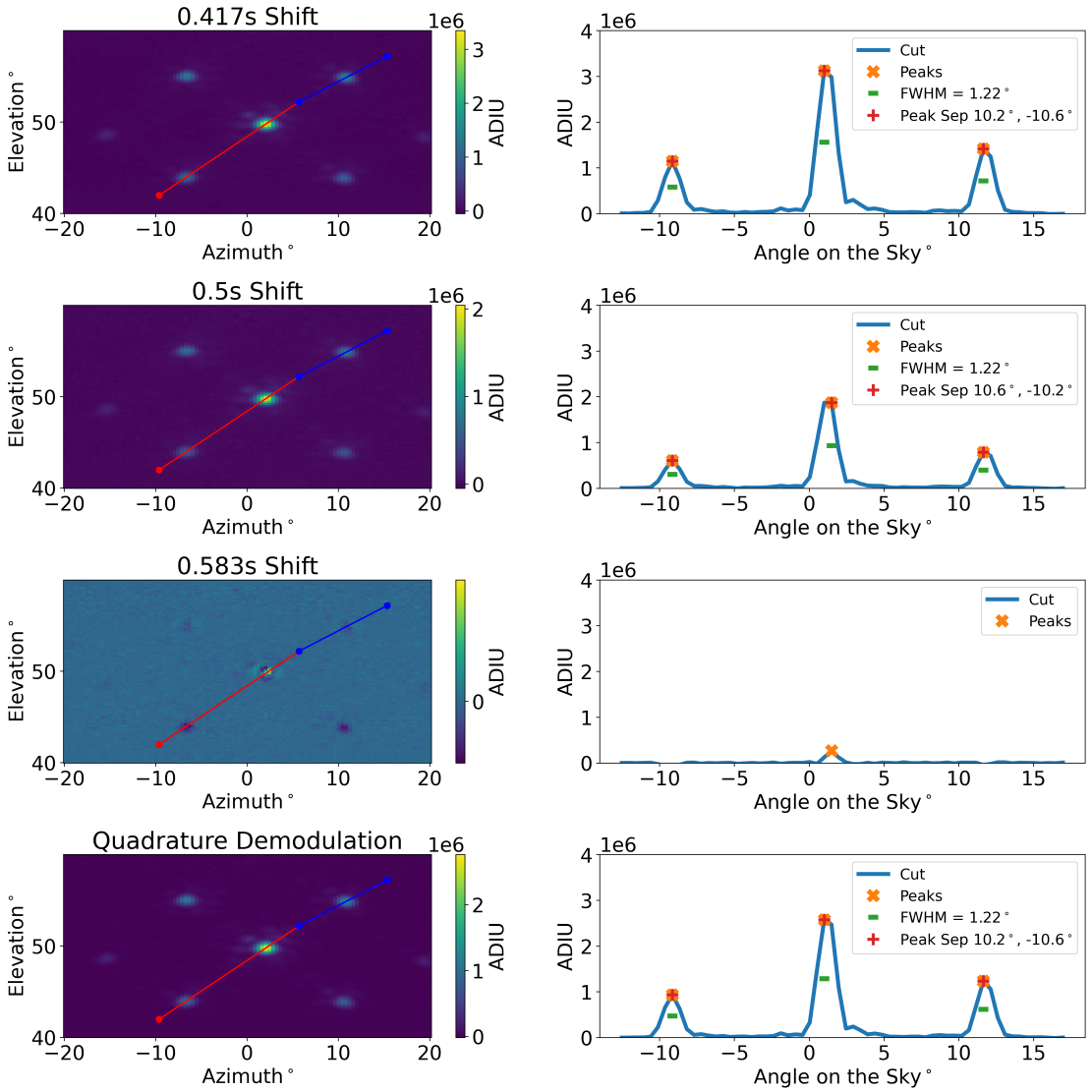

(b) Demodulated maps and cuts of shifts from 0.417 to 0.583 s and with a quadrature example. Shifts after 0.583 s return negative values as seen with the 0 s shift.

Figure 6.10: *Image on the sky* maps (left) and cuts (right) for demodulated data from TES 76 with different shifts applied to the demodulation signal. The quadrature demodulation data are also included at the bottom. The sinusoidal behaviour of amplitude with phase shift is expected from Fig. 6.8. It is clear the 0.33 s shift provides the optimal demodulation when looking at the amplitude of the central peak and side lobes. For the 0 second shift map returns negative demodulation while the absolute value is shown in the cut for these data.

its spectro-imaging performance and is a necessary step for validating QUBIC's performance prior to shipping to Argentina for scientific observations. With the calibration source demodulation optimised, the following sections will extend the map-making to other frequencies across the band and compare them to theoretical analytic predictions and PO simulations.

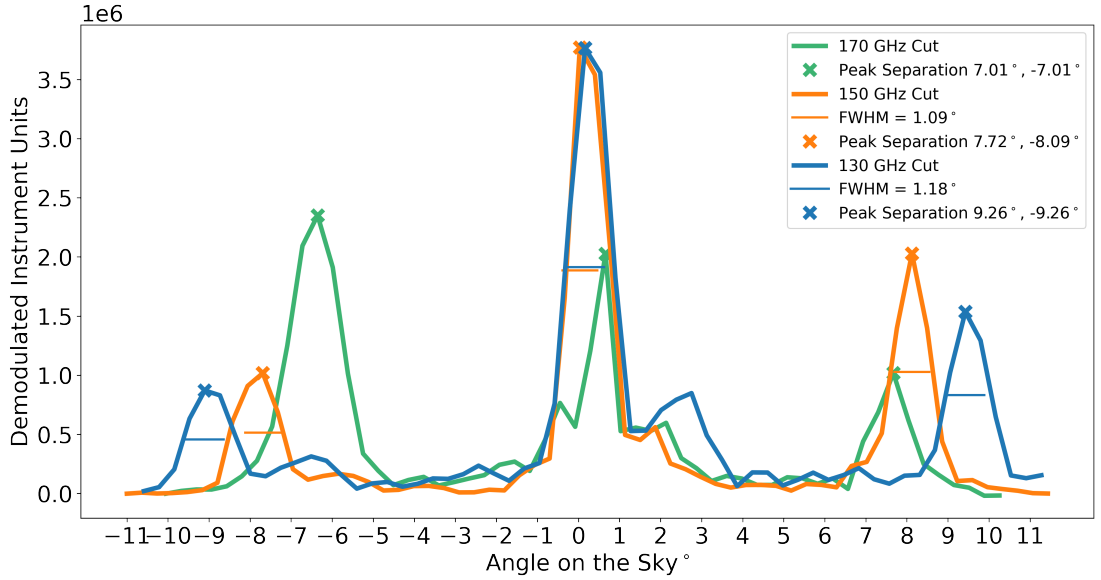

Figure 6.11: Cuts of maps from TES 76 at three frequencies. Their corresponding peaks (x-marks) and FWHMs (horizontal bars) are also plotted. The angular distance from each secondary peak to the main peak is given in the legend. The FWHMs in the legend refer to the central peaks. The 130 GHz data have been normalised to the central peak of the 150 GHz data. The 170 GHz cut has not been normalised in this way due to saturation. The 170 GHz cut shows QUBICs detector saturation has an atypical profile (its not a flat-top and has dips and rises). The 170 GHz peak separations are still useful but the FWHMs are not measured.

6.4 Spectral Map Measurements

Scans of the calibration source (as described in Sec. 6.2.2) were performed in July and August of 2020 at 130, 150, and 170 GHz. The cuts of the spectral map scans are shown in Fig. 6.11. Scans were made at these frequencies since they correspond to QUBIC's lower, middle, and upper single-moded operating frequencies. By measuring the peaks of QUBIC's synthesized-image on the sky (far-field) as a function of frequency, QUBIC's operational capability can be validated.

The maps were produced using the method described in Sec. 6.3 (coherent demodulation with corrected phase shifts) for each frequency. The corrected phase shifts were determined for each dataset by the same method and applied to the demodulation. Cuts along the lines illustrated in Fig. 6.9 were taken for the map from TES 76 and are shown in Fig. 6.11. Each cut comes from a dataset taken on a different day: 30-07-2020, 01-08-2020, and 02-08-2020 at 130, 150, and 170 GHz, respectively.

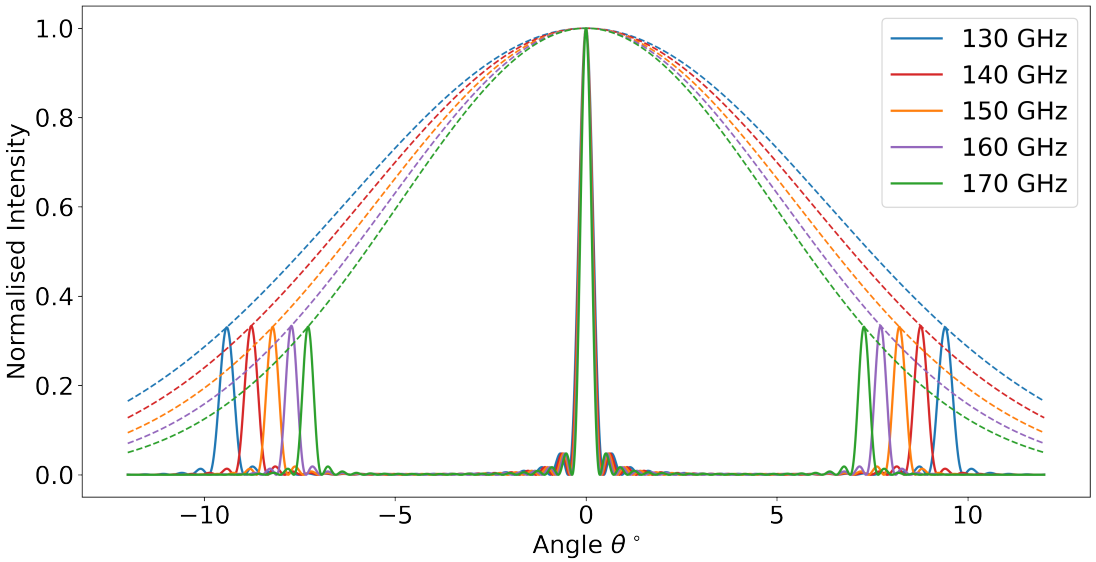

Figure 6.12: Theoretical model of synthesized beam peaks as a function of frequency for a TES in the center of the focal plane. This assumes QUBIC is an ideal and un-aberrated imager.

There are important features to note in Fig. 6.11. The calibration source produces more power as the frequency increases, this induces saturation in the detectors at 170 GHz (see Section 6.2.3). These data were normalised with respect to the 150 GHz signal power rather than with respect to the central peak as was the case with the 130 GHz data. As a result of this analysis and in combination with the horn transmitting more power at higher frequencies, improvements were made to the calibration source settings so future data sets would not be affected by saturation in this manner. For example, by making changes to voltage, amplitude, and duty cycle etc., the calibration source power can be increased at 130 GHz to properly scale with the 150 GHz data (if equal amplitude at all frequencies is desired). The main improvement in the process to be made is decreasing the 170 GHz calibration source power. Ecosorb can sometimes be added inside the calibration horn to act as a NDF. Data analysis techniques were developed to correct saturation, if it occurs.

Fig. 6.12 shows a theoretical prediction of the spectral behaviour of QUBIC's synthesized image for comparison with Fig. 6.11. This figure is for an ideal imager and does not include aberrations and is normalised for each frequency. This is not a perfect comparison since the measured data are from an off-axis TES and off-axis combiner where the figure shows an on-axis ideal imager and TES synthesized pattern. This plot is primarily illustrative and demonstrates the basic behaviour of the synthesized pattern with frequency. The next section will show

quantitative comparisons between the experimental results and analytical models and optical simulation predictions.

6.5 Results

A direct comparison of the spectral synthesized maps to simulations cannot be made since no exactly matching simulation data exist. Instead, synthesized map measurements were compared to three different sets of simulations, each with their own advantages and limitations. By combining these three comparisons (ideal imager prediction, off-axis point-like TES detector at 150 GHz, on-axis point-like TES at 130 - 170 GHz), a validation of QUBIC's optical performance can be made, including spectral performance which is a key feature for QUBIC's necessary functionality.

Measurements were first compared to predictions for the synthesized images of QUBIC as an ideal on-axis imager. In this model, straight-forward equations can be used to predict the peak positions, peak separation, and FWHMs. The model is further limited by the fact that TES 76 is not central on the focal plane (Fig. 6.6) and has a finite area. The effect of TES location and detector area on the synthesized image, described by O'Sullivan et al., (2020) [71], is to cause changes in peak position, FWHM, and amplitude. Nevertheless this comparison is a useful indicator of the behaviour of the instrument.

The measured maps can also be compared to full PO simulations of the synthesized image which accounts for changes in peak position, separation, and FWHM due to optical aberrations from the off-axis optical system and the off-axis location of the TES on the focal plane. Measurements of TES 76 can be compared to a simulated synthesized image of TES 76. This is the preferred method of comparison but is limited by the fact that at the time simulated data were only available for the 150 GHz synthesized image for six TESs because generating these simulations is so computationally intensive. The other limitation is that the simulated data are mostly for a single point in the centre of TES 76 rather than the whole detector area. This effects the FWHM of the peaks as described in O'Sullivan et al., (2020) [71]. Some simulations considering the full TES area were carried out to estimate the size of the effect and compared to measured data following in Sec. 6.5.4.

Frequency (GHz)	Peak Separation°		FWHM°	
	Theory	Measured	Point Source	Measured
130	9.49	9.26 - 9.26	1.18	1.18
150	8.21	7.72 - 8.09	1.02	1.09
170	7.24	7.01 - 7.01	0.90	0.69

Table 6.1: Table of theoretical predictions and map measurement for TES 76. Note that these theoretical predictions describe an ideal-imager with no aberrations. The FWHMs were calculated from the aberrated cuts as shown earlier in this chapter by Fig. 6.9.

Finally, there were optical simulations, as above, available but for a point at the centre of the focal plane at three frequencies. For this simulation setup, 130, 150, and 170 GHz optical model data were available. These data were useful for comparing and validating the map measurement results for instrument data at different frequencies which is a key aspect of this analysis.

6.5.1 Comparison with Theoretical Predictions for an Ideal On-Axis Imager with No Aberrations

Consider an array of horn beams superimposed on the focal plane by an ideal imager, the FWHM of the synthesized beam peaks as a function of wavelength is given by O'Sullivan et al., (2020) [71] as

$$FWHM = \frac{\lambda}{(P-1)\Delta h} \tag{6.5}$$

where the horns are separated by $\Delta h = 14$ mm and P is the number of horns along one side of the 8×8 horn array. Using Eq. 6.5, predictions can be made for each frequency in the analysed data-sets and these are given in Table 6.1. Since these theoretical predictions describe an on-axis ideal-imager, there are no aberrations and only one peak position and width is given for the theoretical predictions. The peak separation (PS) is given by

$$PS = \tan^{-1} \frac{\lambda}{\Delta h}, \tag{6.6}$$

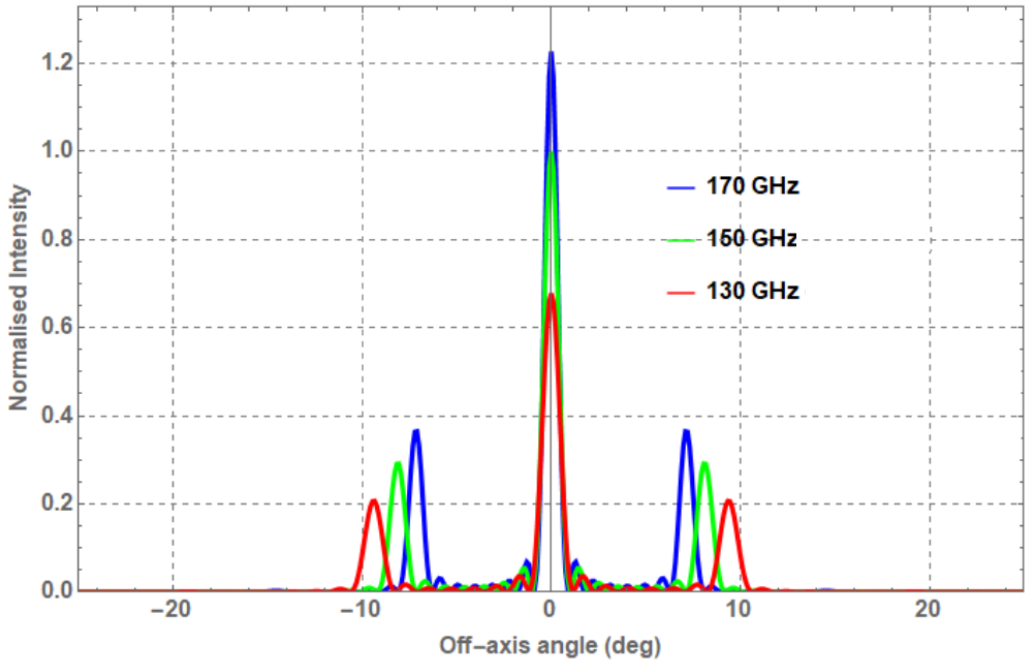

Figure 6.13: Synthesized beams showing the peak separation and position as a function of frequency for QUBIC as an ideal imager and an on-axis TES. This plot is reproduced from Burke (2021) [90], Fig. 4.33.

which gives 8.21° for 150 GHz. In this case the peak separation is symmetric about the central peak. For the measured data secondary peaks separations on either side of the main beam differ slightly due to aberrations.

Fig. 6.13 shows synthesized beams for different frequencies. The data in this figure were produced by using PO. A beam (point source) was propagated from the TES location on the focal plane through the combiner, and then coupled to the horn array. The horn array transmitted the beams through the back-to-back horns onto the sky where they were combined in the far-field. This was done for 130, 150, and 170 GHz. Details on this modelling is provided by Burke (2021) [90]. As the frequency increases more power is coupled to the horn array. This aspect contributes to the saturation of the detectors at 170 GHz, making comparison of amplitude ratios between the frequencies difficult.

Table 6.1 and Fig. 6.13 show that the peak separations decrease as a function of frequency. This is in good agreement with the expected behaviour as outlined in Fig. 6.12. It also shows that all measured positions are close to expected, given the error (±0.1°), with the exception for the first side peak at 150 GHz. This error

was estimated from the scan resolution, for example in this case, 101 elevation scans over a 20° range.

No comparison of amplitude ratio as a function of frequency can be made due to detector saturation from the calibration source settings and change in the horn coupling with frequency. Saturation in QUBIC has a characteristic shape as seen in Fig. 6.11 (170 GHz, green central peak) where the central peak has a dip in intensity before it rises again.

The measured FWHMs are difficult to compare since the theoretical prediction is given for a point detector on the focal plane, while the measured data are for the whole detector area ($2.7 \times 2.7\,\mathrm{mm}^2$). The FWHM is expected to be broader for the finite detector area of the real measurements. For 150 GHz, the FWHM of $1.09 \pm 0.10°$ is sufficiently close to the theoretical prediction (0.91°). This is discussed further in Section 6.5.4. The measured value of 0.69° for 170 GHz is not reliable due to the saturation but is still useful to consider for the indicative trend that FWHM increases as the frequency decreases.

6.5.2 Comparison with Optical Simulation of TES 76 as a Point: 150 GHz (Real Combiner Including Aberrations)

The synthesized image changes slightly for each detector position on the focal plane which is not accounted for in the previous section. Simulation data provided by Burke (2021) [90] are shown in Fig. 6.14 for TES 76 at 150 GHz. This figure shows that the central peak is not exactly in the centre and the intensity of the secondary peaks varies. These simulation data are still for a point source detector rather than a detector of finite area which affects the measurement of the FWHM.

Fig. 6.15 shows the simulated cut compared with the measured cut (150 GHz data from Fig. 6.12). The measured data and simulation data have matching secondary peak positions. The amplitude ratio between the secondary peaks in both cuts are similar. Ideally, this comparison and analysis would be applied to the full frequency range but the simulated data were only available at 150 GHz at that time. Nevertheless, these data demonstrate excellent alignment of central and secondary peaks.

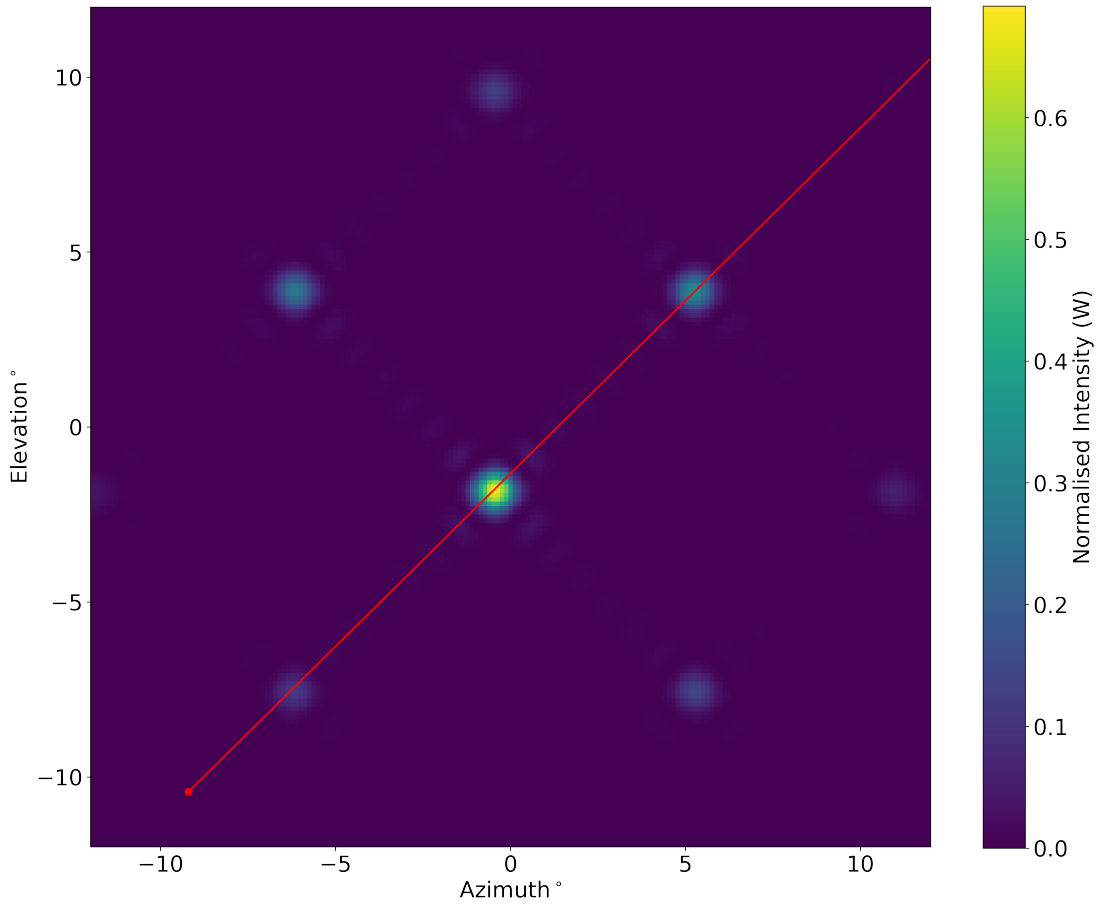

Figure 6.14: Simulated synthesized image on the sky for a point source detector at the location of TES 76 and including aberrations. A line shows the cut taken to measure the peaks.

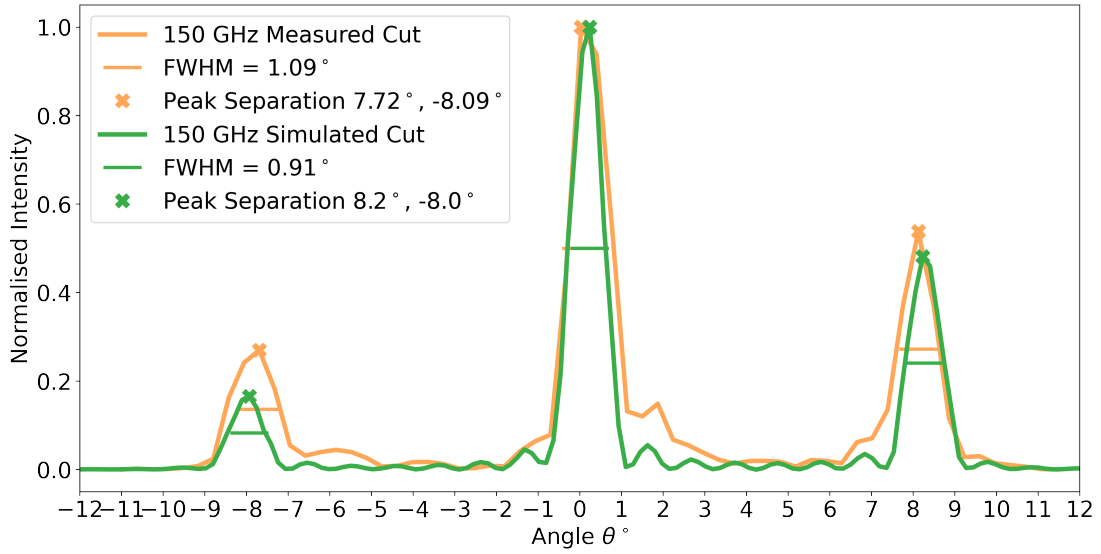

Figure 6.15: The green cut shows the simulated data from Fig. 6.14. The orange measured data is the 150 GHz cut from Fig. 6.11. It's clear how the relative intensities of the secondary peaks changes for an off-axis TES.

Frequency (GHz)	Peak Separation°		FWHM°	
	Simulated	Measured	Point Source	Measured
130	9.31 - 9.51	9.26 - 9.26	1.15	1.18
150	8.11 - 8.18	7.72 - 8.09	0.91	1.09
170	7.14 - 7.16	7.01 - 7.01	0.84	0.69

Table 6.2: Table of predictions from optical simulations and the measurement of the map for TES 76. These optical simulations were generated in MODAL and include realistic optical modelling of mirrors. This means the off-axis nature and aberrations of the combiner are modelled. As such, two peak positions are given unlike in Table 6.1. The predictions are for a TES in the centre of the focal plane and not TES 76.

6.5.3 Comparison with Optical Simulations: 130 - 170 GHz (Real Combiner Including Aberrations)

Table 6.2 shows the optical simulation results by Burke (2021) [90] compared with the same measured instrument data as in Table 6.1. The simulations include realistic PO modelling of the combiner which includes aberrations due to the off-axis optics and short focal length of the combiner. Here the measured results are within the error ($\pm 0.10°$) of the simulated measurements except for one peak at 150 GHz.

All the FWHM measurements from the instrument data are within the error of the measurements of the optical simulations. However, the same caveat applies as with the idealised predictions. The values quoted in Table 6.2 are for a point detector and not the entire bolometer area. Also, the 170 GHz FWHM measurement is subject to saturation.

6.5.4 Effect of TES Finite Area and Location

A calculation of the map peak FWHM when the full bolometer area is considered is provided by Burke (2021) [90] for 150 GHz. This synthesized image on the sky is made by taking beams from point sources at 9 locations within the bolometer area, propagating them through the combiner as before and combining the fields on the sky by incoherent addition. This way the FWHM from a bolometer area rather than a simple point source can be estimated. The FWHM increases from 0.91° to 1.02° when the full bolometer area is considered (Table 6.3). This makes the peak

Frequency (GHz)	Theoretical FWHM Point Source	Simulated FWHM TES Area	Measured FWHM TES 76
150	0.91	1.02	1.09

Table 6.3: These data compare the difference between measurements of FWHM for a theoretical point detector and for the full detector area (simulated and from measurements of instrument data).

FWHM approximately 10% wider for a finite bolometer area compared to a point detector model. If this correction factor is applied to the optical measurement of 1.15° for 130 GHz, the FWHM widens to 1.27°, still within an acceptable range.

In addition, TES 76 is an off-axis detector. This causes the central peak and side lobes to be offset from the center of the map. Using a model of TES 76 (point source), it was possible to make some comparison to the measured maps at 150 GHz. These results showed agreement in terms of amplitude ratio of the secondary peaks and peak position. The FWHMs are similar and the small difference can be explained by the fact that the optical model simulates a point source rather than the finite bolometer area, as is the case with the measured data (Table 6.3). This comparison can only be made at 150 GHz due to the availability of simulated maps (as outlined in Section 6.5).

6.6 Conclusion

The calibration source scanning procedure outlined in this chapter provides a method of validating the QUBIC instrument prior to observations. All of QUBIC's hardware and software was assembled and integrated in APC. The work in this chapter has contributed to validation of the instrument by comparing measured data to simulated predictions. In particular, this chapter has measured and validated the spectral behaviour of synthesized maps. This shows that QUBIC has suitable spectral performance for spectro-imaging, which is necessary for QUBIC to detect the faint B-mode polarisation anisotropies. This is a necessary calibration step before shipment of the instrument to Alto Chorillos in Argentina where scientific observations will be made.

During calibration an issue was discovered with the synchronisation between the calibrator modulation signal and TES signal that was used to demodulate the

detector measurements. Two types of data demodulation, coherent and quadrature were discussed and tested in this context. A method to find and validate the best phase shift for coherent demodulation was determined and this was then used for map-making using data from TES 76 at 130, 150, and 170 GHz. Maps at multiple frequencies are necessary for validating QUBIC's spectro-imaging capability.

The map data were compared with optical simulations made with different levels of assumptions. In particular, the peaks of the synthesised beams, their peak positions and FWHMs, were measured as a function of frequency. These measurements were then compared to simulated predictions for QUBIC. These results show that QUBIC's optics are performing within expected parameters.

The results of these measurements also indicate areas for improvement in the calibration procedure. For example, in the 170 GHz data set, the detectors were saturated making measurements of FWHM and amplitude unreliable. This information was used to tune the calibration source for the next 170 GHz calibration scans. Increasing the scan resolution and map-making resolution will decrease the error on measurements but this is not necessary for the purpose of this initial validation of QUBIC's spectro-imaging capability. The analyses carried out here were focused on the single-moded range (130 - 170 GHz) of QUBIC's observation spectrum as these were the frequencies tested in the laboratory in APC. QUBIC will also observe between 200 and 240 GHz and synthesized beam maps in this range should be analysed similarly in the future when the data are available.

The map measurement software developed here to validate the instrument is also a primary ingredient for analysing QUBIC's scientific observations taking place in the near future as described by Hamilton et al., (2020) [66]. Considering QUBIC's key feature, the ability to use multi-band spectro-imaging to separate Galactic foregrounds from the polarised CMB signal, proper measurement of these maps can be used to aid in QUBIC's control of its instrumental systematics as described by Mousset et al., (2020) [56]. The next phase of this project will focus on generating these maps with measurements of all peaks on all bolometers in order to provide QUBIC with reference data for controlling systematic effects. This is an essential step in data reduction and analysis towards QUBIC's efforts to detect the B-mode polarisation of the CMB.

Chapter 7

Map Artefacts

7.1 Introduction

Analysis of synthesized maps of a far-field source (*images-of-the-sky*) for each detector are an essential part of the calibration campaign. They are used to test optical performance, detector performance, the HWP, the polariser, cooling performance, and all other essential functions. A PO simulation of such a map is shown in Fig. 7.1a along with an example of a measurement of one of these maps for TES 76 in Fig. 7.1b. The measured map compares well with the simulation, given the signal-to-noise ratio.

QUBIC was undergoing a number of cool-downs, configuration changes, and upgrades between 2018 and 2021. In a dataset from 14-01-2020, a problem became apparent in the synthesized maps of the far-field calibrator. The beam pattern was replicated in nearly all functioning detectors. This pattern replication is described as 'ghosting'. An example of this ghosting effect is shown in Fig. 7.1c for TES 76.

This ghosting immediately became a priority issue that needed to be solved as quickly as possible so that the next cool-down and measurement campaign could begin. This chapter analyses the ghosted dataset in order to determine the cause and a solution in time for the next cool-down, which took place two weeks after the ghosting was first observed. This time constraint is a feature of the work in this chapter.

The production, optimisation, and measurements of these maps is the subject of Chapter 6 of this thesis. A more in-depth and discussion on synthesized maps and

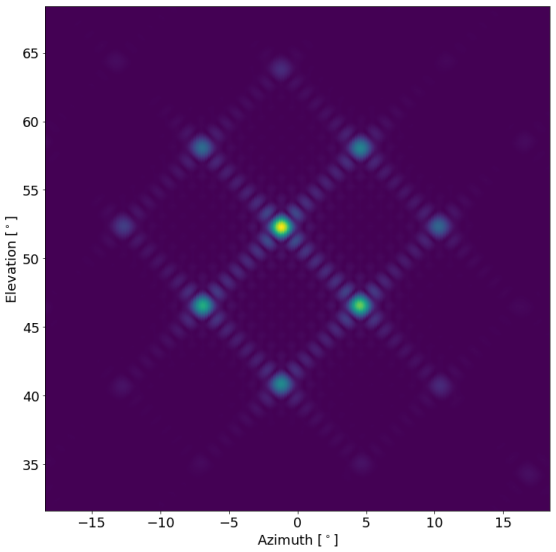

(a) A simulation of the scan for TES 76 by Burke (2021) [90].

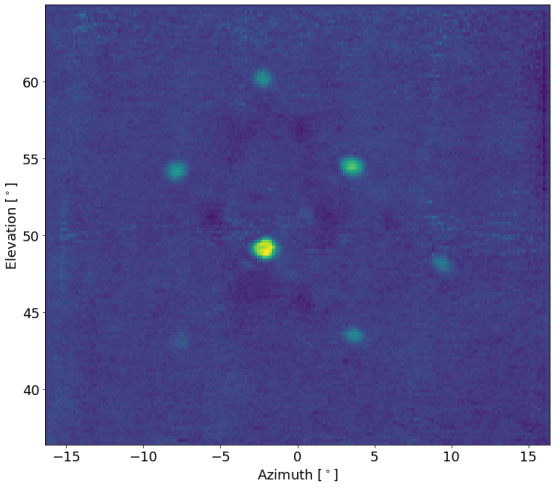

(b) A high resolution synthesized map scan from 06-04-2019 for TES 76.

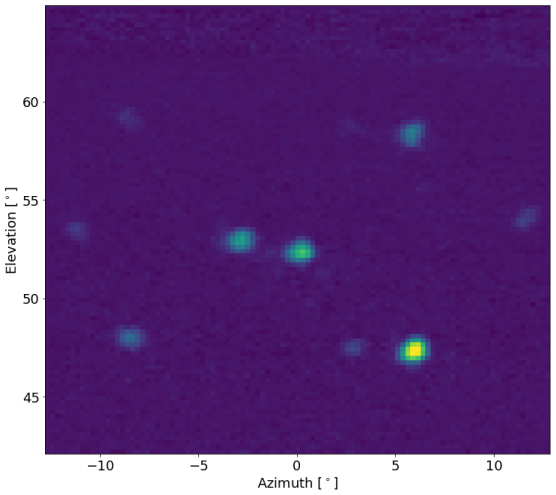

(c) A scan for TES 76 from 14-01-2020 when ghosting was first observed. Replication of the peaks is evident.

Figure 7.1: Image on the sky scans for TES 76. The scan in January 2020 (center) shows the ghosting effect. The figure on the bottom shows the predicted image on the sky from a simulated scan. The top image shows a scan prior to when ghosting was observed. All axes are in azimuth and elevation in degrees.

how they are generated is available therein. Chronologically, the ghost analysis took place before the optimisation and measurements in Chapter 6 but is shown after it in this thesis since Chapter 6 provides a thorough description of synthesized maps and a suitable context from which to analyse the ghost issue.

In this chapter, two categories of ghosting are investigated as the cause of the anomalous data. In hindsight, it appears intuitive and obvious that the configuration change to the optics should cause the ghosting but at the time, QUBIC had just resolved electrical cross-talk in a number of detectors, which was still occurring with much less frequency. So, to many of our collaborators, there was a strong fear there might be additional possible sources of electronic ghosting. This is why there is an investigation into electrical causes of ghosting as well as the more intuitive explanation of optical causes.

This chapter begins with a discussion of ghosting in similar CMB experiments followed by the configuration changes made to the QUBIC instrument immediately prior to observing the ghosting. The ghosting in the maps is measured and characterised for each detector so that its cause can be tested. The two main likely causes investigated are: ghosting by optical reflections or by electrical cross-talk. A Zemax model is also developed and tested to further investigate an optical mechanism that may cause the ghosting. A solution to this ghosting was discussed with the QUBIC collaboration and the results of the subsequent measurements are shown.

7.2 Ghosting in Similar Experiments

Ghosting is not unique to QUBIC and is a design consideration for all CMB instruments (including QUBIC). Discussions of issues regarding ghosting in CMB experiments have been published previously. Some examples are by Duivenvoorden, Gudmundsson, and Rahlin (2019) [105], Fowler et al., (2007) [106], and Aikin et al., (2010) [107]. In particular, two types of optical ghosting are described in these references: standing wave reflections from specific optical components and ghosting due to stray light (BICEP2) and surfaces (Atacama Cosmology Telescope, ACT).

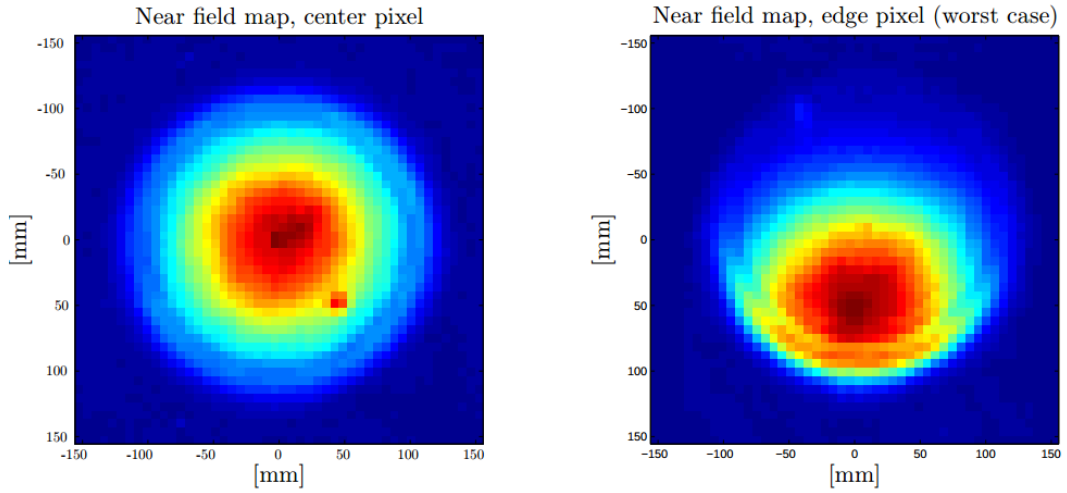

Figure 7.2: The optical ghosting observed by BICEP2 from a centrally located detector (left) and a detector from the edge of the detector array (right). These are similar synthesized images as shown in this chapter where BICEP expected a Gaussian beam and ghosting contributed an additional peak. The effect is stronger for the offset detector and the additional peak is smeared.

Of these ghosting types, QUBIC's ghosting most closely resembles that of the BICEP2 ghosting that was caused by reflections from a nylon blocker with a metal-mesh edge filter. This metal-mesh edge filter has the same type of construction (AIG Cardiff, Ade, Pisano, Tucker, and Weaver (2006) [74]) as the HWP and polariser used in QUBIC. Fig. 7.2 is reproduced from Aikin (2010) [107] and shows the ghosting affecting synthesized maps for detectors in BICEP2. The left of Fig. 7.2 shows an on-axis detector and an additional peak is visible at approximately (50 mm, −50 mm) on the synthesized map. The right of Fig. 7.2 shows the map for an offset detector and the ghosted effect appears smeared.

In the BICEP2 and ACT cases, ghosting contributions were found to be $< 2\%$ of the main beam. The QUBIC ghosts measured in January 2020 appear to be generally higher in amplitude ($\sim$40%) with respect to the main beam.

Typically ghosting is treated as an optical issue but here electronic ghosting (e.g. cross-talk) is also tested. Electronic ghosting, in this context, is a term to describe how different bolometers may electronically interfere with each other. Cross-talk has been noted in QUBIC data previously but the cooling and detector performance has been improving so it was surprising to see a similar ghosting pattern in the January 2020 dataset.

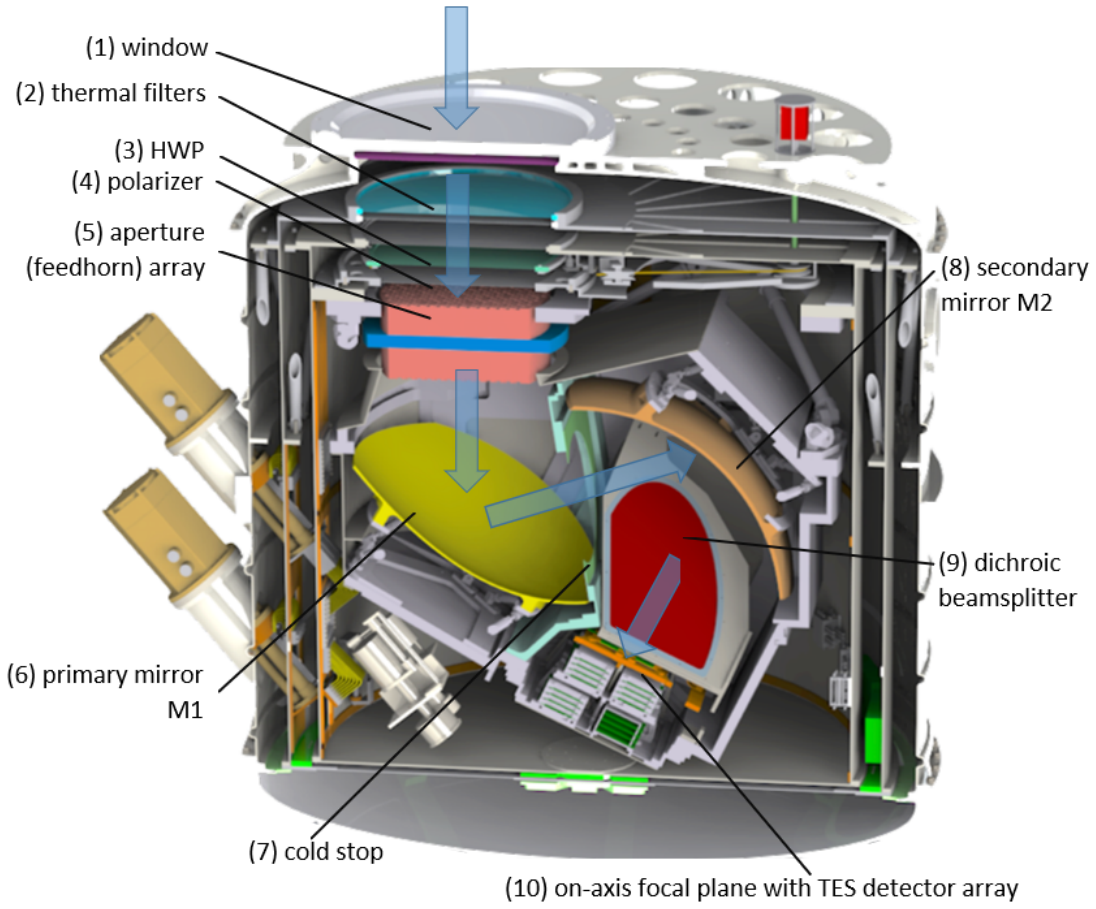

Figure 7.3: An internal cut of QUBIC's cryostat and optical elements reproduced from Mousset et al., (2020) [56]. The detectors and mirrors are mounted inside cryostats at various temperatures. This chapter concerns measurements on the TD, which has smaller mirrors and a smaller horn array compared to what is shown here. This figure was shown previously in Chapter 2.

7.3 Configuration Change Prior to Ghost Measurements

Fig. 7.3 shows the QUBIC FI. It should be noted that the TD discussed in this chapter has smaller mirrors and a smaller horn array compared to what is shown in the figure. The TD was built up over time by installing and testing new parts and functionalities. In January of 2020, the rotating HWP and polariser were added to begin testing the low-temperature mechanical HWP rotation system and the polarisation performance of the instrument. This is a key performance metric due to QUBIC's dependence on low systematic effects particularly with respect to polarisation. The locations of the HWP and polariser are shown in Fig. 7.3. A

neutral density filter (NDF) was also added to the cold-stop aperture, shown in the figure, at this time.

The scan resolution for this dataset was lower than had been used previously. This is evident in Figs. 7.1b and 7.1c where the older dataset had a much higher scan resolution. A low resolution is sufficient for most calibration measurements and saves time. Other than the HWP, polariser, NDF, and scan resolution, the TD configuration for the pre-January 2020 dataset and the January 2020 dataset were identical.

7.4 Ghost Identification and Measurement

The ghosting phenomena occurring in QUBIC's January 2020 dataset is shown in Fig. 7.1c. The ghosting is characterised by a replication of the pattern (shown in Figs. 7.1c and 7.4), the replicated patterns being lower in amplitude, and the pattern being typically shifted in azimuth and elevation from the central peak. These are the characteristics that are analysed to try and learn about the cause of the ghosting.

This section will show the method used to measure the synthesized maps for each detector and characterise the ghosting by location 'on the sky' and amplitude ratio. First, the TESs must be selected for the analysis since some TESs have low SNR or are saturated in this dataset. Second, the selected detector maps are measured. Third, locations of main peaks and the replicated peaks are selected and angular measurements and amplitude ratio measurements are made.

7.4.1 TES Selection

There are 248 detector bolometers (and 8 temperature bolometers) in the quarter focal plane of the TD. In Fig. 7.4, there are examples of TESs that were useful for analysis and examples of TES to be excluded. TES 81, 85, 86, 87, 88, and 89 have sufficient SNR and are included in the dataset. They show a clear replication of the peaks from the synthesised image on the sky. TES 82, 83, 84, and 90 are excluded since they are noisy.

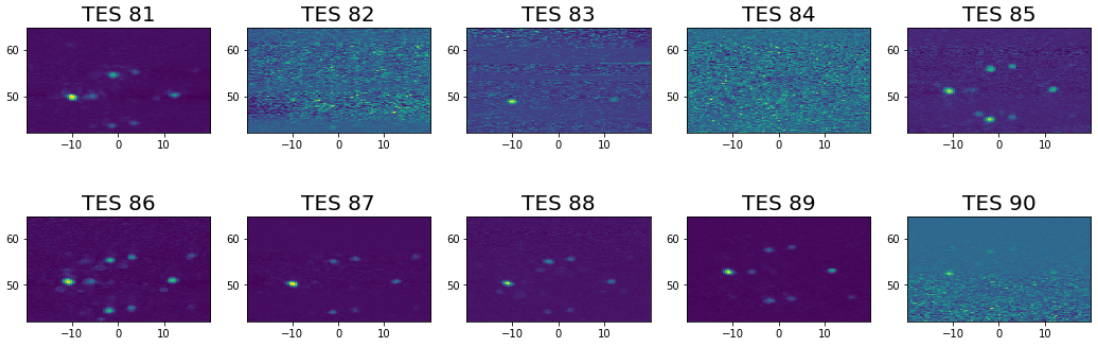

Figure 7.4: An example of synthesized maps from which 'ghosted' TES are selected. TES 81, 85, 86, 87, 88, and 89 show the replicated pattern and are included in the filtered dataset. TES 82, 83, 84, and 90 are noisy and are not suitable for inclusion in the dataset. The axes are azimuth and elevation in degrees as in Fig. 7.1.

A significant point to note here is that all TES that were excluded were noisy or completely blank. Ghosting was evident in all 'good' TESs. This introduces a form of selection bias that must be considered when attempting to understand all of the analysis presented later in this chapter. It is especially important when considering how electronic effects may be causing the ghosting.

From this procedure, 131 TES from the TD quarter focal plane (248 detectors) are chosen for analysis. For this analysis to take place, the relevant data (in the form of synthesized image-on-the-sky maps) must be collected from the full set of maps and this is described by the next section.

7.4.2 Data Processing of Ghost Maps

A program was developed to cycle through the synthesized maps for the ghosted detectors allowing the user to select the approximate location of the peaks by hand. The program then fits a 2D Gaussian to each peak in order to find the amplitude and width.

An example of this is shown in Fig. 7.5. From the procedure, the amplitude, coordinates, and FWHM of the peaks are found and the separation angle of the peaks can be calculated. The angular separation (Fig. 7.6a) is the angle between the peaks on the sky along the optical axis. The angular tilt (Fig. 7.6b) is the angle of the line joining the peaks in terms of azimuth and elevation coordinates on the synthesized map. These are given on the synthesized map for TES 6 in Fig. 7.5. There is occasionally a question regarding the validity of these amplitudes

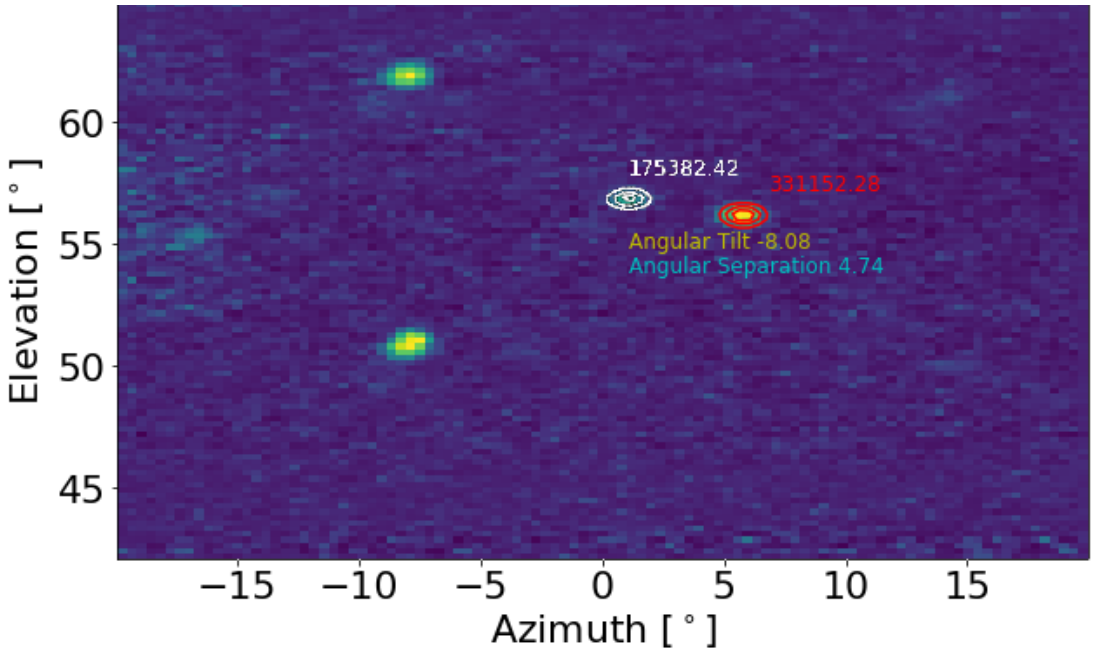

Figure 7.5: An example of the 2D Gaussian fits to the central (white) and replicated peak (red) for TES 6. The amplitude for each peak is shown as are the separation and tilt angles.

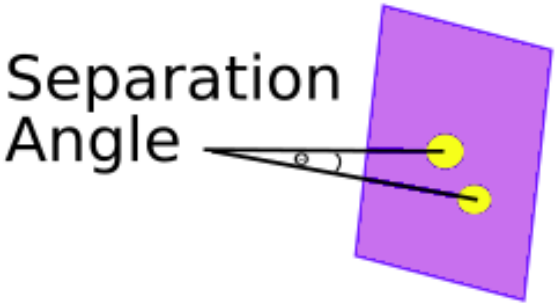

(a) Illustration shows how the term *separation angle* is defined for the purpose of this analysis. This illustration shows a simple on-axis model of the separation angle metric. During these measurements, the QUBIC instrument was centred at an elevation of 50°. Cross-elevation was accounted for in post-processing of the synthesized beam maps.

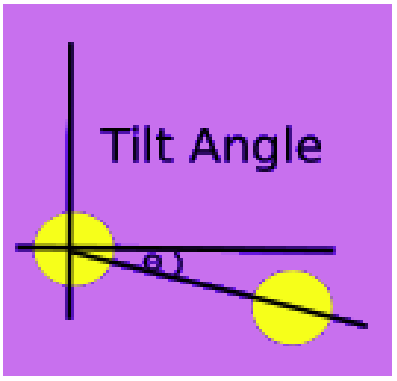

(b) Illustration shows how the term *tilt angle* is defined for the purpose of this analysis. The angle of the ghosted peak is negative from the horizontal axis.

Figure 7.6: Schematic of measurements made between the main and ghosted peaks in a synthesized map for a detector. An example of these data are shown in Fig. 7.5.

since the bolometers can be saturated at the peaks. At the time when these measurements were taken, saturation in the detectors was not fully characterised and this must be borne in mind for this analysis (saturation is evident in Fig. 6.11 in the 170 GHz data where the main peak is smeared and not Gaussian in shape).

These data are collected for each TES selected for ghost analysis and a 131×10 data matrix is made. This matrix contains data for 131 bolometers in the form of: TES Number, peak 1 x-position, peak 1 y-position, peak 2 x-position, peak 2 y-position, amplitude 1, amplitude 2, amplitude ratio, tilt angle, and separation angle. The data in this form can be used to test for both electrical and optical causes of ghosting.

7.5 Electronic Causes of Ghosting

Cross-talk is interference caused by electric or magnetic fields between one detector and another. This could occur at any point in the readout electronics but particularly so where sensitive electronic components are physically close (e.g. adjacent wires, columns or processing boards like ASICs).

This section will investigate if the ghosting could be caused by an electrical effect like cross-talk. This will be investigated by finding detectors where ghosting occurred and seeing if it was particularly strong for bolometers that were close physically or electrically. If an image from one bolometer is recorded by another one, it will appear shifted from the main image due to the bolometer's different location on the focal plane as will be explained.

7.5.1 Physical Proximity of TES

One TES on the focal plane might cause cross-talk in a TES next to it physically on the focal plane. For example, in the top left of Fig. 7.7, TES 125 (highlighted in red) is physically near TES 126, 113, and 114 (highlighted in orange). Each detector has unique pixel identification numbers unique to the physical coordinates of each bolometer on the focal plane (Fig. 7.7). In the quarter focal plane of QUBIC's TD, the bolometers are connected to two ASICS of 128 bolometers each. They are ordered by pixel number 1 - 128 on each ASIC. Pixel numbers are

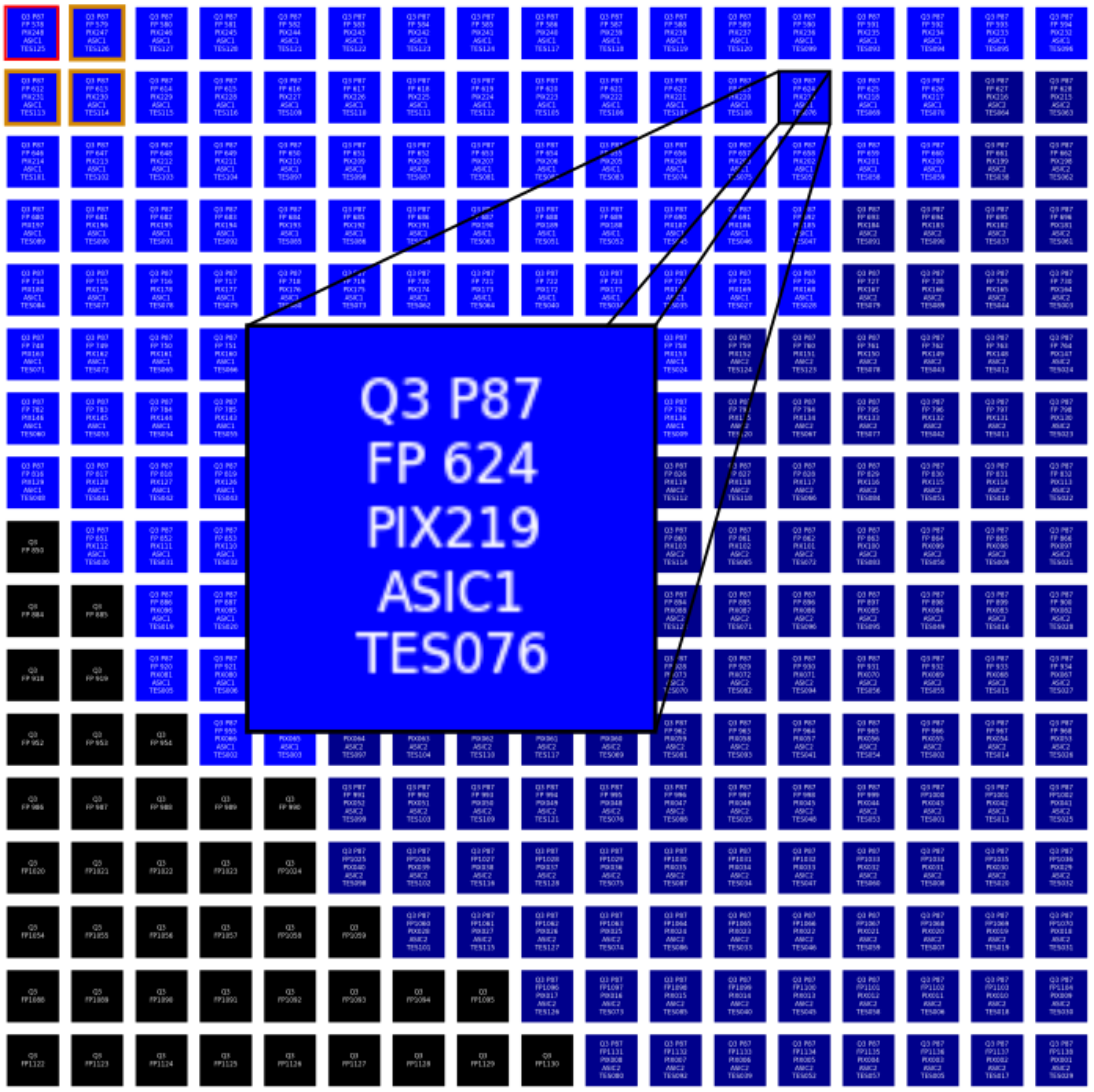

Figure 7.7: Physical locations and number labels for each TES on the TD focal plane. The TD has one quarter of the full array of bolometers. The quarter focal plane quadrant details (there are two ASICs per quarter focal plane, blue and dark blue) and different pixel labels are listed for each TES. A zoomed image of TES 76 is shown as an inset. Four TES are highlighted in the upper left to show how TES 125 (red) might be likely to interfere with TESs 126, 113, and 114 (orange).

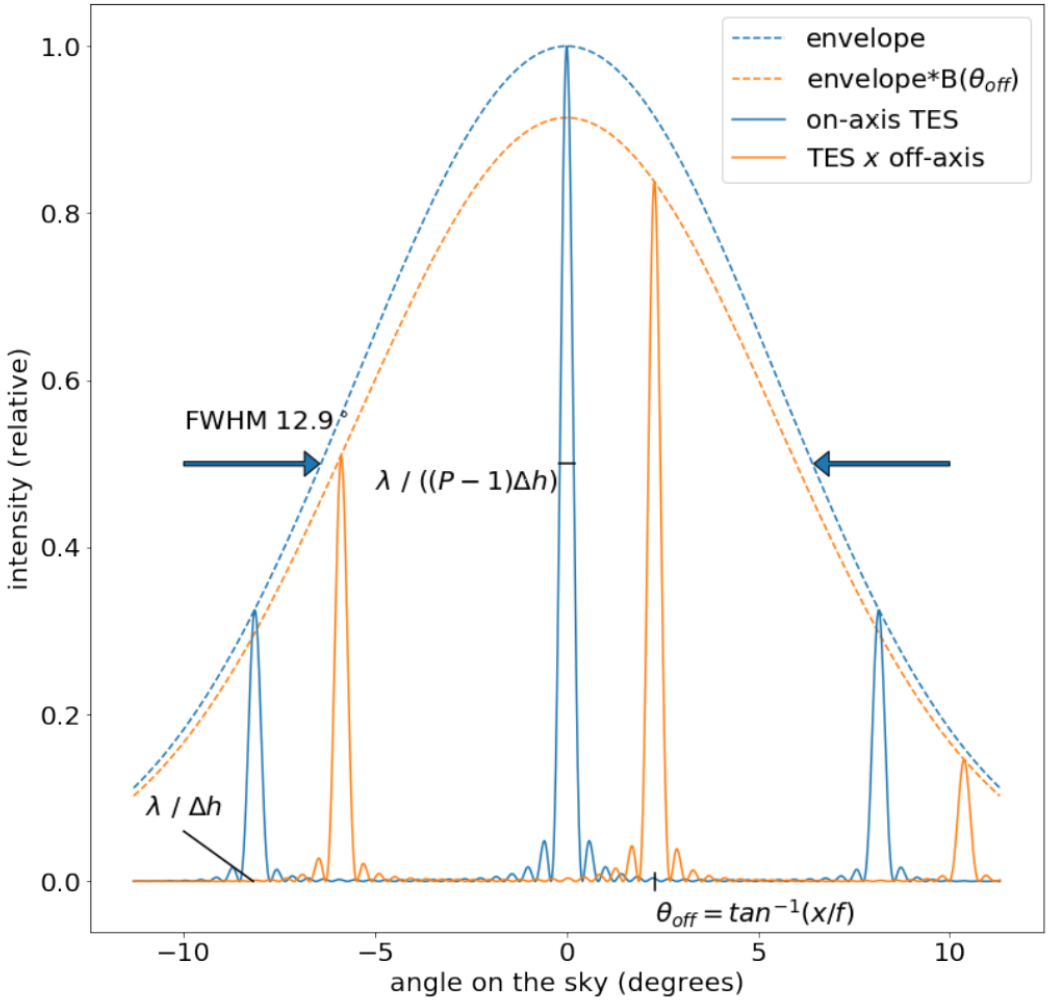

Figure 7.8: The blue line shows the synthesized beam for a fictitious idealised TES at the centre of the focal plane. The orange pattern is for an off-axis TES on the focal plane. The synthesized image pattern is different for all TESs. The pattern is dependent on the inter-horn separation (Δh), the number of horns along one axis of the horn array (P), and the distance of the TES from the centre of the focal plane (x). This figure is reproduced from O'Sullivan et al., (2020) [71].

distributed over the focal plane in a way that appears visually random but there are practical manufacturing and layout reasons for the TES labelling, which are not relevant for the purpose of this thesis.

Fig. 7.7 shows the location of the bolometers and their corresponding TES numbers. Different TESs should produce different synthesized images based on their location on the focal plane. An example of the change in synthesized image for different TES is shown in Fig. 7.8. This is described by O'Sullivan et al., (2020) [71]. The blue line in this figure gives the synthesized image for a bolometer if it

were at the centre of the focal plane. The orange line is the synthesized image for a TES on the focal plane that is 12 mm offset from the centre. The image is offset from the central one due to the bolometer's off-axis position on the focal plane.

This angular offset of these synthesized images can be calculated by an equation given in O'Sullivan et al., (2020) [71] as:

$$\theta_{offset} = \tan^{-1} \frac{x}{f}, \tag{7.1}$$

where x is the off-axis distance of the TES on the focal plane and f is the focal length of the instrument ($f = 300$ mm). Using this, two calculations can be made to understand ghosting and physical proximity of the TES.

The distance between adjacent TESs is 3 mm. Using Eq. 7.1, TESs 3 mm apart would produce a ghost separation angle of 0.57°. TESs 4.2 mm apart (separated diagonally) would produce separation angles of 0.80°. The observed separation angle is 4.85° and is constant across the focal plane for the 131 ghosted TESs. The possibility that TESs near each other on the focal might induce ghosting effects are incompatible with the observed average separation angle of 4.85°, which corresponds to six times the diagonal distance between horns.

Ghost images from one bolometer on a physically nearby one is the simplest explanation of electronic causes of ghosting but no convincing evidence for this has been found. Other possible electronic causes for the ghost images will now be investigated.

7.5.2 Electronic Proximity of TES

The integration of the electronics are described by M. Piat et al., (2021) [67] and the readout electronic multiplexing are described by D. Prêle et al., (2016) [108]. In Fig. 7.9, it can be seen that each ASIC has 4 columns connecting the ASICS to the SQUID boards. Each column has 32 TESs connected to it by wires (Fig. 7.10) throughout the focal plane. The data in Fig. 7.11 describe the relationship between the TESs and how they are ordered into columns. These are some of the possible sources of electronic interference between detector signals that may occur in bolometers not in close proximity on the focal plane. In the processed data, the

detectors are recorded by their TES number so understanding the layout in this form is important since it is necessary if any electrical relationship between the ghosting in detectors is to be found.

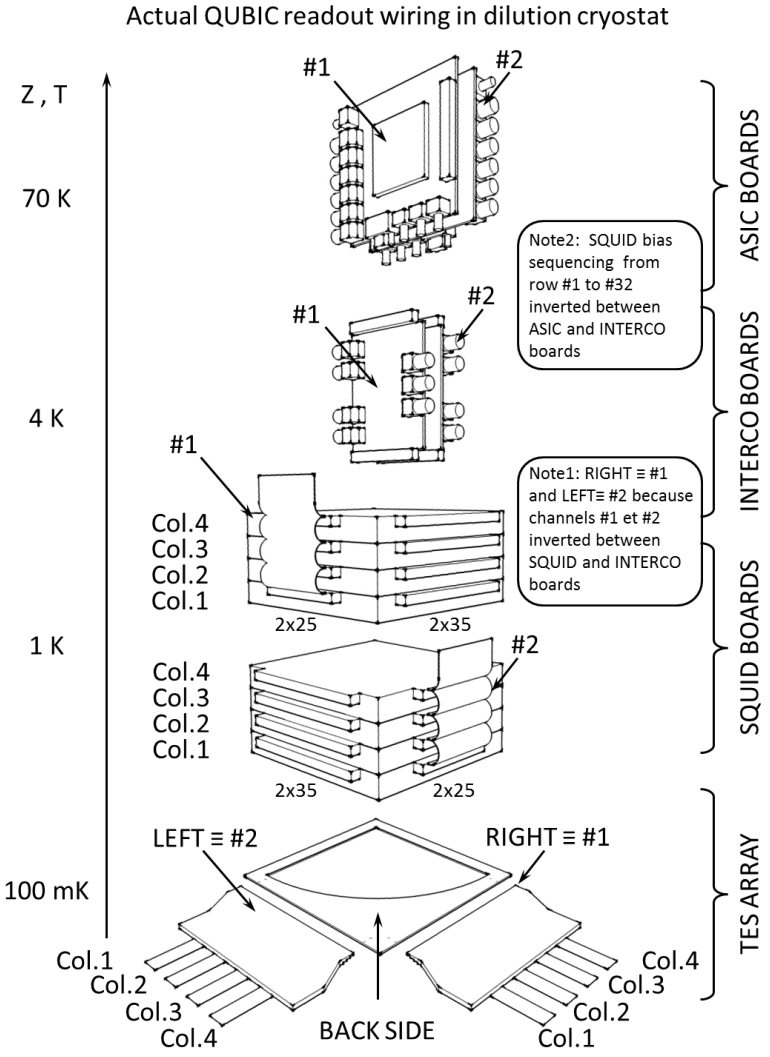

Figure 7.9: A schematic diagram of the detector electronics (image is shown inverted). The temperature of the electronic stages are also shown. The location of the electronics in the instrument is shown in Fig. 7.3.

The effect of this column-wise description of the bolometers is illustrated in Fig. 7.12. Each square is a bolometer. The colour of each square corresponds to a column. In total there are 8 columns represented by 8 colours. For a given colour, there are 32 SQUID numbers. In the figure they are labelled, for example, as SQD1, SQD2, SQD26. They are not necessarily physically near each other on the focal plane, which is evident in Fig. 7.12. As such, it is necessary to test for the electrical proximity of TES in terms of wires and columns.

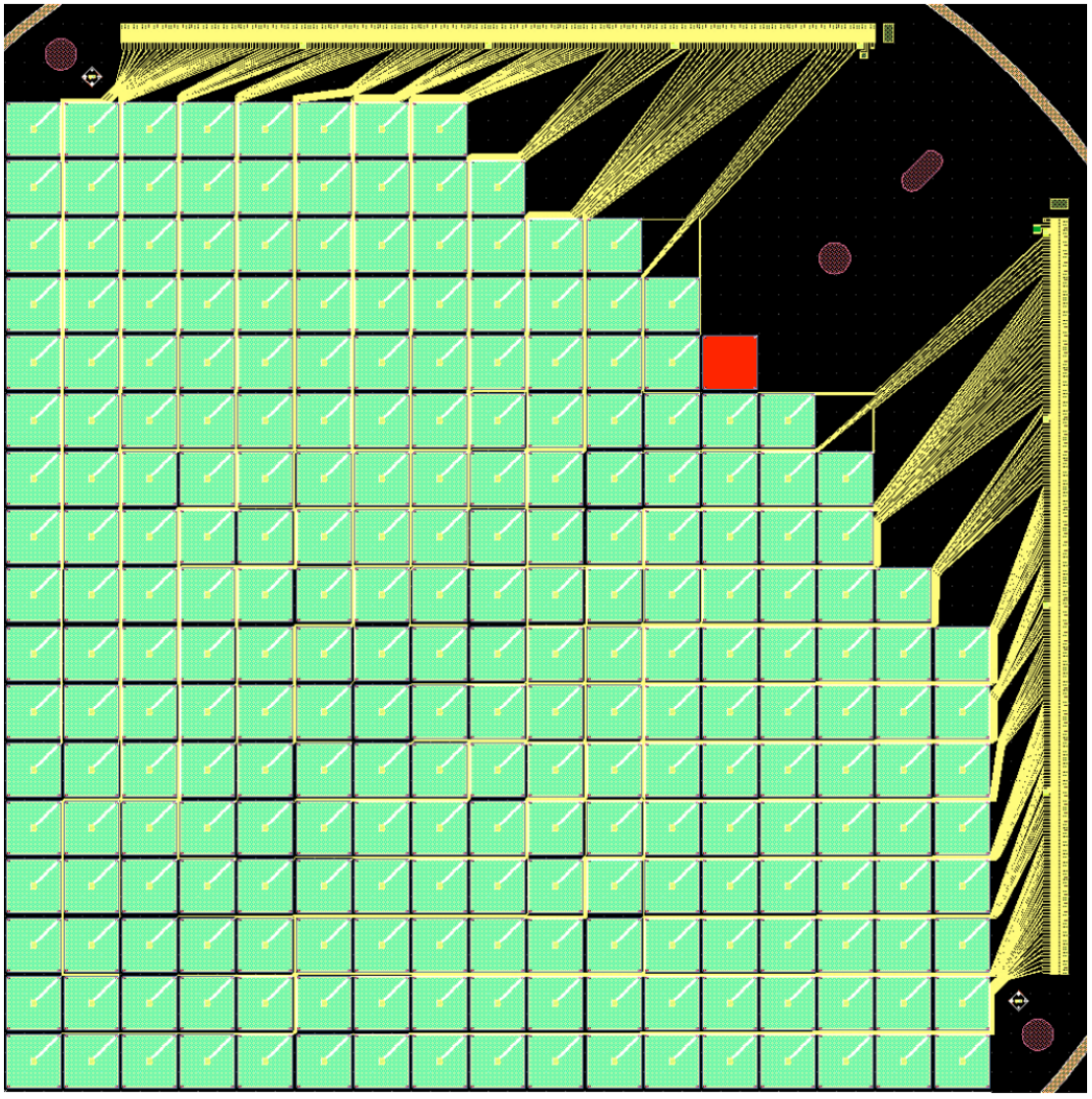

Figure 7.10: The wiring (yellow lines) between the detectors (green) and the columns (yellow bars top and side) are shown here. Here it can be seen that detectors may be near each other on the focal plane, have nearby by wires or be near in the ASIC columns.

7.5.3 Discussion & Analysis

The ghosted TES are grouped according to their electronic columns as described in the previous section. When plotted on the focal plane (Fig. 7.12), each coloured square represents bolometers on a column with the *SQD#* (SQUID number) marked also. TESs from the ghosted dataset are marked by a red diamond.

Fig. 7.12 can be interpreted in multiple ways. In a simplistic view, it appears some ghosts occur in groups. For example, for column 1 of ASIC 2, it looks like

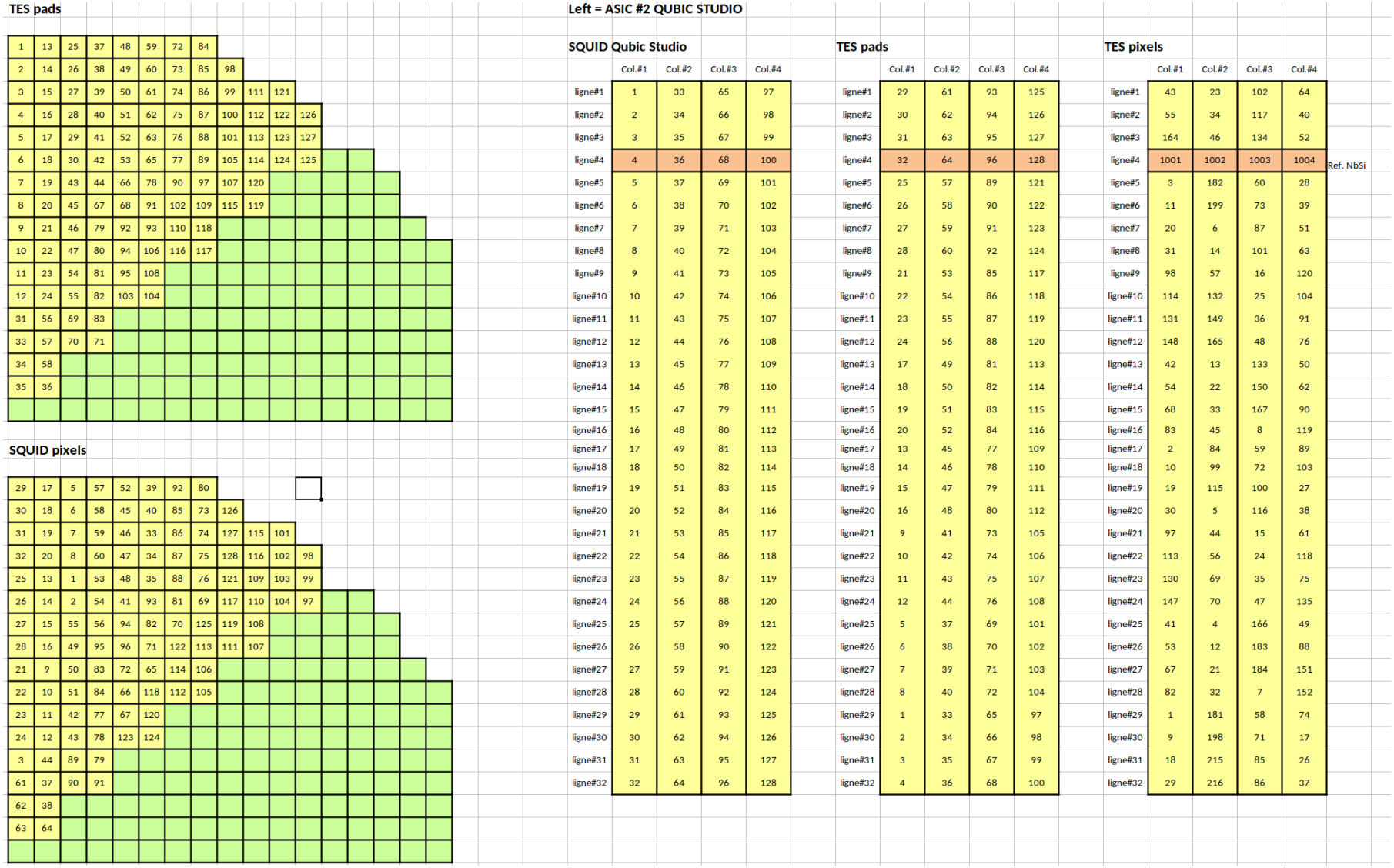

Figure 7.11: An example of the correspondence between TES numbers and SQUID column numbers. Provided by private communication, Torchinsky (2020) [109].

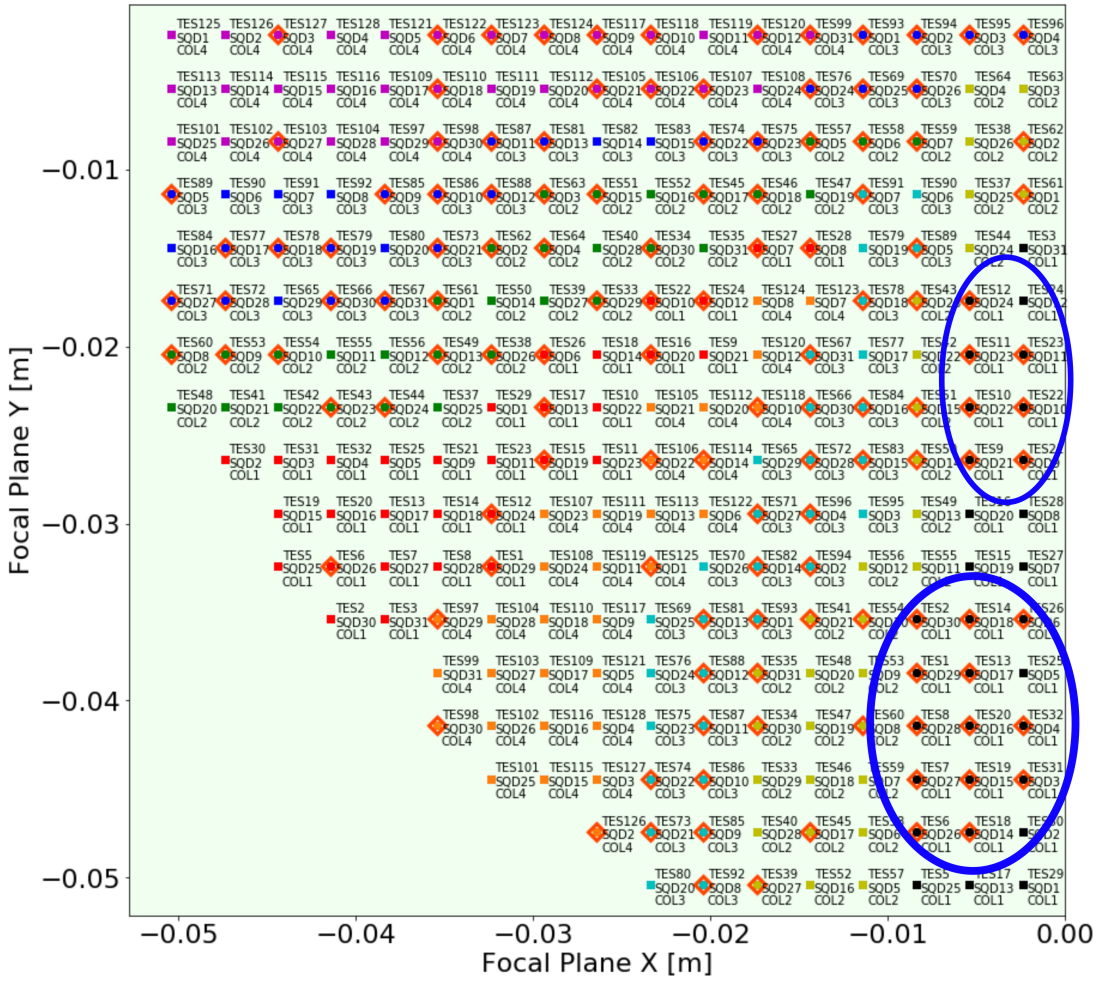

Figure 7.12: Focal plane plot displaying ghosted TESs with red diamonds, ASICs and columns in different colours. ASIC 1 has red, green, blue, and magenta columns, ASIC2 has black, yellow, blue, and orange columns. An example of possible ghosting by physical proximity groupings are highlighted by blue circles.

there are two clear groupings of ghosted TESs circled in blue. It looks like this in other columns too.

A more quantitative and less subjective figure is shown by Fig. 7.13. This figure plots each bolometer on a column with each ghosted TES set to 1. Detectors not in the dataset are zero. Here, the same grouping effect is observed in some columns. In other columns the ghosting appears completely random. From this data there is no clear evidence to show there is an electrical ghosting relationship between the detectors. There appears to be ghosting distributed throughout the whole focal plane with no relation between nearby detectors, columns, SQUIDS, or ASICS.

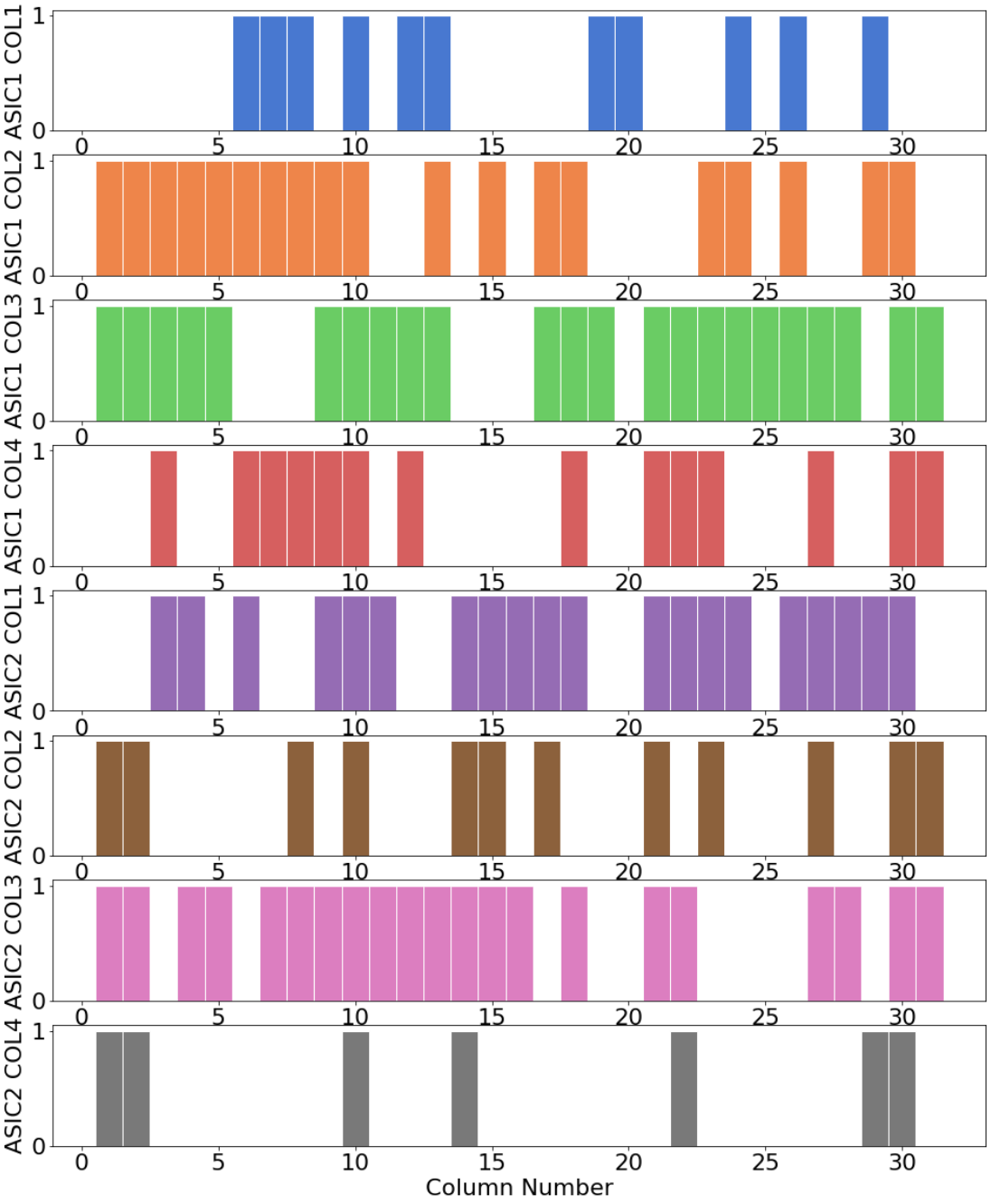

Figure 7.13: Detectors with ghosts in each column are set to 1. If there is no ghost, the value is zero. Each SQUID column has a distinct colour and its own row. There are four columns per ASIC.

The data from Fig. 7.13 is susceptible to selection bias induced during the selection of the 131 of 248 detectors in the dataset. All TESs with a good signal-to-noise ratio (SNR) were selected. The distribution of good TESs with good SNR would likely reproduce the grouping effects. As such, any perceived groupings are likely observed due to selection bias and due to the human tendency to observe patterns in random data (Kahneman and Tversky (1972) [110]).

7.6 Optical Causes of Ghosting

7.6.1 Analysis of Pipeline Data

Using the synthesized image data collected from the ghosted TESs, optical effects are also investigated. For example, if a standing wave is present in the filters, HWP, or polariser, this might cause a ghost effect on the focal plane. A ghost or standing wave effect might also occur from an optical element heating and producing thermal emission. The former case is more likely given the type of peak replication observed in this dataset.

The processed data are used to test for optical ghosting. The tilt angle, separation angle, and relative amplitudes may indicate how optical ghosting is occurring. The radial distance of the TES from the centre of the focal plane is a useful metric to show the processed data. This is because the angle of the optical ghost may be constant across the focal plane or the ghosting angle might change with radial distance on the focal plane. Either case would help in understanding the ghosting in the bolometers. The contrary is also true, if the data look random and uncorrelated data, this would indicate further investigation on electrical causes is required.

The separation angle as a function of radial distance is shown in Fig. 7.14. The separation angle for each TES in the processed dataset is plotted with its radial distance from the centre of the focal plane. A line is fit to the data to test the relationship of tilt angle with radial distance. It shows no change in TES angle across the focal plane. There is a spread in the data so the line's r^2 value is low ($r^2 = 0.0004$). The average separation angle from these data is 4.85° and constant across the focal plane.

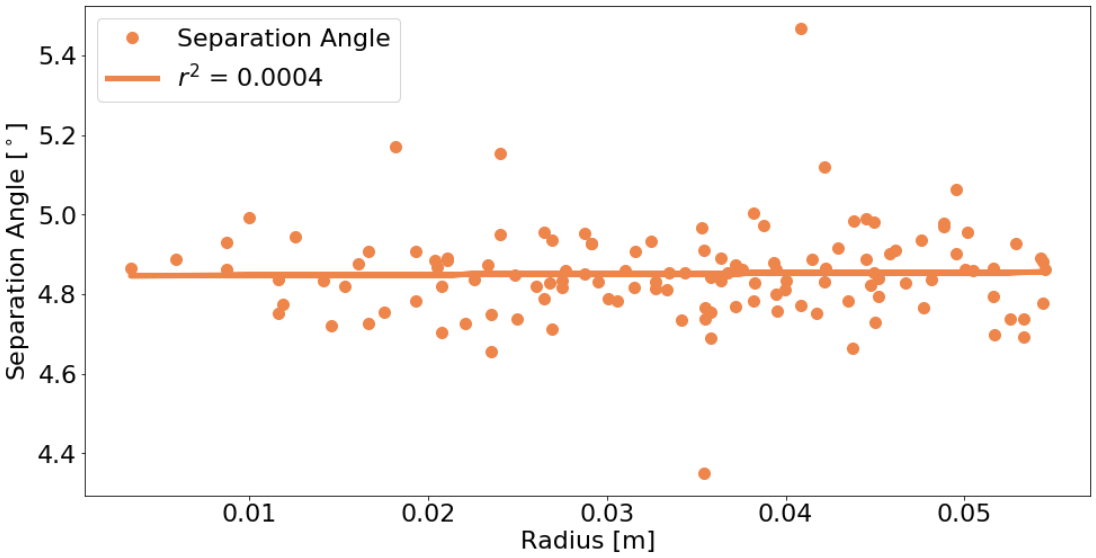

Figure 7.14: Separation angle as a function of radial distance. Each data point corresponds to one of the 131 TESs from the filtered dataset. The x-axis shows the TES's radial distance from the centre of the focal plane.

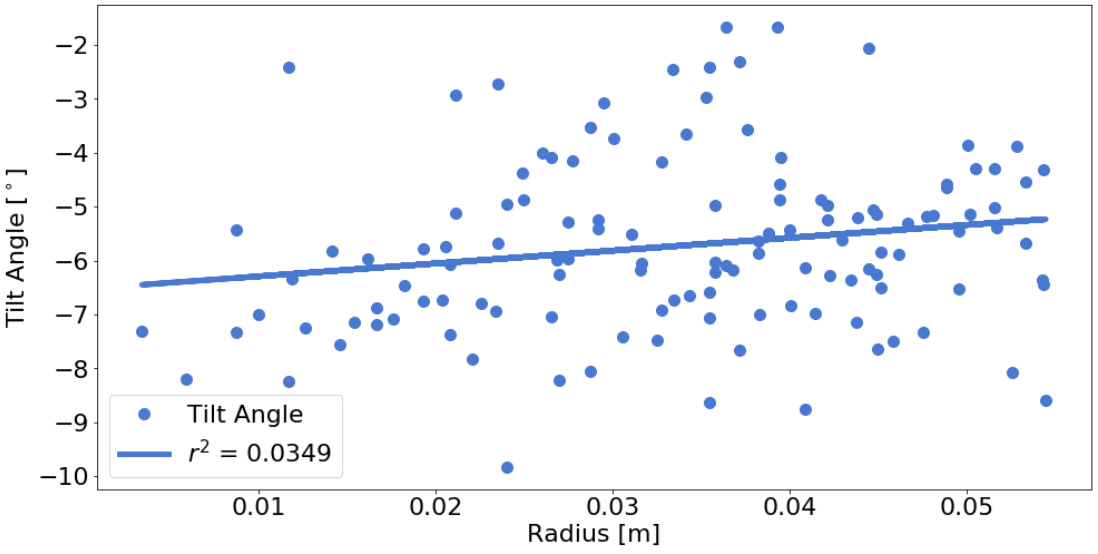

Figure 7.15: Tilt angle as a function of radial distance. Each data point corresponds to one of the 131 TESs from the filtered dataset. The x-axis shows the TES's radial distance from the centre of the focal plane.

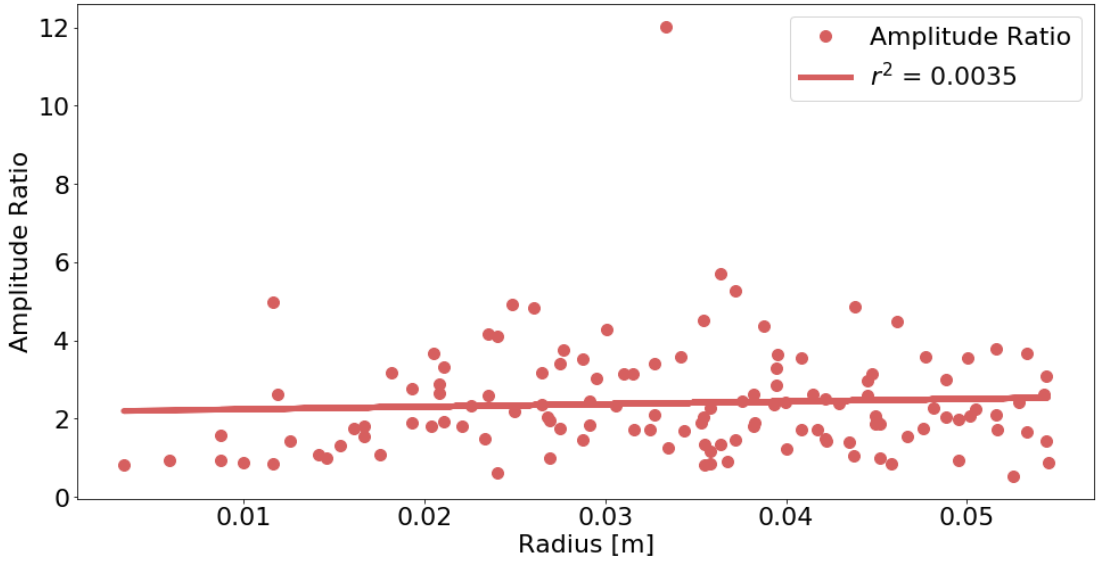

Figure 7.16: Peak amplitude ratio as a function of radial distance. Each data point corresponds to one of the 131 TESs from the filtered dataset. The x-axis shows the TES's radial distance from the centre of the focal plane.

Fig. 7.15 shows a similar result for the tilt angle. The fitted line has a small slope but the spread of data provides another low r^2 value ($r^2 = 0.0349$). Any indication there could be a relationship with tilt angle and radial distance is weak. The mean tilt angle is $-5.69°$ and appears constant with radial distance.

The amplitude ratios of each peak to its ghost image (Fig. 7.16) tell a similar story. The ratio is typically in the 1 - 4 range with an average of 2.37. The amplitude ratio across the focal plane appears approximately constant like the angular tilt and angular separation. These data indicate that the replicated peaks have $\simeq$42% of the intensity of the main peaks. This is a much higher level of ghosting when compared to other CMB experiments that are typically at the $< 2\%$ level (Duivenvoorden, Gudmundsson, and Rahlin (2019) [105], Fowler et al., (2007) [106], and Aikin et al., (2010) [107]). It still has to be considered that at the time these measurements were taken, there was still saturation evident in the detectors at 150 GHz. This means the 42% intensity of the replicated peaks is likely lower since the main peaks would have much higher amplitudes if it were not for saturation.

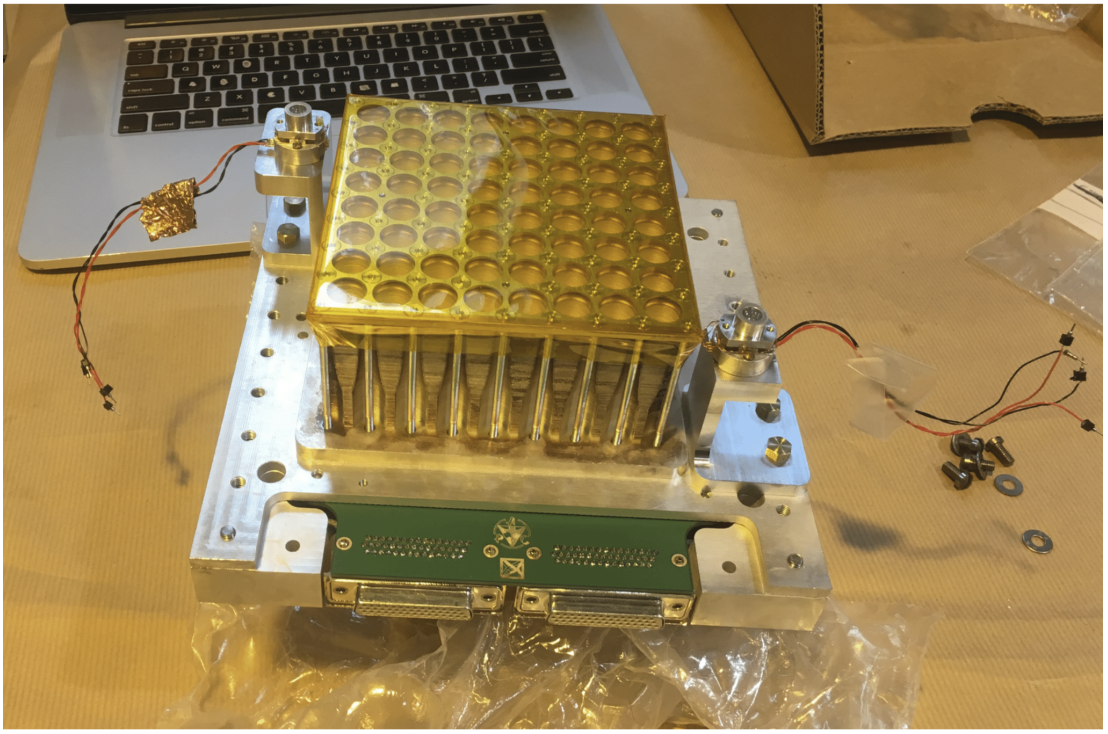

Figure 7.17: The 8×8 TD horn array is shown. The internal calibration sources are mounted at the corners and they face the primary mirror inside the optical combiner. The opposite side of this horn array faces the polariser. The grey/silver region outside the horn array is the area with 'unknown optical properties'. This was also shown in Fig. 2.20 and is reproduced and enlarged here for convenience.

7.6.2 An Optical Mechanism for Ghosting Modelled in Zemax

The QUBIC FI has been designed for absolute control of polarisation. The TD has the same optical setup for the cryostat aperture and filters in front of the horn array as shown in Chapter 2. The TD horn array is reduced in size and this leaves a region outside the horn array which has unknown optical properties and is still in a light receiving path. This is shown in a photograph in Fig. 7.17 by the grey aluminium region surrounding the square TD horn array.

In the FI, un-polarised light (red and green in Fig. 7.18) enters the window and becomes polarised by the rotating HWP and polariser combination according to the law of Malus. Any light reflected after the polariser (e.g. off the TD array or the area between or outside the horns) should be similarly polarised so that it can pass back through the polarisers towards the sky.

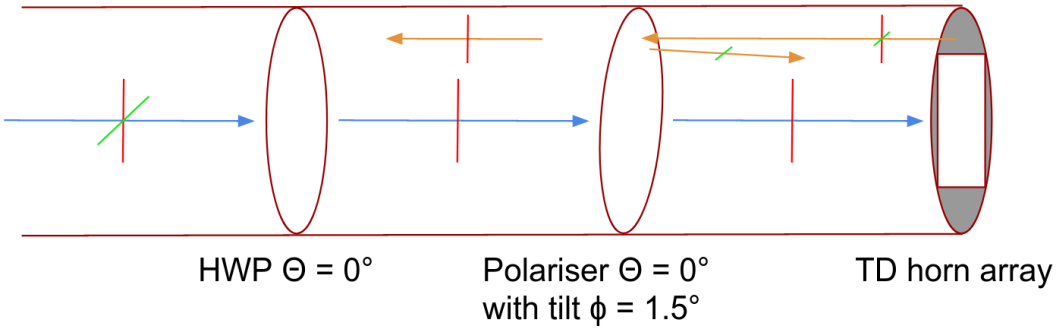

Figure 7.18: The proposed mechanism which could lead to optical ghosting in QUBIC. The blue light on the left enters from the sky un-polarised (red and green). When the HWP and polariser are aligned, linearly polarised light (e.g. red) couples to the horn array. The TD array has a region (grey) to the side with unknown optical properties. If light reflects and some cross-polarisation is induced (red with smaller green cross-polarised component) from this region, the cross-polarised light (green) can reflect off the polariser and enter the combiner. Additionally, the aluminium area shown here does not fully cover the full FI aperture area, the actual unknown area is larger than shown here.

The optical properties of the region outside the TD horn array (greyed region in Fig. 7.18) are unknown so it is possible that some light may get cross-polarised on reflection from this region (see the orange light ray emitting from the grey region on the TD horn array in Fig. 7.18). When these rays reach the polariser again the majority have the polarisation (red) to continue to the sky as intended while the cross-polarised light (green) would reflect off the linear polariser. The linear polariser had been installed with a tilt of $\phi \approx 1.5°$ when the ghost issue occurred. In this configuration there exists a mechanism for some cross-polarised light (from the edge of the horn array) to enter the horn array after reflecting off the tilted polariser. Work by Burke (2021) [90] showed that the power reflected from the horns in the array itself would be too small to explain the effects discussed here.

A Zemax model was developed to test this mechanism. The main elements and their optical properties are highlighted in Fig. 7.19. The simulation setup is shown in Fig. 7.20. A basic model of the QUBIC optical combiner was implemented with the primary and secondary mirrors and the focal plane (white square in Figs. 7.19 and 7.20). The 8×8 horn array for the TD was modelled including the region around the TD horn array (for the FI, the area would be covered entirely by horns). This is evident in Fig. 7.20a (and also Fig. 7.18). In the model the horn area (light blue in Fig. 7.19) is a square aperture while the region around the horn area is modelled as flat reflective material.

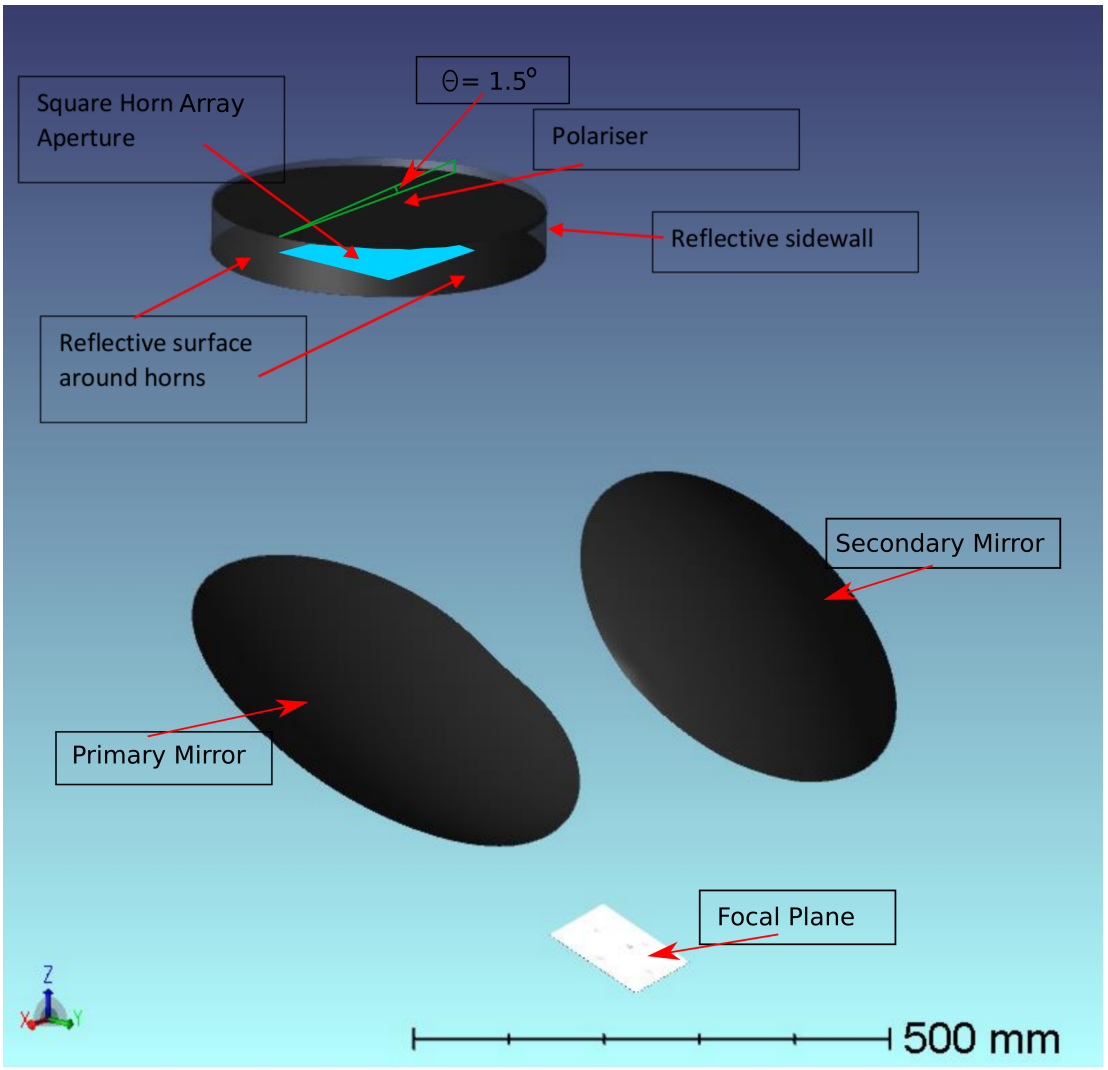

Figure 7.19: The Zemax setup used to test for ghosting (without any simulation rays showing). The TD horn array is coloured in blue and the region around it is set as a reflector. The side walls are cylindrical reflectors. Simulation source rays are propagated from within the polariser and horn array so the polariser is set as a reflector. The tilt of the polariser shown by the green line illustration on the polariser at $\theta = 1.5°$. The focal plane (white) is used as the 'detector' in Zemax. QUBIC's mirrors are also included.

Fig. 7.20a shows how the source layout rays (blue) are emitted from the horn array and surrounding area up towards where the polariser would be (not drawn). With the polariser added to the model at 1.5°, as in Fig. 7.20b, the rays are reflected in the region between the polariser and horn area. The polariser has a secondary angular offset of 1.5° around the z-axis as was noted during the disassembly after a cool-down in APC. Some of the rays pass through the horn array aperture and travel through the optical combiner onto the focal plane (the final ray segments shown in light blue and yellow).

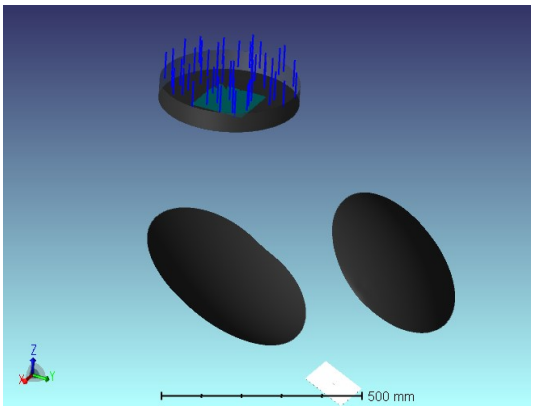

(a) This figure shows the source rays (blue) emitted from a circular disk towards the polariser (not drawn so the rays are visible). The blue square corresponds to the horn array where rays can pass.

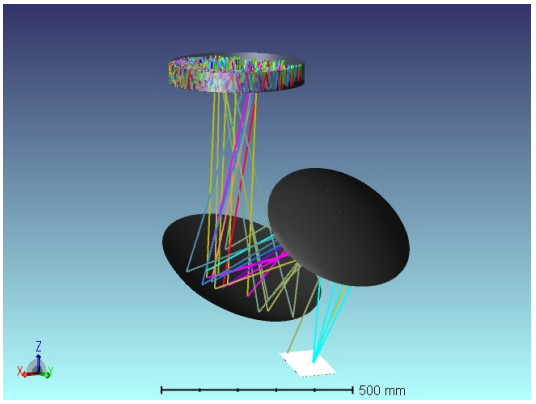

(b) The polariser is added above the horn array at 1.5° and rays reflect in between the polariser and horn array area. Some rays will pass through the horn array into the optical combiner and onto the focal plane (light blue rays on detector).

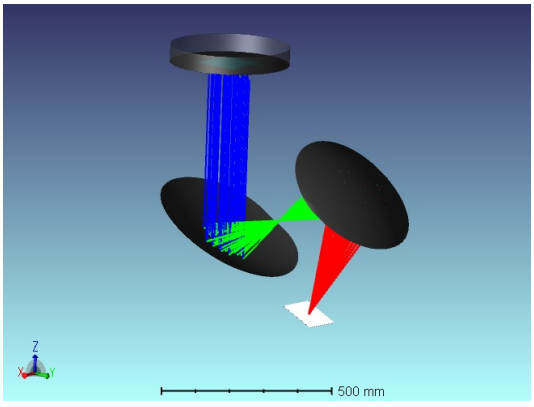

(c) To gauge the relative fraction of rays, a set of nominal rays are added for comparison to the reflected rays. These rays should focus at the centre of the focal plane array.

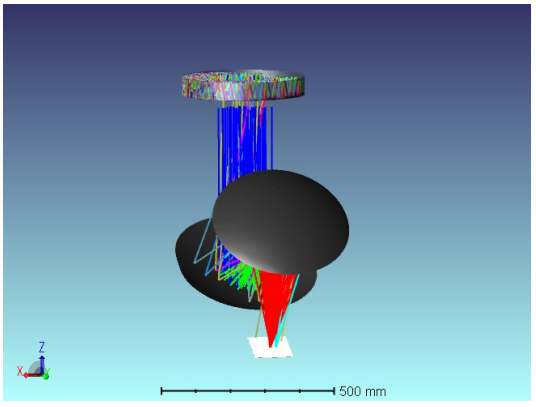

(d) Both ray sets are shown. It is clear that rays from within the polariser and horn array are incident on the focal plane at distinct locations.

Figure 7.20: The setup of the Zemax model used to test the ghosting. The model includes the rays reflected from the horn array and polariser along with a normal nominal case where rays are focused correctly at the centre of the focal plane. The rays are set to change colour after interacting with a surface starting with blue.

Peak	Central	Ghost 1	Ghost 2	Ghost 3
Intensity	0.2404	0.0611	0.0405	0.0561

Table 7.1: The maximum peak intensities (W/mm^2) from Fig. 7.21 are summarised here.

The normal path of rays through the horn array is modelled in Fig. 7.20c. This shows how rays (red) should be focused in the centre of the focal plane. When the two ray sources are combined in the model (Fig. 7.20d) it is clear that the two sets of rays focus at different points on the focal plane (red final ray segments compared to light blue).

The plots in Fig. 7.21 show layout rays for visual demonstration only. In Zemax a number of analysis rays can be selected for each ray source. In this case the number of rays for the two ray sources are made proportional to their coverage relative to the entire polariser aperture size (176 mm diameter) where the horn array is 59% of the polariser area and the region around the horn area is 41% of the polariser area. Both sources were set to have the correct proportion of rays on the horn array area and the surrounding area. As such both sources were set to have a ray density of 16.4 rays/mm^2.

The results on the focal plane are shown in Fig. 7.21. Fig. 7.21a shows the whole detector area that models the QUBIC focal plane and Fig. 7.21b shows a zoom-in of the same data. The central intensity point shows the intensity from the normal rays focusing in the centre of the focal plane at the (0, 0) coordinates. The lower point shows the rays that reflect from the polariser through the horn array. Note that the lower point is also offset in the x coordinate since the polariser was installed with a 1.5° rotation around the z-axis. The first reflected peak intensity in these data (shown in Table 7.1) is approximately 25% of the central peak intensity.

The data in Fig. 7.21 and Table 7.1 also show secondary peaks. These are caused by rays that reflect multiple times off the polariser and area outside the horn array before finding a path into the horn array.

7.6.3 Discussion

From this Zemax model setup the separation between the peaks corresponds to 3.1° on the sky. This can be compared with the data from Fig. 7.14 where the

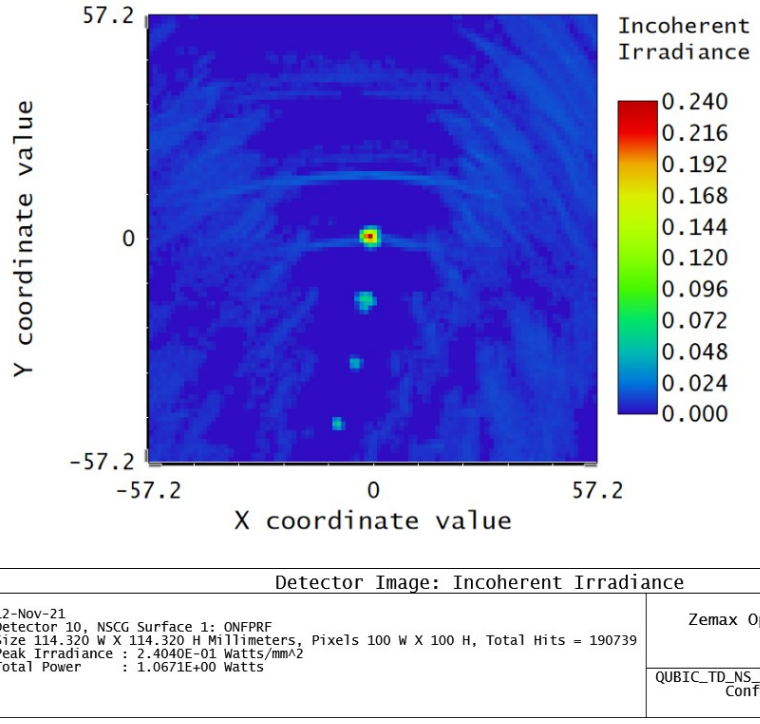

(a) The full Zemax detector area that is setup to model the QUBIC focal plane.

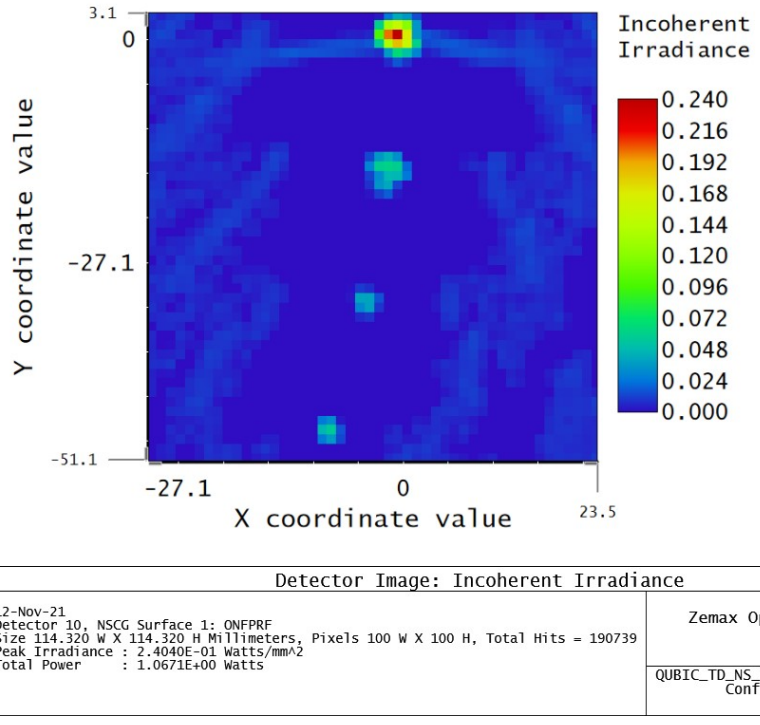

(b) A zoom of the same figure as (a) to show the 'ghosted' peaks more clearly.

Figure 7.21: The detector viewer output from Zemax for the ghosting model. The detector here replicates the physical detector geometry for QUBIC. The x and y coordinate values are in mm. The intensity scale is in W/mm^2. The intensity peak at [0, 0] corresponds to the nominal rays from Fig. 7.20c. The offset 'ghost' peaks correspond to the rays from Fig. 7.20b.

average value for horn separation corresponds to 4.85°. The model as is does not replicate the exact separation angle observed with the model configured in this form. However, the exact angular offset of the polariser was not known; 1.5° was reported as an estimation by colleagues working in APC. It is conceivable that if the polariser angle was different, the Zemax model could be modified to produce the 4.85° angle as observed in the maps.

It is interesting that the model produces an amplitude ratio of 3.9 while the data in Fig. 7.16 ranges from 1 to 6 (averaging 2.37). This agreement is not exact since the levels or saturation in the TES were unknown at this time. With no saturation the measured data would likely have a higher amplitude ratio, perhaps approaching the amplitude of 3.9 for the Zemax model data.

The Zemax model uses geometrical optics with a plane wave type approximation, as shown by Figs. 7.20a and 7.20c. The strength of this modelling approximation is that it can replicate a ghosting effect that would be the same for all TESs in the quarter focal plane as was found in Section 7.6.1 where the ghosting was found to be constant across the focal plane. Therefore, this model replicates the observed behaviour of ghosting measurements in the dataset for a TES with good SNR.

A more sophisticated correlation analysis could be made to further explore if these ghosts are due to electrical cross-talk. However, it has been shown in this chapter optical ghosting seems more likely. The optical part of the analysis has limitations. Since the exact installation angle of the polariser was unknown (the exact z-axis rotation was also unknown), it is impossible to do a more accurate and representative model of the optical elements e.g. the polariser and horn area. The exact optical properties of the area around the horn array were unknown also.

What this model does show is that there is a possible optical mechanism, related to the area outside the TD horn array that could cause the ghosting observed in the data. Other optical mechanisms may exist but the most plausible has been shown here. The analysis of this model (in conjunction with the lack of evidence for any kind of electronic ghosting) indicates that this is the most likely source of the ghosting, while uncertainties still exist.

7.7 Configuration Change

The Zemax model has some limitations and improvements could be made with more time available but a solution needed to be found before the next cool-down. It was necessary to make a decision using the limited data described above.

Discussions were held with QUBIC collaborators in order to determine the best course of action. The analysis of the measurement data and the Zemax model presented in this chapter were used to inform these discussions. It can be assumed that the installation of the HWP and polariser was the likely cause of ghosting as these were significant configuration changes and the data analysis presented here showed no clear evidence for electrical ghosting. Data analysis presented here also showed an angular tilt, separation, and amplitude ratio that were constant across the focal plane for all functioning TESs and this is indicative of optical ghosting. Calculations of the relationship between detector location and angular separation also favour optical causes over electrical. An optical mechanism was tested in Zemax which can replicate some features of the ghosting. Burke (2021) [90] tested a mechanism where cross-polarised light may reflect off the horn array, then back off the polariser and into the horn array but the level of reflections was far too low. From this evidence a number of solutions were discussed based on the evidence and reasonable assumptions:

- Increase the angular tilt sufficiently so that the standing wave (if it was a standing wave) reflects to a region outside of the focal plane. This option was not chosen since the ideal angular increase was not known. The optical properties of the polariser at high angles were not available at the time. It was conceivable that polariser performance might be degraded at high angular tilt.

- Decrease the angular tilt (e.g. 0.75°) so that the theory of reflections from the polariser can be tested and proven. If the theory was correct the ghost angle in synthesized maps should decrease in a way the can be compared in Zemax. This would mean that the next cool-down and dataset would almost certainly have ghosted data in a different position in the synthesized images. This is not a good outcome since the QUBIC project preferred to test further upgrades and develop the instrument further and another ghosted dataset would slow this progress.

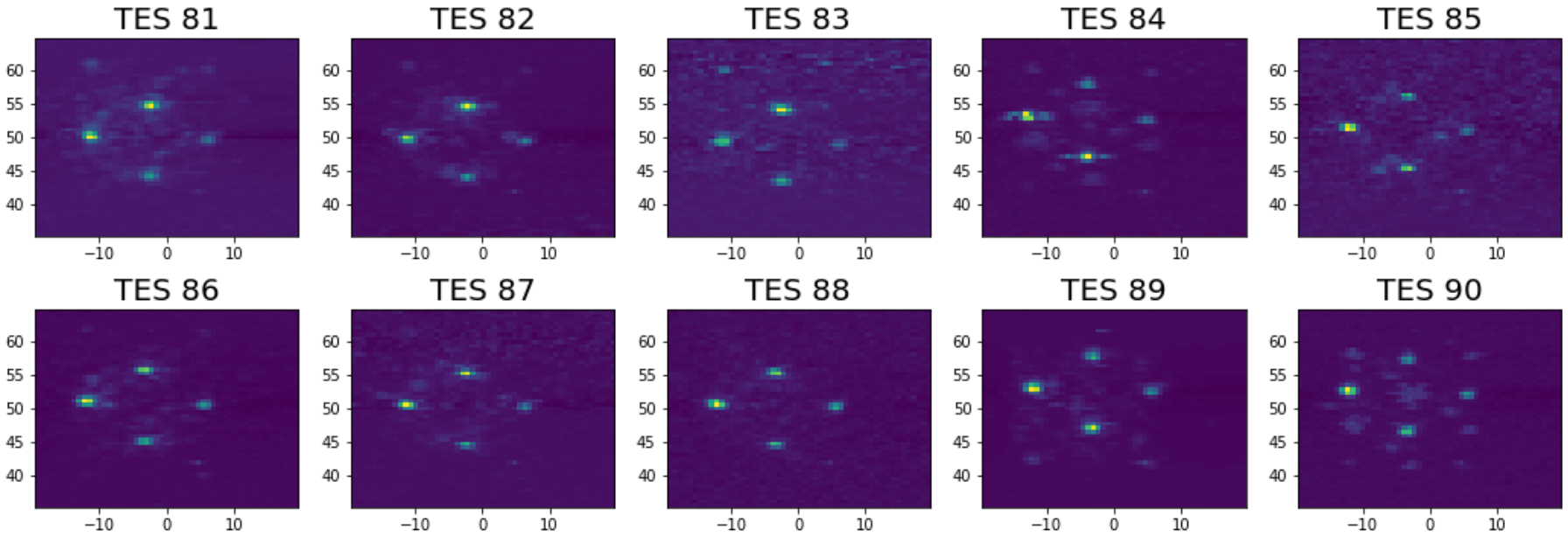

Figure 7.22: An example of TES synthesized maps from which ghosted TES are selected. TES 81, 85, 86, 87, 88, and 89 did show the replicated pattern and are now free from ghosting since the configuration change. The axes are azimuth and elevation in degrees as in Fig. 7.1.

- Moving the polariser closer to the horn array to eliminate the standing wave functionality and keeping the tilt angle. This would substantially reduce the amount of stray light reflections between the polariser and outer region of the horn array. This way the previous ghosting might still be observed but with lower amplitude on the reflected pattern.

- Keep the current configuration and apply an anti-reflective coating to the reflective surface around the horn array facing the polariser. This procedure may involve blocking additional gaps such as where electronic boards are visible to light from the polariser (as shown in Fig. 7.17). Common coatings are anti-reflective to levels greater than 95 - 99.9% (and better AR performance can be gained from custom coatings). The remaining percentage of ghost reflections would be considered a systematic effect for observational science data and some configuration change should still be made to minimise such systematics. However, an anti-reflective coating could still be applied to these surfaces (and others) with an additional configuration change to ensure an absolute minimisation of systematics where possible.

- Moving the polariser closer (fixed to the 1 K cryostat) to the horn array and setting the polariser tilt angle to zero. This solution should eliminate ghosting, as in the Zemax model, entirely. The downside of this solution was that the ghosting could not be studied in further detail. The advantage was that new and important measurements and validation of the instrument could be performed. In the end, this is the option that was chosen.

The result of this configuration change is shown in Fig. 7.22. The ghosts were eliminated from all the TES scan maps. In this figure, TES 85 and 90 do show some small peak replication but this is more similar to a known electronic effect with these TESs and distinct from the type of ghosting shown in Fig. 7.4. The improvement is seen across all TESs on the focal plane.

7.8 Conclusion

The ghosting effect that arose in the QUBIC instrument in January 2020 was a critical issue for the QUBIC collaboration. The problem needed to be analysed and solved under a time constraint and this is the subject of this chapter. The

ghosting was first characterised by developing a data analysis pipeline to measure separation angle, tilt, and peak amplitude of the ghost images with respect to the main image on each bolometer. The processed data were then used to test for possible causes of ghosting, either electrical or optical.

The constant ghost image separation seen on bolometers across the focal plane was more consistent with an optical cause and a Zemax model was developed to try and replicate the observed data. This modelling procedure was limited by a number of unknown factors in the instrument set-up but it did show how reflections from the region around the TD horn array could produce ghost peaks. If the cause of the ghosts was electrical cross-talk then it would depend on the proximity of detectors on the focal plane or the proximity of electrical connections to these bolometers. No evidence of this was found.

Due to the time constraints and the need to decide on a solution before the next cool-down, discussions were held with QUBIC collaborators in order to decide how to solve the issue. Based on the research outlined in this chapter several options were presented to the collaboration and it was decided to modify the location of the polariser. No anti-reflective coating was applied to the indicated source of reflections (the exposed metal on which the horn array is mounted). This modification could still be made to minimise ghosting systematics that may exist on a low level in the current TD configuration. A more detailed stray light analysis that focuses on the entrance aperture, filters, rotating HWP, and horn array, prior to the primary mirror, might prove to be very insightful. This analysis would need to take into account realistic models of the mechanical components and material optical properties in terms of reflections, emissivity, and scattering.

The concluding result is that the modification to the polariser was successful. No ghosting of this kind has been observed since. It is somewhat academically unsatisfying that the exact cause was not determined with absolute certainty. There are too many unknowns specifically around the angle at which the polariser was installed at. The only way to really test and be certain would have been to use a series of cool-downs over time with changes in polariser angle and measuring the synthesized maps as shown in this chapter. Then optical modelling, such as shown in this chapter or by PO, could be used to correlate the ghost images with polariser movements. Operational needs and time constraints meant that the polariser was modified so that it had the best chance of solving the ghosting. It worked and other instrument priorities took precedent such as optimising demodulation and

measuring QUBIC's spectral performance as described in Chapter 6 of this thesis. Nevertheless, the investigations presented in this chapter may prove useful if any artefacts arise in future TD or FI images.

Chapter 8

Baseline Redundancy

8.1 Introduction

The control of systematic effects is one of QUBIC's core design principles. This is true for most modern CMB experiments aiming to detect the B-mode polarisation from Inflation in the early Universe. The B-mode signal is faint ($\sigma(r) < 0.036$ (Keck Collaboration (2021) [25]) and there are strong foreground sources such as gravitational lensing and Galactic dust that can contaminate to a B-mode detection.

A unique feature of QUBIC is redundant baseline self-calibration. By opening and closing the horns in QUBIC's aperture and comparing focal plane data, systematic effects can be characterised and subtracted. This will primarily be achieved by comparing the interference pattern of two horns with that from another *equivalent or redundant* pair of horns. While self-calibration is not unique to QUBIC, radio astronomy (more recently 21 cm and sub-millimetre) has a long history which informs calibration for QUBIC, QUBIC's design and approach is unique and requires additional consideration regarding the non-redundancy of the system. They key distinction is that QUBIC is a bolometric interferometer with off-axis optics while most calibration techniques are developed for interferometer arrays. As such, even though QUBIC was designed to maximise redundancy, there are still aspects of non-redundancy worth studying to ensure that QUBIC can effectively constrain systematics.

This chapter aims to describe the equivalent baseline characteristics for the TD and FI horn arrays. The chapter will then use PO to study if and how the off-axis aberrations affect the redundancy of baselines normally considered equivalent in traditional self-calibration. In order to introduce and setup this discussion, calibration from radio astronomy and a description of QUBIC's bolometric interferometry will be contextualised.

It is of prime importance to study redundant self-calibration for QUBIC, and specifically baseline redundancy, as systematic effects will be a key aspect of the data analysis. This investigation informs how off-axis optics affect the focal plane for self-calibration. It sheds light on the specific differences that can be expected for self-calibration when an ideal focal plane model is used instead of an aberrated model. It also informs the improvement that can be expected if a PO model of redundant baseline types with aberrations are used to compare with each other instead of with the ideal focal plane model.

8.2 Telescope Calibration and Redundant Baselines: Context for QUBIC

Calibration of all types of telescopes in all frequency ranges is fundamental to successful observations. It is important for any of the science results produced by the telescope. It is a broad term and can describe many aspects of preparing a telescope for scientific observations. It may refer to laboratory testing of individual components in a lab. In the context of this chapter, calibration will refer to: measurements used to convert detector data to real units, characterise the noise and systematics of an instrument during or immediately prior to an observation, or post-processing and aperture synthesis methods used to reduce systematic errors. The following concepts described here are standard in the field of radio astronomy and are covered by many text books such as: Thompson, Moran, and Swenson (2017) [111], Burke, Graham, and Smith (2009) [112], and Marr, Snell, and Kurtz (2016) [113]. Calibration techniques from radio and sub-millimetre astronomy are of particular importance to QUBIC as they form the basis of redundant baseline calibration and are highlighted next.

8.2.1 Basic Calibration

Basic calibration, common to these types of instruments, will generally observe known sources in the sky such as planets, active galactic nuclei (AGN), or the Galactic centre in order to get an absolute measurement of gain and noise in the instrument. At this step the antenna beam pattern can also be measured to enable an accurate deconvolution. These steps are of prime importance since the antenna temperature is always less than the noise ($T_A << T_N$). The noise term includes gains and losses (e.g. detector noise, transmission lines) and foregrounds. Basic calibrations like this are a primary step since during this phase the detector signal is converted to a useful flux measurement (F_ν) of the target source (e.g. such as Janskys (Jy)). This is typically described by the following equation where A_ν is the effective area of the telescope, $\Delta\nu$ is the bandwidth, and P is total power detected;

$$P = F_\nu A_{\text{eff}} \Delta\nu. \tag{8.1}$$

There are calibration procedures that take place during observations to remove systematics (e.g. detector noise, thermal noise etc.) that occur on a range of time scales. Telescope mirrors are sensitive to surface deformations with changes in elevation due to a change in gravitational forces acting on the mirror. These can create pointing errors that can be corrected through calibration. Detector noise may vary on short time-scales while a temperature deformation of a mirror may occur of a longer time-scale. This makes determining a useful flux measurement (F_ν) an indirect process especially since $T_A << T_N$. A calibration is necessary to correct these errors and noise sources.

8.2.2 Switching

One calibration method is switching. During an observation, the telescope will observe an observation target (V_{ON}) and record data on a piece of nearby dark sky[1] (V_{OFF}) in order to measure the background telescope noise, correct any drift in the calibration, and observe the target source again. This switching takes place

[1]Here a general radio astronomy technique is described. As QUBIC is a millimetre-wave CMB experiment, there is no dark sky, the CMB signal is isotropic. QUBIC instead will observe a fixed calibration source on a nearby tower as described in Section 2.3.6.

Figure 8.1: The Sub-millimeter Array (SMA), single dish telescopes forming a larger interferometric array where self-calibration can take place from baseline combinations. *Image Credit: Nimesh Patel, SAO*

throughout an observation to correct for calibration drifts. In principle this is quite simple by writing

$$\begin{aligned} V_{\text{on}} &= \alpha G k \Delta\nu \left(T_{\text{A}} + T_{\text{sys}}\right) \\ V_{\text{off}} &= \alpha G k \Delta\nu T_{\text{sys}} \\ V_{\text{on}} - V_{\text{off}} &= \alpha G k \Delta\nu T_{\text{A}} \end{aligned} \tag{8.2}$$

where V_{ON} and V_{OFF} are the voltages measured by the detectors when pointed at or nearby the target source. G is the receiver gain, k is the Boltzmann constant, and α is the responsivity of the detector. T_A and T_N are added when observing the target source and only T_N when observing a blank sky. This is a basic and direct way to calibrate a telescope.

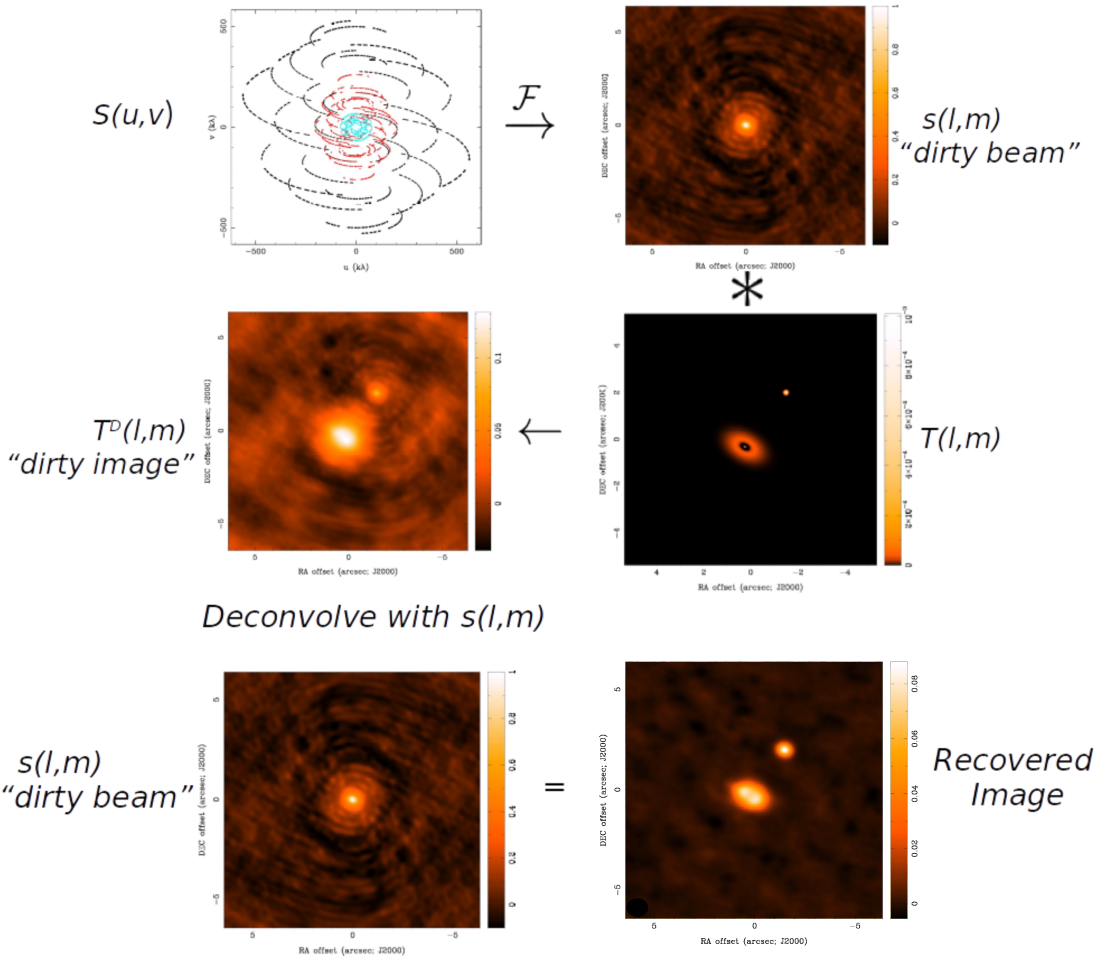

Figure 8.2: The upper left shows the u-v coverage of the sub-millimetre array (SMA) telescopes. The points are smeared due to the Earth's rotation and improves the u-v coverage. A Fourier transform of $S(u, v)$ gives the 'dirty beam' $s(l, m)$. $T(l, m)$ is the actual sky brightness and when convolved with the 'dirty beam' gives the 'dirty image' ($T^D(l, m)$) which is what is measured by the array. By deconvolving the 'dirty image' with the 'dirty beam', a model of the actual sky brightness is made. This figure is based on images from a workshop lecture by Wilner (2014) [114].

8.2.3 Primary Beam and Aperture Synthesis

When an interferometric telescope array is formed (for example, Fig. 8.1), the synthesised beam of the telescope must be considered when processing the observations. The combined telescope aperture is comprised of many smaller individual telescopes with incomplete $u - v$ coverage between them. As such, aperture synthesis is required to properly deconvolve the measured data. The Earth's rotation can fill in the $u - v$ plane and increases the $u - v$ coverage and the technique of Earth rotation synthesis earned Martin Ryle the Nobel prize. The 'dirty beam' $s(l, m)$ is formed by an FT of the antenna distribution $S(u, v)$. When the telescope observes a source or sky intensity $T(l, m)$, this is a convolution of the 'dirty beam' $s(l, m)$ and $T(l, m)$ which results in a 'dirty image' $T^D(l, m)$ as happens for QUBIC. Deconvolving the dirty image $T^D(l, m)$ with the 'dirty beam' $s(l, m)$ will give a useful model of the sky brightness $T(l, m)$. This method is outlined in Fig. 8.2. The CLEAN algorithm, by Högbom (1974) [115], is a common deconvolution method in radio astronomy to find a model of the sky brightness $T(l, m)$ and many variations and alternatives are available. The weighting scheme used by the 'dirty beam' is an important step which is discussed heavily in the literature.

A form of calibration can be made when there are two telescopes, i and j. They observe the sky to get the visibility V_{ij}^{obs} as follows:

$$V_{ij}^{\text{obs}} = V_{ij}^{\text{true}}\, G_i G_j^* G_{ij} + c_{ij} + e_{ij} \tag{8.3}$$

where V_{ij}^{true} is the true visibility for the baseline, G are the gains from both telescopes in the baseline, and $G*$ is a complex gain term. c_{ij} and e_{ij} are noise from the baseline correlator[2] and thermal noise, respectively. If the calibrator is a point source and the flux is known, the G terms, c_{ij} and e_{ij} from 8.3 can be determined and eliminated. This is the basic idea behind self-calibration of a telescope array using interferometric baselines and is outlined by Wieringa (1992) [116].

[2]A baseline correlator solves the inherent signal phase difference between two interferometric telescopes observing the same source. It is similar to the demodulation phase difference described in Section 6.3 and more discussion on this topic is provided by Thompson, Moran, and Swenson (2017) [111] and Marr, Snell, and Kurtz (2016) [113].

8.2.4 Phase Closure

There still exists some sources of error that can reduce the quality of maps produced by these self-calibrated baselines (e.g. by CLEAN). Some examples are incomplete $u-v$ coverage, the atmosphere may be unstable and affect each telescope observing the same source differently, baseline uncertainty, or any residual calibration error. The largest errors are those related to the phase of the received signal of the antennas (e.g. due to thermal expansion of a telescope cable, atmospheric instability). The measured phase difference between two antennas, when observing a reference point source, is

$$\phi_{ij}^{\text{measured}} = \phi_{ij}^{\text{true}} + \Delta\phi_i - \Delta\phi_j \tag{8.4}$$

where $\Delta\phi_i$ and $\Delta\phi_j$ are the individual phase errors. The principle of phase closure works by including a third antenna to construct the closure phase Φ_{ijk} where

$$\Phi_{ijk} = \phi_{ij} + \phi_{jk} + \phi_{ki} \tag{8.5}$$

and combining Eqs. 8.4 and 8.5 so that the antenna based errors cancel as follows:

$$\begin{aligned} \Phi_{ijk}^{\text{measured}} &= \phi_{ij}^{\text{true}} + \Delta\phi_i - \Delta\phi_j + \phi_{jk}^{\text{true}} + \Delta\phi_j - \Delta\phi_k + \phi_{kl}^{\text{true}} + \Delta\phi_k - \Delta\phi_l \\ \Phi_{ijk}^{\text{measured}} &= \phi_{ij}^{\text{true}} + \phi_{jk}^{\text{true}} + \phi_{kl}^{\text{true}} . \end{aligned} \tag{8.6}$$

The closure phase is therefore independent of the individual instrument phase shifts. The closure phase from several groups of antennas can be combined to extract the individual phase corrections. This is the basis of the *hybrid-clean* algorithm by Readhead and Wilkinson (1981) [117] where the map deconvolution (like in CLEAN) and calibration are made together in iterative steps.

8.2.5 Redundant Baseline Self-Calibration

The draw back of these calibration schemes is that they are limited by requiring prior knowledge of the calibration source and foregrounds. Assumptions need to be made about diffuse and polarised emissions which can create uncertainty in

spectral calibration. These limitations are discussed by Liu et al., (2010) [118] and by Dillon et al., (2020) [119]. If, however, the antennas are arranged so that their distances and orientations can form identical baselines, each baseline must measure the same visibility, and the visibilities and gains can be solved for simultaneously. This is called redundant baseline calibration and is described similarly to Eq. 8.3 above,

$$V_{ij}^{\text{obs}} = V_k^{\text{true}}\, G_i G_j^* + e_{ij} \tag{8.7}$$

where G_{ij}, the baseline complex gain, and c_{ij} are neglected. V_k refers to a specific redundant baseline type within an antenna array. Wieringa (1992) [116] and Liu et al., (2010) [118] both show how these redundant baseline equations can be solved to find the gains in each baseline. Liu et al., (2010) [118] also shows this with more recent optimisations of the method. The core idea is that χ^2 is minimised via a non-linear least-squares fitting:

$$\chi^2 \equiv \sum_{i<j} \frac{\left|V_{ij}^{\text{obs}} - g_i g_j^* V_{i-j}\right|^2}{\sigma_{ij}^2} \tag{8.8}$$

where σ_{ij} is the variance of the noise. The strength of redundant baseline calibration is that no prior knowledge of the foregrounds or target sources are required to calibrate and with a sufficient number of redundant baselines, the systematics are over-determined and solvable via the non-linear least-squares fitting.

QUBIC was designed to take advantage of redundant baseline calibration in order to have excellent control of systematics but the off-axis nature of the optical combiner may result in different V_{ij} visibilities within a redundant baseline type. This is an important consideration as the two most common methods of redundant baseline calibration (logarithmic and linearised) will require initial models of the visibilities to begin the algorithm and bad guesses can create mis-fits or lengthen computational time (Liu et al., (2010) [118]). Details of QUBIC's novel self-calibration scheme (*i.e. redundant baseline self-calibration for a bolometric interferometer*) are given by Bigot-Sazy et al., (2013) [65] and by Mousset et al., (2020) [56]. This chapter aims to contribute to these efforts by studying and characterising the non-redundancies unique to a system like QUBIC.

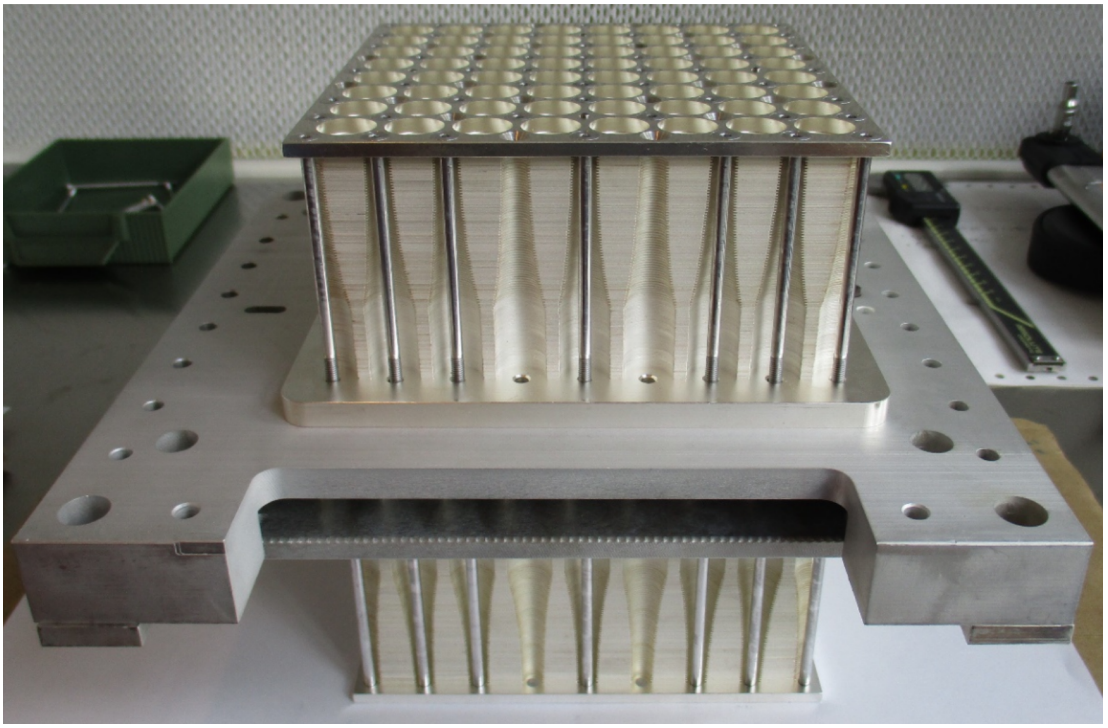

Figure 8.3: A photo of the 8×8 TD horn array. The switch array is located in the centre in-between the sky facing and detector facing horns.

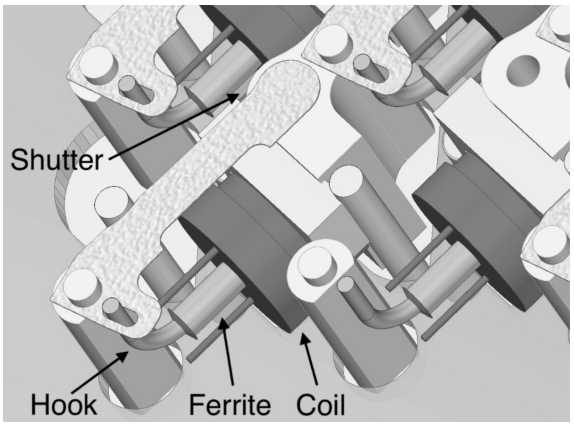

(a) 3D render of switch mechanism. The shutter is in the closed position.

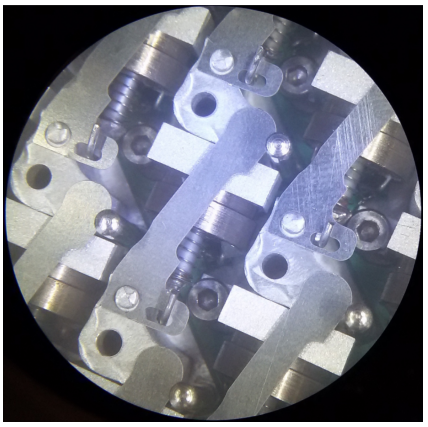

(b) Photograph of the switch mechanism. The shutters are in the open position.

Figure 8.4: The shutter mechanism in open and closed positions allowing different horns to create interferometric patterns on the focal plane. Images from Cavaliere et al., 2021 [70]. The figure was reproduced from Fig. 2.12 for convenience.

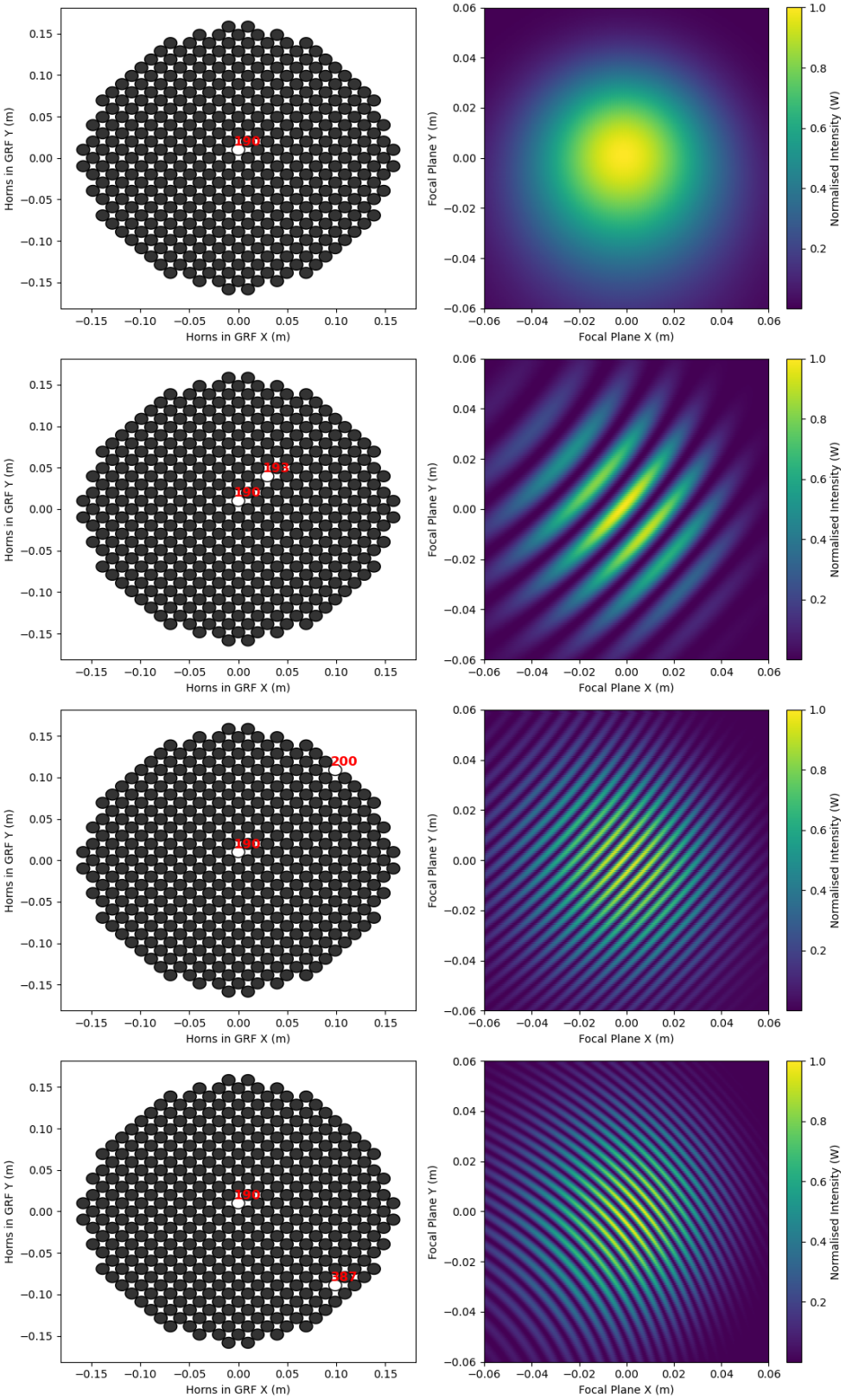

Figure 8.5: Focal plane patterns (right) for different combinations of open horns (left). *Open* horns are in white and *closed* horns are in black in the horn array plotted with respect to the GRF. The open horns are labelled according to QUBIC technical documentation [96]. These examples show the different interferometric patterns formed by baselines for different horn separations and orientations.

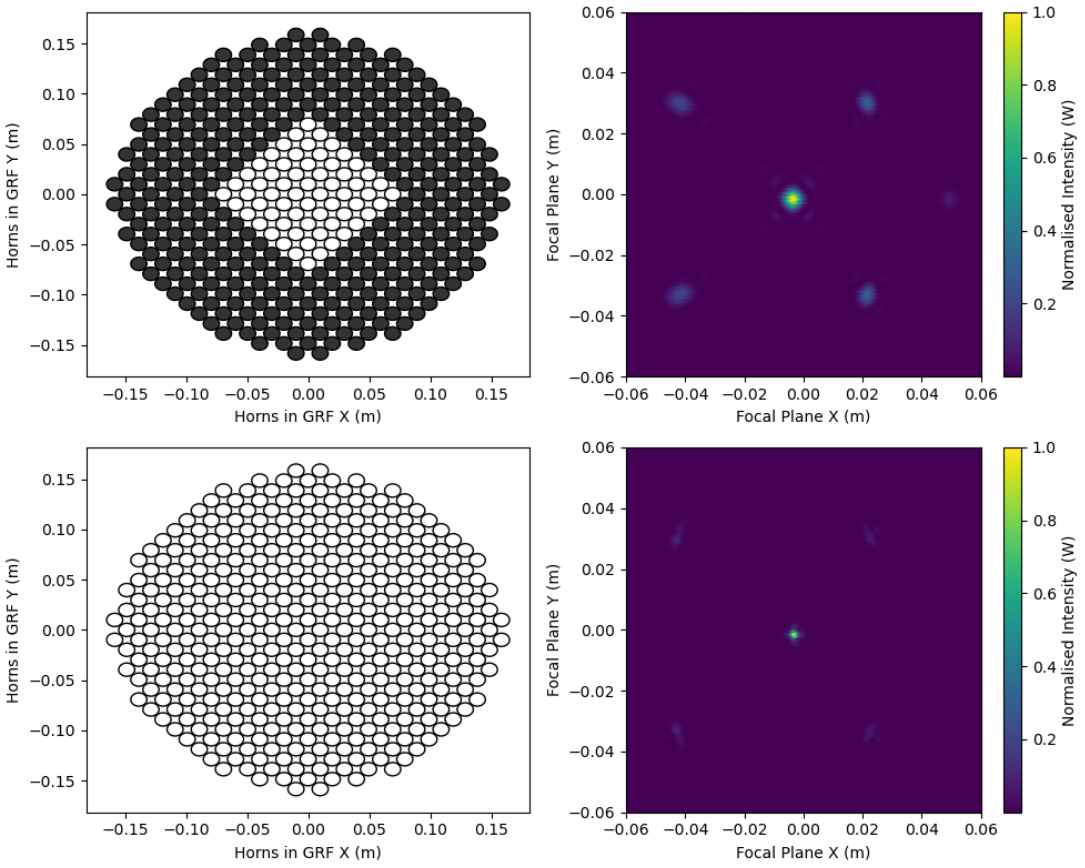

Figure 8.6: Focal plane patterns (right) for different combinations of open horns (left). *Open* horns are in white and *closed* horns are in black in the horn array plotted with respect to the GRF. The top and bottom rows show the PSFs (all horns open) for the TD and FI respectively.

8.3 Description of Baselines for Self-Calibration

A baseline pattern (with specific reference to bolometric interferometry) results from the interference between the beams from two horns when viewed on the focal plane. QUBIC selects a baseline by opening and closing the back-to-back horns using mechanical switches. The mechanical hardware for QUBIC's switches is described by Cavaliere et al., 2021 [70]. An example of QUBIC's horn and switch assembly is shown in a photograph in Fig. 8.3. This photo shows the switches in-between two horn arrays for the TD with 64 horns (where the FI will have 400). The horns and switches are identical in both the TD and FI configurations. Details of the switch mechanism are highlighted by Fig. 8.4. The switch mechanism is shown in the 3D CAD model in Fig. 8.4a with the shutter in the closed position, covering the aperture. Fig. 8.4b is a photograph of the switch mechanism in the

open position. The unblocked apertures connecting the back-to-back horns are evident.

The baseline pattern is dependent on the horn separation and angle as illustrated by Fig. 8.5. Rows two, three and four show open horns and the corresponding focal plane image for a far-field point source. Row 1 shows the beam pattern when only 1 horn is open. Rows two and three show baselines with the same orientation angle but different horn separation. In this case, the baseline patterns have the same fringe direction but more fringes result from a larger horn separation. Rows three and four have the same horn separation but different orientation angle. The number of fringes is the same but the direction of the pattern on the focal plane rotates with the horn angle orientation.

The first row of Fig. 8.6 shows the PSF for the TD (the central 64 horns of the FI open), and second row shows the PSF for the 400 horns of the FI horns open. The FWHM for the FI peaks are smaller but the secondary peak positions on the focal plane are the same for the TD and FI effectively increasing the $u - v$ coverage.

An equivalent baseline occurs when two pairs of horns have the same horn separation and angle. This is demonstrated in Fig. 8.7. In the lower left, horns 190 and 193 are shown in orange and 231 and 233 are shown in green. Their focal plane patterns are shown in the top row. The residual difference of the focal plane patterns is shown in the lower right (notice the scaling of the colour-bar). In the absence of instrumental aberrations this would be zero as equivalent baselines would produce identical patterns.

The residual difference of a nominally redundant baseline can be compared with an arbitrary baseline example in Fig. 8.8 (for illustrative reasons only). The residual difference of these baseline types is clear from scale of the lower right patterns of Figs. 8.7 and 8.8. The residual difference for an arbitrary baseline has wide spread of values while the nominally equivalent baseline has much smaller residuals by comparison, as expected. This is clearly demonstrated by a frequency distribution histogram as shown in Fig. 8.9. When a histogram of points for an equivalent (green) baseline is evaluated, there is a large number of points clustered close to 0 W and no points greater than 0.04 W for the residual difference. The arbitrary baselines have a small number of points near 0 W but a large number of points spread between -0.1 and 0.1 W. This is what is expected from comparing a redundant baseline to an arbitrarily selected baseline.

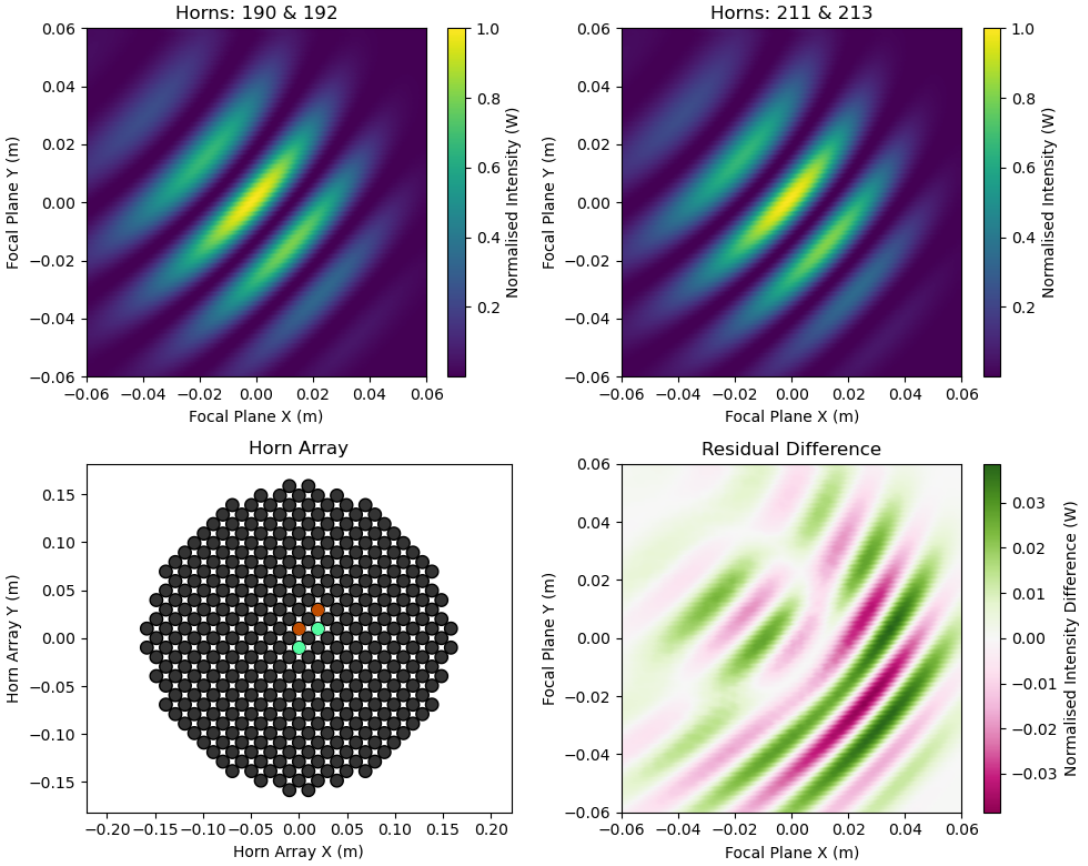

Figure 8.7: Equivalent baselines in QUBIC. Here, baselines are compared where the horn separation and orientation angle are the same for each pair of horns. The number and direction of the fringes are the same as expected. The baseline of row three from Fig. 8.5, horns 190 and 192 (orange pair lower left) are compared with an equivalent pair (horns 211 and 213, green pair lower left). The difference between the two focal plane patterns is shown in the lower right. In the absence of aberrations, the residual difference would be zero.

8.4 Off-Axis Aberrations as a Systematic Effect

Traditional redundant baseline calibration assumes perfect or near-perfect redundancy between baselines while QUBIC's form of redundant baseline self-calibration has some special characteristics worth considering.

QUBIC is a bolometric interferometer and, as has just been shown, may induce additional aberrations due to its off-axis optics that have not been a consideration for traditional calibration of this type in radio and sub-millimetre astronomy. Some typical non-redundancies are: baseline position uncertainty, antenna polarisation uncertainty, or differing atmospheric affects on long baselines. QUBIC was designed to minimise these non-redundancies.

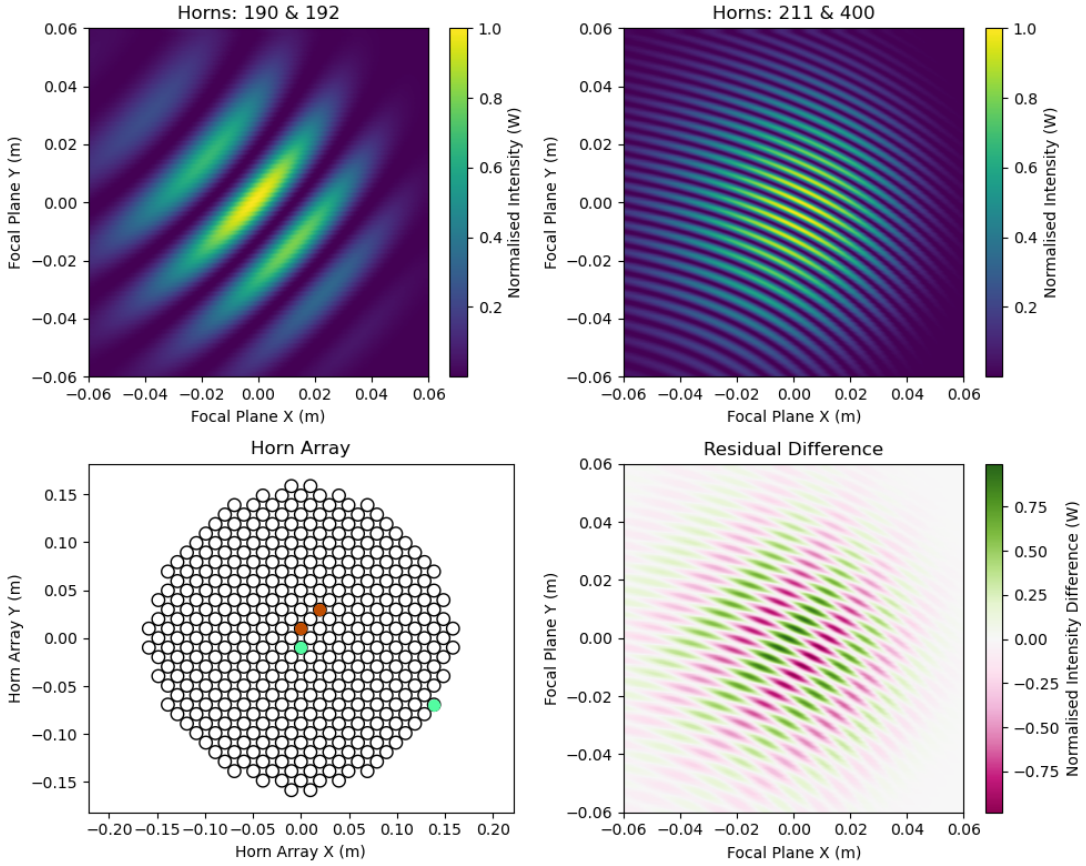

Figure 8.8: This figure shows an arbitrary baseline in QUBIC. Here, baselines are compared where horn separation and angle are different for each pair of horns. The number of fringes and the direction of fringes are different. This figure is the same as Fig. 8.7 except horn 213 is swapped for horn 400 and only serves the purpose of demonstrating the residual difference between arbitrary and equivalent baselines.

While the beam from each horn in the array has the same path length to the focal plane, each beam takes a unique path (via reflections off mirrors) through the optical combiner. These paths were studied in detail during the design and development of QUBIC by Scully 2016 [77]. The paths are summarised by Fig. 8.10.

Fig. 8.10a uses three sample horns from outer edges of the horn array to show that although the path lengths to the focal plane are the same, each horn has a unique path length to the optical components as also evidenced by their beam-width as a function of distance. Consider that horn 1 reflects off the primary mirror after 0.276 m while horn 3 reflects after 0.461 m but both horns have the same total path length to the focal plane and end up with almost the same beam-width.

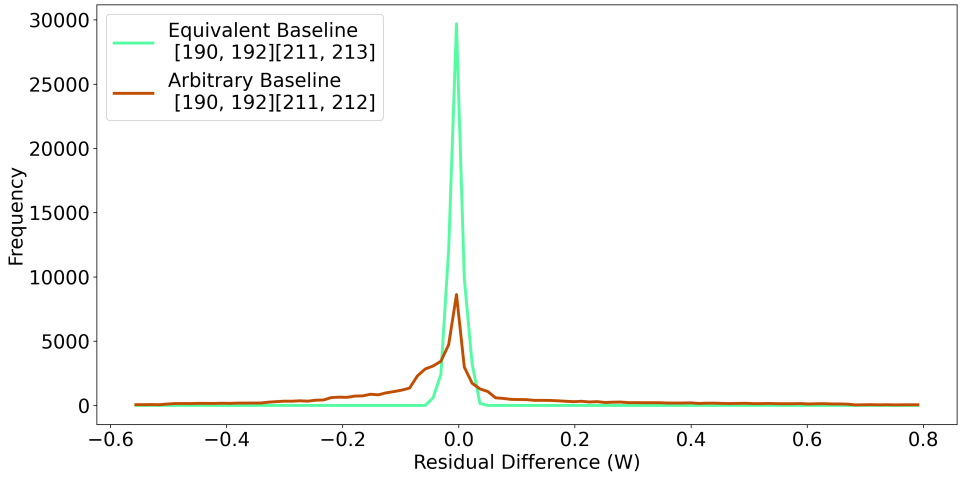

Figure 8.9: This histogram compares equivalent (green) and arbitrary (brown) baseline residual differences using data from the lower right of Figs. 8.7 and 8.8. This histogram evaluates the number of points (*labelled as Frequency*) in each residual difference map (58081 points per map) with x-axis bins ranging from -1 to 1 in 101 steps (bin-width of 0.02 W where each baseline map is normalised to 1 W).

In Fig. 8.10b the beam waist radius, *the width of the beam at a given point along its axis of travel*, is included for the sample paths as the horn beams travel to the focal plane. The same reflections, as in Fig. 8.10a, with the primary and secondary mirrors are also evident in this figure. There is a small difference in beam waist radius at the focal plane for each horn (at $x = 1.4$ m in the figure); the beam waist radius would be the same for each horn in an ideal system.

Horns closer together on the focal plane will be more similar in terms of aberrations than horns farther apart and this is apparent when horns are combined to form a baseline pattern on the focal plane. This is demonstrated by Figs. 8.11, 8.12, and 8.13. Fig. 8.11 shows a selection of redundant baselines in the horn array. The dark blue horns are horn numbers 1 and 3 (Appendix B). The baseline formed by horns 1 and 3 are compared with the other highlighted horns in Fig. 8.12 with colours corresponding to Fig. 8.11. The trend shows that redundant baselines closer together (e.g. horns 1 and 3 compared with horns 25 and 27, in light blue), have 'high-redundancy' and are more equivalent than baselines more widely separated on the horn array (e.g. horns 1 and 3 compared with horns 383 and 385, in dark brown).

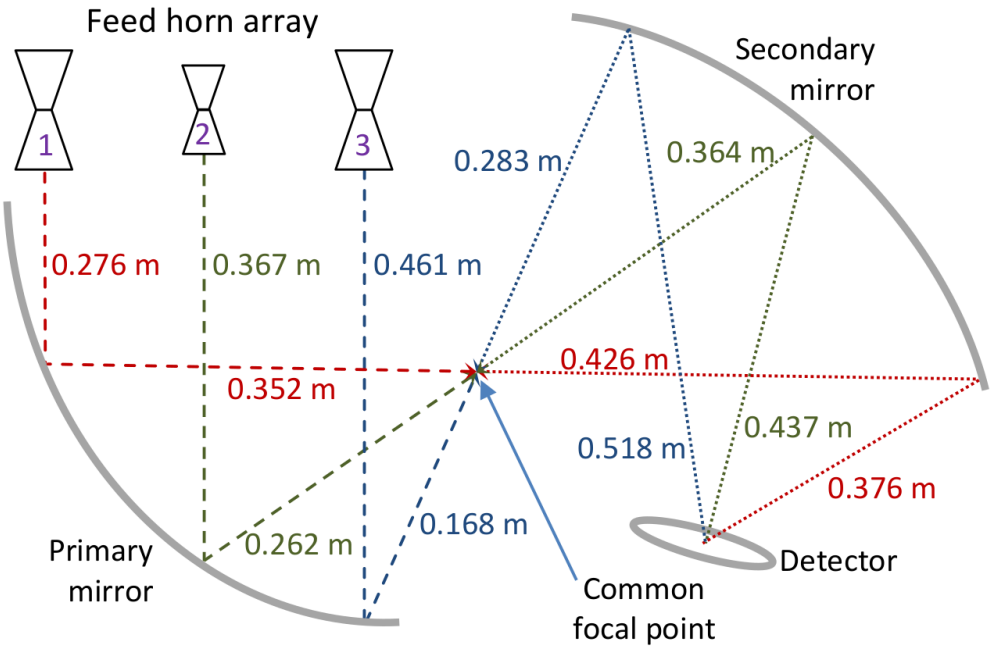

(a) This figure shows a schematic of horn paths and distances between reflections from the mirrors. It shows how the horn array and mirror geometry gives beams from horns different paths to the focal plane (*labelled as 'Detector'*) but having equivalent path lengths.

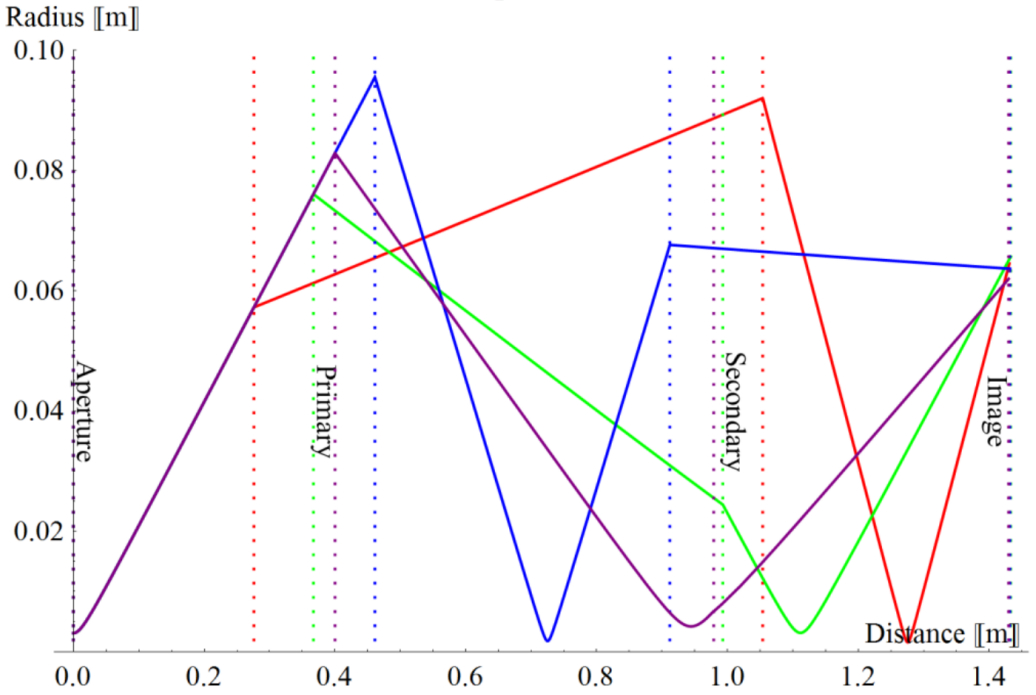

(b) This figure similarly shows the path lengths for different horns between reflections but also includes the beam radius (y-axis) as it travels to the focal plane (*labelled as 'Image'*). Note here that the beam radius for the horns have a small discrepancy at the focal plane (resulting in a small aberration for each horn on the focal plane).

Figure 8.10: These figures show the paths for horns on the outer edge of the horn array to the focal plane. Reproduced from the PhD thesis by Scully (2016) [77]. The coloured lines show unique ray paths to the focal plane from different horn locations.

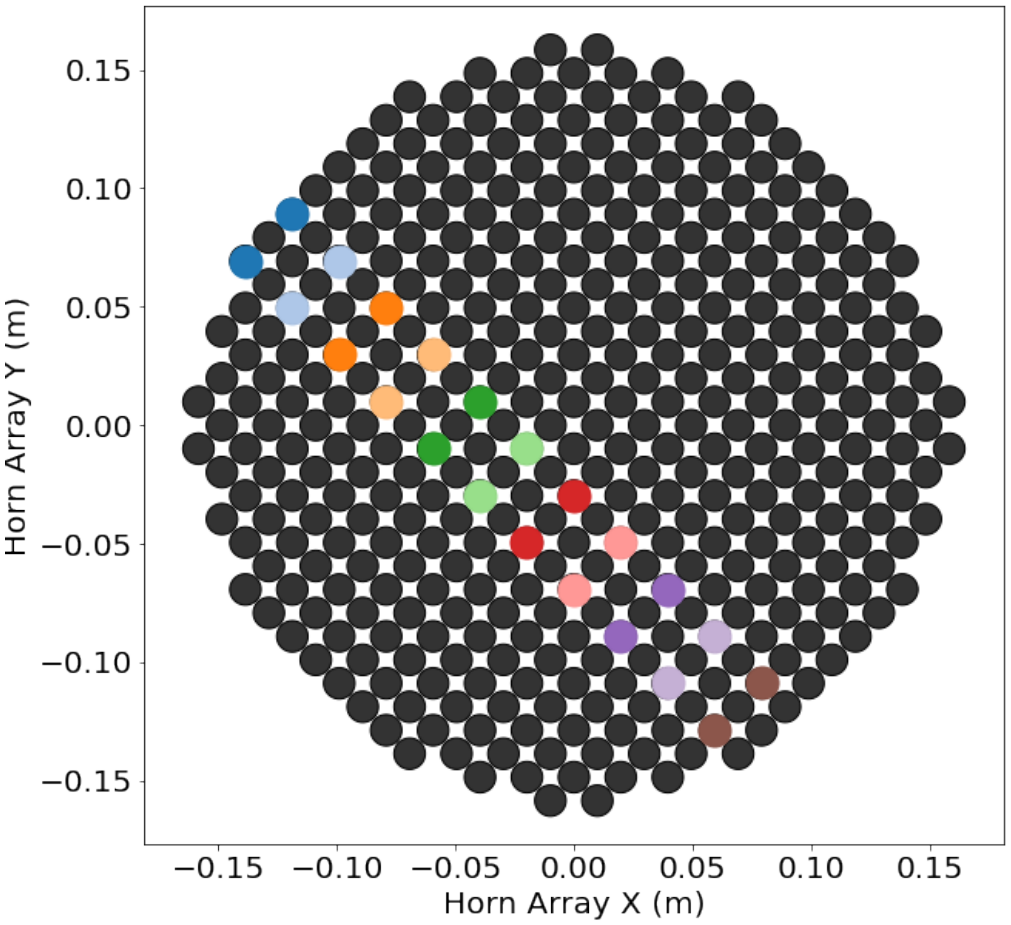

Figure 8.11: The baseline horns used to demonstrate the relation of residual difference of baseline patterns and their physical separation. Each baseline is compared with the dark blue pair in the upper left of the horn array. The distance between each baseline pair is 28 mm and the separation between the compared baseline pairs is also 28 mm.

The examples shown demonstrate that within a set of baselines normally considered redundant baselines, some baselines are more equivalent than others. This is important to consider with self-calibration algorithms since they depend on good starting guesses and the effect will be analysed by the following sections.

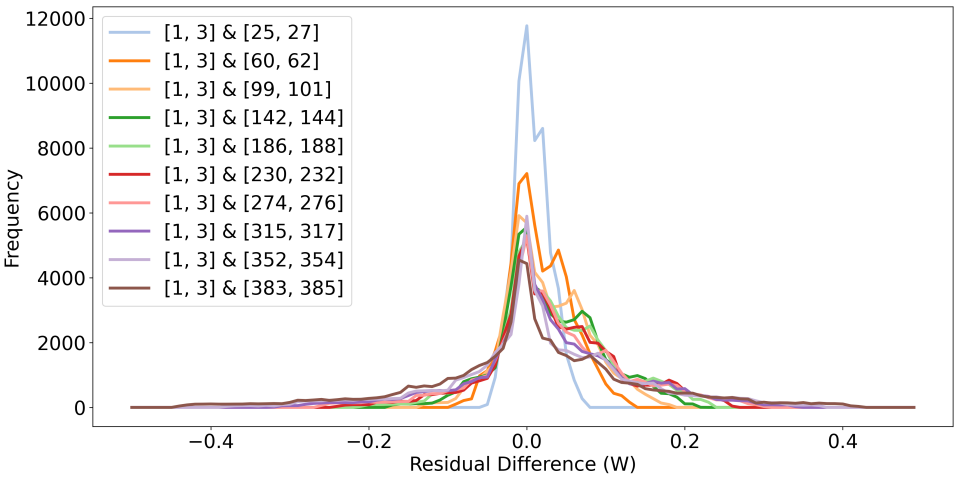

Figure 8.12: A histogram of the residual differences of baseline patterns shown in Fig. 8.11. The residual difference is evaluated between -0.5 and 0.5 over 101 bins where the original intensity maps were normalised to one. The number of points in each bin is on the y-axis.

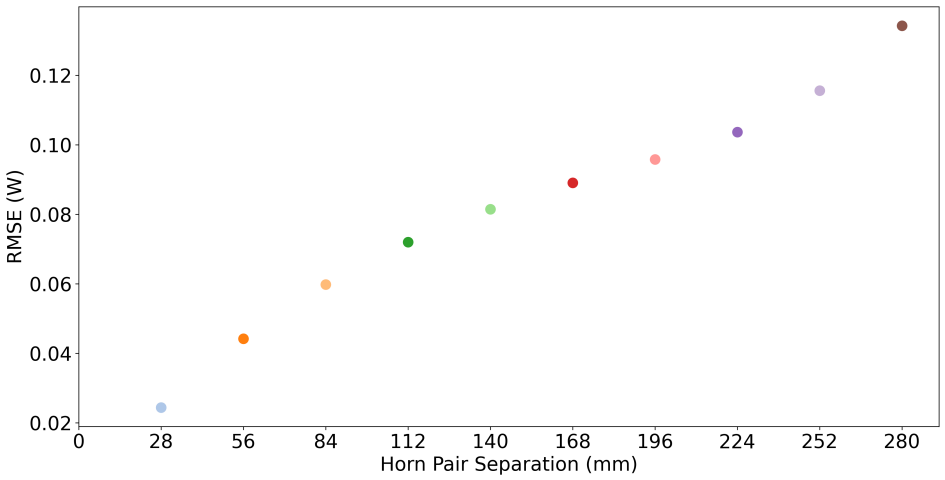

Figure 8.13: The horn separation and RMSE of residual difference maps as detailed by Figs. 8.11 and 8.12, the colours also correspond to the data in these figures. This figure shows the RMSE increases as the radial separation between horn pairs increases.

8.5 Method

The baseline redundancy as a systematic effect is investigated by first producing a list of all equivalent baseline pairs for the TD (and later the FI) where the horn separation and horn angle are the same. This was first described for the QUBIC TD by Charlassier (2010) [120] and was later implemented into *qubicsoft* [104] which was used as a basis for this analysis.

Optical model intensity data (produced in GRASP) are used to generate the baseline pattern for two pairs of horns in the equivalent baseline sets (these were already shown in Fig. 8.7, for example). Each baseline pattern is formed by a grid of 58081 points. These are the same PO models and data generated in Chapter 5[3].

The residual difference is calculated by subtracting the baseline maps. The Root Mean Squared Error (RMSE) is calculated for each residual difference map as

$$RMSE = \sqrt{\sum_{i=1}^{n} \frac{(\hat{y}_i - y_i)^2}{n}} \tag{8.9}$$

where $\hat{y}_i$ is a data point for intensity[4] for one baseline pattern on the focal plane, y_i is an intensity data point for another baseline, and n is the number of data points in the intensity grid for the focal plane. This is repeated for all horn pairs in an equivalent baseline set and the data are recorded. This is then repeated for all equivalent baseline sets.

An example is shown in Fig. 8.13 where the horn pairs and residual data of Figs. 8.11 and 8.12 are used to show the relation between horn pair separation and RMSE of a residual difference map. This shows how closer horn pairs are more equivalent than horn pairs with a larger separation. The RMSE metric on a residual difference map was found to be useful for characterising the equivalency of redundant baselines. This example only shows a subset of one redundant baseline type for the FI while the following sections will analyse all redundant baselines for the TD and FI by the same metrics as shown above.

[3]The realistic rims, measured surfaces at 4 K, tabulated source, and cold-stop are included in the model data.

[4]Intensity is used, rather than amplitude, since the detectors are bolometers.

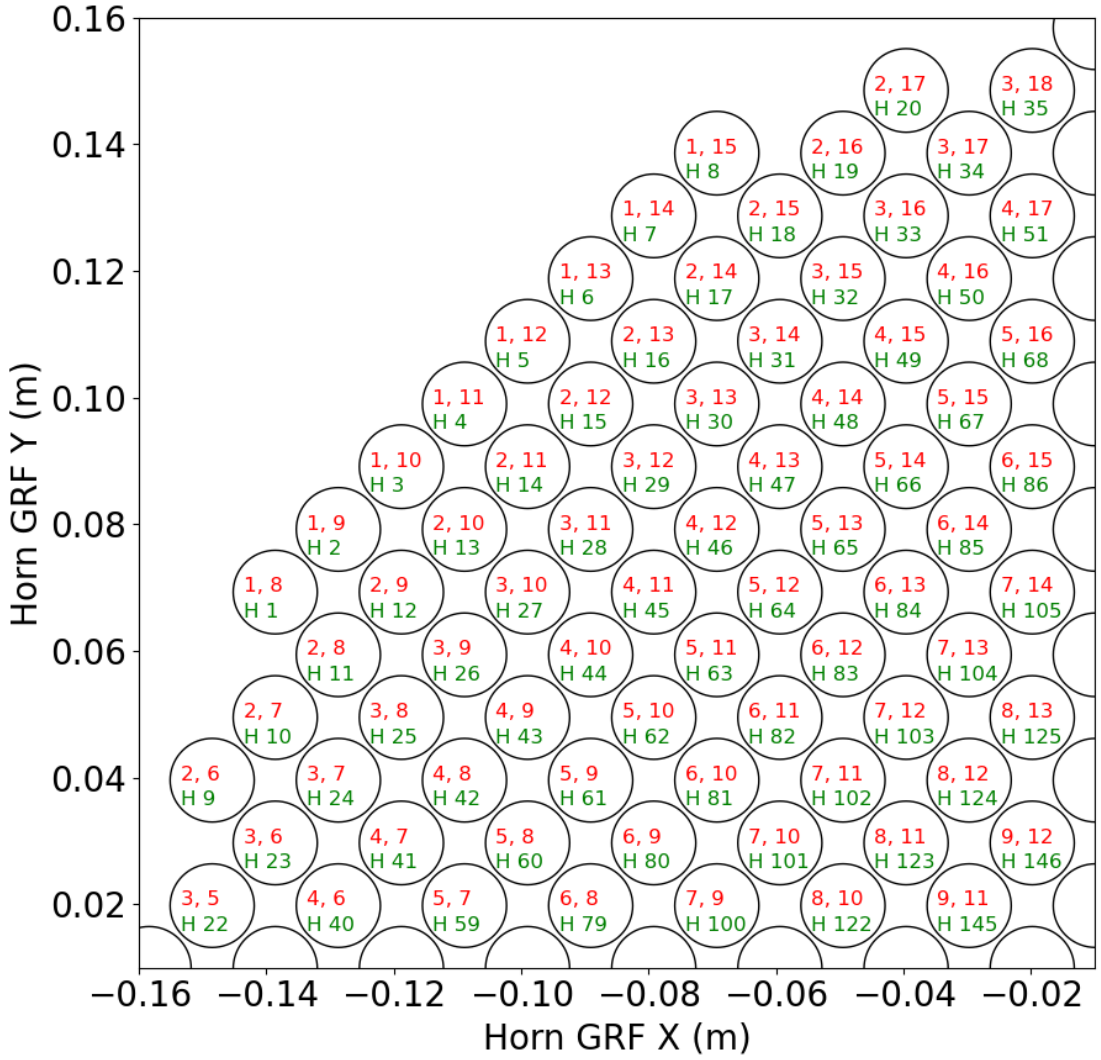

Figure 8.14: A zoomed in illustration of horn labelling and indexing from the upper left of the horn array. The red labels refer to the row and column of each horn. The green refers to the horn number. Each of the horns can also be described with the x and y coordinate values in the horn reference frame. As an example, horns [1, 8] & [1, 9] form a baseline and all baselines with the same horn separation and angular orientation are redundant baselines (e.g. [9, 11] & [9, 12]). Appendix B shows the horn numbering and indexing for the full FI array.

8.6 Pseudo-Vectorised Horn Layout

The following sections will be referring to horn locations, distances between horns, and the angular relation between horns. The horns and their locations, as shown in Fig. 8.14 (and Appendix B), can be described in a number of ways, for example their labels (1 - 400), coordinates in a reference frame (x and y locations for the horns 1 - 400), or by indices (where each horn is labelled by row and column). In

this chapter, the horn separations and angular relation are described using the row and column indices. Therefore, when describing the distance and angular relation between horns, the dimensions are 'pseudo-vectors' in units of horn separation.

The horn separation is calculated using the indexed values as L^2 where

$$L^2 = (x_i - x_j)^2 + (y_i - y_j)^2 \tag{8.10}$$

and i and j are subscripts for two horns and x and y are the row and column for those horns. Similarly the horn orientation α is found from indices

$$\tan(\alpha) = (y_j - y_i) \,/\, (x_j - x_i)\,. \tag{8.11}$$

8.7 Technical Demonstrator Baselines

8.7.1 Description of Baselines

The TD configuration of QUBIC has a square 8×8 array with a total of 64 horns (Fig. 8.15). There are 2,016 ($N(N-1)/2$, where N is the number of horns) possible baselines for the square 64 horn array. There are fewer redundant baselines. For the QUBIC TD there are 112 unique baseline types, where the distance between the baseline horns and the orientation angle are the same, and each baseline type has a number of baselines that match those criteria. Within a baseline type there are $n(n-1)/2$ unique combinations of baseline pairs that can be compared with each other for redundant baseline calibration. Here n is the number of baseline pairs of a given type. For example in the baseline type with 56 matching baselines, there are 1,540 combinations of redundant baseline pairs.

There are only one of some baseline types while there are as many as 56 of others. The distribution of baseline types for the TD is shown in Fig. 8.16. In this figure the horn separation is plotted radially (and logarithmically) in units of the physical spacing between the horns (14 mm). The plot is made with a logarithmic radial axis to make reading the data easier. In this format, each data point represents one baseline type (where horn separation and angular orientation are matching

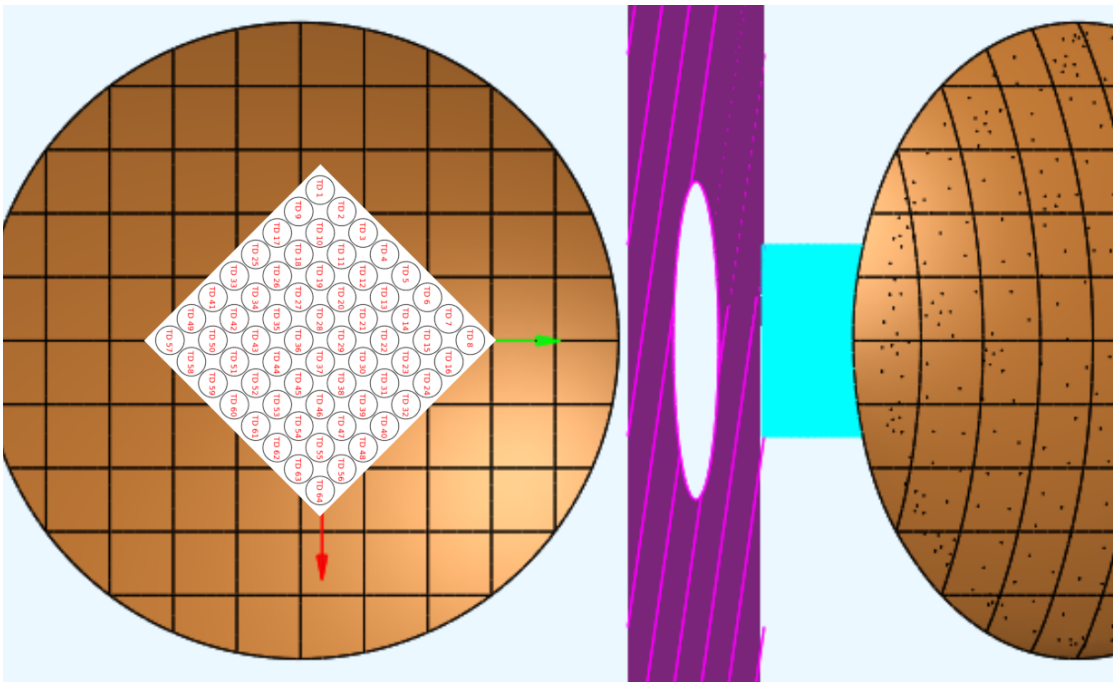

Figure 8.15: The red (x) and green (y) arrows show the GRF coordinates for QUBIC. The TD horn array is located centrally in the GRF. The primary mirror is below the horn array, horn beams pass through the cold-stop (pink), reflect off the secondary mirror and onto the focal plane (blue). The horn numbers are labelled in each horn location. Appendix B shows the horn numbering and indexing.

for the baselines) and the colour scale corresponds to the number of baselines of that redundant baseline type.

The data in Fig. 8.16 show that baseline types with shorter horn separations have the highest number of baselines of that type. Larger horn separations result in a lower number of baselines of a given type. The highest possible number of baselines (56) occurs twice where the horn separation is 1 unit and the angular orientation is 0° and 90°.

Calibration can be carried out by comparing a pair of baselines for a given type. In a simple example from the QUBIC TD (summarised in Table 8.1) where there are 4 baselines in a redundant baseline type, there are 6 ($n(n-1)/2$ with $n = 4$) unique combinations of pairs for redundant baseline calibration. For each baseline type, each combination of redundant baselines is evaluated as described by Section 8.5.

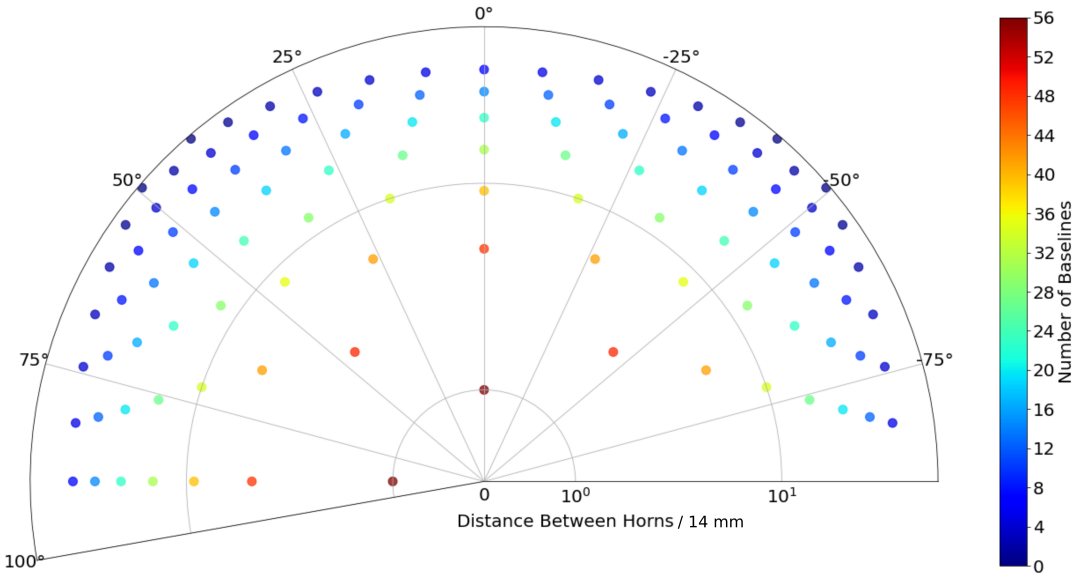

Figure 8.16: Each data point represents a unique baseline type for a given horn separation and horn orientation. The horn separation is plotted in a pseudo-vectorised way so that the physical spacing between the horns (14 mm) in the horn array is equal to one and in arbitrary units. The horn orientation is calculated in the same way. The colour scale corresponds to the number of baselines for that baseline type. The radius is plotted on a logarithmic scale so that shorter horn separations are easily readable.

Pair 1		Pair 2	
Horn 1	Horn 2	Horn 1	Horn 2
1	55	2	56
1	55	9	63
1	55	10	64
2	56	9	63
2	56	10	64
9	63	10	64

Table 8.1: This table shows an example of the combinations of horn baseline pairs than can be made for a baseline type with four matching baselines. The six unique combinations that can be made are shown.

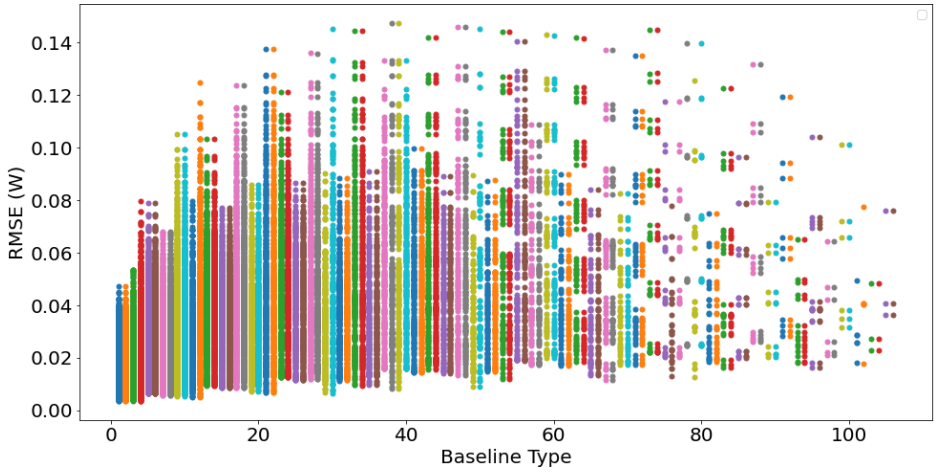

(a) Each baseline type is assigned a colour and position on the x-axis. Each point represents the RMSE of the residual difference of two baseline focal plane patterns. The y-axis shows the RMSE value.

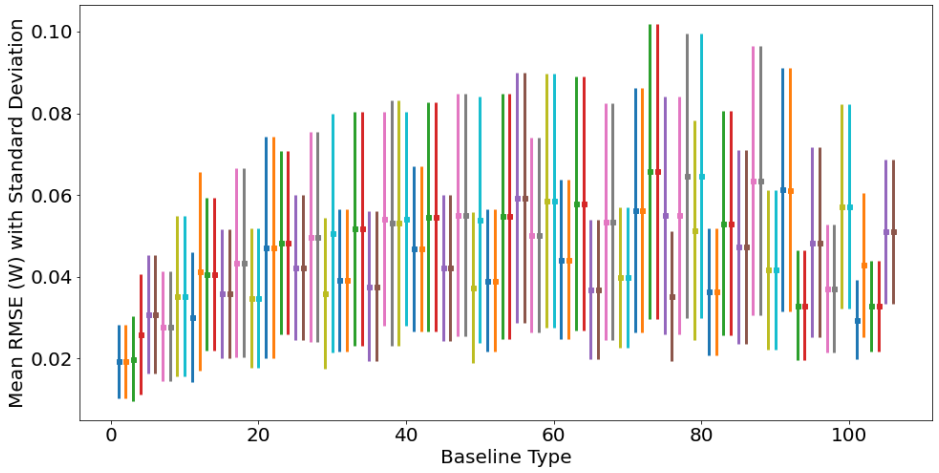

(b) Each baseline type is assigned a colour and position on the x-axis. The square marker shows the average of the RMSEs of a given baseline type. The bar shows the standard deviation of the RMSE values for a baseline type.

Figure 8.17: The RMSE values for each baseline type for the QUBIC TD configuration. The colors are used to visually distinguish between baseline types and have no physical meaning.

8.7.2 TD Aberrations

Section 8.5 showed how RMSE was used as a metric for describing the differences caused by aberrations on the focal plane. This method is applied to each unique combination of horn pairs within a baseline type, and then for each baseline type. The results are summarised in Fig. 8.17. Baseline types with fewer than three matching baselines were excluded. Fig. 8.17a shows RMSE values for each combination of horn pairs for each of the 112 baseline types. Fig. 8.17b shows the same data with the average of the RMSEs and the standard deviation of the RMSE values in a baseline type.

The data in Fig. 8.17 show that some baseline types have lower average RMSEs and these usually have a smaller standard deviation. Within baseline types, some baseline RMSEs are lower than others. Some baseline types also have a wider range of RMSE values. This indicates that some baseline types have different levels of non-redundancy due to the off-axis aberrations.

Fig. 8.17b shows an interesting characteristic where there appears to be groupings of data that make similar jumps for each data point index. For example, the first three baseline types have almost identical RMSE characteristics, five and six have near identical RMSEs, as do seven and eight. This pattern repeats periodically for all the data in the plot. This is due to the algorithm used to sort the baseline types during the analysis. First, baselines with the smallest horn separation (i.e. pseudo-vector one or 14 mm) where found along with the corresponding horn orientation. Then, baseline types of the next horn separation were found and so on. As such, baseline types with similar characteristics (horn separation or horn orientation) are plotted next to each other and naturally often have similar data as with the RMSE noted above.

Fig. 8.18 shows a polar plot, using the data from Fig. 8.17, of mean RMSE for the different baseline types and horn pair separation. These data show that RMSE is minimised when the horn separation on the TD horn array is small. The RMSEs are lowest for the TD baseline types with smallest horn separation (1) and the highest number of possible baselines (56).

This is an important result since these data show the RMSE varies by a factor of 3.4 for different baseline types and so some baselines may be more useful than others for calibration. Off-axis aberrations clearly affect baseline redundancy and

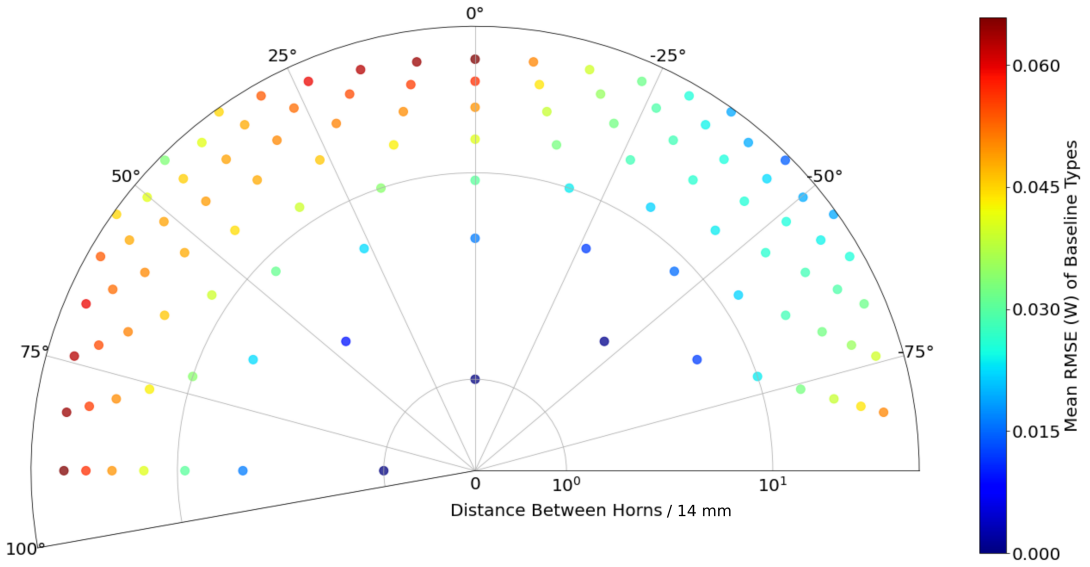

Figure 8.18: Each data point represents a unique baseline type for a given horn separation and horn orientation on a polar plot with a logarithmic radial axis. The horn separation is plotted in a pseudo-vectorised way so that the physical spacing between the horns (14 mm) in the horn array is equal to one and in arbitrary units. The horn orientation is calculated in the same way. The colour scale corresponds to the mean RMSE for the horn pair combinations of a given baseline type.

cause the variation in RMSE shown in Fig. 8.18 and in Fig. 8.17. These data show clearly that, for the TD, off-axis aberrations will likely effect the performance of QUBIC's self-calibration procedures. This effect will be present during the initial science observation campaign with the TD configuration. The level of aberrations is likely to be even higher for the future FI upgrade and this is studied next.

The FI will have 400 horns and a larger 300 mm diameter horn array. This will result in a larger number of baseline types with more horn pair combinations of each type. This configuration is studied in the next section.

8.8 Full Instrument Baselines

8.8.1 Description of Baselines

The horn array and mirror layout of the FI is shown in Fig. 8.19. There are 400 horns arranged in a circular pattern. The diameter of the horn array is 308 mm where there are 22 horns separated by 14 mm. There are 79,800 ($N(N-1)/2$,

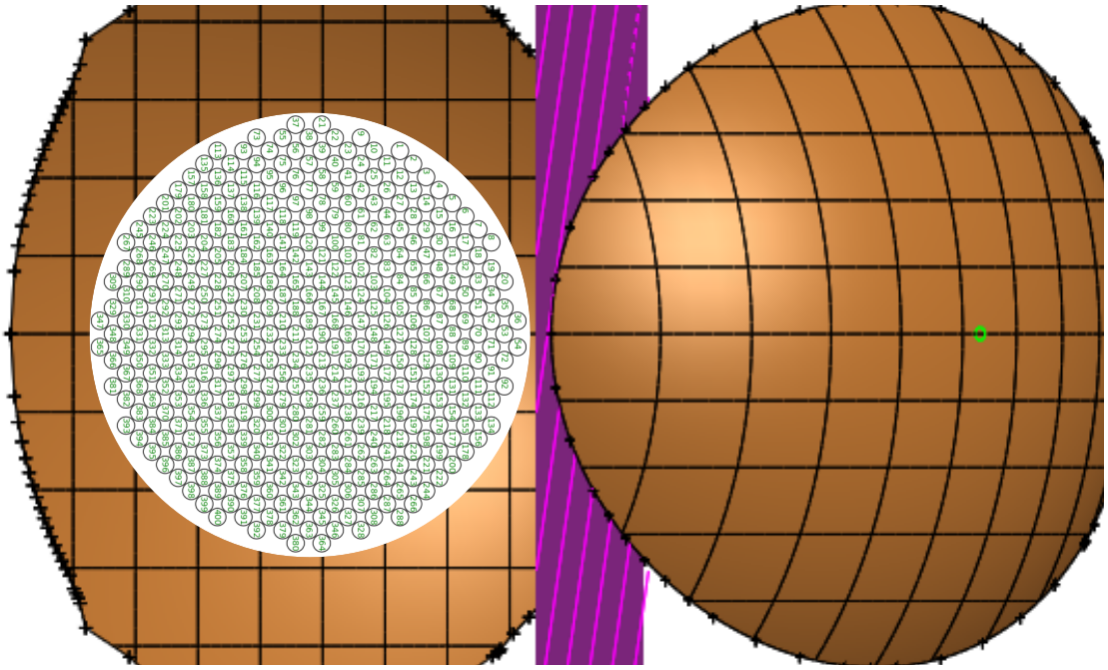

Figure 8.19: The FI horn array is centred on (0, 0, 0) in the GRF. After reflection from the primary mirror, shown below the horn array, horn beams pass through the cold-stop (pink), reflect off the secondary mirror and onto the focal plane. The horn numbers are labelled in each horn location. Appendix B shows the horn numbering and indexing.

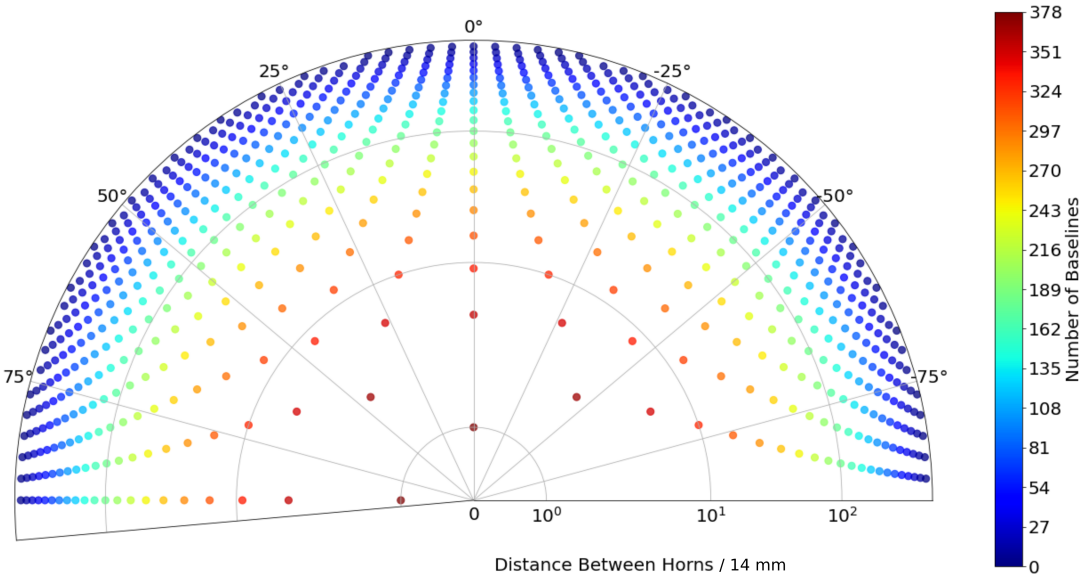

Figure 8.20: A polar plot of the number of baselines of each baseline type for the FI. Each data point represents a unique baseline type (horn separation and orientation). The radial axis is plotted logarithmically. The colour scale corresponds to the number of baselines of each baseline type.

where $N = 400$) possible baselines for a 400 horn array. When the conditions for the horn separation and orientation angle are applied, there are 774 unique baseline types.

The number of baselines of each of the 774 types varies from 1 to 378. For the 378 baselines of one type, there are 71,253 ($n(n-1)/2$, where n is the number of baselines) possible pairs that can be compared with each other. Considering all the baseline types of the FI, there are a total of 7,275,160 pairs of baselines that can be compared.

The horn separation, horn orientation, and number of baselines for the FI are shown in a polar plot in Fig. 8.20. Here, each data point shows one of the 774 unique baseline types and the colour shows the number of horn pairs of that type. As with the TD, shorter baseline types have the highest number of horn pairs of the baseline type. There are more baselines available for the FI due to the increased number of horns and the greater number of baseline types available.

8.8.2 FI Aberrations

The analysis technique from Sections 8.5 and 8.7.2 is applied to the FI horn array geometry. Due to the larger number of possible baselines (7,275,160, described in Section 8.8.1), this creates a computational time problem when calculating the residuals and RMSE's where it would take at least 300 days for the computer to process according to the TD method. Two changes to the TD method were implemented to solve this.

First, a limit was set on the number of baseline combinations where residuals and RMSEs were calculated. If the number of combinations in a type was greater than 105 combinations, a random selection of 105 equivalent baselines were selected for analysis instead of the full set of combinations. 105 is a sufficiently large number to attain good statistics while reducing the total time taken per baseline type.

Secondly, parallel processing utilised the full CPU capability. The python packages *multiprocessing*, *joblib*, and *tqdm* were used in this implementation. The original analysis code for the TD method was made using the *jupyter notebook* package which normally only utilises one CPU core. The analysis was setup so that each core of the CPU was calculating RMSE values for a baseline type and writing the data to a file. Once a computation for a baseline type was complete, the

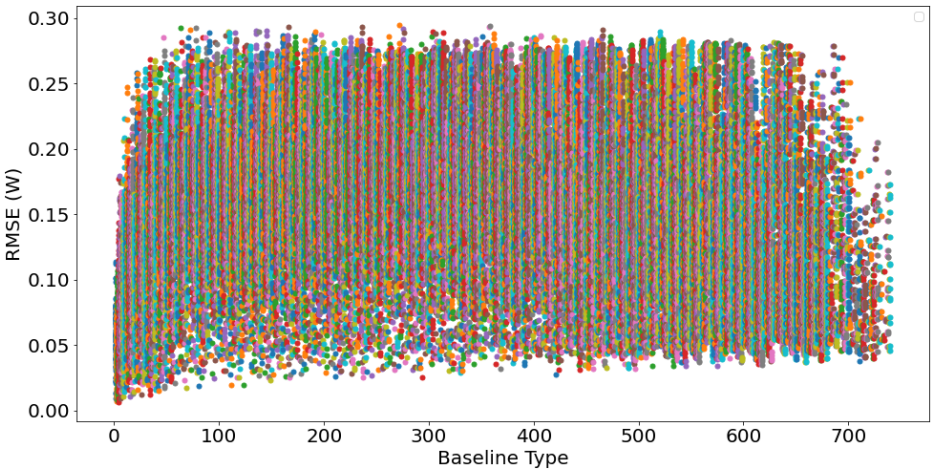

(a) Each baseline type is assigned a colour and position on the x-axis. Each point represents the RMSE of the residual difference of two baseline focal plane patterns. The y-axis shows the RMSE value.

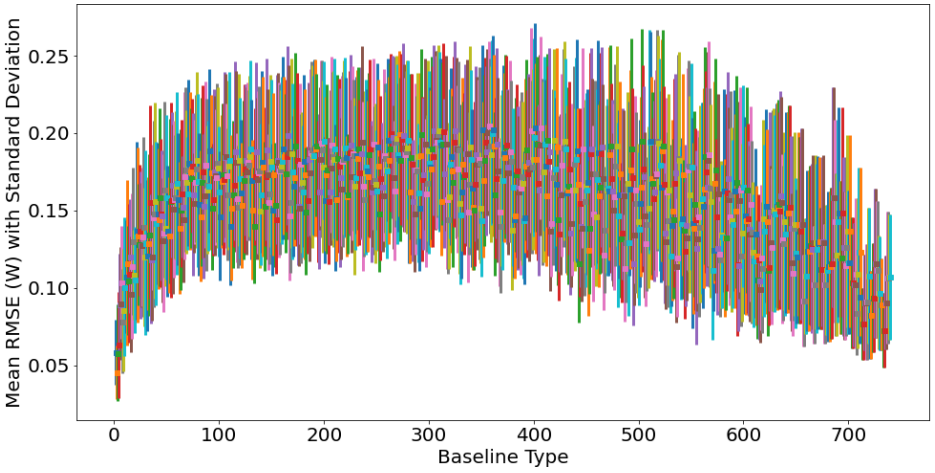

(b) Each baseline type is assigned a colour and position on the x-axis. The square marker shows the average of the RMSEs of a given baseline type. The bar shows the standard deviation of the RMSE values for a baseline type.

Figure 8.21: The RMSE values for each baseline type for the QUBIC FI configuration. The colors are used to visually distinguish between baseline types and have no physical meaning.

core would do the same process for another baseline type. By applying the 105 random combination limit and using parallel processing, the computational time was reduced to 2.4 hours.

The figures in Fig. 8.21 have the same format as those of Fig. 8.17 except they show the data for the FI rather than the TD. Since the FI has 774 unique baselines compared to the TD's 112 baselines, the figures are more densely populated.

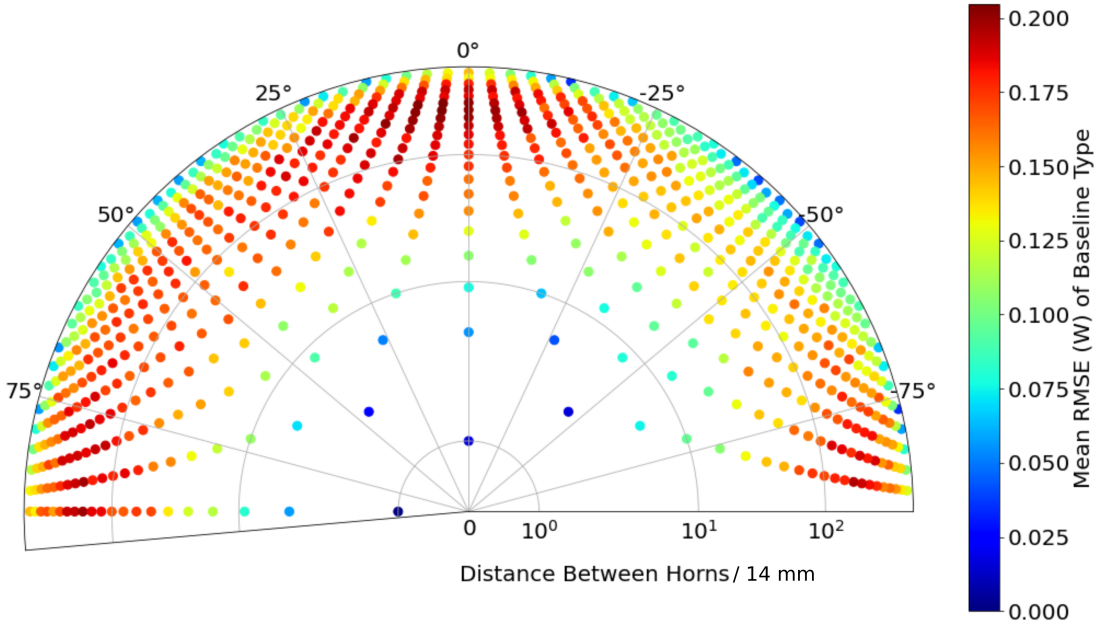

Figure 8.22: Each data point represent a unique baseline type (horn separation and orientation) on the polar plot. The radial axis is plotted logarithmically. Each data point is coloured according to the mean RMSE value computed for baselines of that baseline type.

As with Fig. 8.17, the data in Fig. 8.21 show that some baseline types have smaller average RMSEs and that these usually have a smaller standard deviation. This trend is observed in both the TD and FI. The maximum RMSE for the FI ($RMSE = 0.30$) is higher than the TD ($RMSE = 0.14$). This is expected due to the increased size of the horn array and mirror geometry.

A polar plot (Fig. 8.22), with the mean RMSE data of Fig. 8.21b, shows the physical locations associated with the mean RMSE of each baseline type. Each point refers to a unique baseline defined with mean RMSE indicated on the colour scale. It's clear that the very smallest and the very largest redundant baselines produce the smallest RMSEs ($RMSE < 0.08$). The horn orientation appears to have a lesser effect except at $-45°$ where the RMSE is below 0.015 for all horn separations. Horn separations between 100 and 250 produce RMSEs greater than 0.016. The maximum RMSEs are produced when the horn separation is close to 200 and the orientation angle is 0°. The minimum RMSE conditions occur for baseline separations of 1 unit.

The analysis was repeated but the focal plane pattern was also integrated over the detector geometry. The data are shown in Fig. 8.23. Fig. 8.23a shows that

all mean RMSEs are lower than 0.20. The clearest trend is evident on the polar plot of Fig. 8.23b where the difference in RMSE with horn separation and horn orientation is shown. Here smaller horn separations (between 3 and 125) have the highest RMSEs ($RMSE > 0.15$), other than the very shortest horn separations. Then as the horn separation increases, the RMSE decreases. At an orientation angle of $-45°$, the RMSEs are less than 0.15 for all horn separations while the opposite trend is evident at $45°$. This shows that the pixelisation of the focal plane data acts like a spatial filter. This same result can be extended to the TD configuration.

These data show that special geometries may be considered to optimise the self-calibration algorithm (for example by choosing baseline types with minimal RMSE and high number of redundant baselines). The smallest RMSEs correspond to the baselines with the maximum number of baselines available. These baseline types are preferable for self-calibration since there are more individual baselines and they are less affected by aberrations.

This study has shown that off-axis aberrations do reduce the redundancy of baselines normally considered perfectly redundant. This raises further research questions. Will these aberrations still have an effect once the detector geometry is considered? Is the effect sufficiently large that models of aberrated fringe patterns should be used rather than assuming the ideal pattern? The following sections will address these questions.

8.9 Ideal vs Aberrated Combiner (FI)

In this section, the difference between a realistic aberrated focal plane pattern of a calibration source will be compared to an idealised (non-aberrated) on-axis thin lens approximation focal plane pattern. In an ideal model of QUBIC the focal plane patterns can be calculated for horn combinations using an on-axis model of QUBIC that uses paraxial lenses instead of mirrors (see Fig. 2.15) or by assuming the focal plane pattern is the Fourier Transform of the horn aperture array field. This model has no aberrations and perfect redundancy between equivalent horn pairs can be assumed. This model in the qubicsoft[5] package calculates focal plane patterns over the focal plane detector area.

[5] github.com/qubicsoft/qubic

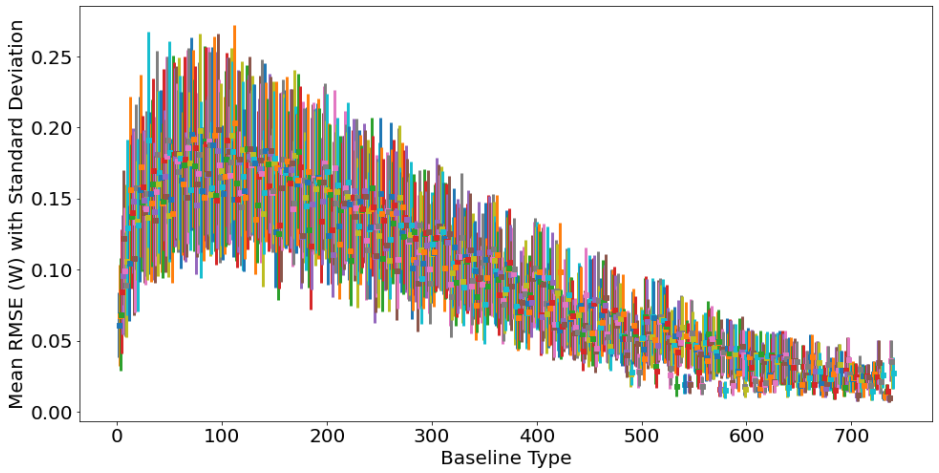

(a) Each baseline type is assigned a colour and position on the x-axis. The square marker shows the average of the RMSEs of a given baseline type. The bar shows the standard deviation of the RMSE values for a baseline type.

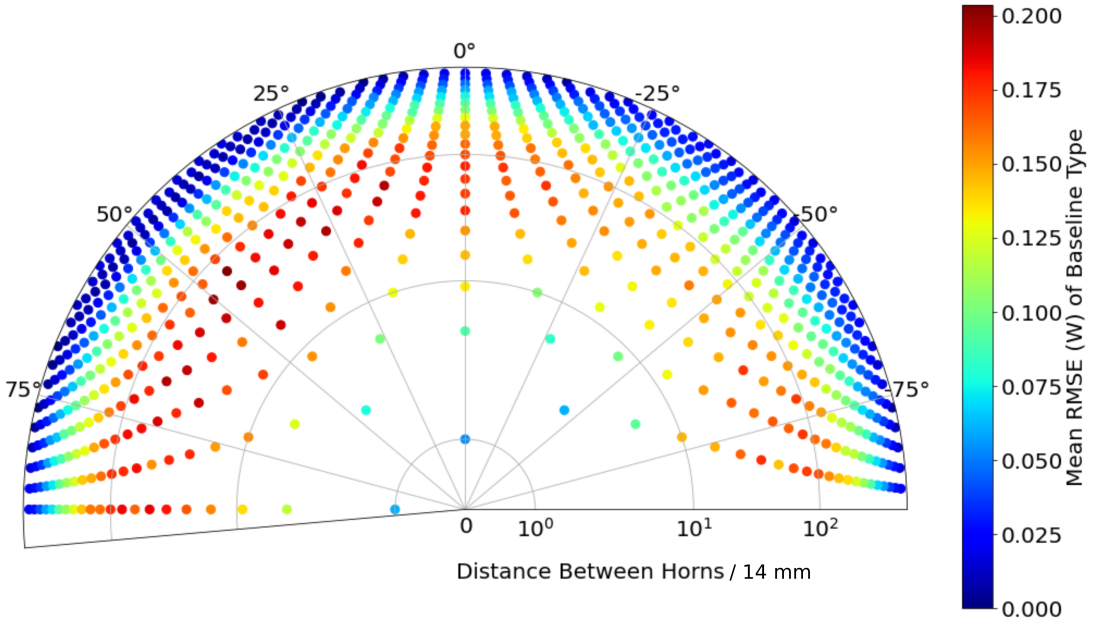

(b) Each data point represents a unique baseline type (horn separation and orientation). The radial axis is logarithmic. Each data point is coloured according to the mean RMSE value computed for baselines of that baseline type.

Figure 8.23: Mean RMSE plots for FI aberrated horn pairs compared with other horn pairs within a baseline type. These data are calculated for the 992 detectors.

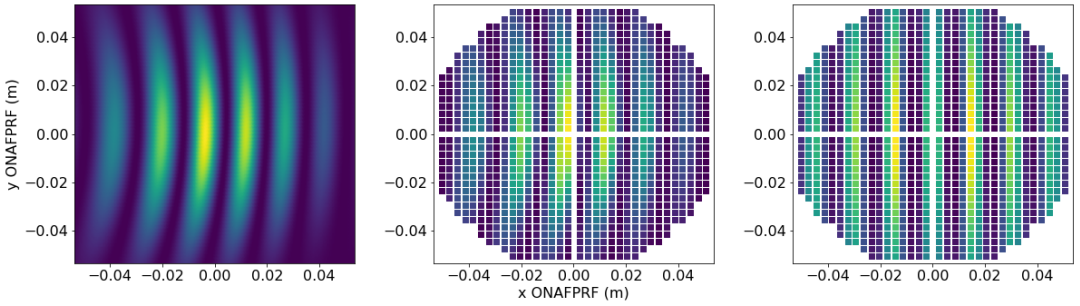

Figure 8.24: Different focal plane geometry used in this chapter. The full focal plane (left) is the grid calculated during PO modelling of the aberrations. This PO model data with aberrations can be integrated in the realistic detector geometry (centre). The ideal on-axis analytic model is shown on the right. Here the effects of the aberrations are clear where the fringe pattern (horns 47 and 82) is straight and symmetric for the ideal model and curves are evident in the aberrated models.

Fig. 8.24 demonstrates these different cases for the focal plane pattern formed by horns 47 and 82. In the left of Fig. 8.24 an area covering the whole focal plane is shown generated by a realistic PO model of QUBIC and includes the off-axis aberrations. The previous sections used this kind of data for the analysis. In the centre of Fig. 8.24 that same data are integrated into the detector geometry. The qubicsoft ideal model of the same horn pair is shown in the right of Fig. 8.24. This plot demonstrates that for the same horns, when the detector geometry is considered, there are some detectors which have very different intensity levels in aberrated and ideal cases.

8.9.1 Ideal vs Aberrated Model

For a given baseline type, in the ideal model, each focal plane baseline pattern is identical. In the example of the FI where there are 378 horn pairs with one particular horn separation and horn orientation, for example, each one will produce the exact same ideal and non-aberrated pattern. The previous sections have shown this is not realistic as the combiner's off-axis optics create aberrations. Different horn pairs in the same baseline type will have different focal plane patterns. This needs to be considered for self-calibration because typically, an ideal model of the focal plane pattern would be used in the calibration algorithm.

Each horn pair in a baseline type, with matching horn separation and angular orientation, is compared to the corresponding ideal on-axis pattern. The RMSE

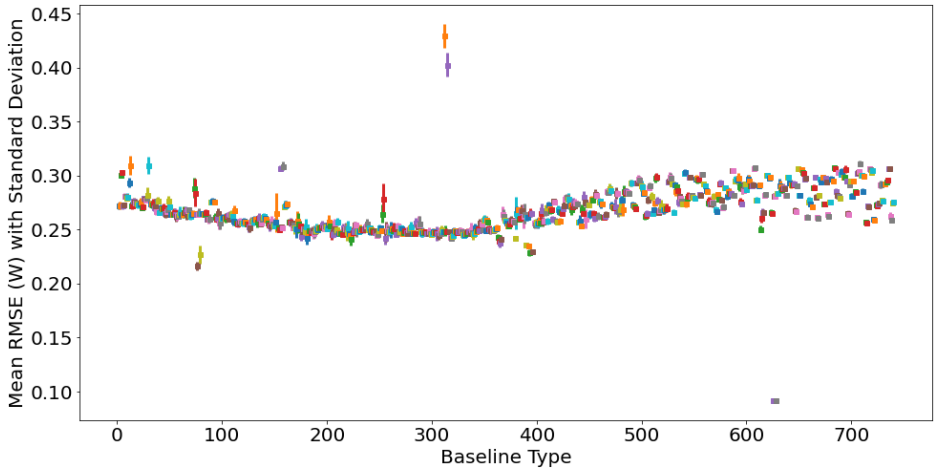

(a) Horn pairs in each baseline type are compared to the ideal model of that baseline type. The square marker shows the average of the RMSE's of a given baseline type. The bar shows the standard deviation of the RMSE values for a baseline type.

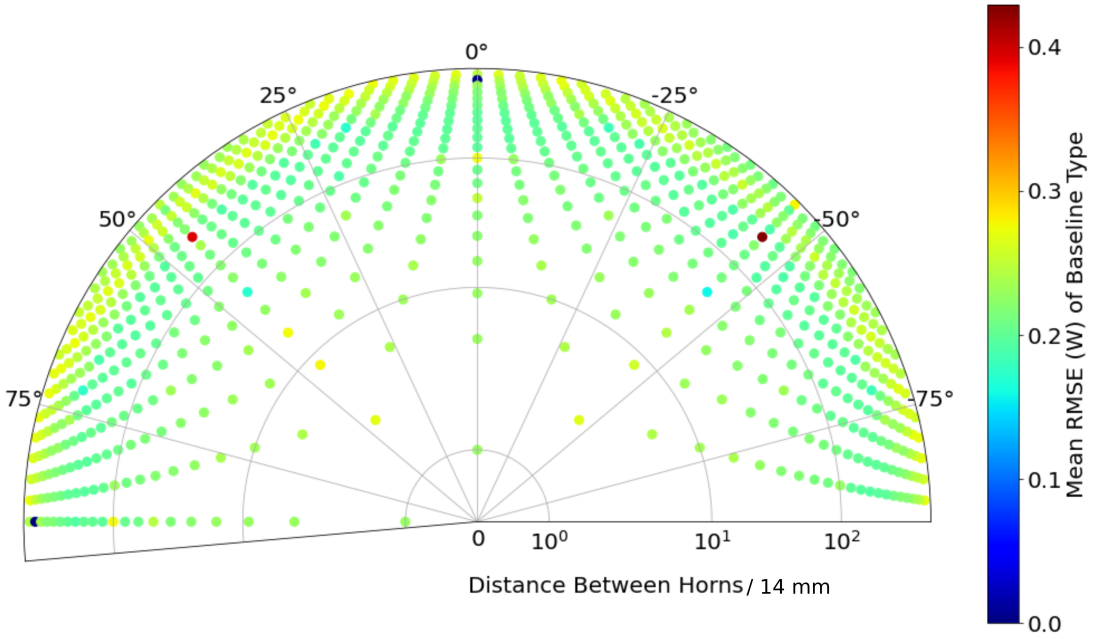

(b) A polar plot shows the same mean RMSE data with horn separation and horn orientation. The radial axis is logarithmic. Each data point is coloured according to the mean RMSE value computed for baselines of that baseline type.

Figure 8.25: Mean RMSE plots for aberrated horn pairs compared to the ideal model of that baseline type in the FI. These data are calculated for the 992 detectors.

is calculated for the focal plane pattern with the detector geometry considered. For example, in Fig. 8.24 there is one ideal on-axis focal plane pattern (right) that corresponds to a number of equivalent aberrated horn pairs. Each aberrated pattern is compared with the same ideal pattern.

The data are summarised in Fig. 8.25 for the FI. Fig. 8.25a shows the RMSE (y-axis) for each of the 774 baseline types on the x-axis. This plot can be compared directly with Figs. 8.21b and 8.17b. In Fig. 8.25a the standard deviation is smaller but the mean RMSE is consistently higher for each baseline type when compared to the previous analyses using only aberrated models. It can be concluded that comparing aberrated baselines with others of the same type (albeit with perhaps different aberrations) is preferable to comparing to an ideal model.

The polar plot in Fig. 8.25b shows the mean RMSE data with the horn separation and horn orientation. The data show consistent RMSE ($RMSE \approx 0.275$) for every baseline type. The uniformity of the data is evident with respect to horn separation and horn orientation.

The data in Fig. 8.23 can also be compared with the data in Figs. 8.21b and 8.22. This comparison shows an interesting feature when the full focal plane data are compared to the same data but integrated over the detector geometry. The mean RMSE values are largely reduced for nearly all baseline types (including horn separation and horn orientation) when the detector geometry is considered. This shows that the aberrations noted due to off-axis optics are not as severe when realistic detector geometry is considered. This suggests that for QUBIC, the off-axis aberrations exist when detector geometry is considered in the analysis. It also indicates that using an ideal analytic focal plane model for the first calibration iteration in the redundant baseline self-calibration procedure is sub-optimal and performance gains can be made by considering aberrations.

In the case of the Simons Observatory (SO), which plans to test and implement forms of self-calibration (a summary of calibration and self-calibration plans are given by Bryan et al., (2018) [121]), there are both off-axis optics (Crossed-Dragone design) and a large number of detectors (35,000) (the optical design is given by Dicker et al., (2019) [122]). These results show that a similar study for SO would be insightful. This would be particularly important if the SO collaboration chose to implement a redundant baseline self-calibration with the 19 optical tubes.

8.10 Conclusion

This chapter has shown how redundant baseline calibration can be affected by off-axis optics. A description of the number of unique baseline types, in terms of horn separation and horn orientation, and the number of baselines of each type has been given for the TD and FI. The number of horn pairs for each baseline type has also been discussed. These data inform all the possible baselines that QUBIC can use for redundant baseline self-calibration in both the TD and FI configurations.

The RMSE of PO focal plane data was used as a metric for analysing the aberrations in each baseline type. The mean RMSE demonstrates how the degree of redundancy is affected by off-axis optics. The mean RMSE of the focal plane patterns was calculated for each possible combination of horns in a baseline type. The polar plots are especially informative to show the total number of baselines and their RMSE vary with baseline type. The data show aberrations do exist for horn pair baselines that would be typically considered perfectly redundant in other systems such as those from radio and sub-millimetre astronomy.

The aberrations on the focal plane raise a question about whether they will affect QUBIC's self-calibration. Typically an analytic model of the focal plane is used in self-calibration, which in QUBIC's case is an ideal one without any aberrations. The effect of aberrations when baselines are compared to the ideal ones was tested. These data showed RMSEs higher than were seen previously when aberrated baselines were compared with each other. The polar plot showed that the mean RMSE was consistent for all horn separations and horn orientations.

It was then investigated for the FI if these RMSEs would be lower once the detector geometry is considered and it was found that indeed, once the focal plane data are averaged over the detector area, the RMSE is reduced. This is especially so for the longer baselines. This result can be extended to the TD configuration as well. This suggests that the current method of redundant baseline self-calibration is sub-optimal for QUBIC.

QUBIC's observational performance is critically dependant on redundant baseline self-calibration. It is important for systematic control but also from an operational point of view. Self-calibration, horn switching, and the associated calibration data analysis is time consuming. The calibration will be performed by observing a calibration source (Fig. 2.18) so time spent in calibration takes time from observing,

so a balance has to be found. By considering the results of this chapter, efficiency improvements in the algorithm (unique to QUBIC's off-axis optics) would reduce the time required for calibration and increase the amount of data generated from observations. This is an exciting prospect since QUBIC could then detect the B-mode polarisation sooner than originally predicted.

Improvement of the self-calibration scheme could come in a few possible forms. The first is that a PO model of the aberrated baseline pattern for each baseline type could be generated and used in place of the ideal pattern (for that baseline type). Another way to achieve some improvement is to simply use an equivalent baseline as a starting point with a known low value of RMSE. Additionally, this method could be extended to all iterations in the algorithm. The baseline pattern of any preceding iteration in the self-calibration algorithm (from within the same baseline type so horn separation and horn orientation are preserved) can be used as a starting point. As an extra step for minimising baseline pattern RMSE, baselines within baseline types could be chosen so that RMSE is minimised. There is a large amount of scope to design QUBIC's redundant baseline self-calibration algorithm for improvements over the standard radio form by considering the aberrations unique to QUBIC.

When QUBIC reaches the phase of its deployment when self-calibration is tested in Salta or during its first sky observation campaign, these self-calibration schemes could be tested in order to optimise the self-calibration algorithm. During this testing phase, the spectral performance of self-calibration in the 130 - 170 GHz and 200 - 240 GHz bands should be tested also. These tests may indicate that the self-calibration scheme that QUBIC will use could gain operational efficiency by considering the effects of off-axis aberrations.

Chapter 9

Conclusion

The research for this thesis began at a very exciting time in QUBIC's life-cycle, parts had been manufactured and were being quickly assembled in Paris. Vast amounts of data would soon need to be analysed in order to ensure the instrument was working properly and optimally. The thesis concludes at another milestone moment for QUBIC, the instrument has arrived in Argentina and is undergoing final tests in Salta Provence before deployment on a desert mountain site, Alto Chorillos, at an altitude of 4869 m above sea level. This is where QUBIC's first observations on the sky will begin. The philosophy of this thesis has been to facilitate as best as possible the successful deployment of the instrument. It is this philosophy which has led to the scope of topics covered. Two chapters were dedicated to traditional quasi-optical modelling, in-line with the expertise of the Experimental Physics Department of Maynooth University where the research was hosted. Three other chapters investigate data-analysis problems that arose during the integration and calibration efforts in Paris. The chapters analysing laboratory measurements were completed by comparing the instrument measurements with predictions from the optical models.

Chapter 1 introduced the cosmological background and motivation for QUBIC. Here, the Big Bang theory was briefly described. Inflation has been proposed as an add-on to the Big Bang theory to solve the horizon problem, flatness problem, and the exotic particle problem. If B-mode polarisation anisotropies are observed, this would provide evidence for Inflation as being a significant piece in the cosmological puzzle. The B-mode polarisation anisotropies are incredibly faint so QUBIC has

been designed with unique features to detect these primordial and faint CMB signals.

The way in which these instrument design features are implemented in order to overcome the observational and technical challenges was the subject of Chapter 2. The instrument was described starting from the outer elements (e.g. cryogenics), then the optical components, and finishing with a description of the electronics and detectors. Each aspect is unique and has important features to make it possible to detect the faint B-modes. An overview of the instrument like this is justified since the range of topics covered by this research requires an understanding of how all the unique sub-systems are integrated and work together.

Chapter 3 gave an overview of the optical techniques, in particular physical optics (and also geometrical optics), required for the modelling and analysis of QUBIC. The PO software used in this thesis, GRASP and MODAL, were described, as well as Zemax, which was used for geometrical optical modelling.

Chapter 4 produced a model for the beams on the focal plane for the two internal calibration sources installed on the TD. They were installed with the intention of producing a flat field on the focal plane for the inter-calibration of the TES detectors. The modelling results indicated that the real beams do not behave as originally intended. The beams produced a power gradient across the focal plane. In addition, there is aliasing due to diffraction. The diffraction occurred due to the width of the beam (48°) in relation to the rims of the mirrors. The modelling also indicated that the focal plane pattern is somewhat sensitive to the addition of the cold-stop in the model which produces smoothing effect on the pattern. These data were used to validate QUBIC's earliest laboratory dataset, a milestone for QUBIC. More recently, these data are being used again by collaborators for accurate inter-calibration of the TD detectors. This is a crucial step required to characterise the detector array and prepare QUBIC for science observations.

Chapter 5 described an accurate modelling of the future upgrade of QUBIC from the TD to the FI. The FI will have the full array of 400 horns, larger mirrors, and a full array of detectors. This configuration of QUBIC requires an accurate model of QUBIC that models surface imperfections resulting from manufacturing. This is essential for QUBIC's strict requirement on systematic control and calibration. As such, the realistic and aberrated PSFs were generated between 130 - 170 GHz for the full focal plane area and detector geometry. This was only possible by

integrating features of both GRASP and MODAL software. It was shown how the off-axis PO model of QUBIC differs with respect to the ideal on-axis model. Much of the historical literature regarding QUBIC and current studies are using the on-axis models of the PSF and this chapter has shown that in the future off-axis aberrated models should be considered. As such, these data will be essential for future work on spectro-imaging and redundant baseline self-calibration and these data also proved useful in Chapter 8 when analysing the effects of off-axis aberrations on self-calibration. The data from this optical model was also used for the validation of the orientation of the horn array as described by Torchinsky et al., (2021) [53]. In the future, when detector inter-calibration is complete, these spectral PSF data will be used to validate measured PSF data on the focal plane.

In Chapter 6, an optimisation of the time ordered data demodulation was made in order to make a measurement of synthetic maps for the purpose of instrument validation. The optimisation was required to improve the SNR ratio in the demodulated maps. This work also uncovered and characterised a hardware problem where the calibration source and instrument detectors were unsynchronised despite both having GPS timing. As a result, the issue was corrected and will no longer affect future data-sets. Synthetic maps on the sky with improved SNR ratio were produced for 130, 150, and 170 GHz. Now, the method of data reduction and demodulation of datasets is much improved, streamlined, and easier for collaborators to work on in the future. Particularly, it is now possible for coherent demodulation to be used. This is normally preferable over quadrature demodulation, which was used previously by the QUBIC collaboration. Now, it is possible for the preferred coherent demodulation to be used. These maps were then compared against theoretical predictions and optical models. In this way, the spectral performance of the instrument was validated. This is a key result due to QUBIC having a critical dependence on spectral performance. The analysis in this chapter is summarised in Murphy et al., (2020) [123] and by Torchinsky et al., (2022) [53]. Similarly to the PSF models of Chapter 5, these synthetic map measurements are an excellent metric of instrument performance and will be a crucial ingredient for spectro-imaging and calibration efforts in the future.

In January of 2020, a problematic replication of the synthetic map patterns emerged for all detectors after a configuration upgrade to the instrument. The cause and solution were studied in Chapter 7. It was not known if the cause was an electronic issue (e.g. cross-talk) or an optical reflection or standing wave. By studying the

configuration change, the relationship of the ghosting to electronic components, and other factors, it was determined the cause of the ghosting was optical in nature. A mechanism to explain the ghosting was also modelled by ray-tracing in Zemax. The results of this analysis were discussed with colleagues responsible for QUBIC's different sub-systems. A number of solutions and configuration changes were discussed and it was decided to move the polariser. The next cool-down and dataset showed the ghosting was eradicated in the synthetic maps. This was of critical time importance and it allowed vital testing and measurements to proceed on the rotating HWP, and horn switches.

The effect of off-axis optics on redundant baseline self-calibration for QUBIC was studied in Chapter 8. The current and historical telescope arrays (primarily radio and sub-millimetre) implementing redundant baseline self-calibration do not need to account for off-axis aberrations as their designs have no inherent need to consider off-axis aberrations. QUBIC is a bolometric interferometer and redundant baseline self-calibration has not been implemented on this kind of instrument before. It was not previously considered if QUBIC's off-axis optics could affect the performance of a redundant baseline self-calibration algorithm. The work in this chapter investigated this effect for both the TD and the FI while characterising the number of possible redundant baselines for each horn array configuration. The results showed clearly the aberrations are significantly different to ideal models of focal plane patterns. Significant performance could be gained in the algorithm by considering the aberrations of horn pair combinations. This is a very important result for QUBIC as it indicates that off-axis aberrations should be considered in redundant baseline self-calibration algorithms. This is important because QUBIC will spend a fraction of time observing an external calibration source doing self-calibration. The rest of the time the instrument will be making science observations. A balance has to be found and this chapter has shown normal redundant baseline self-calibration (using an ideal optical combiner and focal plane model) is inherently sub-optimal and there are methods available to make efficiency gains, which would result in an increased amount of science observations. This is a highly appealing outcome in terms of B-mode detection.

The research conducted in this thesis has successfully developed optical models for the validation and calibration of QUBIC. The results of these optical models have been integral to the analysis of measured instrument data for validating the performance of the instrument and making it ready for deployment on-site in Alto

Chorillos. The data have also been shared with colleagues so they can perform their own analyses. While the internal calibrator model, FI PSF model, synthetic map optimisation, and ghost analysis solved current issues in time, the FI model and baseline redundancy analysis provide useful data and insight for colleagues to continue this work in future facilitating the successful deployment and scientific observations of QUBIC.

9.1 Publications

9.1.1 JCAP Special Edition

During my PhD research, as a QUBIC collaborator, I have been co-author on numerous peer-reviewed articles and conference proceedings. Eight articles, including one article still undergoing a final review, have been accepted for publication in a special edition of the Journal of Cosmology and Astroparticle Physics[1]. This special edition will describe QUBIC's most recent calibration and integration developments mainly carried out in APC over the last five years. I have made direct and significant contributions[2], in particular, to QUBIC papers III and VIII.

Hamilton, J.C., Mousset, L., Battistelli, E.S., Bigot-Sazy, M.A., Chanial, P., Charlassier, R., D'Alessandro, G., de Bernardis, P., De Petris, M., Lerena, M.M.G., Grandsire, L., Lau, S., Marnieros, S., Masi, S., Mennella, A., O'Sullivan, C., Piat, M., Riccardi, G., Sc´occola, C., Stolpovskiy, M., Tartari, A., Torchinsky, S.A., Voisin, F., Zannoni, M., Ade, P., Alberro, J.G., Almela, A., Amico, G., Arnaldi, L.H., Auguste, D., Aumont, J., Azzoni, S., Banfi, S., B´elier, B., Ba'u, A., Bennett, D., Berg´e, L., Bernard, J.P., Bersanelli, M., Bonaparte, J., Bonis, J., Bunn, E., Burke, D., Buzi, D., Cavaliere, F., Chapron, C., Cerutti, A.C.C., Columbro, F., Coppolecchia, A., Gasperis, G.D., Leo, M.D., Dheilly, S., Duca, C., Dumoulin, L., Etchegoyen, A., Fasciszewski, A., Ferreyro, L.P., Fracchia, D., Franceschet, C., Ganga, K.M., Garc´ıa, B., Redondo, M.E.G., Gaspard, M., Gayer, D., Gervasi, M., Giard, M., Gilles, V., Giraud-Heraud, Y., Berisso, M.G., Gonz´alez, M., Gradziel, M., Hampel, M.R., Harari, D., Henrot-Versill´e, S., Incardona, F., Jules, E., Kaplan, J., Kristukat, C., Lamagna, L., Loucatos, S., Louis, T., Maffei, B., Marty, W., Mattei, A., May, A., McCulloch, M., Mele, L., Melo, D., Montier, L., Mundo, L.M., Murphy, J.A., **Murphy, J.D.**, Nati, F., Olivieri, E., Oriol, C., Paiella, A., Pajot, F., Passerini, A., Pastoriza, H., Pelosi, A., Perbost, C., Perciballi, M., Pezzotta, F., Piacentini, F., Piccirillo, L., Pisano, G., Platino, M., Polenta, G., Prˆele, D., Puddu, R., Rambaud, D., Ringegni, P., Romero, G.E., Rasztocky, E., Salum, J.M., Schillaci, A., Scully, S., Spinelli, S., Stankowiak, G., Supanitsky, A.D., Thermeau, J.P., Timbie, P., Tomasi, M., Tucker, C., Tucker,

[1]For the sake of brevity, where I am a third order author, I will write the first author's name and *"the QUBIC Collaboration incl. Murphy, J.D."*. For QUBIC I, the full list of authors is given.

[2]In this case, where I am a second order author, I will list the first author and all other second order authors.

G., Vigan'o, D., Vittorio, N., Wicek, F., Wright, M., and Zullo, A.
QUBIC I: Overview and Science Program. *Journal of Cosmology and Astroparticle Physics*, 2022. URL https://arxiv.org/abs/2011.02213v2

Mousset, L., the QUBIC Collaboration, incl. **Murphy, J.D.**.
QUBIC II: Spectro-polarimetry with bolometric interferometry. *Journal of Cosmology and Astroparticle Physics*, 2022. URL https://arxiv.org/abs/2010.15119v2

Torchinsky, S.A., Hamilton, J.C., Piat, M., Battistelli, E.S., Chapron, C., D'Alessandro, G., de Bernardis, P., De Petris, M., Lerena, M.M.G., Gonz´alez, M., Grandsire, L., Masi, S., Marnieros, S., Mennella, A., Mousset, L., **Murphy, J.D.**, Prˆele, D., Stankowiak, G., O'Sullivan, C., Tartari, A., Thermeau, J.P., Voisin, F., Zannoni, M., et al.
QUBIC III: Laboratory characterization. *Journal of Cosmology and Astroparticle Physics*, 2022. URL https://arxiv.org/abs/2008.10056v3

Piat, M., the QUBIC Collaboration, incl. **Murphy, J.D.**.
QUBIC IV: Performance of TES Bolometers and Readout Electronics. *Journal of Cosmology and Astroparticle Physics*, 2022. URL https://arxiv.org/abs/2101.06787v2

Masi, S., the QUBIC Collaboration, incl. **Murphy, J.D.**.
QUBIC V: Cryogenic system design and performance. *Journal of Cosmology and Astroparticle Physics*, 2022. URL https://arxiv.org/abs/2008.10659v2

D'Alessandro, G., the QUBIC Collaboration, incl. **Murphy, J.D.**.
QUBIC VI: cryogenic half wave plate rotator, design and performances. *Journal of Cosmology and Astroparticle Physics*, 2022. URL https://arxiv.org/abs/2008.10667v2

Cavaliere, F., the QUBIC Collaboration, incl. **Murphy, J.D.**.
QUBIC VII: The feedhorn-switch system of the technological demonstrator. *Journal of Cosmology and Astroparticle Physics*, 2022. URL https://arxiv.org/abs/2008.12721v2

O'Sullivan, C., De Petris, M., Amico, G., Battistelli, E.S., Burke, D., Buzi, D., Chapron, C., Conversi, L., D'Alessandro, G., de Bernardis, P., Leo, M.D., Gayer, D., Grandsire, L., Hamilton, J.C., Marnieros, S., Masi, S., Mattei, A., Mennella, A., Mousset, L., **Murphy, J.D.**, Pelosi, A., Perciballi, M., Piat, M., Scully, S.,

Tartari, A., Torchinsky, S.A., Voisin, F., Zannoni, M., Zullo, A., et al.
QUBIC VIII: Optical design and performance. *Journal of Cosmology and Astroparticle Physics*, 2022. URL `https://arxiv.org/abs/2008.10119v2`

9.1.2 General Publications

My contributions are noted in the following publications, including conference proceedings for SPIE Astronomical Telescopes and Instrumentation, which were accompanied by a video presentation, due to COVID-19, and a poster presentation.

Murphy, J.D., Burke, D., Lerena, M.M.G., Hamilton, J.C., Mousset, L., De Petris, M., O'Sullivan, C., Torchinsky, S.A., et al.
Calibration of QUBIC: The Q and U bolometric interferometer for cosmology. In Zmuidzinas, J. and Gao, J.R., editors, *Millimeter, Submillimeter, and Far-Infrared Detectors and Instrumentation for Astronomy X*, volume 11453, pages 378 – 387. International Society for Optics and Photonics, SPIE, 2020. doi: 10.1117/12.2560172. URL `https://doi.org/10.1117/12.2560172`

O'Sullivan, C., Burke, D., Gayer, D., **Murphy, J.D.**, Scully, S., Leo, M.D., De Petris, M., Mattei, A., Zullo, A., Mennella, A., Zannoni, M., Bleurvacq, N., Chapron, C., Hamilton, J.C., Piat, M., et al.
Simulations and performance of the QUBIC optical beam combiner. *Proceedings of SPIE*, 10708:107082I, 2018. URL `https://mural.maynoothuniversity.ie/13433/`

Burke, D., Gayer, D., Kalinauskaite, E., O'Sullivan, C., **Murphy, J.D.**, Scully, S.P., De Petris, M., Leo, M.D., Mennella, A., Torchinsky, S.A., Zannoni, M., et al.
Optical modelling and analysis of the Q and U bolometric interferometer for cosmology. In Sadwick, L.P. and Yang, T., editors, *Terahertz, RF, Millimeter, and Submillimeter-Wave Technology and Applications XI*, volume 10531, pages 59 – 72. International Society for Optics and Photonics, SPIE, 2018. doi: 10.1117/12.2287158. URL `https://doi.org/10.1117/12.2287158`

May, A.J., the QUBIC Collaboration, incl. **Murphy, J.D.**.
Thermal architecture for the QUBIC cryogenic receiver. In Zmuidzinas, J. and Gao, J.R., editors, *Millimeter, Submillimeter, and Far-Infrared Detectors and Instrumentation for Astronomy IX*, volume 10708, pages 610 – 623. International

Society for Optics and Photonics, SPIE, 2018. doi: 10.1117/12.2312085. URL https://doi.org/10.1117/12.2312085

Piat, M., the QUBIC Collaboration, incl. **Murphy, J.D.**.
QUBIC: using NbSi TESs with a bolometric interferometer to characterize the polarisation of the CMB. *Journal of Low Temperature Physics*, 200:363–373, 2019. URL https://ui.adsabs.harvard.edu/abs/2020JLTP..200..363P/abstract

Mennella, A., the QUBIC Collaboration, incl. **Murphy, J.D.**.
QUBIC: Exploring the primordial universe with the q & u bolometric interferometer. *Universe*, 5(2), 2019. ISSN 2218-1997. doi: 10.3390/universe5020042. URL https://www.mdpi.com/2218-1997/5/2/42

Mele, L., the QUBIC Collaboration, incl. **Murphy, J.D.**.
The QUBIC instrument for CMB polarization measurements. *Journal of Physics: Conference Series*, 1548(1):012016, May 2020. doi: 10.1088/1742-6596/1548/1/012016. URL https://doi.org/10.1088/1742-6596/1548/1/012016

O'Sullivan, C., the QUBIC Collaboration, incl. **Murphy, J.D.**.
QUBIC: the Q and U bolometric interferometer for cosmology. In Zmuidzinas, J. and Gao, J.R., editors, *Millimeter, Submillimeter, and Far-Infrared Detectors and Instrumentation for Astronomy IX*, volume 10708, pages 289 – 302. International Society for Optics and Photonics, SPIE, 2018. doi: 10.1117/12.2313332. URL https://doi.org/10.1117/12.2313332

Marnieros, S., the QUBIC Collaboration, incl. **Murphy, J.D.**.
TES Bolometer Arrays for the QUBIC B-Mode CMB Experiment. *Journal of Low Temperature Physics*, 199(3-4):955–961, January 2020. doi: 10.1007/s10909-019-02304-5

Gamboa Lerena, M.M., the QUBIC Collaboration, incl. **Murphy, J.D.**.
Angular resolution at map level in the QUBIC instrument. *Boletin de la Asociacion Argentina de Astronomia La Plata Argentina*, 61B:155–158, July 2020

Salatino, M., the QUBIC Collaboration, incl. **Murphy, J.D.**.
Performance of NbSi transition-edge sensors readout with a 128 MUX factor for the QUBIC experiment. In Zmuidzinas, J. and Gao, J.R., editors, *Millimeter, Submillimeter, and Far-Infrared Detectors and Instrumentation for Astronomy IX*, volume 10708, pages 732 – 743. International Society for Optics and Photonics, SPIE, 2018. doi: 10.1117/12.2312080. URL https://doi.org/10.1117/12.2312080

Stankowiak, G., the QUBIC Collaboration, incl. **Murphy, J.D.**.
Detection chain and electronic readout of the QUBIC instrument. In Zmuidzinas, J. and Gao, J.R., editors, *Millimeter, Submillimeter, and Far-Infrared Detectors and Instrumentation for Astronomy X*, volume 11453, pages 314 – 327. International Society for Optics and Photonics, SPIE, 2020. doi:10.1117/12.2561567. URL `https://doi.org/10.1117/12.2561567`

Scóccola, C.G., the QUBIC Collaboration, incl. **Murphy, J.D.**.
Current status of the QUBIC experiment. *Boletin de la Asociacion Argentina de Astronomia La Plata Argentina*, 62:177–179, July 2021

D'Alessandro, G., the QUBIC Collaboration, incl. **Murphy, J.D.**.
The QUBIC experiment. In Auge, E., Dumarchez, J., and Tran Thanh Van, J., editors, *Proceedings of the 53rd Rencontres de Moriond on Cosmology 2018, Proceedings of the 53rd Rencontres de Moriond on Cosmology 2018*, pages 145–148, 2020. ARISF. ISBN 9791096879076. Publisher Copyright: © 2018 ARISF.; 53rd Rencontres de Moriond on Cosmology 2018 ; Conference date: 17-03-2018 Through 24-03-2018

Battistelli, E.S., the QUBIC Collaboration, incl. **Murphy, J.D.**.
QUBIC: The Q & U Bolometric Interferometer for Cosmology. *Journal of Low Temperature Physics*, 199(1-2):482–490, Feb 2020. ISSN 1573-7357. doi: 10.1007/s10909-020-02370-0. URL `http://dx.doi.org/10.1007/s10909-020-02370-0`

9.1.3 Software

During this research I have contributed to the QUBIC collaboration software, qubicsoft (Mousset et al., (2021) [104], below). In addition, I have developed software and scripts for GRASP and MODAL optical analysis, scripts for generating batch mode files, and Zemax analysis code.

Mousset, L., Gamboa Lerena, M.M., Chanial, P., Hamilton, J.C., **Murphy, J.D.**, Incardona, F., Stolpovskiy, M., Biquard, S., Torchinsky, S., Scoccola, C., Tristram, M., Kaplan, J., Henrot-Versille, S., Mennella, M.R.A., Granese, N.M., and Tomasi, M.
qubicsoft. `https://github.com/qubicsoft/qubic.git`, 2021

Murphy, J.D.. multifrequency. `https://github.com/seamusomurchu/multifrequency.git`, 2021

Murphy, J.D.. ZemaxIO. `https://github.com/seamusomurchu/ZemaxIO.git`, 2021

Murphy, J.D.. graspoutputs. `https://github.com/seamusomurchu/graspoutputs.git`, 2021

Appendix A

Spectral Focal Plane Data for the Internal Calibrators

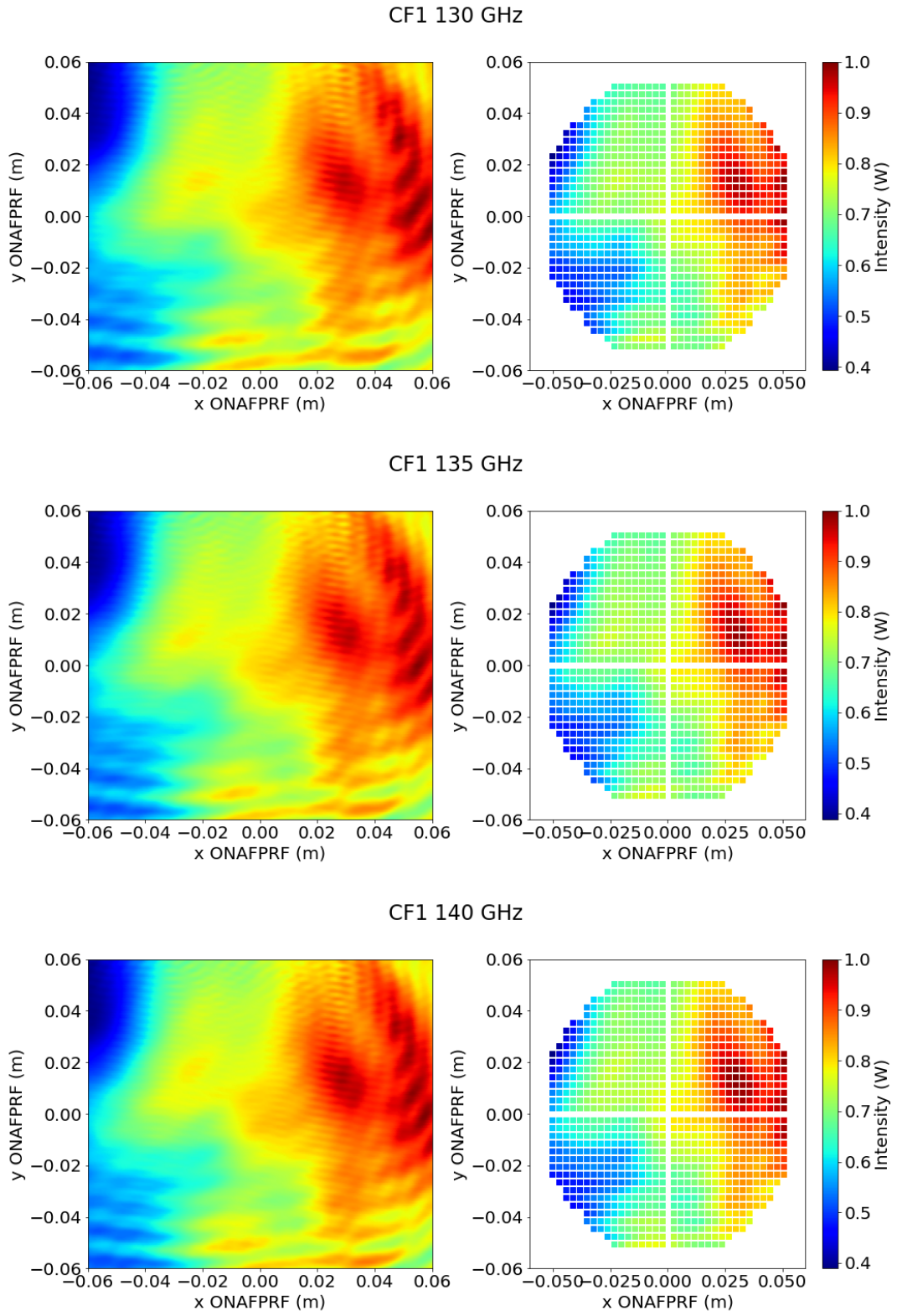

Figure A.1: CF1 internal calibrator at individual frequencies.

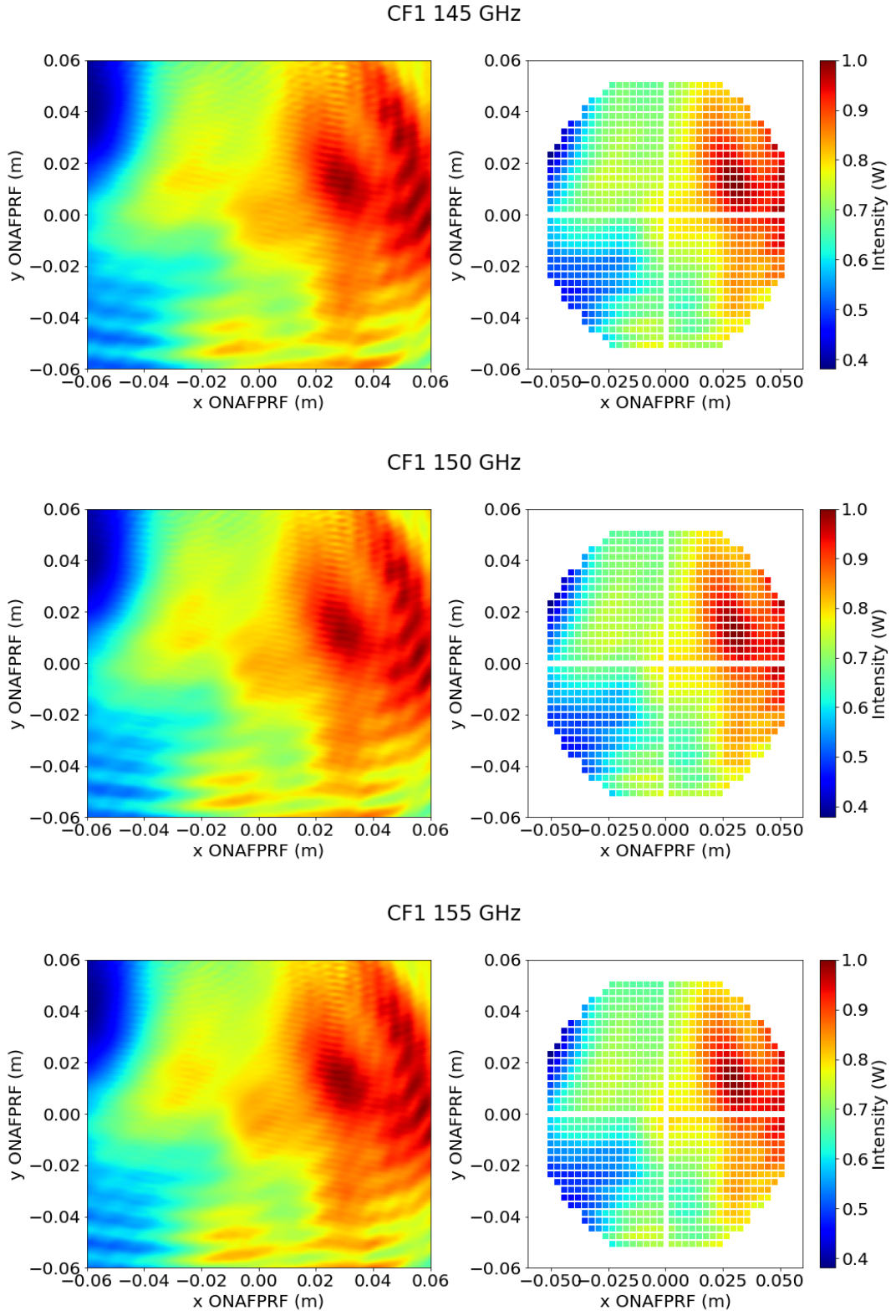

Figure A.1: CF1 internal calibrator at individual frequencies (cont.)

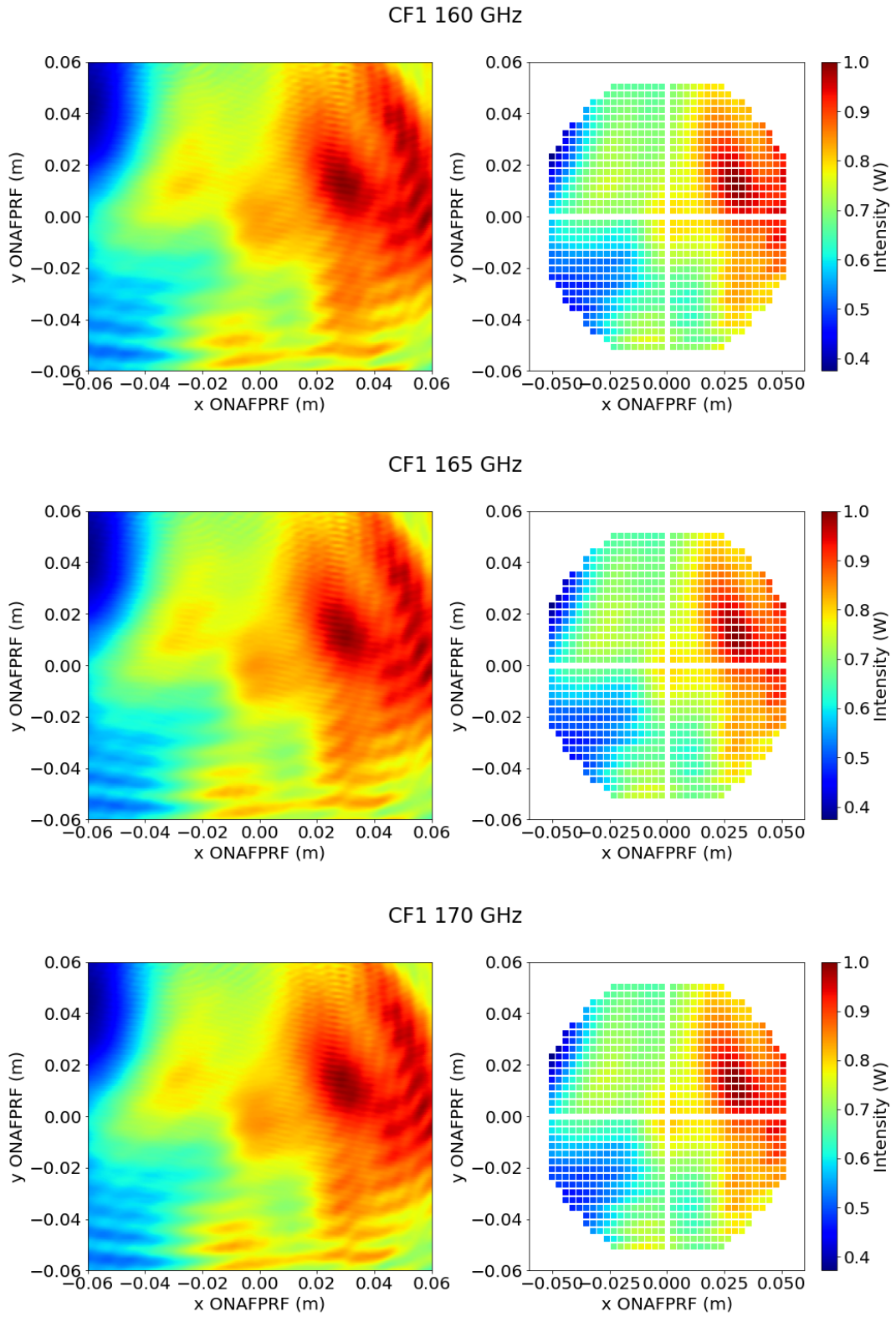

Figure A.1: CF1 internal calibrator at individual frequencies (cont.)

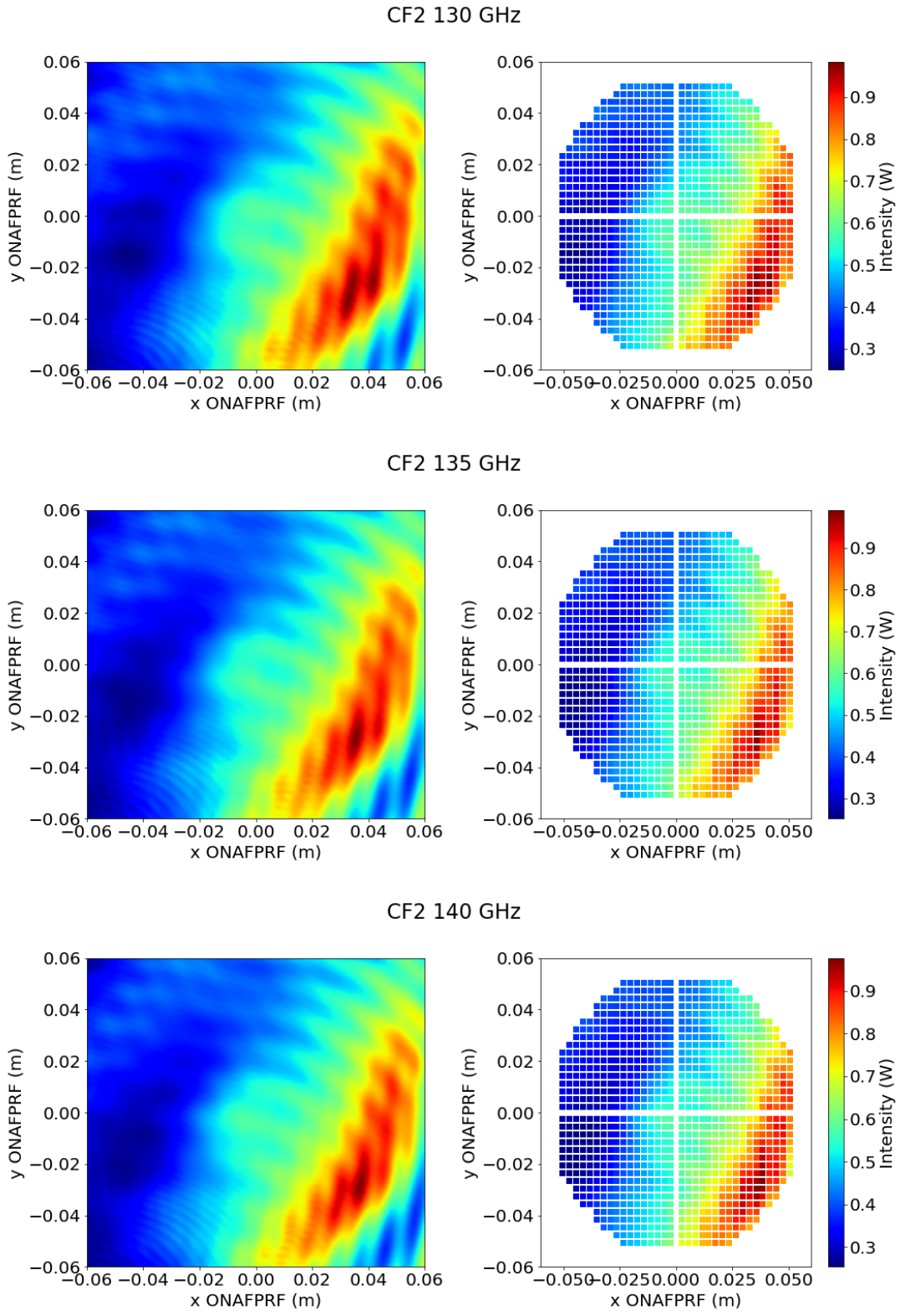

Figure A.2: CF2 internal calibrator at individual frequencies.

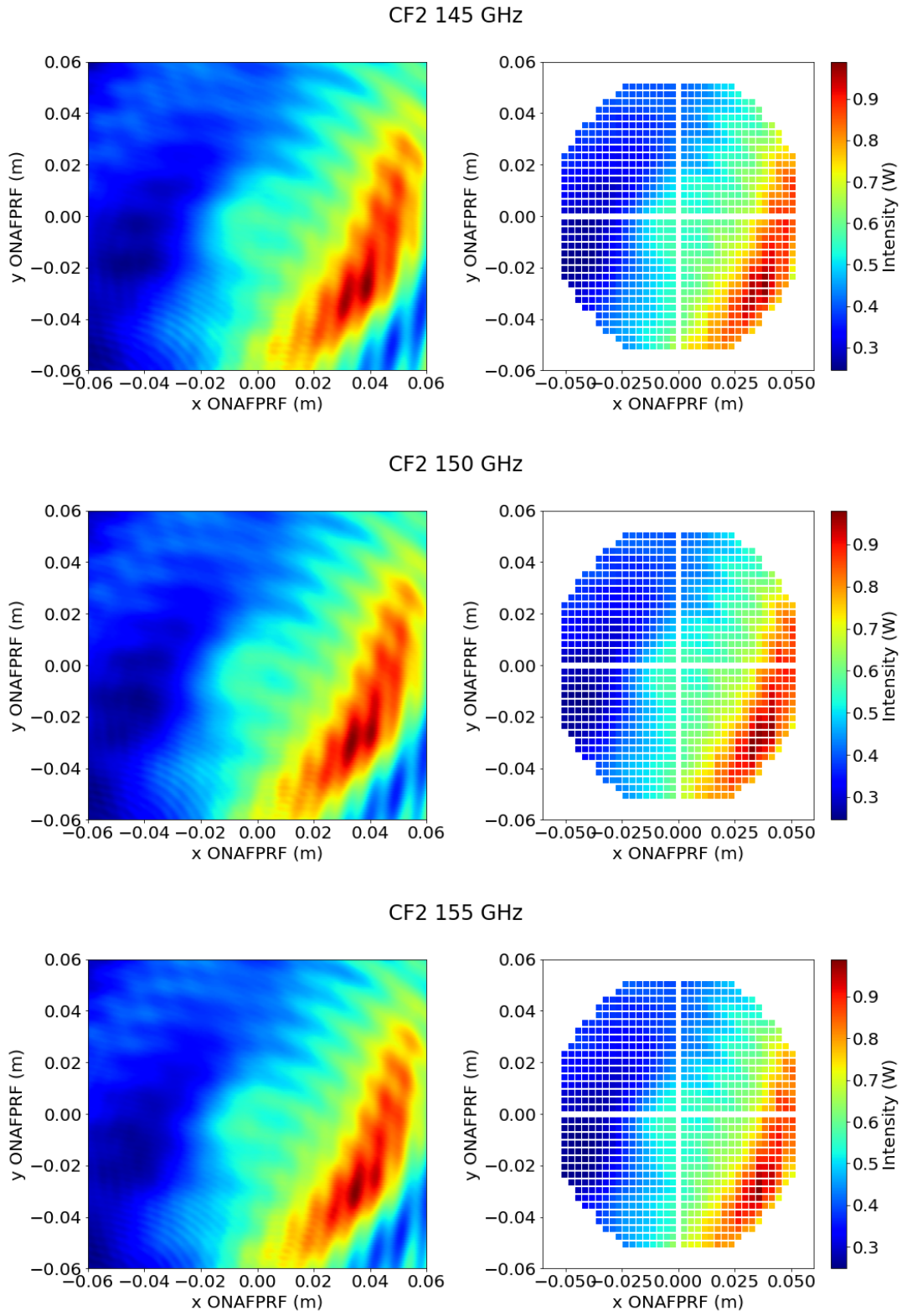

Figure A.2: CF2 internal calibrator at individual frequencies (cont.)

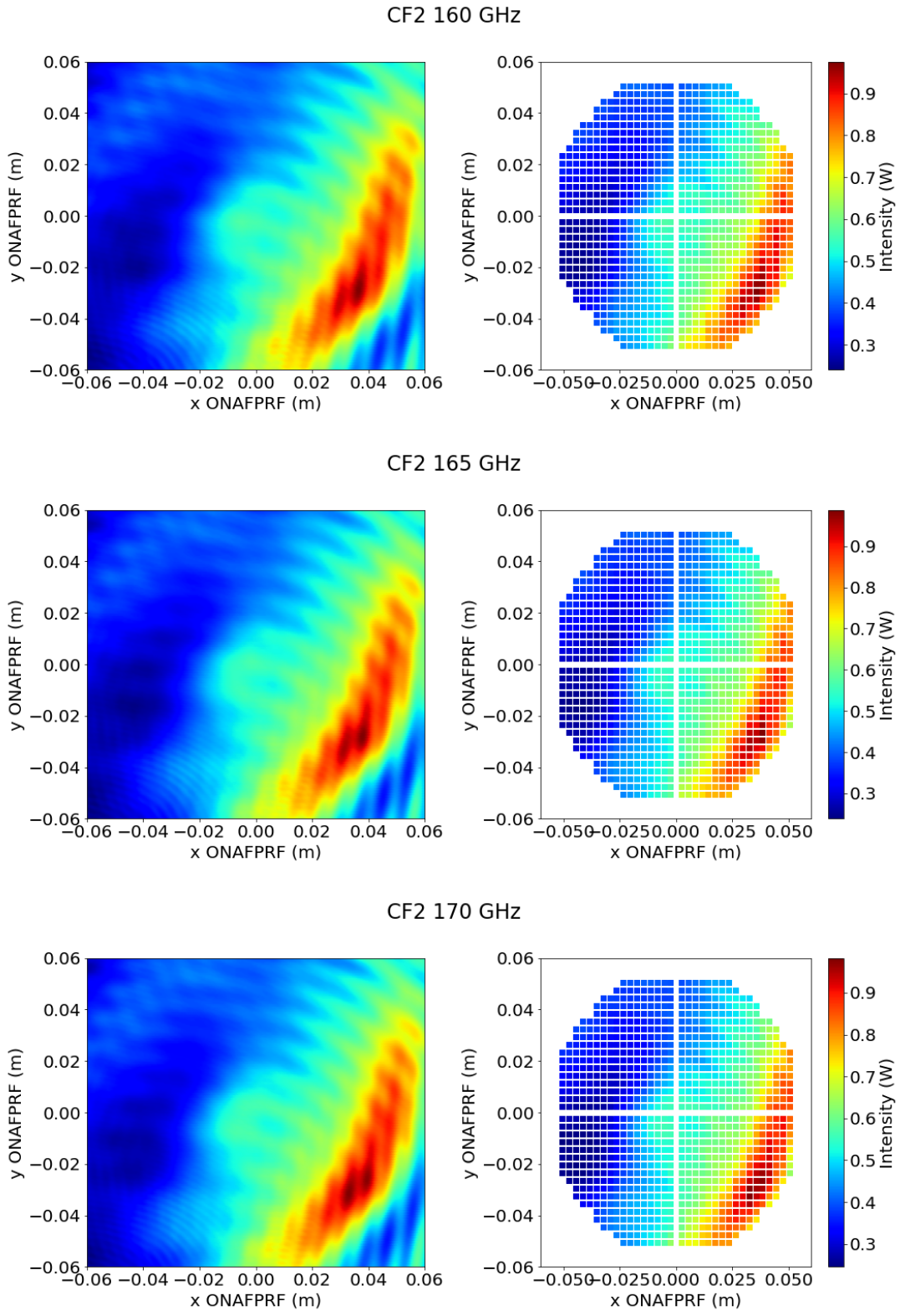

Figure A.2: CF2 internal calibrator at individual frequencies (cont.)

Appendix B

Horn Numbering and Indexing

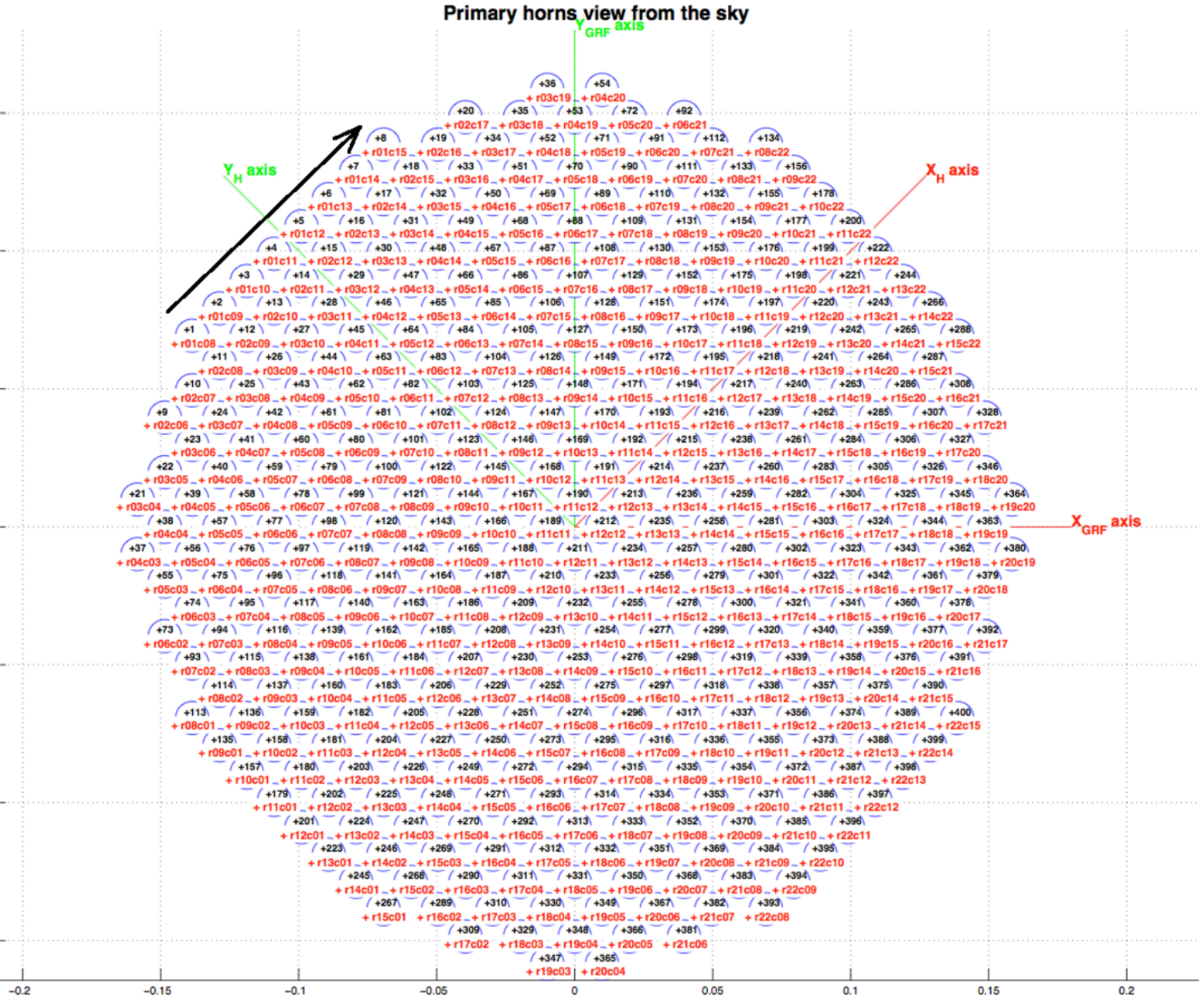

Figure B.1: The horn numbers with corresponding row and column indexing for identifying horns in the horn array. The axis units are in meters. Two axis reference frames are shown, Global Reference Frame (GRF) and 'SECHO ARF' as defined by Brossard et al., (2017) [91]. The TD horns are the central 64 horns formed by an 8×8 square array. Figure reproduced from an internal document by Brossard and Chanial (2014) [96].

Appendix C

300 K Ideal Mirror Definitions

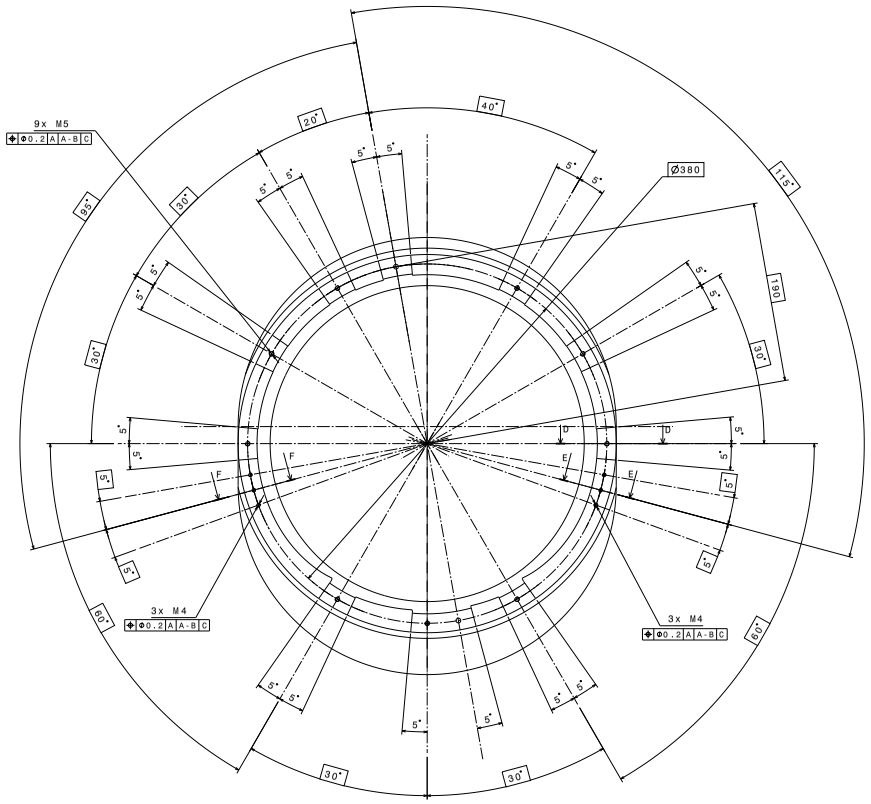

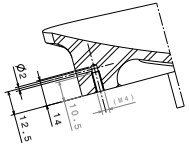

3x identical Sectional view F-F
Scale : 1:1

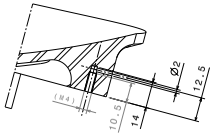

3x identical Sectional view E-E
Scale : 1:1

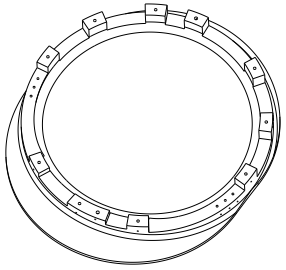

Isometric view
Scale : 1:3

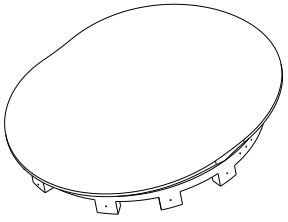

Isometric view
Scale : 1:3

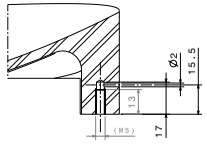

9x identical Sectional view D-D
Scale : 1:1

Sectional view C-C
Scale : 1:1

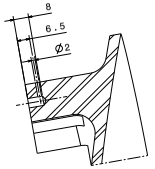

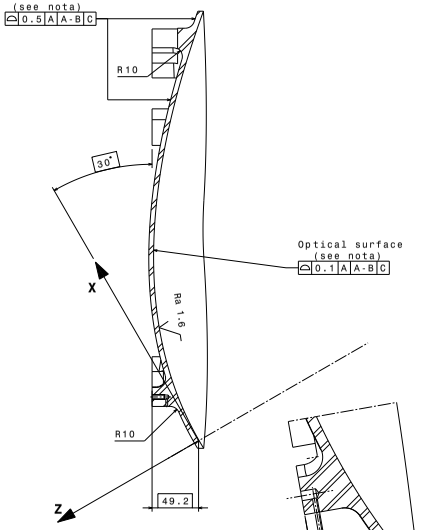

Sectional view A-A

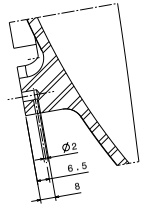

Sectional view B-B
Scale : 1:1

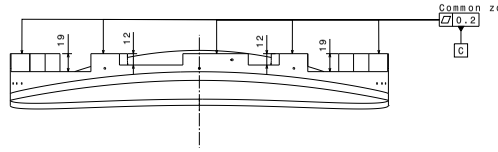

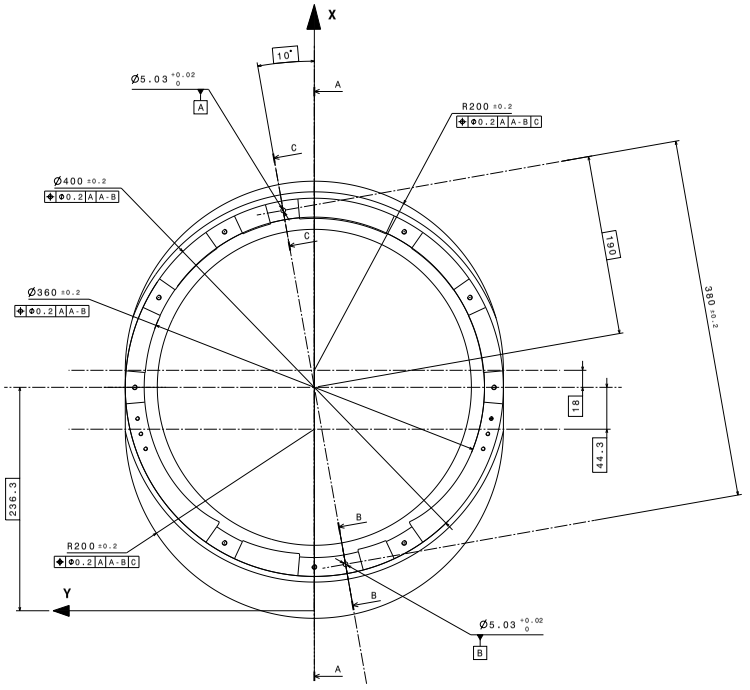

Bottom view

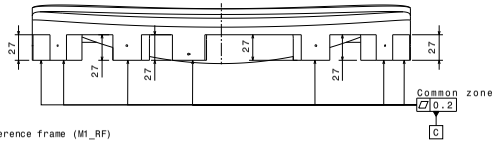

NOTA :

- Axis X, Y, Z : Mirror M1 reference frame (M1_RF)

- Mass : 3.8 kg +/- 10%

- Rear surface is a paraboloid with rotary axis Z of the M1_RF.
  Rear surface equation in plan XZ of the M1_RF : $z = x^2/P+K$
  where x and z are in 'millimeter unit' and with, at 300K :
  P = -670
  K = 5

- Optical surface equation in the M1_RF : $Ax^4+By^2+Cz^2+Dxy+Exz+Fyz+Gx+Hy+Iz+J = 0$
  where x, y and z are in 'meter unit' and with, at 300K :
  A = -0.00274866
  B = -0.00274866
  C = -7.089287 E-05
  D = 1.420595 E-23
  E = 4.792501 E-21
  F = 1.016066 E-22
  G = 5.587171 E-19
  H = 1.709066 E-20
  I = -0.00183404
  J = -0.000001

Rev 1.0 Draft 00	Updating Creation		15/03/2016 27/01/2016
Indice	Modification		Date
Surface state Ra = 3,2 Except contrary indication	General tolerances : ISO 2768-mK	Matter : 6082 T6	
		Treatment : /	
Date : 15/03/2016	Scale 1:2	Demonstrator MIRROR M1	
Drawn by :			
Checked by :	ASTRO PARTICULE et COSMOLOGIE 10, rue Alice Domon et Léonie Duquet 75205 Paris Cedex 13		
Approved :	A0	QCB0054	Rev 1.0 / Atrium ID 96535 / 1/1

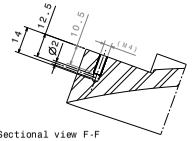

3x identical Sectional view F-F
Scale : 1:1

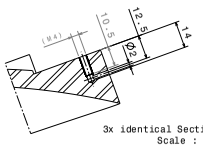

3x identical Sectional view E-E
Scale : 1:1

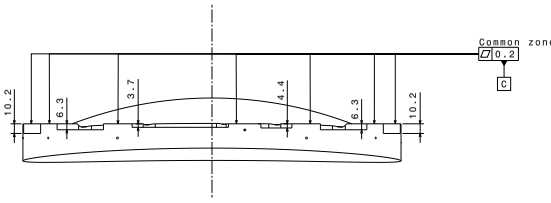

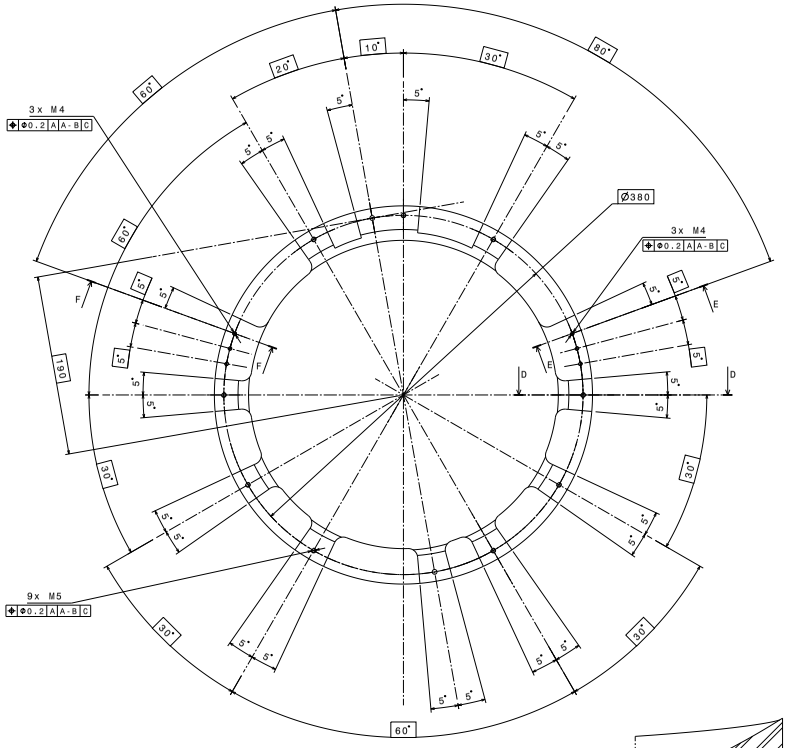

Bottom view

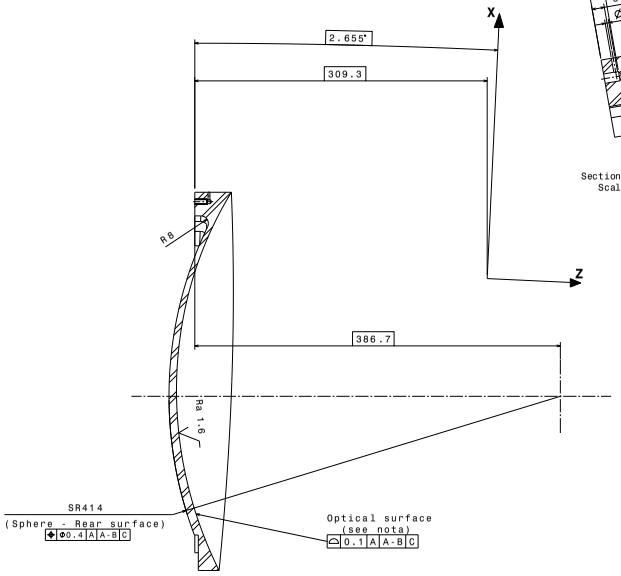

Sectional view A-A

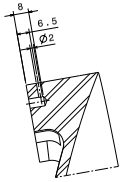

Sectional view C-C
Scale : 1:1

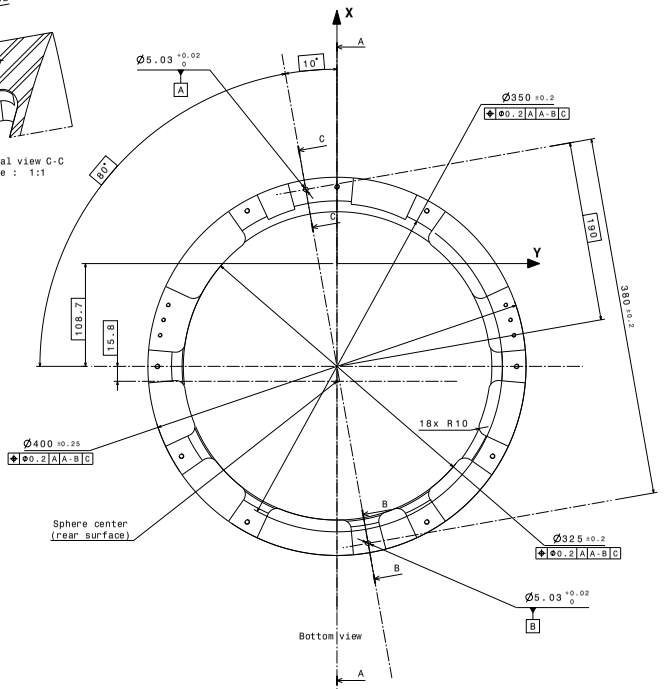

Bottom view

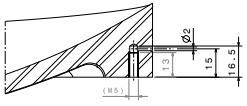

9x identical Sectional view D-D
Scale : 1:1

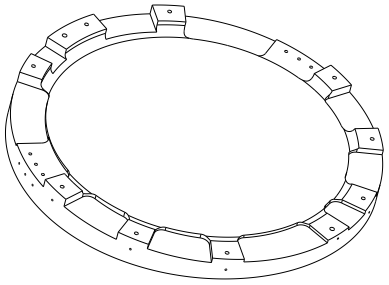

Isometric view
Scale : 1:2

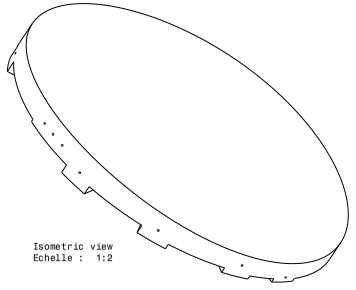

Isometric view
Echelle : 1:2

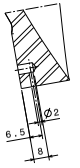

Sectional view B-B
Scale : 1:1

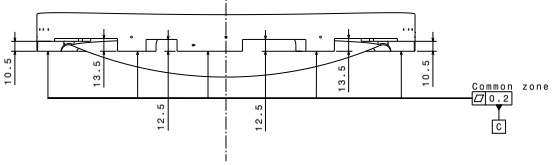

NOTA :

- Axis X, Y, Z : Mirror M2 reference frame (M2_RF)
- Mass : 4.1 kg +/- 10%
- Rear surface is a sphere
- Optical surface equation in the M2_RF : $Ax^3+By^3+Cz^3+Dxy+Exz+Fyz+Gx+Hy+Iz+J=0$ where x, y and z are in "meter unit" and with (at 300K) :

A = 0.991323
B = 1.114128
C = 1.092735
D = 0
E = 0.102517
F = 0
G = 0.258740
H = 0
I = -0.107996
J = -0.136285

	Rev 1.0 Draft 00	Updating Creation		15/03/2016 27/01/2016
	Indice	Modification		Date
Surface state Ra = 3,2 Except contrary indication	General tolerances : ISO 2768-mK		Matter : 6082 T6	
			Treatment : /	
Date : 15/03/2016	Scale 1:2	Demonstrator MIRROR M2		
Drawn by :				
Checked by :	ASTRO PARTICULE et COSMOLOGIE 10, rue Alice Domon et Léonie Duquet 75205 Paris Cedex 13			
Approved :		A0	QCB0055	Rev 1.0 / Atrium ID 96539 / 1/1

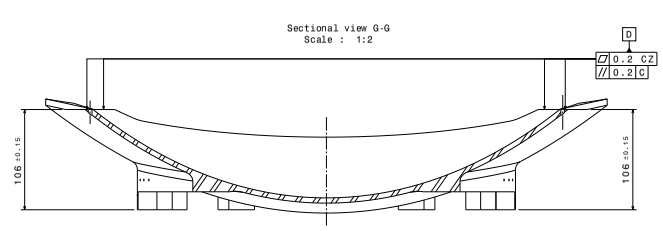

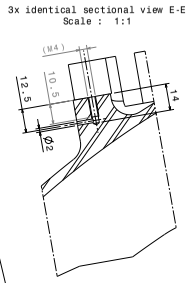

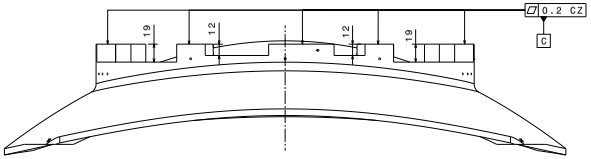

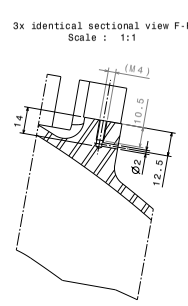

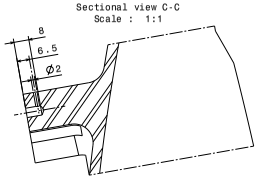

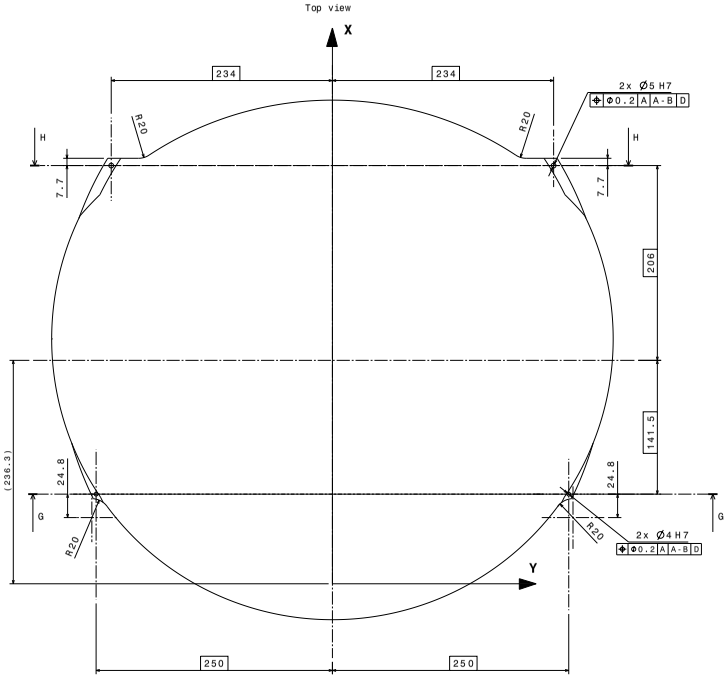

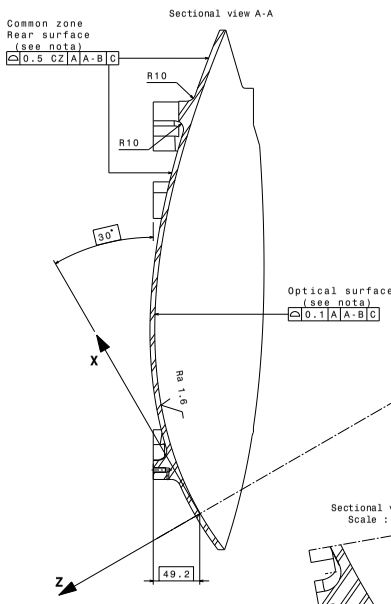

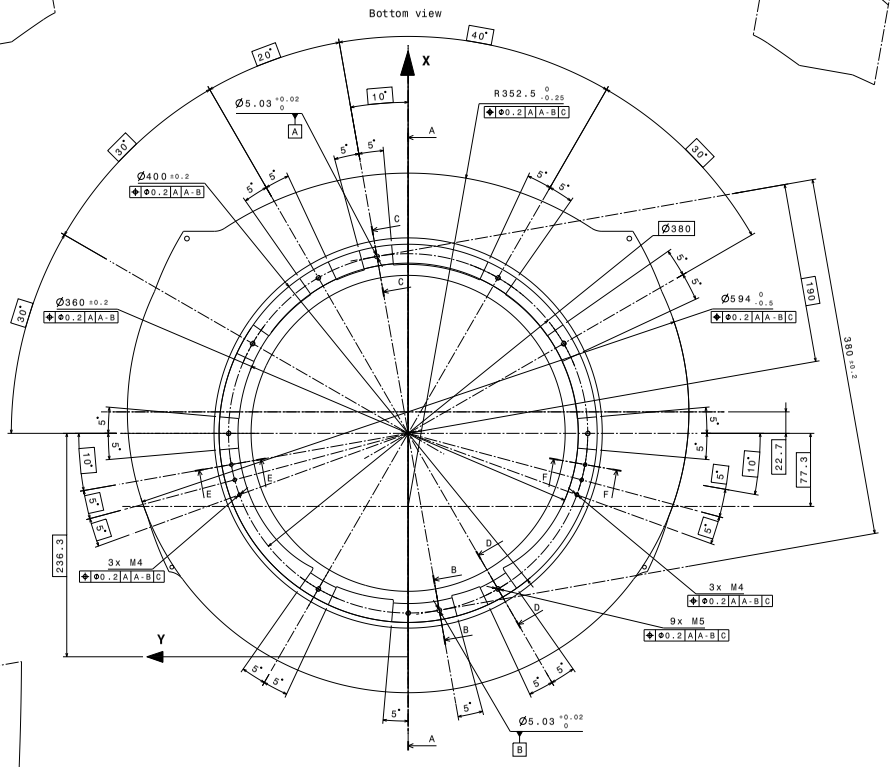

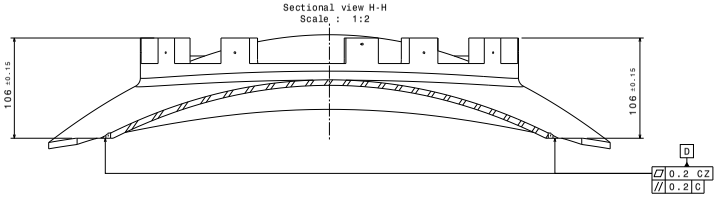

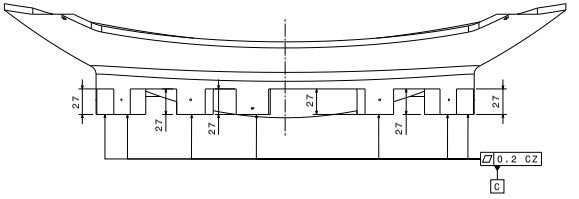

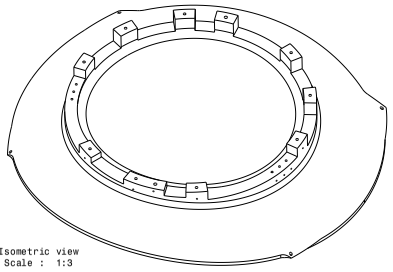

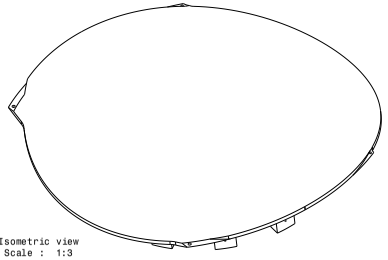

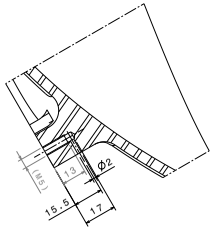

NOTA :

- Axis X, Y, Z : Mirror M1 reference frame (M1_RF)

- Mass : 5.7 kg +/- 10%

- Rear surface is a paraboloid with rotary axis Z of the M1_RF.
  Rear surface equation in plan XZ of the M1_RF : $z = x^2/P+K$
  where x and z are in "millimeter unit" and with, at 300K :
  P = -670
  K = 5

- Optical surface equation in the M1_RF : $Ax^2+By^2+Cz^2+Dxy+Exz+Fyz+Gx+Hy+Iz+J = 0$
  where x, y and z are in "meter unit" and with, at 300K :
  A = -0.00274866
  B = -0.00274866
  C = -7.089287 E-05
  D = 1.420595 E-23
  E = 4.792501 E-21
  F = 1.016066 E-22
  G = 5.587171 E-19
  H = 1.709066 E-20
  I = -0.00183404
  J = -0.000001

Indice	Modification	Date
0.0	Creation	08/06/2018

Surface state Ra = 3,2 Except contrary indication	General tolerances : ISO 2768-mK	Matter : 6082 T6 Treatment : /
Date : 08/06/2018	Scale 1:2	MIRROR M1
Drawn by :		
Checked by :		ASTRO PARTICULE et COSMOLOGIE 10, rue Alice Domon et Léonie Duquet 75205 Paris Cedex 13
Approved :		A0 | QCB0031 | Rev 0.0 | Atrium ID 77566 | 1/1

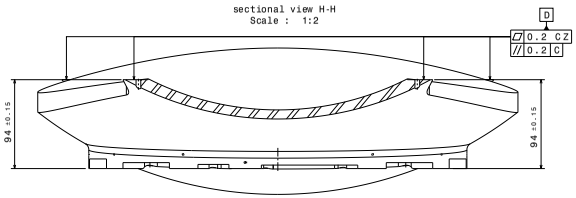

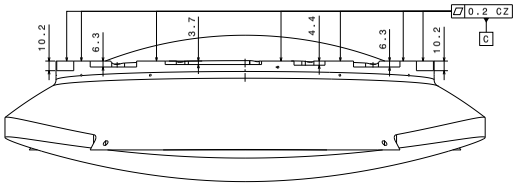

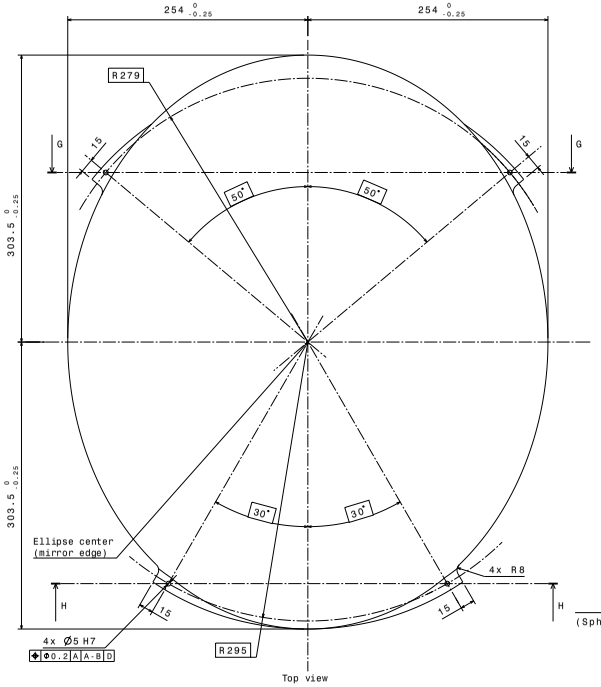

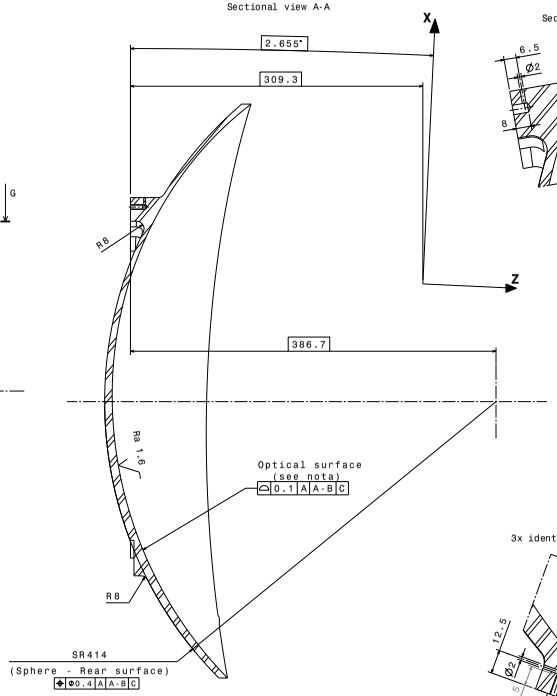

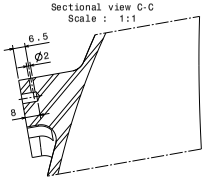

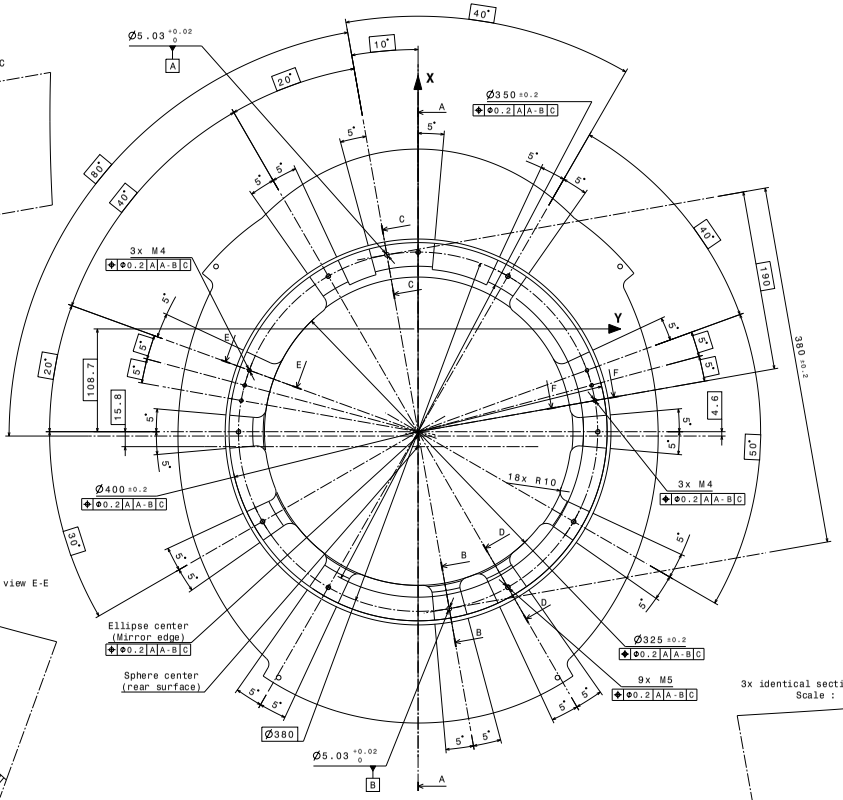

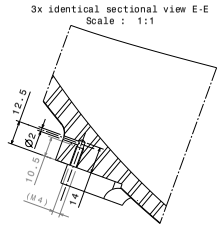

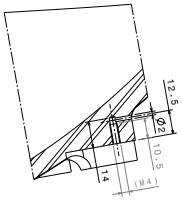

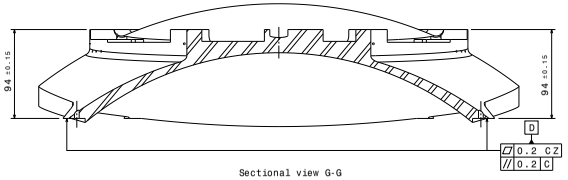

Sectional view G-G
Scale : 1:2

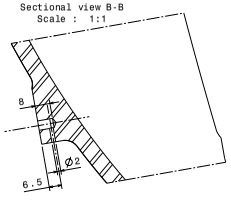

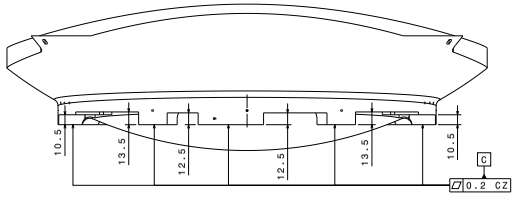

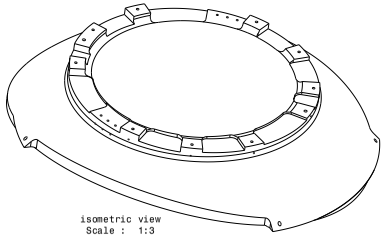

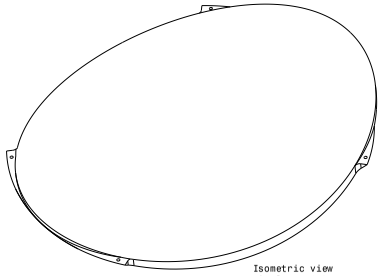

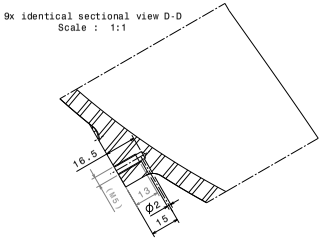

NOTA :

- Axis X, Y, Z : Mirror M2 reference frame (M2_RF)
- Mass : 8 kg +/- 10%
- Rear surface is a sphere
- Optical surface equation in the M2_RF : $Ax^2+By^2+Cz^2+Dxy+Exz+Fyz+Gx+Hy+Iz+J = 0$
where x, y and z are in "meter unit" and with (at 300K) :
  - A = 0.991323
  - B = 1.114128
  - C = 1.092735
  - D = 0
  - E = 0.102517
  - F = 0
  - G = 0.258740
  - H = 0
  - I = -0.107996
  - J = -0.136285

Indice	Modification	Date
0.0	Creation	08/06/2018

Surface state Ra = 3,2 Except contrary indication	General tolerances : ISO 2768-mK	Matter : 6082 T6 Treatment : /
Date : 08/06/2018	Scale 1:2	MIRROR M2
Drawn by :		
Checked by :	Astro Particule et Cosmologie 10, rue Alice Domon et Léonie Duquet 75205 Paris Cedex 13	
Approved :	A0	QCB0032 Rev 0.0 Atrium ID 77565 1/1

Appendix D

QUBIC Reference Frames

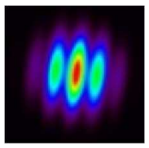

QUBIC

NOTE

Ref:	QUBIC1_FRAMES
Version:	5
REF.	ATRIUM-77650
Date:	25/06/2019
Page:	1/8

QUBIC 1st module Frames definition.

Author(s)	J. Brossard, M. Piat, P. Chanial, C. Chapron (APC, France) C. O'Sullivan, S. Scully, D. Gayer (NUI-Maynooth, Ireland) M. De Petris, D. Buzi (La Sapienza univ., Italy) B. Maffei (Manchester University)			
Project	QUBIC 1st module and Technological Demonstrator			
Recipient	All members of the team: APC, CSNSM, IRAP, NUIM, Manchester univ., Roma (La Sapienza univ.), Milano.			
Annexe	Name			Reference
Validation	BROSSARD Julien "System Engineer"	PIAT Michel "Instrument Scientist"	GRANDSIRE Laurent "Project Manager"	HAMILTON Jean-Christophe "Project Scientist"
	DE PETRIS Marco "Optic group coordinator"			

Change record:

Issue	Date	Sheet	Description of change
Version 1	09.07.2014	All	Initial draft (replace part of the doc. EDMS I-037150 - Draft 9) EDMS I-037150 is obsolete
Version 2	17.07.2014	§5	PG_RF is defined according to I-038238 v.2
Version 3	18.05.2016	§5	CS_RF modified due to resizing of cold stop
Version 4	18.05.2017	§5	CS_RF modified due to changing of the shape of the cold stop (circular)
Version 5	25.06.2019	§5+§7	Updated Table in §5 and added §7 with Forebaffle definition

TABLE OF CONTENTS:

1 APPLICABLES DOCUMENTS

[AD.1]: “Temperature and pressure specifications”, To be written.
[AD.2]: “Horns beam”, ATRIUM-77658.
[AD.3]: “ForeBaffle”, to be written..

2 NOMINAL CONDITIONS ASSUMPTION

All the dimensions, positions and orientation given in this document assume “nominal temperature and pressure conditions” (as defined in AD.1).

3 QUBIC 1ST MODULE GLOBAL REFERENCE FRAME DEFINITION:

The “QUBIC Reference Frame” (QUBIC_GRF) is a right-handed orthonormal frame defined as follows:

3.1 Origin definition:

The following drawings are not at scale and should be used for illustration only.

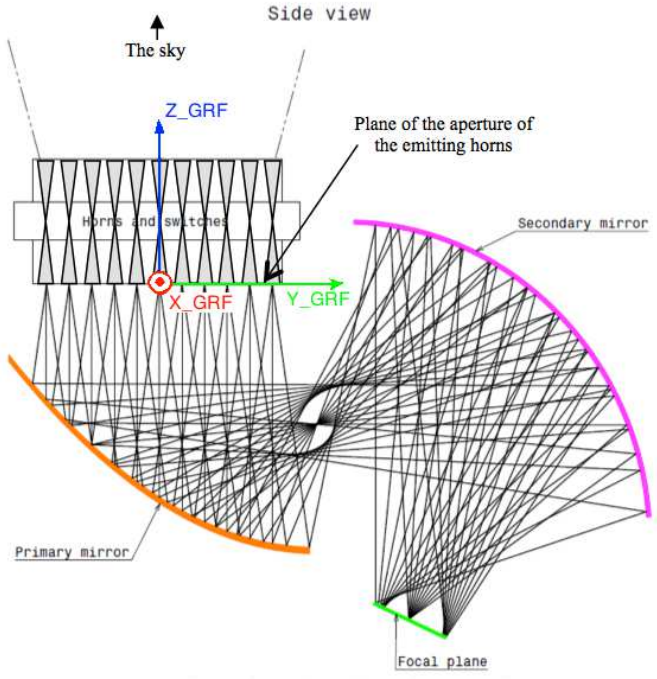

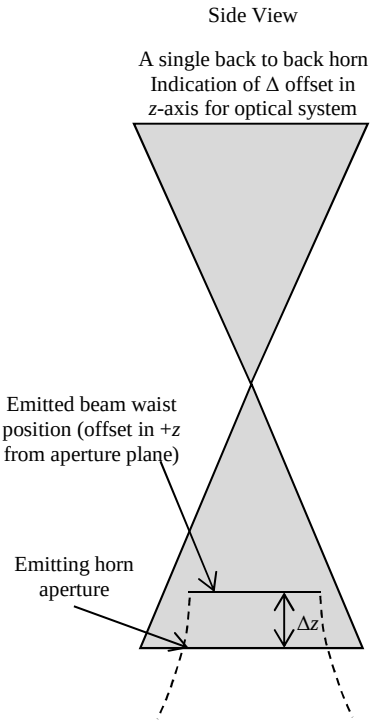

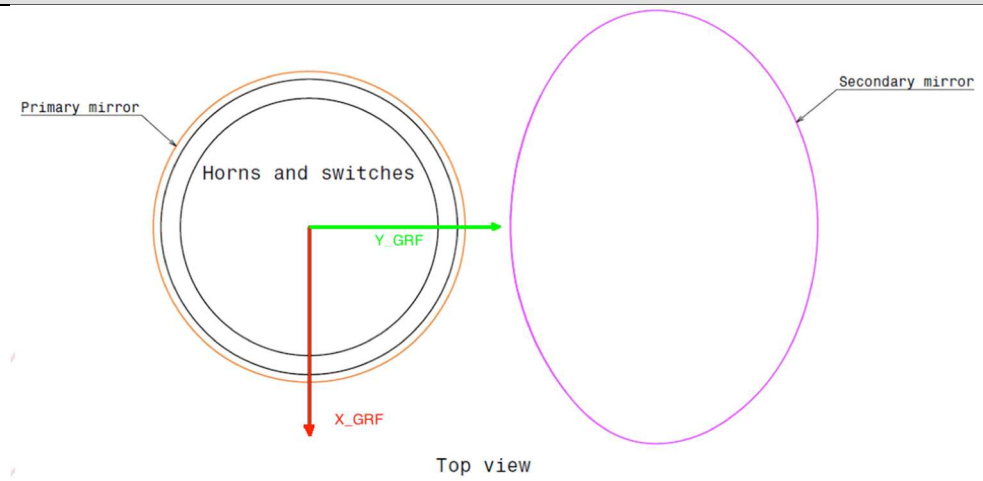

3.2 Z-axis definition (Z_GRF):

See §3.1 Perpendicular to the secondary horn array aperture plane, at the centre of the array, positive towards the sky

3.3 Y-axis definition (Y_GRF):

See §3.1 Parallel to the secondary horn array plane, positive from horn array centre towards secondary mirror centre.

3.4 X-axis definition (Z_GRF):

See §3.1 Parallel to the secondary horn array plane, perpendicular to the y-axis

4 RULES FOR THE DEFINITION OF OTHER FRAMES

All coordinate system defined in QUBIC collaboration must be orthonormal right-handed and defined w.r.t the QUBIC_GRF using the following rules.

4.1 Origin definition rule

The position of the origin of the new coordinate system must be defined w.r.t QUBIC_GRF using the Cartesian coordinates definition (x, y, z) and expressed in unit of meter (see below).

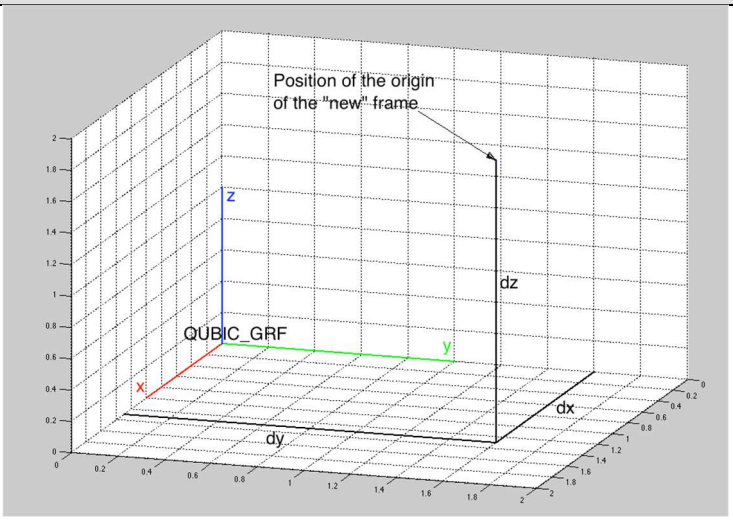

4.2 Orientation definition rule

The orientation of the new frame w.r.t the QUBIC_GRF should be defined according to the "Euler ZYZ" convention (see below), with angles alpha, beta, and gamma in radians.

Euler angles

The angles define the relative orientation between xyz and XYZ by three successive rotations of one coordinate system xyz that align it with the other one XYZ.

1. Rotate xyz counterclockwise around its z axis by α to give x'y'z'.
2. Rotate x'y'z' counterclockwise around its y' axis by β to give x"y"z".
3. Rotate x"y"z" counterclockwise around its z" axis by γ to give the final XYZ.

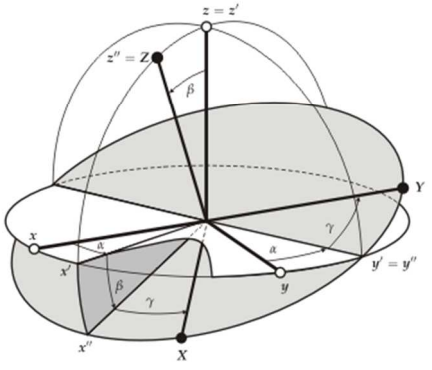

This is called the zyz or y convention, for obvious reasons.

5 QUBIC FRAMES DEFINITION

Following rules defined in §4, the table below defined some important QUBIC reference frames.

	dx [m]	dy [m]	dz [m]	alpha [rad]	beta [rad]	gamma [rad]
QUBIC_GRF[1]	0	0	0	0	0	0
SECHO_ARF[2]	0	0	0	π/4	0	0
SECHO_BWP[3]	0	0	Δz	π/4	0	0
M1_RF[4]	0	0.209576	-0.466757+Δz	0	π	-π/2

[1] QUBIC Global Reference Frame
[2] SECondary HOrns Aperture Reference Frame
[3] SECondary Horns Beam Waist Plane

CS_RF[5]	0	0.23504	-0.29261+Δz	-π/2	-1.42768	0
M2_RF[6]	0	0.209576	-0.302273+Δz	π/2	-2.40253	0
ONA_FPRF[7]	0	0.331210	-0.563118+Δz	-π/2	-0.44377	0
OFA_FPRF[8]	0.11	0.378428	-0.463773+Δz	0	-π/2	-1.12702
PG_RF[9]	0	0.378438	-0.463773+Δz	0.40555	0.87800	1.38033
FB_RF	0	0	527	0	0	0

Notes:

- "SECHO_BWP" is the reference frame passing through all the beam waist of the secondary horns.. Δz value is defined in [AD.2].

6 REFLECTORS DEFINITION

6.1 Reflector definition rule

In QUBIC, a reflector is defined (in a specified orthonormal right-handed reference frame) as the intersection (see figure below) between a (x,y) area and one "z" solution of a quadric equation:

$Ax^2+By^2+Cz^2+Dxy+Exz+Fyz+Gx+Hy+Iz+J=0$ [eq.1] where x, y and z are in "meter unit".

The (x,y) area could be defined using the equation of its rim.

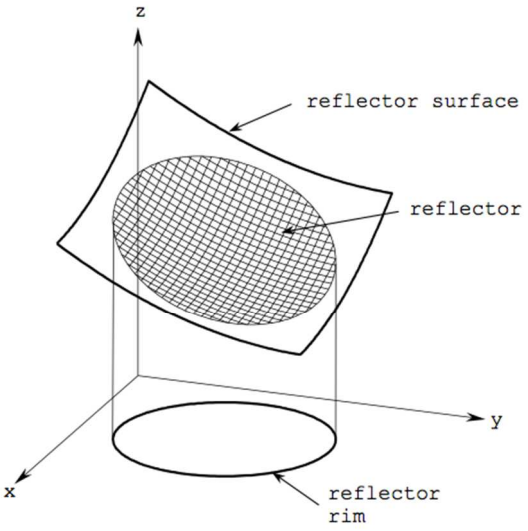

Figure 2.2-1 A reflector is defined by a reflector surface cut by a cylinder with the reflector rim as the cross section.

7 FOREBAFFLE DEFINITION

7.1 ForeBaffle definition rule

The ForeBaffle is described in AD.3. We define the origin of the ForeBaffle Reference Frame as the

[4] M1 Reference Frame
[5] Cold Stop Reference Frame
[6] M2 Reference Frame
[7] ON Axis Focal Plane Reference Frame
[8] OFf Axis Focal Plane Reference Frame
[9] Polarization Grid Reference Frame

centre of the aperture at the base of the conic. See the following drawing not at scale, used for illustration only.

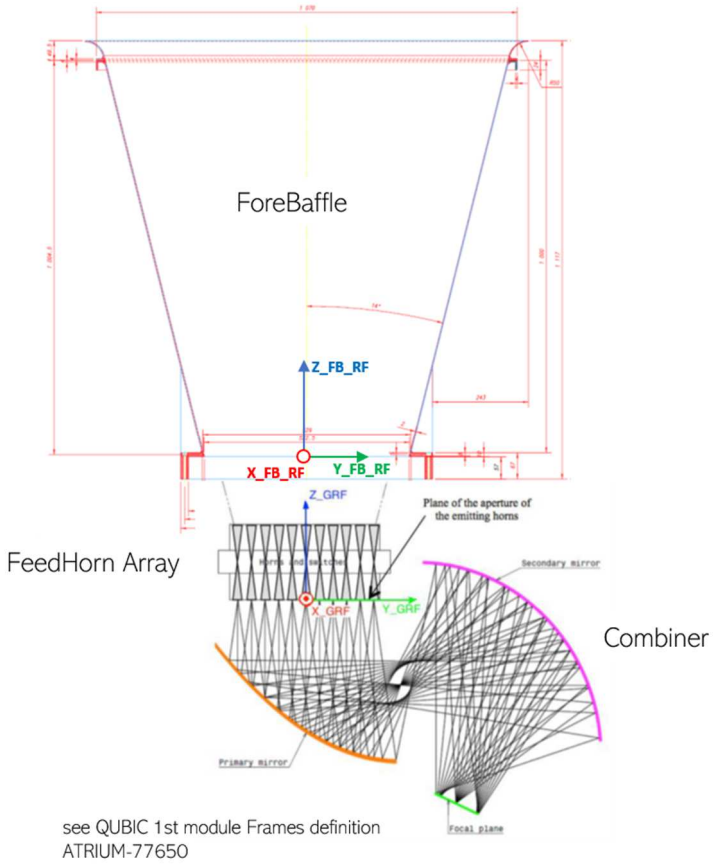

END OF THE DOCUMENT

References

[1] Hinderks, J., Ade, P., Bock, J., Bowden, M., Cahill, G., Carlstrom, J., Castro, P., Church, S., Culverhouse, T., Friedman, R., Ganga, K., Gear, W., Gupta, S., Harris, J., Haynes, V., Keating, B., Kovac, J., Kirby, E., Lange, A., Leitch, E., Mallie, O., Melhuish, S., Memari, Y., Murphy, J., Orlando, A., Schwarz, R., O'Sullivan, C., Piccirillo, L., Pryke, C., Rajguru, N., Rusholme, B., Taylor, A., Thompson, K., Tucker, C., Turner, A., Wu, E., and Zemcov, M. Quad: A high-resolution cosmic microwave background polarimeter. *Astrophysical Journal*, 692(2):1221–1246, February 2009. URL `https://mural.maynoothuniversity.ie/2096/`.

[2] Murphy, J., Peacocke, T., Maffei, B., McAuley, I., Noviello, F., Yurchenko, V., Ade, P., Savini, G., Lamarre, J.M., Brossard, J., Colgan, R., Gleeson, E., Lange, A., Longval, Y., Pisano, G., Puget, J.L., Ristorcelli, I., Sudiwala, R., and Wylde, R. Multi-mode horn design and beam characteristics for the planck satellite. *Journal of Instrumentation*, 5(T04001):1–21, 2010. URL `https://mural.maynoothuniversity.ie/4036/`. The definitive version of this article is available at doi:10.1088/1748-0221/5/04/T04001 . © 2010 IOP Publishing Ltd and SISSA.

[3] Trappe, N., Murphy, J.A., Kruizinga, B., Visser, H., Jellema, W., Wildeman, K.J., and van de Stadt, H. Quasi-optical analysis of the HIFI instrument for the Herschel Space Observatory. In *Opto-Ireland 2002: Optics and Photonics Technologies and Applications*, volume 4876, pages 1091 – 1099. International Society for Optics and Photonics, SPIE, 2003. doi: 10.1117/12.463910. URL `https://doi.org/10.1117/12.463910`.

[4] Tucker, G.S., Kim, J., Timbie, P., Ali, S., Piccirillo, L., and Calderon, C. Bolometric interferometry: the millimeter-wave bolometric interferometer. *New Astronomy Reviews*, 47(11-12):1173–1176, December 2003. doi: 10.1016/j.newar.2003.09.024.

[5] Polenta, G. The BRAIN CMB polarization experiment. *New Astronomy Reviews*, 51(3-4):256–259, March 2007. doi: 10.1016/j.newar.2006.11.065.

[6] Hubble, E. A Relation between Distance and Radial Velocity among Extra-Galactic Nebulae. *Proceedings of the National Academy of Science*, 15(3): 168–173, March 1929. doi: 10.1073/pnas.15.3.168.

[7] Lemaître, A.G. A Homogeneous Universe of Constant Mass and Increasing Radius accounting for the Radial Velocity of Extra-galactic Nebulæ. *Monthly Notices of the Royal Astronomical Society*, 91(5):483–490, 03 1931. ISSN 0035-8711. doi: 10.1093/mnras/91.5.483. URL `https://doi.org/10.1093/mnras/91.5.483`.

[8] Friedmann, A. Über die Krümmung des Raumes. *Zeitschrift fur Physik*, 10: 377–386, January 1922. doi: 10.1007/BF01332580.

[9] Einstein, A. Kosmologische Betrachtungen zur allgemeinen Relativitätstheorie. *Sitzungsberichte der Königlich Preußischen Akademie der Wissenschaften (Berlin)*, pages 142–152, January 1917.

[10] de Sitter, W. Einstein's theory of gravitation and its astronomical consequences. Third paper. *Monthly Notices of the RAS*, 78:3–28, November 1917. doi: 10.1093/mnras/78.1.3.

[11] Alpher, R.A., Bethe, H., and Gamow, G. The origin of chemical elements. *Phys. Rev.*, 73:803–804, Apr 1948. doi: 10.1103/PhysRev.73.803. URL `https://link.aps.org/doi/10.1103/PhysRev.73.803`.

[12] Penzias, A.A. and Wilson, R.W. A Measurement of Excess Antenna Temperature at 4080 Mc/s. *Astrophysical Journal*, 142:419–421, July 1965. doi: 10.1086/148307.

[13] Dicke, R.H., Peebles, P.J.E., Roll, P.G., and Wilkinson, D.T. Cosmic Black-Body Radiation. *Astrophysical Journal*, 142:414–419, July 1965. doi: 10.1086/148306.

[14] Mather, J.C., Cheng, E.S., Cottingham, D.A., Eplee, J., R. E., Fixsen, D.J., Hewagama, T., Isaacman, R.B., Jensen, K.A., Meyer, S.S., Noerdlinger, P.D., Read, S.M., Rosen, L.P., Shafer, R.A., Wright, E.L., Bennett, C.L., Boggess, N.W., Hauser, M.G., Kelsall, T., Moseley, J., S. H., Silverberg, R.F., Smoot, G.F., Weiss, R., and Wilkinson, D.T. Measurement of the

Cosmic Microwave Background Spectrum by the COBE FIRAS Instrument. *Astrophysical Journal*, 420:439, January 1994. doi: 10.1086/173574.

[15] Smoot, G.F., Bennett, C.L., Kogut, A., Wright, E.L., Aymon, J., Boggess, N.W., Cheng, E.S., de Amici, G., Gulkis, S., Hauser, M.G., Hinshaw, G., Jackson, P.D., Janssen, M., Kaita, E., Kelsall, T., Keegstra, P., Lineweaver, C., Loewenstein, K., Lubin, P., Mather, J., Meyer, S.S., Moseley, S.H., Murdock, T., Rokke, L., Silverberg, R.F., Tenorio, L., Weiss, R., and Wilkinson, D.T. Structure in the COBE Differential Microwave Radiometer First-Year Maps. *Astrophysical Journal, Letters*, 396:L1, September 1992. doi: 10.1086/186504.

[16] Vazquez Gonzalez, J.A., Padilla, L.E., and Matos, T. Inflationary cosmology: from theory to observations. *Revista Mexicana de Física E*, 17(1 Jan-Jun): 73–91, Jan 2020. ISSN 1870-3542. doi: 10.31349/revmexfise.17.73. URL `http://dx.doi.org/10.31349/RevMexFisE.17.73`.

[17] Sachs, R.K. and Wolfe, A.M. Perturbations of a Cosmological Model and Angular Variations of the Microwave Background. *Astrophysical Journal*, 147:73, January 1967. doi: 10.1086/148982.

[18] Hu, W. and Dodelson, S. Cosmic microwave background anisotropies. *Annual Review of Astronomy and Astrophysics*, 40(1):171–216, Sep 2002. ISSN 1545-4282. doi: 10.1146/annurev.astro.40.060401.093926. URL `http://dx.doi.org/10.1146/annurev.astro.40.060401.093926`.

[19] Bennett, C.L., Larson, D., Weiland, J.L., Jarosik, N., Hinshaw, G., Odegard, N., Smith, K.M., Hill, R.S., Gold, B., Halpern, M., Komatsu, E., Nolta, M.R., Page, L., Spergel, D.N., Wollack, E., Dunkley, J., Kogut, A., Limon, M., Meyer, S.S., Tucker, G.S., and Wright, E.L. Nine-Year Wilkinson Microwave Anisotropy Probe (WMAP) Observations: Final Maps and Results. *American Astronomical Society*, 208(2):20, sep 2013. doi: 10.1088/0067-0049/208/2/20. URL `https://doi.org/10.1088/0067-0049/208/2/20`.

[20] Aghanim, N., Akrami, Y., Arroja, F., Ashdown, M., Aumont, J., Baccigalupi, C., Ballardini, M., Banday, A.J., Barreiro, R.B., and et al. Planck 2018 results. *Astronomy & Astrophysics*, 641:A1, Sep 2020. ISSN 1432-0746. doi: 10.1051/0004-6361/201833880. URL `http://dx.doi.org/10.1051/0004-6361/201833880`.

[21] Ade, P.A.R., Aghanim, N., Alves, M.I.R., Armitage-Caplan, C., Arnaud, M., Ashdown, M., Atrio-Barandela, F., Aumont, J., Aussel, H., and et al. Planck 2013 results. I. Overview of products and scientific results. *Astronomy & Astrophysics*, 571:A1, Oct 2014. ISSN 1432-0746. doi: 10.1051/0004-6361/201321529. URL http://dx.doi.org/10.1051/0004-6361/201321529.

[22] O'Sullivan, C., Burke, D., Gayer, D., **Murphy, J.D.**, Scully, S., Leo, M.D., De Petris, M., Mattei, A., Zullo, A., Mennella, A., Zannoni, M., Bleurvacq, N., Chapron, C., Hamilton, J.C., Piat, M., et al. Simulations and performance of the QUBIC optical beam combiner. *Proceedings of SPIE*, 10708: 107082I, 2018. URL https://mural.maynoothuniversity.ie/13433/.

[23] Hu, W. and White, M. A cmb polarization primer. *New Astronomy*, 2(4): 323–344, Oct 1997. ISSN 1384-1076. doi: 10.1016/s1384-1076(97)00022-5. URL http://dx.doi.org/10.1016/S1384-1076(97)00022-5.

[24] Guth, A.H. Inflationary universe: A possible solution to the horizon and flatness problems. *Phys. Rev. D*, 23:347–356, Jan 1981. doi: 10.1103/PhysRevD.23.347. URL https://link.aps.org/doi/10.1103/PhysRevD.23.347.

[25] Bicep/Keck Collaboration et al. Improved Constraints on Primordial Gravitational Waves using Planck, WMAP, and BICEP/Keck Observations through the 2018 Observing Season. *Physical Review Letters*, 127(15): 151301, October 2021. doi: 10.1103/PhysRevLett.127.151301.

[26] Dickinson, C. CMB foregrounds - A brief review. In *51st Rencontres de Moriond on Cosmology*, pages 53–62, 6 2016.

[27] Orlando, E. and Strong, A. Galactic synchrotron emission with cosmic ray propagation models. *Monthly Notices of the Royal Astronomical Society*, 436 (3):2127–2142, 10 2013. ISSN 0035-8711. doi: 10.1093/mnras/stt1718. URL https://doi.org/10.1093/mnras/stt1718.

[28] Lewis, A. and Challinor, A. Weak gravitational lensing of the cmb. *Physics Reports*, 429(1):1–65, 2006. ISSN 0370-1573. doi: https://doi.org/10.1016/j.physrep.2006.03.002. URL https://www.sciencedirect.com/science/article/pii/S0370157306000810.

[29] Sunyaev, R.A. and Zeldovich, Y.B. The velocity of clusters of galaxies relative to the microwave background. The possibility of its measurement. *Monthly Notices of the Royal Astronomical Society*, 190(3):413–420, 03 1980. ISSN 0035-8711. doi: 10.1093/mnras/190.3.413. URL `https://doi.org/10.1093/mnras/190.3.413`.

[30] Carlstrom, J.E., Holder, G.P., and Reese, E.D. Cosmology with the sunyaev-zel'dovich effect. *Annual Review of Astronomy and Astrophysics*, 40(1): 643–680, Sep 2002. ISSN 1545-4282. doi: 10.1146/annurev.astro.40.060401.093803. URL `http://dx.doi.org/10.1146/annurev.astro.40.060401.093803`.

[31] Ichiki, K. CMB foreground: A concise review. *Progress of Theoretical and Experimental Physics*, 2014(6), 06 2014. ISSN 2050-3911. doi: 10.1093/ptep/ptu065. URL `https://doi.org/10.1093/ptep/ptu065`. 06B109.

[32] Sayre, J.T., Reichardt, C.L., Henning, J.W., Ade, P.A.R., Anderson, A.J., Austermann, J.E., Avva, J.S., Beall, J.A., Bender, A.N., Benson, B.A., Bianchini, F., Bleem, L.E., Carlstrom, J.E., Chang, C.L., Chaubal, P., Chiang, H.C., Citron, R., Corbett Moran, C., Crawford, T.M., Crites, A.T., de Haan, T., Dobbs, M.A., Everett, W., Gallicchio, J., George, E.M., Gilbert, A., Gupta, N., Halverson, N.W., Harrington, N., Hilton, G.C., Holder, G.P., Holzapfel, W.L., Hrubes, J.D., Huang, N., Hubmayr, J., Irwin, K.D., Knox, L., Lee, A.T., Li, D., Lowitz, A., McMahon, J.J., Meyer, S.S., Mocanu, L.M., Montgomery, J., Nadolski, A., Natoli, T., Nibarger, J.P., Noble, G., Novosad, V., Padin, S., Patil, S., Pryke, C., Ruhl, J.E., Saliwanchik, B.R., Schaffer, K.K., Sievers, C., Smecher, G., Stark, A.A., Tucker, C., Vanderlinde, K., Veach, T., Vieira, J.D., Wang, G., Whitehorn, N., Wu, W.L.K., and Yefremenko, V. Measurements of B-mode polarization of the cosmic microwave background from 500 square degrees of SPTpol data. *Phys. Rev. D*, 101:122003, Jun 2020. doi: 10.1103/PhysRevD.101.122003. URL `https://link.aps.org/doi/10.1103/PhysRevD.101.122003`.

[33] Ade, P., Akiba, Y., Anthony, A., Arnold, K., Atlas, M., Barron, D., Boettger, D., Borrill, J., Chapman, S., Chinone, Y., et al. A measurement of the cosmic microwave background B-mode polarization power spectrum at sub-degree scales with POLARBEAR. *ApJ*, 794(2):171, 2014.

[34] Louis, T., Grace, E., Hasselfield, M., Lungu, M., Maurin, L., Addison, G.E., Ade, P.A., Aiola, S., Allison, R., Amiri, M., et al. The Atacama Cosmology Telescope: two-season ACTPol spectra and parameters. *J. Cosmo. Astroparticle Phys.*, 2017(06):031, 2017.

[35] Ade, P., Ahmed, Z., Aikin, R., Alexander, K., Barkats, D., Benton, S., Bischoff, C., Bock, J., Bowens-Rubin, R., Brevik, J., et al. Constraints on Primordial Gravitational Waves Using Planck, WMAP, and New BICEP2/Keck Observations through the 2015 Season. *Phys. Rev. Lett.*, 121 (22):221301, 2018.

[36] Dahal, S., Amiri, M., Appel, J.W., Bennett, C.L., Corbett, L., Datta, R., Denis, K., Essinger-Hileman, T., Halpern, M., Helson, K., et al. The CLASS 150/220 GHz Polarimeter Array: Design, Assembly, and Characterization. *J. Low. Temp. Phys.*, pages 1–9, 2020.

[37] Suzuki, A. et al. The Polarbear-2 and the Simons Array Experiments. *J. Low. Temp. Phys.*, 184(3-4):805–810, August 2016. doi: 10.1007/s10909-015-1425-4.

[38] Henderson, S.W. et al. Advanced ACTPol Cryogenic Detector Arrays and Readout. *J. Cosmo. Astroparticle Phys.*, 184(3-4):772–779, August 2016. doi: 10.1007/s10909-016-1575-z.

[39] Grayson, J.A., Ade, P.A.R., Ahmed, Z., Alexander, K.D., Amiri, M., Barkats, D., Benton, S.J., Bischoff, C.A., Bock, J.J., Boenish, H., and et al. BICEP3 performance overview and planned Keck Array upgrade. *Millimeter, Submillimeter, and Far-Infrared Detectors and Instrumentation for Astronomy VIII*, Jul 2016. doi: 10.1117/12.2233894. URL `http://dx.doi.org/10.1117/12.2233894`.

[40] Ade, P.A.R., Aghanim, N., Ahmed, Z., Aikin, R.W., et al. Joint Analysis of BICEP2/Keck Array and Planck Data. *Phys. Rev. Lett.*, 114:101301, Mar 2015. doi: 10.1103/PhysRevLett.114.101301. URL `https://link.aps.org/doi/10.1103/PhysRevLett.114.101301`.

[41] Ade, P. et al. The Simons Observatory: science goals and forecasts. *J. Cosmo. Astroparticle Phys.*, 2019(2):056, February 2019. doi: 10.1088/1475-7516/2019/02/056.

[42] Gandilo, N.N. et al. The Primordial Inflation Polarization Explorer (PIPER). In *Proc. SPIE*, volume 9914 of *Society of Photo-Optical Instrumentation Engineers (SPIE) Conference Series*, page 99141J, July 2016. doi: 10.1117/12.2231109.

[43] Addamo, G., Ade, P., Baccigalupi, C., Baldini, A., Battaglia, P., Battistelli, E., Baù, A., de Bernardis, P., Bersanelli, M., Biasotti, M., et al. The large scale polarization explorer (LSPE) for CMB measurements: performance forecast. *Journal of Cosmology and Astroparticle Physics*, 2021(08):008, aug 2021. doi: 10.1088/1475-7516/2021/08/008. URL `https://doi.org/10.1088/1475-7516/2021/08/008`.

[44] Abazajian, K. et al. CMB-S4 Science Case, Reference Design, and Project Plan. *arXiv e-prints*, art. arXiv:1907.04473, July 2019.

[45] Hazumi, M., Ade, P.A., Akiba, Y., Alonso, D., Arnold, K., and et al. LiteBIRD: A Satellite for the Studies of B-Mode Polarization and Inflation from Cosmic Background Radiation Detection. *J. Low. Temp. Phys.*, 194(5-6): 443–452, 2019. ISSN 15737357. doi: 10.1007/s10909-019-02150-5.

[46] Hanany, S. et al. PICO: Probe of Inflation and Cosmic Origins. In *Bulletin of the American Astronomical Society*, volume 51, page 194, September 2019.

[47] Niemack, M., Ade, P., Bernardis, F., Boulanger, F., Bryan, S., Devlin, M., Dunkley, J., Eales, S., Gomez, H., Groppi, C., Henderson, S., Hillbrand, S., Hubmayr, J., Mauskopf, P., McMahon, J., Miville-Deschenes, M.A., Pascale, E., Pisano, G., Novak, G., and Tucker, C. BFORE: The B-mode Foreground Experiment. *Journal of Low Temperature Physics*, 184, 08 2016. doi: 10.1007/s10909-015-1395-6.

[48] Tristram, M., Banday, A.J., Górski, K.M., Keskitalo, R., Lawrence, C.R., Andersen, K.J., Barreiro, R.B., Borrill, J., Eriksen, H.K., Fernandez-Cobos, R., and et al. Planck constraints on the tensor-to-scalar ratio. *Astronomy & Astrophysics*, 647:A128, Mar 2021. ISSN 1432-0746. doi: 10.1051/0004-6361/202039585. URL `http://dx.doi.org/10.1051/0004-6361/202039585`.

[49] Korotkov, A.L., Kim, J., Tucker, G.S., Gault, A., Hyland, P., Malu, S., Timbie, P.T., Bunn, E.F., Bierman, E., Keating, B., Murphy, A.,

O'Sullivan, C., Ade, P.A.R., Calderon, C., and Piccirillo, L. The millimeter-wave bolometric interferometer. In *Millimeter and Submillimeter Detectors and Instrumentation for Astronomy III*, volume 6275, pages 285 – 293. International Society for Optics and Photonics, SPIE, 2006. URL https://doi.org/10.1117/12.672246.

[50] Kaplan, J. QUBIC, a bolometric interferometer to measure the B modes of the CMB, 2009. URL http://dx.doi.org/10.1016/j.astropartphys.2011.01.012.

[51] Battistelli, E., Baú, A., Bennett, D., Bergé, L., Bernard, J.P., de Bernardis, P., Bordier, G., Bounab, A., Bréelle, e., Bunn, E., and et al. QUBIC: The QU bolometric interferometer for cosmology. *Astroparticle Physics*, 34(9): 705–716, Apr 2011. ISSN 0927-6505. doi: 10.1016/j.astropartphys.2011.01.012. URL http://dx.doi.org/10.1016/j.astropartphys.2011.01.012.

[52] Aumont, J. et al. QUBIC Technical Design Report. https://arxiv.org/abs/1609.04372, 2016.

[53] Torchinsky, S.A., Hamilton, J.C., Piat, M., Battistelli, E.S., Chapron, C., D'Alessandro, G., de Bernardis, P., De Petris, M., Lerena, M.M.G., González, M., Grandsire, L., Masi, S., Marnieros, S., Mennella, A., Mousset, L., **Murphy, J.D.**, Prêle, D., Stankowiak, G., O'Sullivan, C., Tartari, A., Thermeau, J.P., Voisin, F., Zannoni, M., et al.
QUBIC III: Laboratory characterization. *Journal of Cosmology and Astroparticle Physics*, 2022. URL https://arxiv.org/abs/2008.10056v3.

[54] Hamilton, J.C., Charlassier, R., Cressiot, C., Kaplan, J., Piat, M., and Rosset, C. Sensitivity of a bolometric interferometer to the cosmic microwave backgroud power spectrum. *Astronomy & Astrophysics*, 491(3):923–927, Oct 2008. ISSN 1432-0746. doi: 10.1051/0004-6361:200810504. URL http://dx.doi.org/10.1051/0004-6361:200810504.

[55] Ghribi, A., Tartari, A., Galli, S., Piat, M., Breelle, E., Hamilton, J.C., Spinelli, S., Gervasi, M., and Zannoni, M. A demonstrator for bolometric interferometry, February 2009. URL http://hal.in2p3.fr/in2p3-00359121. 15 pages, 14 figures.

[56] Mousset, L., the QUBIC Collaboration, incl. **Murphy, J.D.** .
QUBIC II: Spectro-polarimetry with bolometric interferometry. *Journal of*

Cosmology and Astroparticle Physics, 2022. URL https://arxiv.org/abs/2010.15119v2.

[57] Hazumi, M. and et al. LiteBIRD satellite: JAXA's new strategic L-class mission for all-sky surveys of cosmic microwave background polarization. In Lystrup, M., Perrin, M.D., Batalha, N., Siegler, N., and Tong, E.C., editors, *Space Telescopes and Instrumentation 2020: Optical, Infrared, and Millimeter Wave*, volume 11443, pages 431 – 450. International Society for Optics and Photonics, SPIE, 2020. doi: 10.1117/12.2563050. URL https://doi.org/10.1117/12.2563050.

[58] Nagata, R. and Namikawa, T. A numerical study of observational systematic errors in lensing analysis of CMB polarization. *Progress of Theoretical and Experimental Physics*, 2021(5), 04 2021. ISSN 2050-3911. doi: 10.1093/ptep/ptab040. URL https://doi.org/10.1093/ptep/ptab040. 053E01.

[59] Su, M., Yadav, A.P.S., and Zaldarriaga, M. Impact of instrumental systematic contamination on the lensing mass reconstruction using the cmb polarization. *Physical Review D*, 79(12), Jun 2009. ISSN 1550-2368. doi: 10.1103/physrevd.79.123002. URL http://dx.doi.org/10.1103/PhysRevD.79.123002.

[60] Ade, P.A.R., Aghanim, N., Armitage-Caplan, C., Arnaud, M., Ashdown, M., Atrio-Barandela, F., Aumont, J., Baccigalupi, C., Banday, A.J., and et al. Planck 2013 results. XV. CMB power spectra and likelihood. *Astronomy & Astrophysics*, 571:A15, Oct 2014. ISSN 1432-0746. doi: 10.1051/0004-6361/201321573. URL http://dx.doi.org/10.1051/0004-6361/201321573.

[61] Aghanim, N., Armitage-Caplan, C., Arnaud, M., Ashdown, M., Atrio-Barandela, F., Aumont, J., Baccigalupi, C., Banday, A.J., Barreiro, R.B., and et al. Planck 2013 results. III. LFI systematic uncertainties. *Astronomy & Astrophysics*, 571:A3, Oct 2014. ISSN 1432-0746. doi: 10.1051/0004-6361/201321574. URL http://dx.doi.org/10.1051/0004-6361/201321574.

[62] Wallis, C.G.R., Brown, M.L., Battye, R.A., and Delabrouille, J. Optimal scan strategies for future CMB satellite experiments. *Monthly Notices of the Royal Astronomical Society*, 466(1):425–442, 10 2016. ISSN 0035-8711. doi: 10.1093/mnras/stw2577. URL https://doi.org/10.1093/mnras/stw2577.

[63] Hivon, Eric, Mottet, Sylvain, and Ponthieu, Nicolas. Quickpol: Fast calculation of effective beam matrices for cmb polarization. *A&A*, 598:A25, 2017. doi: 10.1051/0004-6361/201629626. URL `https://doi.org/10.1051/0004-6361/201629626`.

[64] Pearson, T.J. and Readhead, A.C.S. Image formation by self-calibration in radio astronomy. *Annual Review of Astronomy and Astrophysics*, 22(1):97–130, 1984. doi: 10.1146/annurev.aa.22.090184.000525. URL `https://doi.org/10.1146/annurev.aa.22.090184.000525`.

[65] Bigot-Sazy, M.A., Charlassier, R., Hamilton, J.C., Kaplan, J., and Zahariade, G. Self-calibration: an efficient method to control systematic effects in bolometric interferometry. *Astronomy & Astrophysics*, 550:A59, Jan 2013. ISSN 1432-0746. doi: 10.1051/0004-6361/201220429. URL `http://dx.doi.org/10.1051/0004-6361/201220429`.

[66] Hamilton, J.C., Mousset, L., Battistelli, E.S., Bigot-Sazy, M.A., Chanial, P., Charlassier, R., D'Alessandro, G., de Bernardis, P., De Petris, M., Lerena, M.M.G., Grandsire, L., Lau, S., Marnieros, S., Masi, S., Mennella, A., O'Sullivan, C., Piat, M., Riccardi, G., Scóccola, C., Stolpovskiy, M., Tartari, A., Torchinsky, S.A., Voisin, F., Zannoni, M., Ade, P., Alberro, J.G., Almela, A., Amico, G., Arnaldi, L.H., Auguste, D., Aumont, J., Azzoni, S., Banfi, S., Bélier, B., Baù, A., Bennett, D., Bergé, L., Bernard, J.P., Bersanelli, M., Bonaparte, J., Bonis, J., Bunn, E., Burke, D., Buzi, D., Cavaliere, F., Chapron, C., Cerutti, A.C.C., Columbro, F., Coppolecchia, A., Gasperis, G.D., Leo, M.D., Dheilly, S., Duca, C., Dumoulin, L., Etchegoyen, A., Fasciszewski, A., Ferreyro, L.P., Fracchia, D., Franceschet, C., Ganga, K.M., García, B., Redondo, M.E.G., Gaspard, M., Gayer, D., Gervasi, M., Giard, M., Gilles, V., Giraud-Heraud, Y., Berisso, M.G., González, M., Gradziel, M., Hampel, M.R., Harari, D., Henrot-Versillé, S., Incardona, F., Jules, E., Kaplan, J., Kristukat, C., Lamagna, L., Loucatos, S., Louis, T., Maffei, B., Marty, W., Mattei, A., May, A., McCulloch, M., Mele, L., Melo, D., Montier, L., Mundo, L.M., Murphy, J.A., **J.D. Murphy**, Nati, F., Olivieri, E., Oriol, C., Paiella, A., Pajot, F., Passerini, A., Pastoriza, H., Pelosi, A., Perbost, C., Perciballi, M., Pezzotta, F., Piacentini, F., Piccirillo, L., Pisano, G., Platino, M., Polenta, G., Prêle, D., Puddu, R., Rambaud, D., Ringegni, P., Romero, G.E., Rasztocky, E., Salum, J.M., Schillaci, A., Scully, S., Spinelli, S., Stankowiak, G., Supanitsky, A.D., Thermeau, J.P., Timbie, P., Tomasi,

M., Tucker, C., Tucker, G., Viganò, D., Vittorio, N., Wicek, F., Wright, M., and Zullo, A.
QUBIC I: Overview and Science Program. *Journal of Cosmology and Astroparticle Physics*, 2022. URL `https://arxiv.org/abs/2011.02213v2`.

[67] Piat, M., the QUBIC Collaboration, incl. **Murphy, J.D.**
QUBIC IV: Performance of TES Bolometers and Readout Electronics. *Journal of Cosmology and Astroparticle Physics*, 2022. URL `https://arxiv.org/abs/2101.06787v2`.

[68] Masi, S., the QUBIC Collaboration, incl. **Murphy, J.D.**
QUBIC V: Cryogenic system design and performance. *Journal of Cosmology and Astroparticle Physics*, 2022. URL `https://arxiv.org/abs/2008.10659v2`.

[69] D'Alessandro, G., the QUBIC Collaboration, incl. **Murphy, J.D.**
QUBIC VI: cryogenic half wave plate rotator, design and performances. *Journal of Cosmology and Astroparticle Physics*, 2022. URL `https://arxiv.org/abs/2008.10667v2`.

[70] Cavaliere, F., the QUBIC Collaboration, incl. **Murphy, J.D.**
QUBIC VII: The feedhorn-switch system of the technological demonstrator. *Journal of Cosmology and Astroparticle Physics*, 2022. URL `https://arxiv.org/abs/2008.12721v2`.

[71] O'Sullivan, C., De Petris, M., Amico, G., Battistelli, E.S., Burke, D., Buzi, D., Chapron, C., Conversi, L., D'Alessandro, G., de Bernardis, P., Leo, M.D., Gayer, D., Grandsire, L., Hamilton, J.C., Marnieros, S., Masi, S., Mattei, A., Mennella, A., Mousset, L., **Murphy, J.D.**, Pelosi, A., Perciballi, M., Piat, M., Scully, S., Tartari, A., Torchinsky, S.A., Voisin, F., Zannoni, M., Zullo, A., et al.
QUBIC VIII: Optical design and performance. *Journal of Cosmology and Astroparticle Physics*, 2022. URL `https://arxiv.org/abs/2008.10119v2`.

[72] May, A.J., the QUBIC Collaboration, incl. **Murphy, J.D.**
Thermal architecture for the QUBIC cryogenic receiver. In Zmuidzinas, J. and Gao, J.R., editors, *Millimeter, Submillimeter, and Far-Infrared Detectors and Instrumentation for Astronomy IX*, volume 10708, pages 610 – 623. International Society for Optics and Photonics, SPIE, 2018. doi: 10.1117/12.2312085. URL `https://doi.org/10.1117/12.2312085`.

[73] Tucker, C.E. and Ade, P.A.R. Thermal filtering for large aperture cryogenic detector arrays. In Zmuidzinas, J., Holland, W.S., Withington, S., and Duncan, W.D., editors, *Millimeter and Submillimeter Detectors and Instrumentation for Astronomy III*, volume 6275, pages 239 – 247. International Society for Optics and Photonics, SPIE, 2006. URL `https://doi.org/10.1117/12.673159`.

[74] Ade, P.A.R., Pisano, G., Tucker, C., and Weaver, S. A review of metal mesh filters. In Zmuidzinas, J., Holland, W.S., Withington, S., and Duncan, W.D., editors, *Millimeter and Submillimeter Detectors and Instrumentation for Astronomy III*, volume 6275, pages 248 – 262. International Society for Optics and Photonics, SPIE, 2006. URL `https://doi.org/10.1117/12.673162`.

[75] Piccirillo, L., Ade, P., Audley, M.D., Baines, C., et al. The ClOVER experiment. In Duncan, W.D., Holland, W.S., Withington, S., and Zmuidzinas, J., editors, *Millimeter and Submillimeter Detectors and Instrumentation for Astronomy IV*, volume 7020 of *Society of Photo-Optical Instrumentation Engineers (SPIE) Conference Series*, page 70201E, July 2008. doi: 10.1117/12.788927.

[76] Ade, P.A., Wylde, R.J., and Zhang, J. Ultra-Gaussian Horns for ClOVER - a B-Mode CMB Experiment. In Bryerton, E., Kerr, A., and Lichtenberger, A., editors, *Twentieth International Symposium on Space Terahertz Technology*, page 128, April 2009.

[77] Scully, S. *Quasi-Optical Design and Analysis of a Bolometric Interferometer for Cosmic Microwave Background Radiation Experiments*. PhD thesis, National University of Ireland Maynooth, 2016. URL `http://eprints.maynoothuniversity.ie/7083/`.

[78] Enss, C., editor. *Cryogenic particle detection*, volume 99 of *Topics in applied physics*. Springer, Berlin, Germany, 2005.

[79] Pajot, F., Ade, P. A. R., Beney, J.-L., Bréelle, E., et al. Planck pre-launch status: HFI ground calibration. *A&A*, 520:A10, 2010. doi: 10.1051/0004-6361/200913203. URL `https://doi.org/10.1051/0004-6361/200913203`.

[80] Henrot-Versillé, S., Cizeron, R., and Couchot, F. Pulsed carbon fiber illuminators for fir instrument characterization. *Infrared Physics & Technology*, 52(5):159 – 165, 2009. ISSN 1350-4495. doi: https://doi.org/10.1016/j.infrared.2009.07.001. URL `http://www.sciencedirect.com/science/article/pii/S1350449509000735`.

[81] Chanial, P. and Barbey, N. Pyoperators: Operators and solvers for high-performance computing. *sf2a*, pages 513–517, 2012.

[82] Balanis, C.A. *Antenna theory: analysis and design*. Wiley, Hoboken, New Jersey, 4th edition, 2016. ISBN 978-1-118-64206-1.

[83] Johansen, P.M. Uniform physical theory of diffraction equivalent edge currents for truncated wedge strips. *IEEE Transactions on Antennas and Propagation*, 44:989–995, 1996.

[84] Johansen, P. Uniform physical theory of diffraction equivalent edge currents for implementation in general computer codes. In *IEEE Antennas and Propagation Society International Symposium. 1996 Digest*, volume 2, pages 784–787 vol.2, 1996. doi: 10.1109/APS.1996.549713.

[85] Shore, R. and Yaghjian, A. Incremental diffraction coefficients for planar surfaces. *IEEE Transactions on Antennas and Propagation*, 36(1):55–70, 1988. doi: 10.1109/8.1075.

[86] TICRA. GRASP, 2015. URL `https://www.ticra.com/software/grasp/`.

[87] Pontoppidan, K. *GRASP Technical Description*. TICRA, 2015.

[88] Nave, C.R. Huygens' principle, 2019. URL `http://hyperphysics.phy-astr.gsu.edu/hbase/phyopt/huygen.html`.

[89] Gradziel, M., O'Sullivan, C., Murphy, J., Cahill, G., Curran, G., Pryke, C., Gear, W., and Church, S. Modelling of the optical performance of millimetre-wave instruments in modal. In *Terahertz and Gigahertz Electronics and Photonics VI*, volume 6472, 5 2007. ISBN 0819465852. doi: 10.1117/12.700680.

[90] Burke, D. *Design and Analysis of the Optical Beam Combiner and Corrugated Feed Horns for the QUBIC Instrument*. PhD thesis, National University of Ireland, Maynooth, 2021. URL `https://mural.maynoothuniversity.ie/14879/`.

[91] Brossard, J., Piat, M., Chanial, P., Chapron, C., O'Sullivan, C., Scully, S., Gayer, D., De Petris, M., Buzi, D., and Maffei, B. QUBIC 1st module frames definition, ref: ATRIUM-77650, 2017.

[92] Goldsmith, P., Theory, I.M., and Society, T. *Quasioptical Systems: Gaussian Beam Quasioptical Propagation and Applications*. IEEE Press/Chapman & Hall Publishers series on microwave technology and RF. IEEE Press, 1998. ISBN 9780470546291. URL `https://books.google.ie/books?id=3bxpswEACAAJ`.

[93] Brossard, J., Piat, M., Grandsire, L., and Christophe, J.C. TES pixel and matrix dimensions for the 1st module of QUBIC, document no. I-037739, 2015.

[94] Cs filter assembly, document no. I-112593, 2017.

[95] Henrot-Versillé, S. *Archeops et Planck-HFI : Etudes des systématiques pour l'analyse du fond diffus cosmologique*. Habilitation à diriger des recherches, Université Paris Sud - Paris XI, June 2006. URL `https://tel.archives-ouvertes.fr/tel-00102694`. LAL 06-54.

[96] Brossard, J. and Chanial, P. HORNS location for the 1st module of QUBIC, document no. I-037491, 2014.

[97] Chapron, C. Mirror M1 Atrium ID-77566. Technical Drawing, 2018. Online; accessed 11 May 2020.

[98] Gayer, D. Thesis in QUBIC Optics. National University of Ireland Maynooth, 2021. Anticipated PhD Thesis.

[99] Virtanen, P., Gommers, R., Oliphant, T.E., Haberland, M., Reddy, T., Cournapeau, D., Burovski, E., Peterson, P., Weckesser, W., Bright, J., van der Walt, S.J., Brett, M., Wilson, J., Jarrod Millman, K., Mayorov, N., Nelson, A.R.J., Jones, E., Kern, R., Larson, E., Carey, C., Polat, İ., Feng, Y., Moore, E.W., Vand erPlas, J., Laxalde, D., Perktold, J., Cimrman, R., Henriksen, I., Quintero, E.A., Harris, C.R., Archibald, A.M., Ribeiro, A.H., Pedregosa, F., van Mulbregt, P., and Contributors, S... SciPy 1.0: Fundamental Algorithms for Scientific Computing in Python. *Nature Methods*, 17: 261–272, 2020. doi: https://doi.org/10.1038/s41592-019-0686-2.

[100] Barber, C.B., Dobkin, D.P., and Huhdanpaa, H. The quickhull algorithm for convex hulls. *ACM Trans. Math. Softw.*, 22(4):469–483, December 1996. ISSN 0098-3500. doi: 10.1145/235815.235821. URL `https://doi.org/10.1145/235815.235821`.

[101] Claude Chapron. Mirror M2 Atrium ID-77565. Technical Drawing, 2018. Online; accessed 11 May 2020.

[102] Virginia Diodes Inc. *130 - 170 GHz Tx User Guide*, 2017.

[103] Haykin, S. *Communication Systems*. Wiley Publishing, 5th edition, 2009. ISBN 0471697907.

[104] Mousset, L., Lerena, M.M.G., Chanial, P., Hamilton, J.C., **Murphy, J.D.**, Incardona, F., Stolpovskiy, M., Torchinsky, S., Scoccola, C., Tristram, M., Kaplan, J., Henrot-Versille, S., Regnier, M., and Tomasi, M.
qubicsoft. `https://github.com/mousset/qubic`, 2021.

[105] Duivenvoorden, A.J., Gudmundsson, J.E., and Rahlin, A.S. Full-sky beam convolution for cosmic microwave background applications. *Monthly Notices of the Royal Astronomical Society*, 486(4):5448–5467, May 2019. ISSN 1365-2966. doi: 10.1093/mnras/stz1143. URL `http://dx.doi.org/10.1093/mnras/stz1143`.

[106] Fowler, J.W., Niemack, M.D., Dicker, S.R., Aboobaker, A.M., Ade, P.A.R., Battistelli, E.S., Devlin, M.J., Fisher, R.P., Halpern, M., Hargrave, P.C., and et al. Optical design of the atacama cosmology telescope and the millimeter bolometric array camera. *Applied Optics*, 46(17):3444, May 2007. ISSN 1539-4522. doi: 10.1364/ao.46.003444. URL `http://dx.doi.org/10.1364/AO.46.003444`.

[107] Aikin, R., Bock, J., Brevik, J., Dowell, C., Filippini, J., Golwala, S., Hristov, V., Lange, A., Nguyen, H., Orlando, A., Richter, S., Runyan, M., and Teply, G. Optical performance of the BICEP2 Telescope at the South Pole. *Proc SPIE*, 7741:77410V, 07 2010. doi: 10.1117/12.857868.

[108] Prêle, D., Voisin, F., Piat, M., Decourcelle, T., Perbost, C., Chapron, C., Rambaud, D., Maestre, S., Marty, W., and Montier, L. A 128 Multiplexing Factor Time-Domain SQUID Multiplexer. *Journal of Low Temperature Physics*, 184(1-2):363–368, July 2016. doi: 10.1007/s10909-015-1449-9.

[109] Torchinsky, S. Private Communication, 2020.

[110] Kahneman, D. and Tversky, A. Subjective probability: A judgment of representativeness. *Cognitive Psychology*, 3(3):430 – 454, 1972. ISSN 0010-0285. doi: https://doi.org/10.1016/0010-0285(72)90016-3. URL `http://www.sciencedirect.com/science/article/pii/0010028572900163`.

[111] Thompson, A.R., Moran, J.M., and Swenson, J., George W. *Interferometry and Synthesis in Radio Astronomy, 3rd Edition*. 2017. doi: 10.1007/978-3-319-44431-4.

[112] Burke, B.F. and Graham-Smith, F. *An Introduction to Radio Astronomy*. Cambridge University Press, 3 edition, 2009. doi: 10.1017/CBO9780511801310.

[113] Marr, J.M., Snell, R.L., and Kurtz, S. *Fundamentals of radio astronomy: observational methods*. CRC Press, Boca Raton, FL, 2016. ISBN 13: 978-1-4987-7019-4.

[114] Wilner, D.J. Imaging and deconvolution. `https://science.nrao.edu/science/meetings/2014/14th-synthesis-imaging-workshop/lectures-files/wilner_siw2014.pdf`, 2014. Accessed: 28-10-2010.

[115] Högbom, J.A. Aperture Synthesis with a Non-Regular Distribution of Interferometer Baselines. *Astronomy and Astrophysics, Supplement*, 15:417, June 1974.

[116] Wieringa, M.H. An investigation of the telescope based calibration methods 'redundancy' and 'self-cal'. *Experimental Astronomy*, 2(4):203–225, July 1992. doi: 10.1007/BF00420576.

[117] Readhead, A.C.S. and Wilkinson, P.N. The mapping of compact radio sources from VLBI data. *Astrophysical Journal*, 223:25–36, July 1978. doi: 10.1086/156232.

[118] Liu, A., Tegmark, M., Morrison, S., Lutomirski, A., and Zaldarriaga, M. Precision calibration of radio interferometers using redundant baselines. *Monthly Notices of the Royal Astronomical Society*, 408(2):1029–1050, Jul 2010. ISSN 0035-8711. doi: 10.1111/j.1365-2966.2010.17174.x. URL `http://dx.doi.org/10.1111/j.1365-2966.2010.17174.x`.

[119] Dillon, J.S., Lee, M., Ali, Z.S., Parsons, A.R., et al. Redundant-baseline calibration of the hydrogen epoch of reionization array. *Monthly Notices of the Royal Astronomical Society*, 499(4):5840–5861, Oct 2020. ISSN 1365-2966. doi: 10.1093/mnras/staa3001. URL `http://dx.doi.org/10.1093/mnras/staa3001`.

[120] Charlassier, R. *Mesure des anisotropies de polarisation du fond diffus cosmologique avec l'interféromètre bolométrique QUBIC.* Theses, Université Paris-Diderot - Paris VII, July 2010. URL `https://tel.archives-ouvertes.fr/tel-00725929`.

[121] Bryan, S.A., Simon, S.M., Gerbino, M., Teply, G., et al. Development of calibration strategies for the Simons Observatory. In Zmuidzinas, J. and Gao, J.R., editors, *Millimeter, Submillimeter, and Far-Infrared Detectors and Instrumentation for Astronomy IX*, volume 10708, pages 685 – 697. International Society for Optics and Photonics, SPIE, 2018. doi: 10.1117/12.2313832. URL `https://doi.org/10.1117/12.2313832`.

[122] Dicker, S.R., Gallardo, P.A., Gudmundsson, J.E., Mauskopf, P.D., Ali, A., Ashton, P.C., Coppi, G., Devlin, M.J., Galitzki, N., Ho, S.P., Hill, C.A., Hubmayr, J., Keating, B., Lee, A.T., Limon, M., Matsuda, F., McMahon, J., Niemack, M.D., Orlowski-Scherer, J.L., Piccirillo, L., Salatino, M., Simon, S.M., Staggs, S.T., Thornton, R., Ullom, J.N., Vavagiakis, E.M., Wollack, E.J., Xu, Z., and Zhu, N. Cold optical design for the large aperture Simons' Observatory telescope. In Marshall, H.K. and Spyromilio, J., editors, *Ground-based and Airborne Telescopes VII*, volume 10700, pages 1064 – 1076. International Society for Optics and Photonics, SPIE, 2018. doi: 10.1117/12.2313444. URL `https://doi.org/10.1117/12.2313444`.

[123] **Murphy, J.D.**, Burke, D., Lerena, M.M.G., Hamilton, J.C., Mousset, L., De Petris, M., O'Sullivan, C., Torchinsky, S.A., et al.
Calibration of QUBIC: The Q and U bolometric interferometer for cosmology. In Zmuidzinas, J. and Gao, J.R., editors, *Millimeter, Submillimeter, and Far-Infrared Detectors and Instrumentation for Astronomy X*, volume 11453, pages 378 – 387. International Society for Optics and Photonics, SPIE, 2020. doi: 10.1117/12.2560172. URL `https://doi.org/10.1117/12.2560172`.